Theory of nonlinear acoustic forces acting on fluids and particles in microsystems

Karlsen, Jonas Tobias

Publication date:
2018

Document Version
Publisher's PDF, also known as Version of record

DTU Physics
Department of Physics

Jonas T. Karlsen

Theory of nonlinear acoustic forces acting on fluids and particles in microsystems

PhD thesis
Copenhagen, January 2018

Advised by Professor Henrik Bruus

Cover illustration: —

Theory of nonlinear acoustic forces acting on fluids and particles in microsystems

Typeset using LaTeX.

Department of Physics
Technical University of Denmark
DTU Physics Building 309, DK-2800 Kongens Lyngby, Denmark
http://www.fysik.dtu.dk/microfluidics

To the memory of my father

Abstract

Acoustofluidics is the combined science of *acoustics* and *microfluidics*. In acoustofluidics, ultrasound acoustic waves are used to generate forces for manipulation of fluids and particles in networks of microchannels in a microfluidic chip. The microscale systems are designed to enable fundamentally new capabilities in chemical, biomedical, or clinical studies of single cells and bioparticles.

This thesis, entitled *Theory of nonlinear acoustic forces acting on fluids and particles in microsystems*, advances the fundamental understanding of acoustofluidics by addressing the origin of the nonlinear acoustic forces acting on fluids and particles. Classical results in nonlinear acoustics for the non-dissipative acoustic radiation force acting on a particle or an interface, as well as the dissipative acoustic force densities driving acoustic streaming, are derived and discussed in terms of a single principal equation. This principal equation relates the acoustic force density to the divergence in the acoustic (pseudo-)momentum-flux-density tensor, dependent only on the linear acoustic fields.

Extending the principal equation to the case of an inhomogeneous fluid with variations in the continuous fluid parameters of density and compressibility, e.g., due to a solute concentration field, the thesis presents novel analytical results on the acoustic force density acting on inhomogeneous fluids in acoustic fields. This inhomogeneity-induced acoustic force density is non-dissipative in origin, in contrast to the force densities driving acoustic streaming in a homogeneous fluid. It depends on the linear acoustic fields and the gradients in the fluid density and compressibility, and leads to a dynamic relocation and stabilization of inhomogeneities in acoustic fields, as demonstrated by simulations as well as experiments with aqueous solutions in an acoustofluidic glass-silicon microchip.

The ability of the acoustic force density to stabilize fluid inhomogeneities makes possible the development of a microfluidic analog to density-gradient centrifugation, called iso-acoustic focusing, which is demonstrated for acousto-mechanical phenotyping of single white blood cells and cancer cells in continuous flow. The theory of the acoustic force density furthermore leads to the prediction of the possibility of using acoustic tweezers to actively manipulate miscible-fluid interfaces and concentration fields at the microscale. Experimental work in progress verifies the validity of this prediction.

Finally, boundary-driven acoustic streaming, historically limited to the study of homogeneous fluids, is brought into the realm of inhomogeneous fluids in a theoretical, numerical, and experimental study of acoustic streaming in inhomogeneous fluids. The study presents the discovery and description of a new class of suppressed acoustic streaming flows resulting from the competition between the classical dissipative boundary-driven

acoustic force density and the inhomogeneity-induced acoustic force density that stabilizes the inhomogeneity configuration, thereby suppressing the advective streaming flow. The suppressed acoustic streaming flow evolves towards the well-known boundary-driven streaming pattern, as the acoustically stabilized inhomogeneity profile flattens by diffusion and advection on a one-minute time scale.

More theoretical and experimental work is needed to fully understand the implications of the theory of acoustofluidics in inhomogeneous fluids presented in this thesis, and I can only hope that this thesis will inspire such research activities.

Resumé

Akustofluidik er videnskaben, der vedrører sammenspillet mellem *akustik* og *mikrofluidik*. I akustofluidik bruges ultralydsbølger til at generere kræfter til manipulation af væsker og partikler i et netværk a mikrokanaler på en mikrochip. Mikrochipsystemerne er designet til at muliggøre nye typer af studier af enkelte celler og biopartikler med kemiske, biomedicinske, og kliniske anvendelser.

Denne afhandling, med titlen *Teori for ikke-lineære akustiske kræfter virkende på væsker og partikler i mikrosystemer*, fremmer den grundlæggende forståelse af akustofluidik ved at analysere årsagen til de ikke-lineære akustiske kræfter, der virker på væsker og partikler. Klassiske resultater fra ikke-lineær akustik for den ikke-dissipative akustiske strålingskraft på en partikel eller en grænseflade, såvel som for den dissipative akustiske krafttæthed, der driver akustisk strømning, udledes og diskuteres ud fra en enkelt grundlæggende ligning. Denne grundlæggende ligning relaterer den akustiske krafttæthed til divergensen i den akustiske (pseudo-)impuls-flux-tæthedstensor, som kun afhænger af de lineære akustiske felter.

Afhandlingen præsenterer nye analytiske resultater for den akustiske krafttæthed virkende på en inhomogen væske med kontinuerte variationer i densitet og kompressibilitet, som for eksempel kan forårsages af et varierende koncentrationsfelt. Den akustiske krafttæthed virkende på en inhomogen væske er grundlæggende ikke-dissipativ i modsætning til krafttæthederne, der driver akustisk strømning i en homogen væske. Den afhænger af de lineære akustiske felter og af gradienterne i væskens densitet og kompressibilitet, og fører til en dynamisk omfordeling og stabilisering af væskeinhomogeniteter i akustiske felter. Dette er demonstreret gennem numeriske simuleringer såvel som gennem forsøg med vandige opløsninger i en akustofluidisk mikrochip produceret i silicium og glas.

Den akustiske krafttætheds evne til at stabilisere væskeinhomogeniteter gør det muligt at udvikle en mikrofluidisk analog til densitetsgradientcentrifugering kaldet iso-akustisk fokusering. Metoden er demonstreret til bestemmelse af fænotype af enkelte celler, herunder hvide blodceller og kræftceller, i kontinuerlig strømning. Teorien for den akustiske krafttæthed fører endvidere til forudsigelsen af muligheden for at anvende en akustisk pincet til aktivt at manipulere blandbare væskegrænseflader samt koncentrationsfelter på mikroskala. Igangværende eksperimentelt arbejde verificerer gyldigheden af denne forudsigelse.

Endelig foretages et teoretisk, numerisk, og eksperimentelt studie af grænsedrevet akustisk strømning i inhomogene væsker. Dette studie udvider de klassiske studier af akustisk strømning, som har været begrænset til homogene væsker. Studiet præsenterer

en ny klasse af undertrykte akustiske strømninger, som skyldes konkurrencen mellem den dissipative grænsedrevne akustiske krafttæthed og den inhomogenitetsfremkaldte akustiske krafttæthed, der stabiliserer inhomogenitetskonfigurationen og derved undertrykker den advektive strømning. Den undertrykte akustiske strømning udvikler sig mod det velkendte grænsedrevne strømningsmønster på en 1-min tidsskala, efterhånden som den akustisk stabiliserede inhomogenitetsprofil aftager ved diffusion og advektion.

Der er behov for mere teoretisk og eksperimentelt arbejde for fuldt ud at forstå konsekvenserne af teorien for akustofluidik i inhomogene væsker præsenteret i denne afhandling. Jeg kan kun håbe, at afhandlingen vil inspirere sådanne forskningsaktiviteter.

Preface

This thesis is submitted in candidacy for the degree of Doctor of Philosophy (PhD) from the Technical University of Denmark (DTU). The work was carried out in the Department of Physics, Section of Biophysics and Fluids, in the Theoretical Microfluidics Group, during the three years and five months from 15 August 2014 to 13 January 2018, under supervision of Professor Henrik Bruus. The project included an external research stay from April 2017 to June 2017 in the group of Professor Michaël Baudoin, Université Lille 1, IEMN, France. The project was funded by an internal scholarship from DTU, and further supported by the Danish Ministry of Science's Elite Research Initiative.

Copenhagen, January 2018

Jonas T. Karlsen

Acknowledgements

First, I would like to thank my supervisor Henrik Bruus for his endless enthusiasm for physics, and for his encouragement of my efforts in physics. Many late afternoons and evenings, especially in my early PhD studies, were spent in his office scrutinizing some argument or equation on the whiteboard, and these sessions have formed me as a physicist. Café physics was introduced to me by Henrik, and I have enjoyed many physics discussions with Henrik at cafés around the world, from Paris to Salt Lake City.

Second, I would like to thank my collaborators. Most importantly Per Augustsson, Lund University, who introduced me to acoustofluidics in inhomogeneous fluids after a PhD defence, and who invited me to join his studies with Hao Wei-Su and Joel Voldman, MIT, when, one week later, I sent him an email with a simple model explaining some of his observations. Thanks go to Mads Givskov Senstius, DTU, who assisted with experiments as part of a course project. Finally, I would like to thank Wei Qiu, DTU, who worked committed with the experiments at Lund University.

Third, I would like to thank Professor Michaël Baudoin and the members in his section and group at Université Lille 1, IEMN, for welcoming me in Lille during my external research stay from April to June 2017. In particular, Jean-Claude Gerbedoen, SATT du Nord, IEMN, who patiently introduced me to the experimental lab facilities and taught me how to survive in the clean room.

A special thanks goes to past and present members of the Theoretical Microfluidics Group for helping create a productive and enjoyable working environment. First, my good friend and former office buddy Mikkel Wennemoes Hvitfeld Ley. In addition, Peter Muller Tribler, Christoffer Peder Nielsen, Rayisa Moiseyenko, Fabio Garofalo, Jacob Søberg Bach, Nils Refstrup Skov, and Wei Qiu.

I am grateful for my good friends from my time as a physics student at DTU, many of whom have been around since the beginning of our studies in 2008.

I wish to thank my girlfriend and, as of 23 September 2017, wife Emilie for always supporting me in my endeavours, for calling me on the phone and encouraging me before a big talk at a conference, and for helping me keep my feet on the ground. Furthermore, my son Sixten, for letting me rediscover the world through the eyes of a child.

I am grateful to my parents and my siblings for enduring a restless soul like mine. Many grateful thoughts go to my mother, and to the memory of my father. I am grateful to you both for inspiring in me the confidence to pursue my own ideas.

Contents

List of publications

Peer-reviewed journal papers

I. J.T. Karlsen and H. Bruus, *Forces acting on a small particle in an acoustical field in a thermoviscous fluid*, Phys. Rev. E **92**, 043010 (2015). Editors' Suggestion. Enclosed in Chapter 6, Ref. [1].

II. P. Augustsson, J.T. Karlsen, H.-W. Su, H. Bruus, and J. Voldman, *Iso-acoustic focusing of cells for size-insensitive acousto-mechanical phenotyping*, Nat. Commun. **7**, 11556 (2016). Enclosed in Chapter 7, Ref. [2].

III. J.T. Karlsen, P. Augustsson, and H. Bruus, *Acoustic force density acting on inhomogeneous fluids in acoustic fields*, Phys. Rev. Lett. **117**, 114504 (2016). Editors' Suggestion. Enclosed in Chapter 8, Ref. [3].

IV. J.T. Karlsen and H. Bruus, *Acoustic tweezing and patterning of concentration fields in microfluidics*, Phys. Rev. Applied **7**, 034017 (2017). Enclosed in Chapter 9, Ref. [4].

V. J.T. Karlsen, W. Qui, P. Augustsson, and H. Bruus, *Acoustic streaming and its suppression in inhomogeneous fluids*, Phys. Rev. Lett. **in press** (accepted 9 January 2018), https://arxiv.org/abs/1707.07369 (old version). Revised accepted version enclosed in Chapter 10, Ref. [5].

Peer-reviewed conference contributions

1. J.T. Karlsen, W. Qiu, P. Augustsson, and H. Bruus, *Acoustic streaming in inhomogeneous fluids - a numerical study*, Proc. Acoustofluidics 2017 Conference, 28-29 August 2017, San Diego, CA, USA, **poster presentation**. Remark: presented by H. Bruus.

2. W. Qiu, J.T. Karlsen, H. Bruus, and P. Augustsson, *Acoustic streaming in inhomogeneous fluids - an experimental study*, Proc. Acoustofluidics 2017 Conference, 28-29 August 2017, San Diego, CA, USA, **poster presentation**.

3. J.T. Karlsen and H. Bruus, *Acoustic tweezing and patterning of concentration fields in microfluidics*, Flow17 Conference on Microfluidics, 3-5 July 2017, Paris, France, **oral presentation**.

4. J.T. Karlsen, P. Augustsson, and H. Bruus, *Theory of the acoustic force density acting on inhomogeneous fluids*, 20th MicroTAS Conference, 9-13 October 2016, Dublin, Ireland, **poster presentation**.

5. P. Augustsson, J.T. Karlsen, and H. Bruus, *Acoustophoretic manipulation of submicron objects enabled by density gradients*, 20th MicroTAS Conference, 9-13 October 2016, Dublin, Ireland, **oral presentation**.

6. J.T. Karlsen, P. Augustsson, and H. Bruus, *The acoustic force density acting on inhomogeneous fluids with spatial variations in density and compressibility*, Proc. Acoustofluidics 2016 Conference, 22-23 September 2016, Kongens Lyngby, Denmark, **oral presentation**.

7. J.T. Karlsen, P. Augustsson, and H. Bruus, *Nonlinear acoustic forces acting on inhomogeneous fluids at slow time-scales*, 171st Meeting of the Acoustical Society of America, 23-27 May 2016, Salt Lake City, UT, USA, **oral presentation**.

8. H. Bruus and J.T. Karlsen, *Acoustic forces acting on particles and fluids in microscale acoustofluidics*, 171st Meeting of the Acoustical Society of America, 23-27 May 2016, Salt Lake City, UT, USA, **invited oral presentation**.

9. M.J.H. Jensen, J.T. Karlsen, and H. Bruus, *Theory and simulation of the acoustic radiation force on a single microparticle in an ultrasonic standing wave including thermoviscous effects*, Proc. 22nd Intl. Congress on Sound and Vibration, 8 pages, 12-16 July 2015, Firenze, Italy, **oral presentation**.

10. J.T. Karlsen, M.J.H. Jensen, and H. Bruus, *Thermoviscous theory of ultrasound scattering on microparticles and droplets*, Proc. Acoustofluidics 2014 Conference, 11-12 September 2014, Prato, Italy, **oral presentation**.

Other conference contributions

11. J.T. Karlsen and H. Bruus, *Shaping and control of concentration fields in acoustofluidics*, The Swedish Center for Acoustofluidics and Cell Separation (SWECACS) meeting, 29-30 November 2016, Lund, Sweden, **oral presentation**.

12. J.T. Karlsen and H. Bruus, *The acoustic radiation force on a small thermoviscous or thermoelastic particle suspended in a viscous and heat-conducting fluid*, 68th Annual Meeting of the American Physical Society Division of Fluid Dynamics, 22-24 November 2015, Boston, MA, USA, **oral presentation**.

13. J.T. Karlsen and H. Bruus, *Size-dependent acoustophoretic contrast factor of microparticles and droplets*, Intl. Summer School Complex Motion in Fluids, 9-15 August 2015, Krogerup, Denmark, **oral presentation**.

14. J.T. Karlsen and H. Bruus, *Thermoviscous effects on the acoustic radiation force*, DANSIS Research Seminar, 20 May 2015, Kongens Lyngby, Denmark, **oral presentation**.

Chapter 1

Introduction

In this chapter, the research field of *acoustofluidics* is introduced from a broad perspective, and the motivation of the field is presented and discussed in relation to the thesis. First, Section 1.1 provides a brief and informal zoom-in on acoustofluidics from human experience, meant as an introduction to the layman. Section 1.2 then discusses in more detail the challenges addressed by *microfluidics*. This brings the reader to Section 1.3 on *acoustofluidics*, and Section 1.4 on the approach to studying the *fundamentals* of acoustofluidics. Finally, Section 1.5 presents the structure of the thesis.

1.1 Zooming in on acoustofluidics from human experience

Acoustic waves, or sound waves, are pressure disturbances transmitted through a medium such as air or water, or perhaps the metallic heating pipes in your five-story apartment building. Most human beings accurately sense such pressure disturbances, with the inner ear automatically transforming the disturbances into the electrical signals that the brain interprets as sound. Thus we are able to sense our surroundings, enjoy a beautifully composed piece of music, or communicate with one another, all enabled by acoustic waves. The audible range extends from frequencies between about 20 Hz and 20 kHz, with the deepest bass and the highest pitch, respectively, at the lower and upper end of the range. Acoustics further enables a range of technologies, typically reliant on sound waves outside of the audible range, with the best known example being ultrasound scanners working at MHz frequency, as used in medical imaging for cancer diagnosis, or, in a more joyful context, for fetal imaging of unborn babies, Fig. 1.1(a).

Fluids, i.e., liquids and gasses, are also an important part, even a prerequisite, of human experience. Indeed, the human body consists of a vast amount of fluids, making up approximately half of the body weight [6]. The most prominent of these biofluids is the blood. About half of the blood volume is made up of blood plasma, and the other half by red blood cells. The blood plasma consists of water containing a number of dissolved species such as proteins and glucose. From the naive point of view of a physicist, 1 mL of blood contains on the order of 10^{22} water molecules, 10^9 red blood cells (erythrocytes), 10^8 platelets (thrombocytes), and 10^6 white blood cells (leukocytes), Fig. 1.1(b) [7]. Now, from

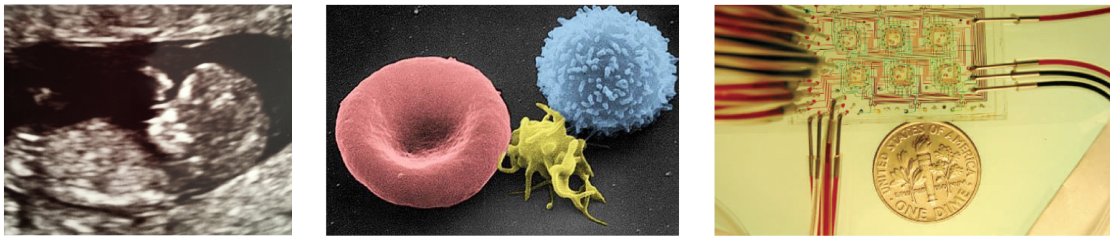

(a) (b) (c)

Figure 1.1: (a) Fetal ultrasound image of my son Sixten. **(b)** Image of a red blood cell (red), a blood platelet (yellow), and a white blood cell (blue) obtained by scanning electron microscopy [12]. **(b)** The concept of a lab-on-a-chip is to scale down laboratory processes onto a single microfluidic chip. Adapted from Belagaddé *et al.*, Ref. [13].

the point of view of a medical doctor, blood is much more than that. Indeed, blood samples can be used to tap into the physical health of an individual by monitoring the levels of a specific "particle", e.g., a protein or a cell, in the blood. However, conventional methods for detection of rare particles in the blood often require large blood volumes to be sent to central laboratories for processing, and the process is both time-consuming and expensive, if at all possible [7]. *Microfluidics* holds promise for faster and cheaper point-of-care diagnostics, i.e., diagnostics performed on-site without the need of a clinical laboratory, by scaling down the laboratory process [8]. The idea is that the conventional laboratory process can be scaled down and automated on a so-called lab-on-a-chip, Fig. 1.1(c).

Acoustofluidics is the combined science of acoustics and microfluidics. Researchers in the field utilize that ultrasound acoustic waves can generate forces that can be used to manipulate fluids and particles in microchannels, often with biomedical or diagnostic applications [9, 10, 11]. Building on the state-of-the-art, this thesis develops the *theory of nonlinear acoustic forces acting on fluids and particles in microsystems.*

1.2 Motivating microfluidics

Consider the detection of circulating tumor cells (CTCs) in patient blood as an example for motivating microfluidic technologies. CTCs are tumor cells, shed from a cancer tumor, that circulate the bloodstream in very low concentration with the potential to form metastases [14]. CTCs are of interest both as diagnostic and prognostic markers, as they may indicate the presence of a tumor at an early stage, and also may be used as an indicator for disease progression and response to treatments [15]. Consider again the 1 mL blood (Section 1.1) containing on the order of 10^9 and 10^6 red and white blood cells, respectively. In a cancer patient, 1 mL of blood contains on the order of 1-10 CTCs [14, 16]. Thus, even with lysis of the red blood cells, the ratio of CTCs to white blood cells could be as low as 1 to 10^6. Considering that a standard clinical blood sample is around 5 mL, the need for microfluidic methods should be evident. Indeed, it is highly unlikely that 1 in 10^6 cells could be detected by any kind of macroscopic ensemble average. Thus single-cell measurements are needed, which, in turn, requires handling of fluids and cells at the

microscale.

The detection and isolation of CTCs in blood is just one of many cases where microfluidic technologies are needed to enable fundamentally new capabilities not offered by existing macroscopic technologies [7]. Sepsis, a disease caused by bacterial infection in the bloodstream, is considered one of the leading causes of preventable deaths in the developed world with an estimated 300 annual incidents per 100,000 people in developed countries, and a mortality rate close to 30% [17, 18]. The disease can be treated with the proper antibiotics, however, the low concentrations of bacteria in the blood make detection difficult, and the standard approach requires blood culturing in clinical laboratories with detection times between 29-130 h [19]. A point-of-care microfluidic device for sepsis diagnosis could potentially speed up this process and save thousands of lives. Point-of-care diagnostics, and devices continually monitoring the health condition of individuals, will likely play an important role in the future of healthcare, as suggested by the trend of personalized medicine. Examples of two well-known commercial microfluidic point-of-care tests currently available to end users are the glucose meter and the pregnancy test [8].

Microfluidic networks in combination with actuation and sensing technologies enable advanced on-chip cell studies, as well as the ability to isolate, concentrate, capture, and separate bioparticles and cells from complex biofluids [20, 21]. While conventional macroscopic methods for isolation of particles typically rely on centrifugation or filtration, microfluidic systems have been developed to utilize a range of different force fields [7, 21]. These include hydrodynamic inertial forces [22], dielectric forces [23], magnetic forces [24], optical forces [25], and finally the *acoustic forces* investigated in this thesis.

1.3 Motivating acoustofluidics

The research in acoustofluidics [9, 10, 11] is for the most part driven by engineers exploring the capabilities of acoustofluidics to solve outstanding problems in chemical and biomedical engineering. In relation to the examples discussed in Section 1.2, acoustofluidics has been employed to isolate CTCs [26, 27, 16] as well as bacteria [28, 29, 30, 31] from blood. Considering the latter, an integrated acoustofluidic system designed for rapid sepsis diagnosis could potentially reduce detection time from the standard 29-130 h to about 2 h [19]. For patients with septic shock, every hour of delay of proper antibiotic treatment, in the first 6 h, is associated with a 7.6% decrease in survival rate [32], stressing the importance of the further development of such methods.

Acoustofluidic particle-manipulation is contact-less and label-free, and methods have been developed for concentrating [33, 29], trapping [34, 35], washing [36], patterning [37], and separating cells [38, 27] and bacteria [28, 19], as well as microvesicles [39, 40]. While the high electric and magnetic fields used in dielectric and magnetic manipulation methods can pose problems to living cells, acoustic fields show excellent biocompatibility [41, 42]. Compared to optics, acoustics has the advantage of yielding a larger force for a given intensity, which means that relatively large forces can be obtained without thermal damage due to absorption [43]. While optical tweezers have an unmatched precision in single-particle manipulation, acoustics allow for thousands of particles to be manipulated in parallel, as uti-

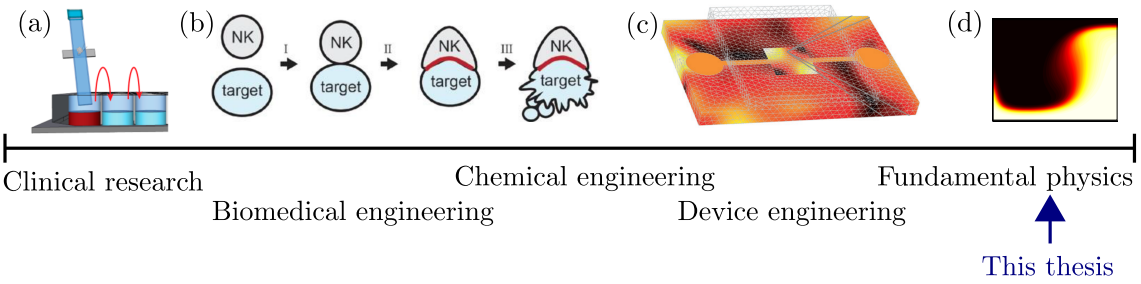

Figure 1.2: Spectrum of acoustofluidic research with examples from the literature. **(a)** Detection of bacteria in clinically relevant blood samples by Hammarström *et. al* [31]. **(b)** Acoustically-induced interactions of Natural Killer (NK) cells and target cancer cells by Wiklund *et al.* [34]. **(c)** Full-chip acoustofluidic device modeling by Hahn *et al.* [59]. **(d)** Theory of the acoustic force density acting on inhomogeneous fluids by Karlsen *et al.* [3]. The illustrations are adapted from the references in this caption.

lized, e.g., in acoustic force spectroscopy of biomolecules [44]. Moreover, acoustic fields can be dynamically tailored at the microscale using a number of experimental techniques [45], including bulk acoustic waves [46, 47, 48], surface acoustic waves [49, 50, 51, 52, 53], transducer arrays [54, 55, 56], and 3D-printed transmission holograms or lenses [57, 58]. Compared to hydrodynamic inertial forces, acoustic forces thereby provide dynamical manipulation capabilities, most notably in the form of acoustic tweezers [54, 56, 53].

1.4 Approach of the thesis

Figure 1.2 presents the spectrum of acoustofluidics research, from the most applied clinical research, to the research in the fundamentals of acoustofluidics. This thesis addresses the fundamental physics of acoustofluidics, namely the *theory of nonlinear acoustic forces acting on fluids and particles in microsystems*. However, Fig. 1.2, together with the broad introduction in the previous sections, presents the point of view that fundamental physics research, or biomedical engineering research for that matter, should not be carried out in a "vacuum".

In my opinion, the results achieved in engineering applications ultimately depend on the amount of physical insights used in the design of the studies, and similarly, the significance of fundamental physical theories depend on the level of relevance they have to the design of an applied study. As a consequence, I have, since Paper I [1], tried to initiate and engage in broad collaborations with researchers working with applied aspects of acoustofluidics. This approach has facilitated theoretical investigations of unexplained experimental observations, Papers II and III [2, 3], as well as theoretical predictions and suggestions for experiments, Papers IV and V [4, 5], and has proven an interesting and rewarding way of working with the fundamentals of acoustofluidics.

Although a modern understanding of acoustics was established already by Lord Rayleigh in *The theory of sound*, first published in 1877 [60], microfluidics and acoustofluidics have only been around for a few decades. The scaling down of fluidic systems to the microscale

generally leads to dramatic changes in the physics governing the systems, as dictated by the relative importance of surface and volume effects, which means that new phenomena emerge [61, 62].

In this thesis, the study of acoustofluidic phenomena is approached from the point of view of a physicist by (i) scaling arguments, (ii) analytical theory, (iii) numerical modeling, and (iv) experiments. (i) Scaling arguments are used whenever possible to get intuition about the physical phenomenon. (ii) Analytical theories present an organized approach to understanding the physical phenomenon in various limits yielding insights that cannot be extracted from experiments and simulations. (iii) Numerical modeling allows for solutions of complex problems and validation of analytical theories by comparing simulations to experiments. (iv) Any theory or model is only as good as its predictions, and hence experimental validation is necessary if the theory is to have any significance.

1.5 Structure of the thesis

Having spent a considerable amount of time and effort in carefully preparing the five published research Papers I, II, III, IV, and V [1, 2, 3, 4, 5], I have chosen to include them as the main part of this thesis. The other chapters are designed to put the papers into context by providing the background and context of the studies, as well as describing the relation between the five works. The main chapters of the thesis are as follows.

Chapter 1 Introduction — Broad introduction to the field of acoustofluidics, and the motivations for the research in this thesis in a broader perspective.

Chapter 2 Acoustofluidics background — Background on theoretical acoustofluidics including modern developments. Hydrodynamic transport, acoustic wave propagation, acoustic streaming, the acoustic radiation force, and acoustophoretic particle trajectories are introduced.

Chapter 3 Finite element modeling background — A tehnical chapter containing a short introduction to finite element modeling using COMSOL MULTIPHYSICS .

Chapter 4 Nonlinear acoustics methodology — The author's account of nonlinear acoustics methodology. The origins of well-known nonlinear acoustics phenomena, as well as phenomena first described in this thesis, are all traced to a single principal equation.

Chapter 5 Summary of the results — Brief summaries of the motivation and the main result of each of the published Papers I, II, III, IV, and V.

Chapters 6 - 10 Papers I to V — The published Papers I, II, III, IV, and V in chronological order, including supplemental material. This is the main part of the thesis.

Chapter 11 Experimental work in progress —Description and highlights of experi-

mental work in progress that the author is currently involved in.

Chapter 12 Conclusion and outlook — Conclusion of the thesis and outlook with suggestions for future research.

Chapter 2

Acoustofluidics background

This chapter provides the background in theoretical acoustofluidics needed to understand and appreciate the theoretical, numerical, and experimental aspects of the thesis work presented in the enclosed Papers I to V in Chapters 6 to 10 [1, 2, 3, 4, 5]. The material in this chapter furthermore lays the foundation for the author's presentation of nonlinear acoustics methodology in Chapter 4.

Section 2.1 starts by establishing the governing hydrodynamic and thermodynamic equations on which the ensuing treatment is based. Section 2.2 then describes the fundamentals of wave propagation in a viscous and heat-conducting homogeneous fluid with a special focus on thermoviscous and non-adiabatic effects. In Sections 2.3 and 2.4, the time-averaged nonlinear phenomena of acoustic streaming flows and the acoustic radiation force acting on a particle are introduced from a historical perspective. A modern context is provided by discussing some recent developments and applications in acoustofluidics, and the acoustic radiation force is discussed in relation to the enclosed Paper I [1]. Acoustic streaming and acoustic radiation forces both play important roles in acoustophoresis, as investigated further in Section 2.5 on acoustophoretic particle trajectories.

2.1 Governing hydrodynamic equations

In this section, the governing hydrodynamic equations are established. The first law of thermodynamics and the equations of state are introduced. The transport equations for conservation of mass, momentum, energy, and solute molecules in a fluid are then derived.

2.1.1 The first law of thermodynamics

Introducing the thermodynamic variables of temperature T, pressure p, density ρ, internal energy ε per mass unit, entropy s per mass unit, and volume per mass unit $1/\rho$, the first law of thermodynamics with s and ρ as the independent variables is

$$\mathrm{d}\varepsilon = T\,\mathrm{d}s - p\,\mathrm{d}\left(\frac{1}{\rho}\right) = T\,\mathrm{d}s + \frac{p}{\rho^2}\,\mathrm{d}\rho. \tag{2.1}$$

It is often convenient to use T and p as the independent thermodynamic variables. This is obtained by a Legendre transformation of the internal energy ε per unit mass to the Gibbs free energy g per unit mass, $g = \varepsilon - Ts + p\,\frac{1}{\rho}$, for which $\mathrm{d}g = -s\,\mathrm{d}T + \frac{1}{\rho}\,\mathrm{d}p$. The first law must be supplemented by suitable equations of state. With T and p as the independent variables, these are of the form $\rho = \rho(p, T)$ and $s = s(p, T)$.

2.1.2 Hydrodynamic transport equations

The governing hydrodynamic equations for the conservation of mass, momentum, and energy requires the introduction of the fluid velocity field $\boldsymbol{v}$, the fluid stress tensor $\boldsymbol{\sigma}$, and the conducted heat-flux-density $\boldsymbol{q}$. Making the assumption of an isotropic and Newtonian fluid, the fluid stress tensor $\boldsymbol{\sigma}$ is expressed in terms of the velocity field $\boldsymbol{v}$, the pressure field p, the dynamic shear viscosity η, and the bulk viscosity η_b (or the viscosity ratio $\beta = \eta_\mathrm{b}/\eta + 1/3$), as [62]

$$\boldsymbol{\sigma} = -p\,\mathbf{I} + \boldsymbol{\tau}, \qquad \boldsymbol{\tau} = \eta\left[\boldsymbol{\nabla}\boldsymbol{v} + (\boldsymbol{\nabla}\boldsymbol{v})^{\mathrm{T}}\right] + (\beta - 1)\eta\,(\boldsymbol{\nabla}\cdot\boldsymbol{v})\;\mathbf{I}. \tag{2.2a}$$

Here, $\mathbf{I}$ is the unit tensor and the superscript "T" indicates tensor transposition. The tensor $\boldsymbol{\tau}$ is the viscous part of the stress tensor.

The constitutive equation for the conducted heat-flux-density $\boldsymbol{q}$ is assumed to take the linear form given by Fourier's law of heat conduction,

$$\boldsymbol{q} = -k_\mathrm{th}\boldsymbol{\nabla}T, \tag{2.3}$$

where k_th is the thermal conductivity of the fluid.

Transport of mass, momentum, and energy

Considering the fluxes of mass, momentum, and energy into a small test volume, Gauss's theorem is used to formulate the governing equations for conservation of mass, momentum and energy in the fluid under the assumption of no net body forces and no heat sources. Without further simplification, the equations take the form

$$\partial_t\rho = \boldsymbol{\nabla}\cdot\big[-\rho\boldsymbol{v}\big], \tag{2.4a}$$

$$\partial_t(\rho\boldsymbol{v}) = \boldsymbol{\nabla}\cdot\big[\boldsymbol{\sigma} - \rho\boldsymbol{v}\boldsymbol{v}\big], \tag{2.4b}$$

$$\partial_t\big(\rho\varepsilon + \tfrac{1}{2}\rho v^2\big) = \boldsymbol{\nabla}\cdot\big[\boldsymbol{v}\cdot\boldsymbol{\sigma} + k_\mathrm{th}\boldsymbol{\nabla}T - \rho(\varepsilon + \tfrac{1}{2}v^2)\boldsymbol{v}\big]. \tag{2.4c}$$

Transport of solute molecules

Likewise, the advection-diffusion equation for a concentration field ζ of a solute with diffusivity D is, using the linear assumption of Fick's law,

$$\partial_t\zeta = \boldsymbol{\nabla}\cdot\big[D\boldsymbol{\nabla}\zeta - \zeta\boldsymbol{v}\big]. \tag{2.5}$$

Diffusivities

The diffusive transport of momentum, heat, and solute molecules is controlled by the momentum diffusivity ν, the thermal diffusivity D_{th}, and the solute diffusivity D, respectively. The former two are related to the fluid parameters η, ρ, k_{th}, and c_p, where c_p is the specific heat capacity at constant pressure. The solute diffusivity D is related to the Stokes radius a of the solute molecule by the Stokes–Einstein equation, as derived for a spherical particle. With k_{B} being the Boltzmann constant, the three relations are

$$\nu = \frac{\eta}{\rho}, \qquad D_{\mathrm{th}} = \frac{k_{\mathrm{th}}}{\rho\, c_p}, \qquad D = \frac{k_{\mathrm{B}} T}{6\pi\eta a}. \tag{2.6}$$

2.2 Acoustic wave propagation

In this section, reliant on parts of Paper I [1], fundamental aspects of linear acoustic wave propagation are derived and discussed starting from the governing hydrodynamic equations Eq. (2.4) of the previous section. A special focus is given to the physical interpretation of the equations, and mathematical manipulations are largely left as an exercise to the reader. The full thermodynamic theory is reviewed, thereby going beyond the standard assumption of adiabatic wave propagation, i.e., the assumption that no heat is exchanged during the compression and decompression phases of the wave propagation, which amounts to zero heat conductivity, $k_{\mathrm{th}} = 0$, and constant entropy, $s =$ constant. The choice to include this material is motivated by the following three considerations: (i) the theory of nonlinear acoustic forces acting on fluids and particles rests on a detailed understanding of linear acoustics, (ii) the adiabatic approximation is an integral part of engineering acoustics, and some students and researchers may be unaware of the thermodynamics of wave propagation, and (iii) non-adiabatic and dissipative effects have particular significance at the microscale where characteristic length scales are comparable to the thermal and viscous boundary layer thicknesses. The treatment relies on parts of the enclosed Paper I [1] and the references therein, most notably the works of Epstein and Carhart [63], Allegra and Hawley [64], and Landau and Lifshitz [65, 66]. Another excellent reference on non-adiabatic acoustics is Morse and Ingard [67]. Some questions that will be answered are: What characterizes adiabatic wave propagation? When is the adiabatic limit appropriate? How do non-adiabatic effects manifest in acoustofluidics? When are non-adiabatic effects expected to be important?

2.2.1 First-order transport equations

Consider a quiescent, homogeneous, and isotropic thermoviscous fluid in equilibrium at constant temperature. This starting point is considered to be the zeroth-order state of the fluid. Then, treating the acoustic field (subscript "1") as a perturbation of this state, the acoustic perturbation parameter $\varepsilon_{\mathrm{ac}}$ is defined as

$$\varepsilon_{\mathrm{ac}} = \frac{|\rho_1|}{\rho_0} \ll 1. \tag{2.7}$$

Expanding all fields as $g = g_0 + g_1$, but with $\boldsymbol{v}_0 = \mathbf{0}$, the linearized first-order mass, momentum, and energy equations obtained from Eqs. (2.1) and (2.4) become

$$\partial_t \rho_1 = -\rho_0 \boldsymbol{\nabla} \cdot \boldsymbol{v}_1, \tag{2.8a}$$

$$\rho_0 \partial_t \boldsymbol{v}_1 = -\boldsymbol{\nabla} p_1 + \eta_0 \nabla^2 \boldsymbol{v}_1 + \beta \eta_0 \boldsymbol{\nabla} (\boldsymbol{\nabla} \cdot \boldsymbol{v}_1), \tag{2.8b}$$

$$\rho_0 T_0 \partial_t s_1 = k_{\text{th}} \nabla^2 T_1. \tag{2.8c}$$

Equation (2.8) presents three equations (one vector- and two scalar equations) with five variables (one vector- and four scalar fields), namely $\boldsymbol{v}_1$, ρ_1, p_1, s_1, and T_1. Thus, two scalar equations are missing.

2.2.2 Thermodynamic equations of state

The remaining two scalar equations are the thermodynamic equations of state $\rho = \rho(p, T)$ and $s = s(p, T)$. The total differentials of ρ and s are,

$$\mathrm{d}\rho = \left(\frac{\partial \rho}{\partial p}\right)_T \mathrm{d}p + \left(\frac{\partial \rho}{\partial T}\right)_p \mathrm{d}T, \tag{2.9a}$$

$$\mathrm{d}s = \left(\frac{\partial s}{\partial p}\right)_T \mathrm{d}p + \left(\frac{\partial s}{\partial T}\right)_p \mathrm{d}T. \tag{2.9b}$$

Linearizing these expressions, the partial derivatives of ρ and s refer to the unperturbed state of the fluid. This begs the introduction of the isothermal compressibility κ_T, the specific heat capacity at constant pressure c_p, the isobaric thermal expansion coefficient α_p, and, in addition, the isentropic compressibility κ_s and the specific heat capacity at constant volume c_V,

$$\kappa_T = \frac{1}{\rho}\left(\frac{\partial \rho}{\partial p}\right)_T, \quad c_p = T\left(\frac{\partial s}{\partial T}\right)_p, \quad \alpha_p = -\frac{1}{\rho}\left(\frac{\partial \rho}{\partial T}\right)_p, \tag{2.10a}$$

$$\kappa_s = \frac{1}{\rho}\left(\frac{\partial \rho}{\partial p}\right)_s, \quad c_V = T\left(\frac{\partial s}{\partial T}\right)_V. \tag{2.10b}$$

Finally, $(\partial s/\partial p)_T = -\alpha_p/\rho$, which may be derived as a Maxwell relation differentiating $g = \varepsilon - Ts + p\,\frac{1}{\rho}$ after p and T. Thus, the linearized form of Eq. (2.9) is

$$\rho_1 = \rho_0\, \kappa_T\, p_1 - \rho_0\, \alpha_p\, T_1, \tag{2.11a}$$

$$s_1 = \frac{c_p}{T_0}\, T_1 - \frac{\alpha_p}{\rho_0}\, p_1. \tag{2.11b}$$

Two well-known thermodynamic identities, relating the isothermal and isentropic compressibilities κ_T and κ_s through the heat capacity ratio γ, may furthermore be derived [65],

$$\kappa_T = \gamma \kappa_s, \qquad \gamma \equiv \frac{c_p}{c_V} = 1 + \frac{\alpha_p^2 T_0}{\rho_0 c_p \kappa_s}. \tag{2.12}$$

Notice that Eq. (2.11) is nothing but simple thermodynamic logic: the density ρ_1 may be changed by changing the pressure p_1 and/or the temperature T_1 [Eq. (2.11a)], and when heat is added $T_0 s_1$, the temperature T_1 and/or pressure p_1 is affected [Eq. (2.11b)]. The material parameters defined in Eq. (2.10) characterize the response of the fluid to external perturbations in pressure or temperature, and are typically known from experiments. In Table II of Paper I (starting on page 51), is presented an exhaustive list of material parameters for water, air, food oil, and solid polystyrene [1].

The adiabatic limit

The typical starting point of adiabatic acoustics is the linearized mass and momentum equations Eqs. (2.8a) and (2.8b) with the equation of state $\rho = \rho(p, s)$ expanded at constant entropy s to yield $\rho = \rho_0 + (\partial\rho/\partial p)_s p_1$, or $\rho_1 = \rho_0 \kappa_s p_1$, which substitutes Eq. (2.11). The full thermodynamic theory should yield the same result in the adiabatic limit, and further point out the behaviour of the temperature field T_1. Transitioning to the adiabatic limit by setting $k_{\text{th}} = 0$ and $s_1 = 0$, Eq. (2.8c) becomes a null equation always fulfilled. On the other hand, Eq. (2.11b) yields $T_1 = \alpha_p T_0/(\rho_0 c_p) p_1 = (\gamma - 1)(\kappa_s/\alpha_p) p_1$, where Eq. (2.12) was used. Inserting this expression for T_1 in Eq. (2.11a) gives $\rho_1 = \rho_0 \kappa_s p_1$, in agreement with adiabatic theory. Hence, adiabatic wave propagation is characterized by in-phase oscillations of the density, temperature, and pressure, $\rho_1, T_1 \propto p_1$.

2.2.3 Velocity potentials

The further reduction of Eq. (2.8) proceeds by eliminating all variables except $\boldsymbol{v}_1$ and T_1, making use of Eq. (2.11) to eliminate p_1 and s_1 and Eq. (2.8a) to eliminate $\partial_t \rho_1$. The velocity field $\boldsymbol{v}_1$ is then decomposed into the gradient of a scalar potential ϕ (the longitudinal component) and the rotation of a divergence-free vector potential $\boldsymbol{\psi}$ (the transverse component),

$$\boldsymbol{v}_1 = \boldsymbol{\nabla}\phi + \boldsymbol{\nabla} \times \boldsymbol{\psi}, \quad \text{with } \boldsymbol{\nabla}\cdot\boldsymbol{\psi} = 0. \tag{2.13}$$

Making use of this Helmholtz decomposition results in two coupled equations for the scalar potential ϕ and T_1, and one for the vector potential $\boldsymbol{\psi}$; see the details in Paper I [1],

$$\partial_t^2 \phi = \left(\frac{1}{\rho_0 \kappa_T} + (1+\beta)\nu_0 \partial_t \right) \nabla^2 \phi - \frac{\alpha_p}{\rho_0 \kappa_T} \partial_t T_1, \tag{2.14a}$$

$$\partial_t T_1 = \gamma D_{\text{th}} \nabla^2 T_1 - \frac{\gamma - 1}{\alpha_p} \nabla^2 \phi, \tag{2.14b}$$

$$\partial_t \boldsymbol{\psi} = \nu_0 \nabla^2 \boldsymbol{\psi}. \tag{2.14c}$$

In the adiabatic limit, for which $D_{\text{th}} = 0$, the well-known adiabatic wave equation for ϕ is obtained by inserting Eq. (2.14b) into (2.14a), from which the adiabatic speed of sound c for longitudinal waves is deduced,

$$c = \frac{1}{\sqrt{\rho_0 \kappa_s}}. \tag{2.15}$$

In the isothermal case, for which $T_1 = 0$, the wave equation (2.14a) instead describes waves traveling at the isothermal speed of sound $c/\sqrt{\gamma} = 1/\sqrt{\rho_0 \kappa_T}$. In ultrasound acoustics, sound propagation in the bulk of a fluid is generally very close to being adiabatic, as will be demonstrated later.

2.2.4 Frequency domain

Notice that the equations for the longitudinal component Eqs. (2.14a) and (2.14b) are coupled, but decoupled from the transverse component Eq. (2.14c). The system of equations can be completely decoupled by going to the frequency domain. Formally, one may Fourier transform the equations into the frequency domain. However, in acoustofluidics one typically considers time-harmonic fields at a single frequency. Hence, a simpler approach is to write any first-order field $g_1(\boldsymbol{r}, t)$ in complex notation as

$$g_1(\boldsymbol{r}, t) = g_1(\boldsymbol{r}) \mathrm{e}^{-\mathrm{i}\omega t}. \tag{2.16}$$

Assuming this form of time-harmonic first-order fields, Eq. (2.14a) immediately yields an expression for T_1 in terms of ϕ, which when inserted in Eq. (2.14b) leaves a bi-harmonic equation for ϕ. This bi-harmonic equation can be factorized into two Helmholtz equations, and then solved by the sum $\phi = \phi_\mathrm{c} + \phi_\mathrm{t}$, where ϕ_c and ϕ_t are solutions of each of the Helmholtz equations; see Paper I for details [1]. The result is three wave equations with three distinct wavenumbers, corresponding to three different modes of wave propagation.

2.2.5 Wave equations and modes

Writing up Eq. (2.14) in frequency domain, the conclusion is that acoustics in thermoviscous fluids can be understood in terms of three distinct modes of wave propagation, each satisfying a Helmholtz wave equation with a unique wavenumber, namely a propagating compressional mode ϕ_c with wavenumber k_c, a damped thermal mode ϕ_t with wavenumber k_t, and a damped shear mode $\boldsymbol{\psi}$ with wavenumber k_s [63, 1],

$$\nabla^2 \phi_\mathrm{c} + k_\mathrm{c}^2 \phi_\mathrm{c} = 0, \qquad k_\mathrm{c} \simeq \frac{\omega}{c}\left[1 + \frac{\mathrm{i}}{2}\left[\Gamma_\mathrm{s} + (\gamma - 1)\Gamma_\mathrm{t}\right]\right], \tag{2.17a}$$

$$\nabla^2 \phi_\mathrm{t} + k_\mathrm{t}^2 \phi_\mathrm{t} = 0, \qquad k_\mathrm{t} \simeq \frac{(1+\mathrm{i})}{\delta_\mathrm{t}}\left[1 + \frac{\mathrm{i}}{2}(\gamma - 1)(\Gamma_\mathrm{s} - \Gamma_\mathrm{t})\right], \tag{2.17b}$$

$$\nabla^2 \boldsymbol{\psi} + k_\mathrm{s}^2 \boldsymbol{\psi} = \boldsymbol{0}, \qquad k_\mathrm{s} = \frac{(1+\mathrm{i})}{\delta_\mathrm{s}}. \tag{2.17c}$$

Here, δ_t and δ_s are the thermal and viscous boundary layer thicknesses, respectively, set by diffusion of heat and momentum from boundaries on the time scale ω^{-1},

$$\delta_\mathrm{t} = \sqrt{\frac{2D_\mathrm{th}}{\omega}}, \qquad \delta_\mathrm{s} = \sqrt{\frac{2\nu_0}{\omega}}, \tag{2.18}$$

and Γ_t and Γ_s are the dimensionless bulk damping factors accounting for thermal and viscous dissipation,

$$\Gamma_\mathrm{t} = \frac{D_\mathrm{th}\omega}{c^2}, \qquad \Gamma_\mathrm{s} = \frac{(1+\beta)\nu_0\omega}{c^2}. \tag{2.19}$$

In the expressions for k_c and k_t it has been assumed that $\Gamma_t, \Gamma_s \ll 1$; see Paper I for the general case [1]. For water at room temperature and 2 MHz frequency, $\Gamma_t, \Gamma_s \sim 10^{-5}$, and this approximation is well-justified.

Inspecting the wavenumbers in Eq. (2.17), the compressional mode ϕ_c with wavenumber k_c describes a weakly damped propagating wave with $\mathrm{Im}[k_c] \ll \mathrm{Re}[k_c] = \omega/c$. In contrast, $\mathrm{Im}[k_t] \simeq \mathrm{Re}[k_t]$ for the thermal mode and $\mathrm{Im}[k_s] = \mathrm{Re}[k_s]$ for the shear mode, which correspond to waves that are damped within their respective wavelengths. Evidently, these modes describe boundary layers near interfaces of walls and particles, which decay exponentially away from these interfaces on the diffusive length scales set by δ_t and δ_s. For water at room temperature and 2 MHz frequency, $\delta_s \simeq 0.4$ µm, $\delta_t \simeq 0.2$ µm, and $\lambda \simeq 760$ µm. Consequently, the length scales of the thermal and viscous boundary-layer thicknesses are the same order of magnitude and much smaller than the acoustic wavelength in this case.

Condition for adiabatic wave propagation

The adiabatic approximation assumes that no heat is exchanged during the compression and decompression phases of the wave propagation. Hence, the physical condition that must be met for this assumption to be approximately valid is that the time $\tau_{\mathrm{diff}} = \lambda^2/(2D_{\mathrm{th}})$ for diffusion of heat a distance of one wavelength λ is much larger than the time $T = 2\pi/\omega$ it takes the wave to propagate the distance λ, i.e., $T \ll \tau_{\mathrm{diff}}$. Consequently, from this scaling argument, the adiabatic assumption holds if

$$\frac{T}{\tau_{\mathrm{diff}}} = \frac{2\pi}{\omega}\frac{\lambda^2}{2D_{\mathrm{th}}} = \frac{D_{\mathrm{th}}\omega}{\pi c^2} = \frac{1}{\pi}\Gamma_t \ll 1, \tag{2.20}$$

where $k_0 = \omega/c = 2\pi/\lambda$ was used. Indeed, this condition is also inferred mathematically from the wavenumber k_c in Eq. (2.17a), since non-adiabatic thermal damping is caused by Γ_t. For ultrasound up to GHz frequencies in water $\Gamma_t \ll 1$, justifying the adiabatic approximation for propagating compressional waves in the bulk fluid. However, waves that are, or have been, in contact with boundaries may be affected by non-adiabatic thermoviscous effects, as will be discussed.

Attenuation, whale song, and noise pollution in the oceans

Consider a compressional plane wave of the form $\phi_0 \mathrm{e}^{\mathrm{i}k_c x}$ traveling in the x-direction. Inserting k_c from Eq. (2.17a) shows that the traveling wave will be damped by the exponential factor $\mathrm{e}^{-\alpha x}$, where α is the attenuation coefficient,

$$\alpha = \frac{\omega}{2c}[\Gamma_s + (\gamma - 1)\Gamma_t] = \frac{2\pi^2 f^2}{\rho_0 c^3}\left[\eta_0^{\mathrm{b}} + \frac{4}{3}\eta_0 + (\gamma - 1)\frac{k_{\mathrm{th}}}{c_p}\right]. \tag{2.21}$$

Hence, the plane wave travels a characteristic length of $\Delta x = 1/\alpha$. Using the parameter values for water given in Table II of Paper I [1], and a frequency of 1 kHz close to that of whale song [68], this yields $\Delta x \approx 5 \times 10^5$ km, or about 1.2 times around the globe. In practice, whales are limited by geometric spreading and by ocean noise levels to about

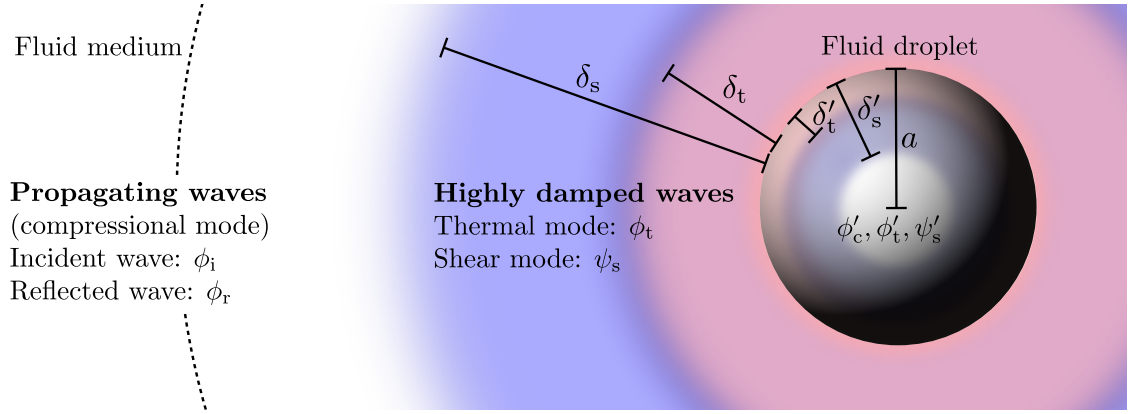

Figure 2.1: A compressional incident wave ϕ_i propagating in a thermoviscous fluid with parameters $\rho_0, \eta_0, \kappa_s, \alpha_p, c_p, \gamma$, and k_th, is incident on a thermoviscous fluid droplet with parameters $\rho_0', \eta_0', \kappa_s', \alpha_p', c_p', \gamma'$, k_th', and of radius a, which results in a compressional scattered wave and highly damped thermal and shear waves both outside in the fluid medium $(\phi_\mathrm{r}, \phi_\mathrm{t}, \psi_\mathrm{s})$ and inside in the fluid droplet $(\phi_\mathrm{c}', \phi_\mathrm{t}', \psi_\mathrm{s}')$. The viscous and thermal boundary layers of width δ_s and δ_t in the fluid medium, and δ_s' and δ_t' inside the droplet, are required to satisfy the boundary conditions at the interface. The escaping propagating compressional wave ϕ_r, coupled to the boundary-layer modes through the boundary conditions, thus carries a signauture of the non-adiabatic and dissipative effects in the scattering. Adapted from Paper I, Ref. [1].

$\sim$ 1000 km, considering the low-frequency calls (15-30 Hz) of blue and fin whales [69]. On an environmental note, the smallness of α also makes the oceans highly susceptible to noise pollution. Low-frequency noise produced by ship traffic, military sonars, and geological surveys is thought to pose a serious threat to marine life dependent on acoustic localization and communication [70].

2.2.6 Thermoviscous effects

Evidently, acoustic waves propagating in narrow channels or pores of dimensions similar to the boundary layers δ_t and δ_s are necessarily affected by non-adiabatic and dissipative thermoviscous effects. Perhaps more elusive is the fact that waves propagating adiabatically far from boundaries may also be affected by non-adiabatic and thermoviscous effects. Notice that the three wave equations in Eq. (2.17) do not couple directly. However, it is crucial to realize that they couple through the boundary conditions, and that this coupling can lead to significant changes in the propagating waves, although they propagate adiabatically, that have been in contact with boundaries. When a propagating compressional wave (wavenumber k_c) scatters off an interface or a particle with differences in material parameters, all three modes in Eq. (2.17) are generally needed to satisfy the boundary conditions of continuous velocity, normal stress, temperature, and heat flux. This scattering process is illustrated for the scattering from a droplet in Fig. 2.1. Although only the propagating compressional wave (wavenumber k_c) escapes the vicinity of the parti-

cle, it carries a signature of the boundary-layer modes and the associated dissipation in its amplitude and phase, and hence the scattered field has changed due to non-adiabatic thermal and viscous effects. In Paper I, it is shown that this change can lead to order-of-magnitude corrections in the nonlinear acoustic radiation force exerted on a particle of radius a comparable to the boundary layer thicknesses δ_s and δ_t [1].

2.2.7 Time-averaged acoustic energy density

The operation of time-averaging over the oscillation period T is denoted by angled brackets,

$$\langle X \rangle \equiv \frac{1}{T}\int_0^T \mathrm{d}t\, X(t). \tag{2.22}$$

A useful expression for the time-average of a product of time-harmonic first-order fields follows, namely

$$\left\langle A_1(\boldsymbol{r})\mathrm{e}^{-\mathrm{i}\omega t} B_1(\boldsymbol{r})\mathrm{e}^{-\mathrm{i}\omega t}\right\rangle = \frac{1}{2}\mathrm{Re}\left[A_1^*(\boldsymbol{r})B_1(\boldsymbol{r})\right]. \tag{2.23}$$

The time-averaged acoustic energy density E_ac, obtained from the sum of the acoustic potential and kinetic energy densities, may thus be evaluated as

$$E_\mathrm{ac} = \frac{1}{2}\kappa_s\langle p_1^2\rangle + \frac{1}{2}\rho_0\langle v_1^2\rangle = \frac{1}{4}\kappa_s|p_1|^2 + \frac{1}{4}\rho_0|\boldsymbol{v}_1|^2. \tag{2.24}$$

When theoretical models are compared to experimental measurements, as in the enclosed Papers II, III, and V, the experimentally measured acoustic energy density E_ac is the only input used in the theory [2, 3, 5]. Typical measured acoustic energy densities in water-filled acoustofluidic cavities are in the range 1-1000 J/m^3 [71, 72, 73, 2, 74]. For $E_\mathrm{ac} = 100$ J/m^3, the oscillating velocity amplitude is $v_\mathrm{a} = 0.6$ m/s, yielding an acoustic perturbation parameter of order $\varepsilon_\mathrm{ac} \sim v_\mathrm{a}/c \sim 10^{-4}$.

2.2.8 Acoustic waves in the non-dissipative limit

In many applications of acoustofluidics, where only propagating waves in the bulk are considered, the boundary layers need not be treated. Furthermore, because $\Gamma_\mathrm{s}, \Gamma_\mathrm{t} \ll 1$, it is often possible to neglect thermoviscous effects entirely in this case. In this non-dissipative limit, the propagating acoustic wave (Eq. (2.17a)) is described by

$$\nabla^2\phi + k_0^2\phi = 0, \quad \boldsymbol{v}_1 = \boldsymbol{\nabla}\phi, \quad p_1 = \mathrm{i}\omega\rho_0\phi, \quad \rho_1 = \frac{1}{c^2}p_1, \quad \text{with} \quad k_0 = \frac{\omega}{c}. \tag{2.25}$$

With no reference to the potential ϕ, Eq. (2.25) is

$$\nabla^2 p_1 + k_0^2 p_1 = 0, \quad \boldsymbol{v}_1 = \frac{-\mathrm{i}}{\rho_0\omega}\boldsymbol{\nabla}p_1, \quad \rho_1 = \frac{1}{c^2}p_1, \quad \text{with} \quad k_0 = \frac{\omega}{c}. \tag{2.26}$$

A solution often referred to, is a one-dimensional standing plane wave along a single direction (the y-direction), with a pressure amplitude of p_a corresponding to a velocity amplitude of $v_\mathrm{a} = p_\mathrm{a}/(\rho_0 c)$, for which

$$p_1 = p_\mathrm{a}\cos(k_0 y), \quad \boldsymbol{v}_1 = \frac{\mathrm{i}}{\rho_0 c}p_\mathrm{a}\sin(k_0 y)\boldsymbol{e}_y, \quad E_\mathrm{ac} = \frac{1}{4}\kappa_s p_\mathrm{a}^2 = \frac{1}{4}\rho_0 v_\mathrm{a}^2. \tag{2.27}$$

Note that the time-averaged acoustic energy density E_{ac} is a constant independent on y. The solution written in Eq. (2.27) is with the pressure anti-node (velocity node) in $y = 0$.

2.2.9 Acoustic waves in thermoelastic solids

The theory presented in this section was developed for homogeneous and isotropic thermoviscous fluids [63]. However, it is readily extended to homogeneous and isotropic thermoelastic solids. In fact, it is shown in Paper I, that the two cases may be treated simultaneously in a unified theoretical framework [1, 64]. The only difference between the two cases lies in the wavenumbers. By (i) defining the solid velocity field as the time-derivative of the displacement field $\boldsymbol{u}_1$, i.e., $\boldsymbol{v}_1 = -\mathrm{i}\omega\boldsymbol{u}_1$, and (ii) introducing the shear constant η_0, which for a fluid is the dynamic viscosity, and for a solid is given by $\eta_0 = \mathrm{i}\rho_0 c_{\mathrm{T}}^2/\omega$, where c_{T} is the isothermal transverse speed of sound, one may write the velocity field $\boldsymbol{v}_1$, the temperature field T_1, and the stress tensor $\boldsymbol{\sigma}_1$ on the same form in both fluids and solids, as given in terms of the potentials ϕ_{c}, ϕ_{t}, and $\boldsymbol{\psi}$. This allows the enforcement of typical boundary conditions on fluid/fluid, fluid/solid, and solid/solid interfaces to be treated simultaneously, as utilized in Paper I. The shear wavenumber $k_{\mathrm{s}} = \sqrt{\mathrm{i}\omega\rho_0/\eta_0}$ furthermore comes out right in both cases. In a fluid this expression yields the damped shear wavenumber $k_{\mathrm{s}} = (1+\mathrm{i})/\delta_{\mathrm{s}}$ describing a viscous boundary layer, while in a solid it yields the purely real wavenumber $k_{\mathrm{s}} = \omega/c_{\mathrm{T}}$ describing propagating transverse waves.

2.3 Acoustic streaming

In this section, reliant on parts of Paper V [5], the phenomenon of acoustic streaming [61, 75] in a homogeneous fluid is introduced. Acoustic streaming is the steady oscillation-time-averaged vortical flow that accompanies the propagation of acoustic waves in viscous fluids. It was studied experimentally as early as 1831 by Faraday observing the motion of powder above a vibrating Chladni plate [76], and theoretically in 1884 by Lord Rayleigh [77].

Acoustic streaming is driven by a divergence in the nonlinear momentum-flux-density tensor arising in the second order of approximation. The nonlinear momentum-flux-density tensor is a central concept in this thesis, and its use in deriving nonlinear acoustic theories will be explored in Chapter 4. For now, it suffices to note that the divergence that drive streaming is caused by one of two dissipation mechanisms. The first is dissipation in the viscous boundary layers (thickness δ_{s}, Eq. (2.17c)), where the acoustic fluid velocity changes to match the velocity of the boundary. The resulting streaming, called boundary-driven Rayleigh streaming [77, 78], is typically observed in standing wave fields near walls [79] or suspended objects [80]. The second mechanism is the attenuation of acoustic waves in the bulk of the fluid (nonzero Γ_{s} and Γ_{t}, Eq. (2.17a)), which produces streaming known as bulk-driven Eckart streaming [81], typically observed in systems much larger than the wavelength [82]. Both cases have been extensively studied theoretically [83, 84, 85, 86], and the phenomenon of acoustic streaming has continued to attract attention due to its importance in thermoacoustic engines [87, 88, 89], ultrasound contrast agents, sonoporation, and drug delivery [90, 91, 92], and the manipulation of particles and cells in microscale acoustofluidics [9, 11, 93, 28, 37, 94, 59, 95].

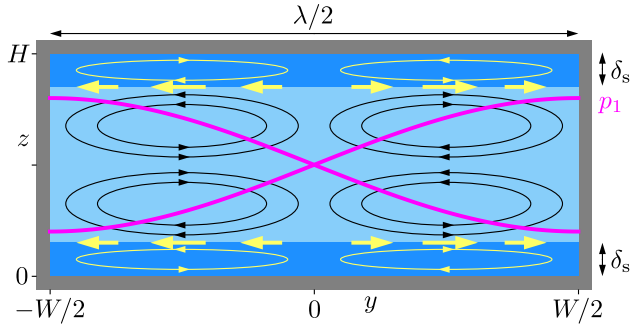

Figure 2.2: Sketch of boundary-driven acoustic streaming in the cross-section of a channel of width W and height H. The horizontal half-wave standing pressure field p_1 (magenta) of wavelength λ, with the pressure node in $y = 0$, induces nonlinear acoustic forces in the boundary layers of thickness δ_s (dark blue). This results in the boundary-layer Schlichting streaming (yellow loops). The Schlichting streaming in turn drives the Rayleigh streaming rolls (black loops) by setting up an effective velocity boundary condition (yellow arrows) on the bulk of the fluid (light blue). Adapted from Ref. [79].

2.3.1 Time-averaged second-order flow

Because the time-average of any time-harmonic first-order field is zero, any steady flow driven by acoustics is necessarily a nonlinear phenomenon. Formally, the steady acoustic streaming velocity field $\langle \boldsymbol{v}_2 \rangle$ is the solution of the time-averaged second-order equations derived from the governing equations Eq. (2.4). Thus the viscous-relaxation time scale of the streaming flow, estimated from $\partial_t \langle \boldsymbol{v}_2 \rangle \approx \nu_0 \nabla^2 \langle \boldsymbol{v}_2 \rangle$, is $t_{\text{stream}} \sim H^2/\nu_0$, where H is a characteristic channel dimension. In typical acoustofluidic devices operating at MHz frequency, $H \sim 100$ μm, which yields $t_{\text{stream}} \sim 10$ ms, while the acoustic time scale is $t_{\text{acoust}} \sim 1/\omega \sim 0.1$ μs. Hence, the streaming flow takes place on a time scale five magnitudes slower than the acoustic time scale, $t_{\text{stream}} \sim 10^5 t_{\text{acoust}}$.

2.3.2 Boundary-driven acoustic streaming

In microscale acoustofluidics, the typical system size is comparable to the acoustic wavelength, which means that boundary-driven streaming dominates over bulk-driven streaming. In Fig. 2.2 is a sketch of the flow patterns in boundary-driven acoustic streaming. Consider a typical water-filled microchannel, such as that used in Paper V [5], with a cross-sectional height $H = 130$ μm and width $W = 375$ μm, and a standing half-wave across the width at $f = 2$ MHz. The boundary layers in which the vorticity that drives streaming is generated is then of thickness $\delta_s = 0.4$ μm, and hence vastly exaggerated in Fig. 2.2. Outside of the boundary layers, the nonlinear acoustic force density that drives the acoustic streaming is zero [79]. Consequently, analytical theories of boundary-driven streaming typically split the fluid domain into two regions of interest, namely the narrow boundary layer region (dark blue in Fig. 2.2), and the bulk region outside of the boundary layers (light blue in Fig. 2.2). The first-order (acoustics) and second-order (streaming)

equations may then be simplified in the two regions of interest [96]. One finds that the Rayleigh bulk streaming rolls [77] (black loops in Fig. 2.2) are driven by the Schlichting streaming rolls inside the boundary layers [78] (yellow loops in Fig. 2.2). Because $\delta_s \ll H$, the outer Schlichting streaming velocity can be considered an effective boundary condition for the bulk streaming velocity field (yellow arrows in Fig. 2.2). Indeed, this approach was used in the derivation of the famous Rayleigh boundary condition on the streaming velocity field $\langle \boldsymbol{v}_2 \rangle$ [77]. For the case illustrated in Fig. 2.2 with the acoustic wave along the horizontal y-direction and boundaries in $z = 0, H$, the effective boundary condition is

$$\langle \boldsymbol{v}_2^{\text{bnd}} \rangle = \frac{3}{8} \frac{v_a^2}{c} \sin(2k_0 y) \boldsymbol{e}_y \qquad \text{for} \quad z = 0, H, \tag{2.28}$$

where v_a is the amplitude of the the oscillating acoustic velocity, and $k_0 = \omega/c = \pi/W$ is the wavenumber in the half-wave resonance. The characteristic Rayleigh streaming velocity amplitude obtained from Eq. (2.28) is $v_R = (3/8)v_a^2/c$. Considering a water-filled acoustofluidic cavity with $E_{ac} = 100$ J/m^3, the oscillating velocity amplitude is $v_a = 0.6$ m/s, and the characteristic streaming velocity evaluates to $v_R = 100$ μm/s.

The idea of using effective boundary conditions obtained from the limiting streaming velocity in the boundary-layers was generalized by Nyborg [84, 97], who presented an expression for the (bulk) streaming velocity boundary condition in terms of the propagating acoustic field only (the ϕ_c mode in Eq. (2.17a)). This limiting-velocity method has been used in recent numerical studies in 3D [98, 99, 59, 100], made possible by the reduction in computational complexity that follows from not having to resolve the boundary layers. For typical standing-wave conditions in acoustofluidics, the problem of boundary-driven acoustic streaming then takes the form of an incompressible Stokes flow satisfying effective boundary conditions [79, 98, 99].

Finally, to get a proper visualization of boundary-driven acoustic streaming in a real microsystem, Fig. 2.3 presents the experimentally measured and numerically simulated acoustic streaming in a homogeneous fluid in the cross-section of the channel from Paper V [5]. In this system, $H = 130$ μm, $W = 375$ μm, $f = 2$ MHz, and $\delta_s = 0.4$ μm. Evidently, the experiment cannot resolve the boundary-layer Schlichting streaming due to the submicron boundary layer thickness. However, in the simulation, which resolves the boundary layers, the counter-rotating boundary-layer streaming is indeed present within the length scale δ_s from the wall, as shown in Fig. 2.3(d).

2.4 Acoustic radiation force on a particle

In this section, reliant on parts of Paper I [1], the acoustic radiation force acting on a particle in an acoustical field is introduced. The acoustic radiation force is the time-averaged force exerted on a particle in an acoustical field due to scattering of the acoustic waves from the particle. Theoretical studies of the acoustic radiation force date back to King in 1934 [101] and Yosioka and Kawasima in 1955 [102], who considered the force on an incompressible and a compressible particle, respectively, in an inviscid ideal fluid. Their work was summarized in 1962 by Gorkov [103], however, with the analysis limited

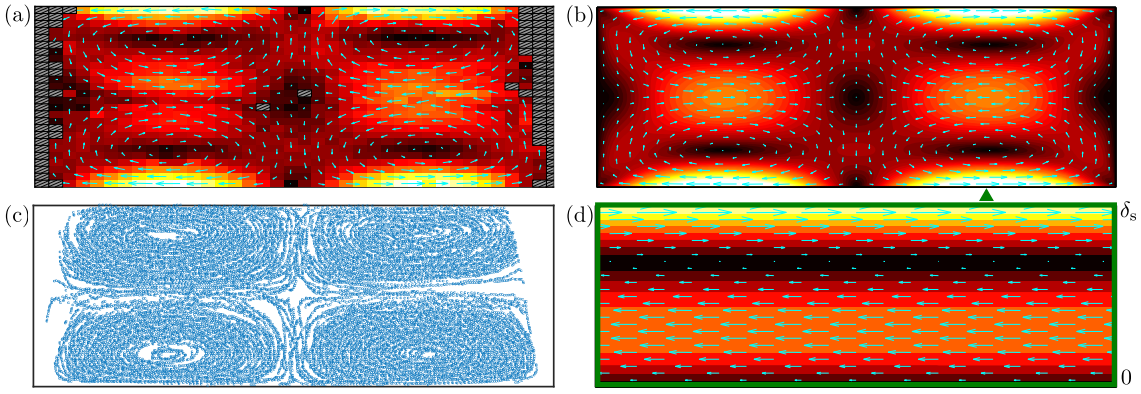

Figure 2.3: Acoustic streaming in the rectangular channel cross-section of height $H = 130$ μm and width $W = 375$ μm, with a 2 MHz standing half-wave across the width. **(a)** Experimental streaming velocity amplitude (0 μm/s, black; 35 μm/s, white) with the arrows (cyan) indicating the direction. Spatial bins with no data points are excluded (grey). **(b)** Simulated streaming velocity amplitude; same colors as in (a). **(c)** Experimental particle positions (blue points) tracing the streaming field. **(d)** Zoom-in of (b) near the bottom wall ($0 \leq z \leq \delta_s = 0.4$ μm $\ll H = 130$ μm) at the location indicated by the green triangle, showing the counter-rotating boundary-layer streaming resolved in the simulation. Adapted from Paper V, Ref. [5].

to ideal fluids in the long-wavelength limit where the particle radius a is much smaller than the acoustic wavelength λ.

The acoustic radiation force is the primary acoustic force used in applications to manipulate particles. Acoustic radiation forces have thus been employed in the development of acoustofluidic devices for separating and concentrating [104, 105, 106, 29, 27, 40, 7], patterning [37], and trapping [28, 39, 107] of cells and particles. Further applications include acoustic force spectroscopy [44], acoustic tweezers [108, 54, 56, 53, 58], acoustic tractor beams [109], acoustic levitators [110, 111, 112, 113, 55], and particle separation in gasses [114, 115, 116]. A number of experimental methods based on different actuation principles have been developed in order to control the acoustic field and thereby the acoustic radiation force exerted on a particle in the field [45, 9]. These methods include the use of bulk acoustic waves [46, 47, 48], surface acoustic waves [49, 50, 51, 52, 53], transducer arrays [54, 55, 56], and 3D-printed transmission holograms or lenses [57, 58].

2.4.1 Time-averaged second-order force

Consider a single particle or droplet suspended in an infinite, quiescent fluid medium perturbed by a time-harmonic acoustic field. The region $\Omega(t)$ occupied by the particle, its surface $\partial\Omega(t)$, and the outward-pointing surface vector $\boldsymbol{n}$ depend on time due to the acoustic field. The instantaneous acoustic force on the particle is given by the surface integral of the fluid stress $\boldsymbol{\sigma}$ acting on the particle surface. However, since the short time scale corresponding to the oscillation period $T = 2\pi/\omega$ is typically not resolved

experimentally, the acoustic force $\boldsymbol{F}_{\mathrm{ac}}$ is defined in the conventional time-averaged sense [101, 102, 103, 117, 118, 119, 120, 121, 43],

$$\boldsymbol{F}_{\mathrm{ac}} = \left\langle \oint_{\partial\Omega(t)} \boldsymbol{\sigma} \cdot \boldsymbol{n} \, \mathrm{d}a \right\rangle, \tag{2.29}$$

where the angled bracket denotes the time average over one oscillation period. Consequently, since the time average of the time-harmonic first-order fields is zero, $\boldsymbol{F}_{\mathrm{ac}}$ is a nonlinear force entering in the second order of approximation. In acoustofluidics at MHz frequency, the time-averaged nonlinear effects typically take place on a 10 ms to 1 s time scale, much larger than the oscillation time scale of order 0.1 µs [3].

Time-periodicity of the system

The fluid-particle system is assumed to be periodic in the acoustic oscillation period T, tantamount to requiring that any non-periodic phenomenon, such as the induced particle drift, is negligible within one oscillation period. Usually, this requirement is not very restrictive, as discussed in Paper I [1]. For a time-periodic state, any field can be written as a Fourier series $f(\boldsymbol{r},t) = \sum_{n=0}^{\infty} f_n(\boldsymbol{r})\, \mathrm{e}^{-\mathrm{i}n\omega t}$, with $\omega = 2\pi/T$, and the time-average of any total time derivative is zero, $\left\langle \frac{\mathrm{d}}{\mathrm{d}t} f(\boldsymbol{r},t) \right\rangle = 0$.

Integration on a static outer surface

From the assumption of time-periodicity, a non-perturbative expression for $\boldsymbol{F}_{\mathrm{ac}}$ is obtained by considering the momentum flux density $\boldsymbol{\sigma} - \rho\boldsymbol{v}\boldsymbol{v}$ entering the fluid volume between the particle surface $\partial\Omega(t)$ and an arbitrary static surface $\partial\Omega_1$ enclosing the particle. The total momentum $\boldsymbol{P}$ of the fluid in this volume is the volume integral of $\rho\boldsymbol{v}$, and the time-averaged rate of change $\left\langle \frac{\mathrm{d}}{\mathrm{d}t}\boldsymbol{P} \right\rangle$ is

$$\begin{aligned}\left\langle \frac{\mathrm{d}\boldsymbol{P}}{\mathrm{d}t} \right\rangle &= \left\langle \oint_{\partial\Omega_1} \Big[\boldsymbol{\sigma} - \rho\boldsymbol{v}\boldsymbol{v}\Big] \cdot \boldsymbol{n} \, \mathrm{d}a \right\rangle + \left\langle \oint_{\partial\Omega(t)} \boldsymbol{\sigma} \cdot (-\boldsymbol{n}) \, \mathrm{d}a \right\rangle \\ &= \left\langle \oint_{\partial\Omega_1} \Big[\boldsymbol{\sigma} - \rho\boldsymbol{v}\boldsymbol{v}\Big] \cdot \boldsymbol{n} \, \mathrm{d}a \right\rangle - \boldsymbol{F}_{\mathrm{ac}}. \end{aligned} \tag{2.30}$$

Here, $\boldsymbol{n}$ is the surface vector pointing out of $\partial\Omega_1$ (out of the fluid) and out of $\partial\Omega(t)$ (into the fluid). The advection term $\rho\boldsymbol{v}\boldsymbol{v}$ is zero at $\partial\Omega(t)$, since there is no advection of momentum through the interface of the particle. Finally, using that the time average of the total time derivative $\left\langle \frac{\mathrm{d}\boldsymbol{P}}{\mathrm{d}t} \right\rangle$ is zero in the time-periodic system, Eq. (2.30) yields

$$\boldsymbol{F}_{\mathrm{ac}} = \left\langle \oint_{\partial\Omega_1} \Big[\boldsymbol{\sigma} - \rho\boldsymbol{v}\boldsymbol{v}\Big] \cdot \boldsymbol{n} \, \mathrm{d}a \right\rangle. \tag{2.31}$$

Thus, even before applying perturbation theory, the acoustic force can be evaluated as the total momentum flux through any static surface $\partial\Omega_1$ enclosing the particle. To second

order in the acoustic perturbation, using the expansions $\rho = \rho_0 + \rho_1 + \rho_2$, $\boldsymbol{v} = \boldsymbol{0} + \boldsymbol{v}_1 + \boldsymbol{v}_2$, and $\boldsymbol{\sigma} = \boldsymbol{\sigma}_0 + \boldsymbol{\sigma}_1 + \boldsymbol{\sigma}_2$, Eq. (2.31) becomes

$$\boldsymbol{F}_{\mathrm{ac}} = \oint_{\partial\Omega_1} \left[\langle \boldsymbol{\sigma}_2 \rangle - \rho_0 \langle \boldsymbol{v}_1 \boldsymbol{v}_1 \rangle \right] \cdot \boldsymbol{n} \, \mathrm{d}a, \tag{2.32}$$

This standard result, often derived by slightly different means, is the typical starting point of most detailed analyses [122, 117, 118, 119, 121, 1, 43].

2.4.2 Acoustic radiation force and streaming

In the above Section 2.4.1, where the acoustic force $\boldsymbol{F}_{\mathrm{ac}}$ on a particle was introduced, a silent distinction was made between the acoustic force $\boldsymbol{F}_{\mathrm{ac}}$ and the acoustic *radiation* force $\boldsymbol{F}_{\mathrm{rad}}$. In an inviscid fluid the two are identical, $\boldsymbol{F}_{\mathrm{ac}} = \boldsymbol{F}_{\mathrm{rad}}$. However, in a viscous fluid the definition of the former Eq. (2.29) includes an acoustic-streaming component $\boldsymbol{F}_{\mathrm{str}}$ from the streaming generated locally near the particle, since the stresses leading to this streaming are contained in the fluid stress tensor $\boldsymbol{\sigma}$. In a finite domain, there would furthermore be a contribution from the external bulk- and boundary-driven acoustic streaming. Formally, one may write

$$\boldsymbol{F}_{\mathrm{ac}} = \boldsymbol{F}_{\mathrm{rad}} + \boldsymbol{F}_{\mathrm{str}}. \tag{2.33}$$

In Eq. (2.32), the acoustic radiation force $\boldsymbol{F}_{\mathrm{rad}}$ is the component derived from the (pseudo-) momentum-flux-density carried by the acoustic waves through the surface $\partial\Omega_1$ [118, 43], i.e., it derives only from products of first-order fields. Hence,

$$\boldsymbol{F}_{\mathrm{rad}} = -\oint_{\partial\Omega_1} \left[\langle p_{11} \rangle \mathbf{I} + \rho_0 \langle \boldsymbol{v}_1 \boldsymbol{v}_1 \rangle \right] \cdot \boldsymbol{n} \, \mathrm{d}a, \quad \text{where} \quad \langle p_{11} \rangle = \frac{1}{4} \kappa_s |p_1|^2 - \frac{1}{4} \rho_0 |\boldsymbol{v}_1|^2, \tag{2.34}$$

As such, $\boldsymbol{F}_{\mathrm{rad}}$ may be obtained from the integration of Eq. (2.32) in an inviscid-fluid far-field calculation (where Eq. (2.32) reduces to Eq. (2.34)), as long as the boundary layers are treated in the near-field. This approach was taken by Settnes and Bruus in the derivation of a useful expression for $\boldsymbol{F}_{\mathrm{rad}}$ in terms of the incident first-order acoustic field p_{in} and $\boldsymbol{v}_{\mathrm{in}}$ and the monopole and dipole scattering coefficients f_0 and f_1 for the suspended particle (long-wavelength limit) [119]. The same line of thought was furthermore used by Karlsen and Bruus in the enclosed Paper I [1]. However, regrettably, the distinction between $\boldsymbol{F}_{\mathrm{ac}}$ and $\boldsymbol{F}_{\mathrm{rad}}$ was not made explicit in either of these works.

The streaming force component $\boldsymbol{F}_{\mathrm{str}}$ derives from the second-order velocity $\langle \boldsymbol{v}_2 \rangle$ in a viscous fluid. As such, $\boldsymbol{F}_{\mathrm{str}}$ takes the character of a drag force, in contrast to the radiative scattering force $\boldsymbol{F}_{\mathrm{rad}}$. $\boldsymbol{F}_{\mathrm{str}}$ is not treated in this thesis, except in the pragmatic approach to acoustophoretic particle trajectories outlined in Section 2.5.

2.4.3 Long-wavelength limit

In the long-wavelength limit the particle radius a is assumed much smaller than the wavelength λ. The long-wavelength limit is thus characterized by the small parameter $\epsilon = k_0 a \ll 1$ with $k_0 = 2\pi/\lambda$. In this limit, the dominant contributions to the scattered

field expanded in a multipole expansion are the $n = 0$ monopole and the $n = 1$ dipole terms, both proportional to ϵ^3, while the contribution of the nth-order multipole for $n > 1$ scales with $\epsilon^{2n+1} \ll \epsilon^3$ [102, 63].

In the far-field, the propagating monopole and dipole scattered field takes a particularly simple form, which was used by Settnes and Bruus to analytically integrate Eq. (2.34). It was shown that the acoustic radiation force may be evaluated directly from the incident first-order acoustic field and the expressions for the monopole and dipole scattering coefficients f_0 and f_1 for the suspended particle, as [119]

$$\boldsymbol{F}_{\mathrm{rad}} = -\pi a^3 \left[\frac{2\kappa_s}{3} \mathrm{Re}\big[f_0^* p_{\mathrm{in}}^* \boldsymbol{\nabla} p_{\mathrm{in}}\big] - \rho_0 \mathrm{Re}\big[f_1^* \boldsymbol{v}_{\mathrm{in}}^* \cdot \boldsymbol{\nabla} \boldsymbol{v}_{\mathrm{in}}\big] \right]. \tag{2.35}$$

Here, p_{in} and $\boldsymbol{v}_{\mathrm{in}}$ are the incident acoustic pressure and velocity fields evaluated at the particle position, and the asterisk denotes complex conjugation. Since the incident wave is the wave propagating in the absence of the particle, p_{in} and $\boldsymbol{v}_{\mathrm{in}}$ are typically well-described by the non-dissipative limit in Eq. (2.26). The thermoviscous effects of the boundary-layer modes enter through f_0 and f_1. It is noted that $\boldsymbol{F}_{\mathrm{rad}}$ is a volume-force $\propto a^3$.

Monopole and dipole scattering coefficients

Equation (2.35) is valid for any incident time-harmonic, acoustic field, and consequently the problem of calculating the radiation force on a small particle reduces to calculating the coefficients f_0 and f_1. Closed, analytical expressions for these are given in the literature for small particles in the special cases of compressible particles in ideal fluids [102, 103] and compressible particles in viscous fluids [119]. Moreover, f_0 and f_1 can be extracted from Refs. [123, 124] for rigid spheres and liquid droplets in thermoviscous fluids for the limiting cases of very thin and very thick boundary layers, $\delta_{\mathrm{s}}, \delta_{\mathrm{t}} \ll a \ll \lambda$ and $a \ll \delta_{\mathrm{s}}, \delta_{\mathrm{t}} \ll \lambda$, respectively. In the enclosed Paper I, closed-form analytical expressions with no restrictions on the boundary-layer thicknesses relative to the particle size, i.e., in the more general limit of $\delta_{\mathrm{s}}, \delta_{\mathrm{t}}, a \ll \lambda$, are derived for f_0 and f_1 in the cases of a spherical thermoviscous droplet and a spherical thermoelastic particle suspended in a thermoviscous fluid [1, 63, 64].

Although the derived thermoviscous expressions for f_0 and f_1 are relatively simple, it suffices to give the ideal-fluid expressions in this introduction, obtained from the full thermoviscous theory in the limit of zero-boundary layer thicknesses $\delta_{\mathrm{s}}, \delta_{\mathrm{t}} = 0$. These are [102, 103, 1],

$$f_0 = 1 - \tilde{\kappa}_s, \qquad f_1 = \frac{2(\tilde{\rho}_0 - 1)}{2\tilde{\rho}_0 + 1}, \qquad \text{(ideal-fluid limit } \delta_{\mathrm{s}}, \delta_{\mathrm{t}} = 0). \tag{2.36}$$

Here, the material parameters with a tilde $\tilde{\kappa}_s$ and $\tilde{\rho}_0$ refer to the ratios of the particle and fluid parameters, e.g., $\tilde{\kappa}_s = \kappa_s'/\kappa_s$ where κ_s' is the compressibility of the suspended particle and κ_s is the compressibility of the fluid medium. Evidently, acoustic scattering is caused by a contrast in the material parameters, and in the absence of such a contrast f_0 and f_1 are zero, and so is the radiation force $\boldsymbol{F}_{\mathrm{rad}}$. Figure 2.4 illustrates how contrasts in the mechanical and thermodynamic parameters of the particle and fluid can generate

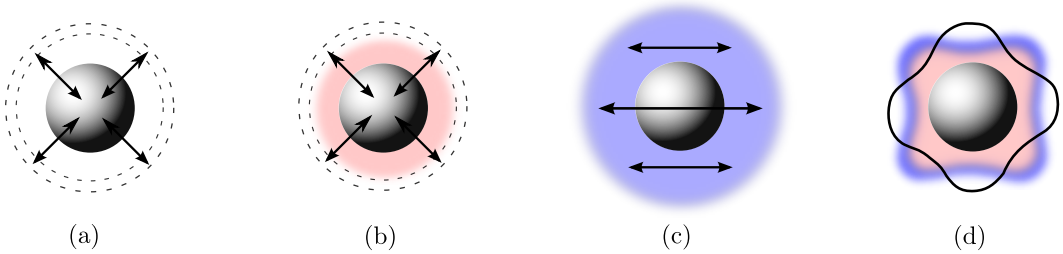

Figure 2.4: Sketches of the physical mechanisms responsible for various multipole components in the acoustic field scattered from a particle. (a) Compressibility contrast: the incident periodic pressure field compresses the particle relative to the fluid, which leads to monopole radiation. (b) Thermal contrast: the incident periodic temperature field leads to thermal expansion of the particle relative to the fluid, which gives rise to monopole radiation and the development of a diffusive thermal boundary layer (pink). (c) Density contrast: a difference in inertia between particle and fluid causes the particle to oscillate relative to the fluid, which yields dipole radiation and the development of a viscous boundary layer (blue). (d) Particle resonances: acoustic wavelengths comparable to the particle size leads to complex shape changes, which gives rise to multipole radiation and a complex thermoviscous boundary layer (pink/blue). Adapted from Paper I, Ref. [1].

monopole, dipole, and multipole scattering from a particle subject to a periodic acoustic field [125]. Note in particular that thermal and viscous effects are expected to couple to the monopole and dipole modes, respectively, while the higher-order multipoles can be understood to play a role for $a \gtrsim \lambda$. Some studies going beyond the long-wavelength limit by taking higher-order multipoles into account are Refs. [120, 121, 126, 127].

2.4.4 Acoustic contrast factor

The special case of a one-dimensional (1D) standing plane wave is widely used in practical applications of the acoustic radiation force in microchannels [128, 71, 129, 47, 105, 28, 130, 40]. It leads to a particularly simple expression for the acoustic radiation force. Inserting into Eq. (2.35) the 1D standing plane wave from Eq. (2.27), with a pressure anti-node (velocity node) in $y = 0$, the expression for $\boldsymbol{F}_{\mathrm{rad}}$ reduces to

$$\boldsymbol{F}_{\mathrm{rad}}^{\mathrm{1D}} = 4\pi\, \Phi_{\mathrm{ac}} a^3 k_0 E_{\mathrm{ac}} \sin(2k_0 y) \boldsymbol{e}_y, \tag{2.37a}$$

$$\Phi_{\mathrm{ac}} = \frac{1}{3}\mathrm{Re}\left[f_0\right] + \frac{1}{2}\mathrm{Re}\left[f_1\right], \tag{2.37b}$$

where Φ_{ac} is the so-called acoustic contrast factor. The radiation force is thus proportional to Φ_{ac}, which contains the effects of contrasts in material parameters in f_0 and f_1. Note that for positive acoustic contrast factors, $\Phi_{\mathrm{ac}} > 0$, the force is directed towards the pressure nodes of the standing wave, while for negative acoustic contrast factors, $\Phi_{\mathrm{ac}} < 0$, it is directed towards the anti-nodes.

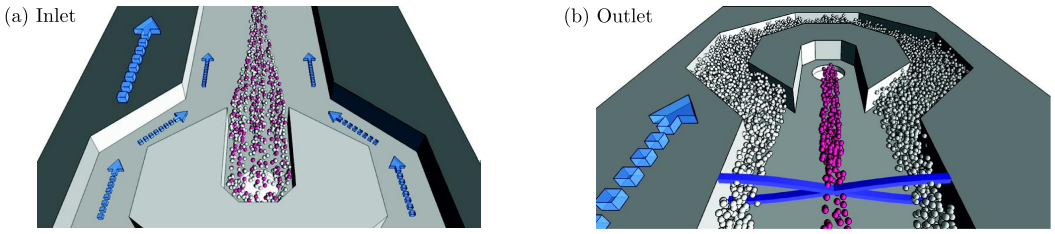

Figure 2.5: Example of acoustophoretic separation of proteins (pink) from fatty lipids (white) in continuous flow (arrows), used in the sample precondition in raw milk analysis. **(a)** At the inlet, the proteins and the lipids are mixed in the central stream of raw milk. **(b)** When reaching the outlet, the lipids ($\Phi_{\text{ac}} < 0$) have been focused in the pressure anti-nodes at the sidewalls, while the small proteins ($\Phi_{\text{ac}} > 0$) remain at the center. Adapted from Grenvall *et al.* [105].

Particle-separation methods

Inspection of Eq. (2.37) immediately reveals a few principles for acoustofluidic particle separation. Methods for separating particles based on mechanical properties typically rely on binary separation of particles into pressure nodes and anti-nodes, one example being the separation of fatty lipids ($\Phi_{\text{ac}} < 0$) from proteins ($\Phi_{\text{ac}} > 0$) in raw milk, see Fig. 2.5 [105]. Another particle-separation method sorts particles by size utilizing the a^3 scaling of the force to move particles transverse to a flow. By properly tuning the time-of-flight through the channel, larger particles will move a greater transverse distance than smaller particles [104, 131]. This method is not without issues, however, since biological particles such as cells show large variations in size within a specific phenotype. In the enclosed Paper II [2], a size-insensitive method called iso-acoustic focusing is developed and applied to phenotyping of single cells. In this method, an inhomogeneous fluid is used to make the acoustic contrast factor a function of position, thereby allowing different phenotypes to be focused in different phenotype-specific points of zero acoustic contrast ($\Phi_{\text{ac}} = 0$). As such, the method can be considered a microfluidic analog to density-gradient centrifugation.

2.5 Acoustophoretic particle trajectories

In this section, the approach used to calculate time-averaged acoustophoretic particle trajectories is outlined. Acoustophoretic particle trajectories are not a main focus in this thesis, but the physics is important to acoustofluidics in general. The Supplemental Material of Papers II and V furthermore includes simulations of acoustophoretic particle trajectories [2, 5]. Here, after a short mentioning of some recent studies on acoustophoretic particle trajectories, the equation of motion for a microparticle suspended in a fluid perturbed by an acoustic field is given, and the assumptions of the models are described.

Acoustophoretic particle trajectories in homogeneous fluids in microchannels, resulting from the nonlinear time-averaged acoustic radiation force and the streaming-induced drag

force, have been the subject of detailed experimental studies using particle tracking in two and three dimensions [71, 79, 94, 132], microparticle image velocimetry [133, 47, 93], and optical traps [73, 74], as well as theoretical investigations by numerical simulations [134, 59, 135]. Considering boundary-driven acoustic streaming in microchannels, the exhaustive study by Muller *et al.* comparing theory and experiments conclude that the two are in quantitative agreement within 20% [79].

2.5.1 The equation of motion

Consider a single spherical particle of radius a suspended in a fluid perturbed by an acoustic field of wavelength $\lambda \gg a$. The particle of density ρ_0' is of mass $m_\mathrm{p} = (4/3)\pi a^3 \rho_0'$. Treating the particle as a point particle with velocity $\boldsymbol{v}_\mathrm{p}$, Newton's second law for the particle motion due to the acoustic radiation force $\boldsymbol{F}_\mathrm{rad}$, the drag force from the fluid $\boldsymbol{F}_\mathrm{drag}$, and the combined force of buoyancy and gravity $\boldsymbol{F}_\mathrm{buoy}$, is

$$m_\mathrm{p} \frac{\mathrm{d}\boldsymbol{v}_\mathrm{p}}{\mathrm{d}t} = \boldsymbol{F}_\mathrm{rad} + \boldsymbol{F}_\mathrm{drag} + \boldsymbol{F}_\mathrm{buoy}. \tag{2.38}$$

The single-particle theory may be applied to dilute suspensions, while effects of particle-particle interactions are expected to become significant for rather dense suspensions above ∼1% particle-volume-concentration [136].

The radiation force

The acoustic radiation force $\boldsymbol{F}_\mathrm{rad}$ acting on the particle is calculated from Eq. (2.35), valid for any incident acoustic field p_in and $\boldsymbol{v}_\mathrm{in}$ in the long-wavelength limit $a \ll \lambda$ [119]. The scattering coefficients f_0 and f_1 are known for spherical particles in thermoviscous fluids [1]. However, for micrometer-sized particles in water at MHz frequency, it typically suffices to use the ideal-fluid expressions given in Eq. (2.36).

The drag force

The viscous drag force $\boldsymbol{F}_\mathrm{drag}$ is caused by the fluid moving relative to the particle. For small Reynolds numbers, $v\, a/\eta_0 \ll 1$, the Stokes drag law applies,

$$\boldsymbol{F}_\mathrm{drag} = 6\pi\eta_0 a(\boldsymbol{v} - \boldsymbol{v}_\mathrm{p}). \tag{2.39}$$

Here, $\boldsymbol{v}$ is the fluid velocity. Neglecting the particle-induced streaming, it is equal to the external boundary-driven streaming velocity. Particles moving close to walls experience an enhanced drag force [137, 138, 93], however, this contribution is neglected in this thesis.

The buoyancy force

Introducing the gravitational acceleration $\boldsymbol{g}$, the combined force of buoyancy and gravity $\boldsymbol{F}_\mathrm{buoy}$, written in terms of $\tilde{\rho}_0 = \rho_0'/\rho_0$, is equal to

$$\boldsymbol{F}_\mathrm{buoy} = \frac{4}{3}\pi a^3 (\tilde{\rho}_0 - 1)\rho_0\, \boldsymbol{g}, \tag{2.40}$$

Note on inhomogeneous fluids

The enclosed Papers II and V (Supplemental Material) include simulations of acoustophoretic particle trajectories in inhomogeneous fluids where the inhomogeneity develops through diffusion and advection [2, 5]. In this case, the fluid parameters of density ρ_0, compressibility κ_s, and viscosity η_0 depend on time and space, introducing additional time and space dependencies in the forces acting on the particle. Most importantly, the acoustic contrast factor Φ_{ac} becomes a function of space $\Phi_{\mathrm{ac}} = \Phi_{\mathrm{ac}}(\boldsymbol{r})$ (and time), such that iso-acoustic points (IAP) of zero radiation force can be created away from nodes and anti-nodes by virtue of $\Phi_{\mathrm{ac}}(\boldsymbol{r}_{\mathrm{IAP}}) = 0$, Eq. (2.37). Note that $\Phi_{\mathrm{ac}} = 0$ does not necessarily imply zero scattering, but rather that the contributions from the monopole and dipole scattering cancel.

2.5.2 Simplification of the equation of motion

The inertial acceleration term in the equation of motion Eq. (2.38) may often be neglected in acoustofluidics. Indeed, the characteristic unsteady time for accelerating a micrometer-sized particle by the drag force to the velocity of the flow, obtained from $m_{\mathrm{p}}\frac{\mathrm{d}\boldsymbol{v}_{\mathrm{p}}}{\mathrm{d}t} = \boldsymbol{F}_{\mathrm{drag}}$ is $\tau_{\mathrm{unsteady}} \sim (2/9)a^2\rho_0'/\eta_0 \sim 1$ µs, while the characteristic time of steady motion at the velocity $\boldsymbol{v}_{\mathrm{p}} = \boldsymbol{F}_{\mathrm{rad}}/(6\pi\eta_0 a)$ is of the order $\tau_{\mathrm{steady}} \sim 1$ ms. Neglecting inertia, the equation of motion Eq. (2.38) immediately yields the particle velocity,

$$\boldsymbol{v}_{\mathrm{p}} = \frac{1}{6\pi\eta_0 a}\left(\boldsymbol{F}_{\mathrm{rad}} + \boldsymbol{F}_{\mathrm{buoy}}\right) + \boldsymbol{v}. \tag{2.41}$$

In typical acoustofluidic experiments with micrometer-sized particles, the radiation force and/or the drag force due to streaming dominate the particle trajectories, while the buoyancy force is often negligible.

2.5.3 Radiation- and streaming-dominated trajectories

There are large qualitative differences between particle trajectories dominated by the radiation force $\boldsymbol{F}_{\mathrm{rad}}$ and the streaming-induced drag force $\boldsymbol{F}_{\mathrm{drag}}$, respectively. Indeed, as illustrated in Fig. 2.6, the radiation force focuses particles in a point of zero force (nodes or anti-nodes in a homogeneous fluid), while the streaming continuously swirls the particles around with the flow. To determine when a particle trajectory is radiation- and streaming-dominated, the ratio of the magnitude of the two forces is calculated. The magnitude of $\boldsymbol{F}_{\mathrm{rad}}$ is determined from Eq. (2.37), while the magnitude of $\boldsymbol{F}_{\mathrm{drag}}$ on a fixed particle ($v_{\mathrm{p}} = 0$) is determined from Eq. (2.39) with the fluid velocity amplitude v equal to the Rayleigh streaming amplitude of Eq. (2.28), $v_{\mathrm{R}} = (3/2)E_{\mathrm{ac}}\rho_0^{-1}c^{-1}$, as expressed in terms of the acoustic energy density E_{ac}, Eq. (2.27). Both forces scale linearly with E_{ac}, and it drops out of the ratio, leaving

$$\frac{|\boldsymbol{F}_{\mathrm{rad}}|}{|\boldsymbol{F}_{\mathrm{drag}}|} = \frac{4}{9}\frac{\Phi_{\mathrm{ac}}a^2\omega}{\nu_0}. \tag{2.42}$$

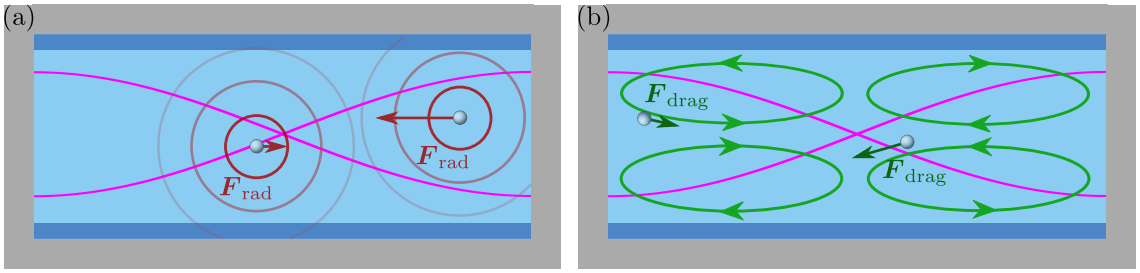

Figure 2.6: Sketch used to infer the typical particle trajectories in a channel cross-section containing a homogeneous fluid with a standing pressure half-wave acoustic field across the width (magenta). **(a)** The acoustic radiation force $\boldsymbol{F}_{\mathrm{rad}}$ (red arrows), induced by scattering as indicated by the circles around the particles, focuses the particles in the pressure node at the center ($\Phi_{\mathrm{ac}} > 0$). **(b)** The streaming-induced drag force $\boldsymbol{F}_{\mathrm{drag}}$ (green arrows) drags the particles along with the streaming flow (green loops) generated in the boundary layers (dark blue) leading to a continuous swirling motion of the particles. Adapted from Ref. [100] courtesy of Mikkel W. H. Ley.

Most important is the quadratic scaling with particle size, from which it follows that the trajectories of large particles are radiation-dominated, while the trajectories of small particles are streaming-dominated [134, 93].

The cross-over from radiation- to streaming-dominated trajectories happens at a critical particle size a_{crit}, obtained by setting the force-ratio Eq. (2.42) equal to one,

$$a_{\mathrm{crit}} \approx \sqrt{\frac{9}{4}\frac{\nu_0}{\Phi_{\mathrm{ac}}\omega}} \approx 1\ \mu\mathrm{m}, \tag{2.43}$$

where the numeric value is calculated for a polystyrene particle in water at 2 MHz. Consequently, in acoustophoresis one typically differentiates between large particles ($2a \gtrsim 5\ \mu$m) such as cells, and submicron nanoparticles ($2a \lesssim 1\ \mu$m) such as bacteria, exosomes, and vira [7]. Evidently, the controlled manipulation of nanoparticles by acoustic radiation forces is hampered by the streaming field due to the unfavorable scaling of the forces. Nanoparticle manipulation has been attempted by suppressing streaming using pulsed actuation [139, 140], and by engineering streaming patterns in special geometries [30, 141, 142]. In the enclosed Paper V [5], the use of an inhomogeneous fluid is shown to suppress streaming in a standard acoustofluidic chip, which opens a new route to acoustophoretic nanoparticle manipulation.

Chapter 3

Finite element modeling background

This short tehnical chapter introduces the finite element method (FEM) for solving partial differential equations (PDEs). The material is based on the lecture notes by Christoffer P. Nielsen [143] and Henrik Bruus [144]. The numerical simulations presented in this thesis are performed using the commercial software COMSOL MULTIPHYSICS 5.2 [145].

3.1 The finite element method

3.1.1 Spatial discretization

In finite element modeling, the spatial domain of interest Ω is discretized by choosing a large number N of grid points $\boldsymbol{r}_n$, $n = 1, 2, ..., N$ that serve as vertices for the mesh elements. Together, all the mesh elements form the complete mesh that discretizes the domain Ω.

A set of test functions $\{\hat{g}_n\}$, with $\hat{g}_n$ localized near the n'th vertex, is now introduced. In Fig. 3.1 is shown a sketch of the domain Ω with one of the test functions $\hat{g}_n$ indicated. In the sketch, $\hat{g}_n$ is a linear function. More generally, the test functions $\hat{g}_n$ are polynomials. The test function $\hat{g}_n$ is defined to be unity at the vertex n and zero at the adjacent vertices and in the rest of the domain, as indicated in the sketch. This means that the set $\{\hat{g}_n\}$ span the entire domain with an overlap between adjacent test functions. It is assumed that any field $g(\boldsymbol{r})$ defined on the domain Ω can be approximately expressed in terms of the finite basis $\{\hat{g}_n\}$,

$$g(\boldsymbol{r}) = \sum_n a_n \hat{g}_n(\boldsymbol{r}), \tag{3.1}$$

where a_n are the expansion coefficients to be determined.

3.1.2 PDE in weak form

Consider the PDE governing the field $g(\boldsymbol{r})$ in the domain Ω, which together with the boundary conditions at the domain boundary $\partial\Omega$ make up the boundary value problem.

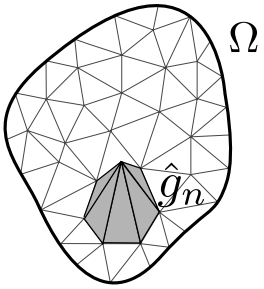

Figure 3.1: Sketch of the test functions $\hat{g}_n$ on the domain Ω. Adapted from the lecture notes by Christoffer P. Nielsen, Ref. [143]

.

Most PDEs governing continuum fields, as derived from conservation laws, can be written on the form

$$\boldsymbol{\nabla} \cdot \boldsymbol{J} - F = 0, \tag{3.2}$$

where $\boldsymbol{J} = \boldsymbol{J}[g(\boldsymbol{r})]$ is a generalized flux and $F = F(\boldsymbol{r})$ is a generalized driving force.

The idea in FEM is that, while the basis of test functions $\{\hat{g}_n\}$ cannot describe a *strong solution* of the problem, valid for every $\boldsymbol{r} \in \Omega$, it can describe an approximate solution, known as a *weak solution*, which is valid, on average, within each mesh element. The weak form equation is thus obtained by projecting the PDE onto the basis of test functions. Multiplying Eq. (3.2) by $\hat{g}_m$ and integrating over the volume, one obtains

$$\int_\Omega \hat{g}_m(\boldsymbol{r}) \Big[\boldsymbol{\nabla} \cdot \boldsymbol{J}[g(\boldsymbol{r})] - F(\boldsymbol{r}) \Big] \, \mathrm{d}V = 0, \quad \text{for all } m. \tag{3.3}$$

This is the *weak form* of the PDE, and a solution $g(\boldsymbol{r})$ satisfying Eq. (3.3) is called a *weak solution*.

For a linear flux operator $\boldsymbol{J}[g(\boldsymbol{r})] = \sum_n a_n \boldsymbol{J}[\hat{g}_n(\boldsymbol{r})]$ using the expansion Eq. (3.1), and hence Eq. (3.3) immediately takes the form of a matrix equation for the expansion coefficients $\boldsymbol{a} = \{a_n\}$,

$$\boldsymbol{K}\boldsymbol{a} = \boldsymbol{F}, \tag{3.4}$$

where $\boldsymbol{K}$ is the so-called stiffness matrix and $\boldsymbol{F}$ is the force vector, with elements

$$K_{mn} = \int_\Omega \hat{g}_m(\boldsymbol{r}) \boldsymbol{\nabla} \cdot \boldsymbol{J}[\hat{g}_n(\boldsymbol{r})] \, \mathrm{d}V, \tag{3.5a}$$

$$F_m = \int_\Omega \hat{g}_m(\boldsymbol{r}) F(\boldsymbol{r}) \, \mathrm{d}V. \tag{3.5b}$$

Thus the problem of obtaining a weak solution to the weak form PDE has been reduced to that of calculating the expansion coefficients $\boldsymbol{a} = \{a_n\}$ by matrix inversion.

3.1.3 Boundary conditions

The boundary conditions are an essential part of the boundary value problem, and they are implemented in a straight-forward way in FEM. Using the identity,

$$\boldsymbol{\nabla} \cdot (\hat{g}_m \boldsymbol{J}) = \boldsymbol{\nabla} \hat{g}_m \cdot \boldsymbol{J} + \hat{g}_m \boldsymbol{\nabla} \cdot \boldsymbol{J}, \tag{3.6}$$

the weak form PDE Eq. (3.3) is rewritten by Gauss' theorem to yield,

$$\oint_{\partial\Omega} \hat{g}_m \boldsymbol{n} \cdot \boldsymbol{J} \, \mathrm{d}A + \int_{\Omega} \left[- \boldsymbol{\nabla} \hat{g}_m \cdot \boldsymbol{J} - \hat{g}_m F \right] \mathrm{d}V = 0. \tag{3.7}$$

Neumann boundary conditions

Neumann boundary conditions, imposing a constraint on the flux,

$$\boldsymbol{n} \cdot \boldsymbol{J} = N(\boldsymbol{r}) \quad \text{for} \quad \boldsymbol{r} \in \partial\Omega, \tag{3.8}$$

are implemented directly by replacing the flux at the boundary $\boldsymbol{n} \cdot \boldsymbol{J}$ in Eq. (3.7) by the desired expression $N(\boldsymbol{r})$.

General boundary conditions

General boundary conditions, imposing the constraint

$$R[g(\boldsymbol{r})] = 0 \quad \text{for} \quad \boldsymbol{r} \in \partial\Omega, \tag{3.9}$$

require the introduction of an auxiliary field, or Lagrange multiplier, $\lambda(\boldsymbol{r})$ on the boundary $\boldsymbol{r} \in \partial\Omega$. The auxiliary field allows the flux $\boldsymbol{n} \cdot \boldsymbol{J}$ to vary as needed in order to fulfill the specific boundary condition Eq. (3.9). Thus, the flux will be replaced by this unknown Lagrange multiplier, $\boldsymbol{n} \cdot \boldsymbol{J} = \lambda(\boldsymbol{r})$, and $\lambda(\boldsymbol{r})$ is now a field to be solved for.

Just like the field $g(\boldsymbol{r})$ is expanded in the test functions $\hat{g}_m$, the auxiliary field $\lambda(\boldsymbol{r})$ is expanded in the test functions $\hat{\lambda}_m$, defined in the mesh elements at the boundary $\partial\Omega$. The weak form equation for the constraint Eq. (3.9) is thus,

$$\oint_{\partial\Omega} \hat{\lambda}_m(\boldsymbol{r}) \, R[g(\boldsymbol{r})] \, \mathrm{d}A = 0, \tag{3.10}$$

and it is added directly to Eq. (3.7), while at the same time making the substitution $\boldsymbol{n} \cdot \boldsymbol{J} = \lambda(\boldsymbol{r})$. Hence, Eq. (3.7) is generalized to

$$\oint_{\partial\Omega} \left[\hat{g}_m \lambda + \hat{\lambda}_m R \right] \mathrm{d}A + \int_{\Omega} \left[- \boldsymbol{\nabla} \hat{g}_m \cdot \boldsymbol{J} - \hat{g}_m F \right] \mathrm{d}V = 0. \tag{3.11}$$

which imposes the general boundary condition in Eq. (3.9).

Dirichlet boundary conditions

Dirichlet boundary conditions, imposing a constraint on the field

$$g(\boldsymbol{r}) = D(\boldsymbol{r}) \quad \text{for} \quad \boldsymbol{r} \in \partial\Omega, \tag{3.12}$$

are a special case of the general boundary condition Eq. (3.9), and can thus be imposed directly by Eq. (3.11) using $R(\boldsymbol{r}) = g(\boldsymbol{r}) - D(\boldsymbol{r})$.

3.2 COMSOL Multiphysics

Comsol Multiphysics [145] includes all the machinery needed to solve complex boundary value problems with multiple coupled nonlinear PDEs. Complete control of the equations that are solved, as well as the boundary conditions that are imposed, is achieved by implementing the equations using the `Weak Form PDE` module instead of using the predefined physics modules. Thus the equations and the boundary conditions Eq. (3.11) are typed in by the user, with the possible addition of extra weak contributions at the boundaries due to the couplings between the physical fields. The integrand of the volume integral is typed into the weak expression of the `Weak Form PDE`, while the integrand of the boundary integral is typed in as a `Weak Contribution` on the boundary, or alternatively, implemented using the `Zero Flux` (default), `Dirichlet Boundary Condition`, or `Constraint` functionalities.

The discretization of the mesh is determined to ensure that the relevant physics is resolved, e.g., the viscous boundary layers in acoustic streaming simulations. To ensure that a proper discretization has been used, the numerical models are tested in a variety of ways, e.g., by monitoring conserved quantities, by visual inspection of the fields, and by careful mesh analysis [134, 146].

Chapter 4

Nonlinear acoustics methodology

"It takes nerve as well as ability to criticize Lord Rayleigh successfully, and Brillouin had both. But as we have seen, even a Brillouin can make a faux pas. On the other hand, so can I, and so can any of you. I've already made plenty on my part; now it's someone else's turn." — Robert T. Beyer in *Acoustic radiation pressure – the history of a mislabeled tensor* [147].

In this chapter, the nonlinear acoustics methodology of the thesis is synthesized and distilled into a single equation, almost a principle, which I believe is the essence of perturbative nonlinear acoustics. It is shown how this equation connects the different works in this thesis on nonlinear acoustic forces acting on fluids and particles. The principle is attributed to Brillouin [148], who generalized the notion of acoustic radiation pressure to that of a force originating from a tensor.

Section 4.1 first presents the necessary theoretical background of the second-order mean Eulerian excess pressure. The author's interpretation of the second-order mean Eulerian excess pressure leads to a central hypothesis of this thesis, used in the derivation of the novel results on the acoustic force density acting on inhomogeneous fluids in acoustic fields presented in Papers III, IV, and V [3, 4, 5]. Section 4.2 then introduces the time-averaged acoustic (pseudo-)momentum-flux-density tensor $\langle \boldsymbol{\Pi}_{\mathrm{ac}} \rangle$, and the time-averaged acoustic force density $\boldsymbol{f}_{\mathrm{ac}} = -\boldsymbol{\nabla} \cdot \langle \boldsymbol{\Pi}_{\mathrm{ac}} \rangle$ that derives from its divergence. The remaining Sections 4.3 to 4.7 demonstrate and briefly discuss how this equation for $\boldsymbol{f}_{\mathrm{ac}}$ can be used to understand a range of nonlinear acoustics phenomena, some of which were first studied in the enclosed Papers I to V [1, 2, 3, 4, 5]. These include the acoustic radiation force acting on an interface (Section 4.3) or a particle (Section 4.4, Paper I), the non-dissipative acoustic force density $\boldsymbol{f}_{\mathrm{ac}}^{\mathrm{invisc}}$ acting on an inhomogeneous inviscid fluid with variations in $\rho_0(\boldsymbol{r})$ and $\kappa_0(\boldsymbol{r})$, which relocates and stabilizes the fluid inhomogeneities (Section 4.5, Papers III and IV), the dissipative acoustic force density in a viscous and homogeneous fluid $\boldsymbol{f}_{\mathrm{ac}}^{\mathrm{hom}}$, which drives Rayleigh and Eckart streaming flows (Section 4.6), and finally, the generalized acoustic force density $\boldsymbol{f}_{\mathrm{ac}}$ in a viscous and inhomogeneous fluid including non-dissipative and dissipative forces, which drives a new class of altered and suppressed acoustic streaming flows (Section 4.7, Paper V). Figure 4.1 of Section 4.2 presents a

graphical summary of the force densities associated with these different phenomena. The phenomena themselves are not studied in this chapter – only their origins – and hence the reader is referred to the enclosed Papers I to V summarized in Chapter 5 and enclosed in Chapters 6 to 10, containing the main results of this thesis.

4.1 Second-order mean Eulerian excess pressure

The effect of a propagating acoustic wave on the second-order momentum balance is considered. For a freely propagating wave, for which viscosity may be neglected, $\eta_0 = 0$, in a homogeneous fluid, the time-averaged second-order momentum equation, obtained from Eq. (2.4b), becomes,

$$\mathbf{0} = -\boldsymbol{\nabla}\langle p_2 \rangle - \boldsymbol{\nabla} \cdot \langle \rho_0 \boldsymbol{v}_1 \boldsymbol{v}_1 \rangle. \tag{4.1}$$

Here, it has been used that the time-average of a total time-derivative is zero. It follows that the second-order mean Eulerian excess pressure $\langle p_2 \rangle$ can be expressed in terms of the first-order acoustic fields.

Using $\boldsymbol{v}_1 = \boldsymbol{\nabla}\phi$, $\nabla^2\phi = (1/c^2)\partial_t^2\phi$, and $p_1 = -\rho_0\partial_t\phi$, Eq. (2.25), as well as the exchange of a time-derivative in a time-averaged product of time-harmonic fields $\langle \partial_t^2\phi\boldsymbol{\nabla}\phi \rangle = -\langle \partial_t\phi\boldsymbol{\nabla}\partial_t\phi \rangle$, the expression for $\langle p_2 \rangle$ obtained from Eq. (4.1) becomes [149, 150, 119, 43],

$$\langle p_2 \rangle = \langle p_{11} \rangle = \frac{1}{2}\kappa_0\langle p_1^2 \rangle - \frac{1}{2}\rho_0\langle v_1^2 \rangle. \tag{4.2}$$

Under certain conditions, the addition of an integration constant C, independent on space and time, may be needed to satisfy external constraints [149]. Note that $\langle p_2 \rangle$ is given by the difference between the acoustic potential and kinetic energy densities. For the purpose of evaluating nonlinear acoustic forces, the second-order mean Eulerian excess pressure is henceforth denoted as $\langle p_{11} \rangle$ to indicate that this pressure is an input at the second order, dependent on products of first-order fields, and not a variable solved for.

A central hypothesis of this thesis is that the expression Eq. (4.2) for $\langle p_{11}(\boldsymbol{r}) \rangle$ gives the *local* mean Eulerian excess pressure associated with the local value of the acoustic disturbances $p_1(\boldsymbol{r})$ and $\boldsymbol{v}_1(\boldsymbol{r})$ in the fluid of local density $\rho_0(\boldsymbol{r})$ and compressibility $\kappa_0(\boldsymbol{r})$. This hypothesis may be considered an extension of the local equilibrium hypothesis of classical irreversible thermodynamics, which was already used in formulating the governing transport equations Eq. (2.4). As such, it can be expected to remain valid as long as the continuum hypothesis is not violated, which means that each fluid cell must be sufficiently large for microscopic fluctuations to be negligible, but sufficiently small so that equilibrium is realized to a good approximation within each cell. As noted by de Groot and Mazur on classical irreversible thermodynamics: *"This hypothesis of "local" equilibrium can, from a macroscopic point of view, only be justified by virtue of the validity of the conclusions derived from it."* [151].

4.2 Acoustic force density

Introducing the momentum-flux-density tensor $\boldsymbol{\Pi}$, the momentum equation Eq. (2.4b) may be written as a continuity equation,

$$\partial_t(\rho \boldsymbol{v}) + \boldsymbol{\nabla}\cdot\boldsymbol{\Pi} = \boldsymbol{0}, \quad \text{with} \quad \boldsymbol{\Pi} = -\boldsymbol{\sigma} + \rho\boldsymbol{v}\boldsymbol{v} \tag{4.3}$$

Hence, the negative divergence of the momentum-flux-density tensor may be interpreted as the force density $\boldsymbol{f} = -\boldsymbol{\nabla}\cdot\boldsymbol{\Pi}$ with units of force per volume.

Going to the second order of approximation, and taking the time-average of Eq. (4.3), the time-averaged acoustic (pseudo-)momentum-flux-density tensor $\langle\boldsymbol{\Pi}_{\text{ac}}\rangle$, which is the part given in terms of products of first-order acoustic fields, becomes [148, 149, 43]

$$\langle\boldsymbol{\Pi}_{\text{ac}}\rangle = \langle p_{11}\rangle\mathbf{I} + \langle\rho_0\boldsymbol{v}_1\boldsymbol{v}_1\rangle, \quad \text{with} \quad \langle p_{11}\rangle = \frac{1}{2}\kappa_0\langle p_1^2\rangle - \frac{1}{2}\rho_0\langle v_1^2\rangle. \tag{4.4}$$

This suggests that the presence of an acoustic field, p_1 and $\boldsymbol{v}_1$, gives rise to a time-averaged acoustic force density $\boldsymbol{f}_{\text{ac}}$, given by

$$\boldsymbol{f}_{\text{ac}} = -\boldsymbol{\nabla}\cdot\langle\boldsymbol{\Pi}_{\text{ac}}\rangle, \quad \text{with} \quad \langle\boldsymbol{\Pi}_{\text{ac}}\rangle = \langle p_{11}\rangle\mathbf{I} + \langle\rho_0\boldsymbol{v}_1\boldsymbol{v}_1\rangle. \tag{4.5}$$

This is the principal equation, referred to throughout this chapter.

The force $\mathrm{d}\boldsymbol{F}_{\text{ac}}$ on a surface element of area $\mathrm{d}a$ with normal vector $\boldsymbol{n}$ is the negative of the momentum-flux-density projected onto that direction, i.e., $\mathrm{d}\boldsymbol{F}_{\text{ac}} = -\langle\boldsymbol{\Pi}_{\text{ac}}\rangle\cdot\boldsymbol{n}\mathrm{d}a$. Considering an arbitrary volume Ω_1 enclosed by the surface $\partial\Omega_1$, the total force on Ω_1 is obtained by integration,

$$\boldsymbol{F}_{\text{ac}} = -\oint_{\partial\Omega_1}\langle\boldsymbol{\Pi}_{\text{ac}}\rangle\cdot\boldsymbol{n}\,\mathrm{d}a = -\int_{\Omega_1}\boldsymbol{\nabla}\cdot\langle\boldsymbol{\Pi}_{\text{ac}}\rangle\,\mathrm{d}\boldsymbol{r}. \tag{4.6}$$

Indeed, the first equality is identical to Eq. (2.34) for $\boldsymbol{F}_{\text{rad}}$ acting on a particle when Ω_1 is a volume enclosing that particle.

Note that for an acoustic wave propagating freely without attenuation in a homogeneous fluid, Eq. (4.1) directly yields $\boldsymbol{\nabla}\cdot\langle\boldsymbol{\Pi}_{\text{ac}}\rangle = \boldsymbol{0}$, which means that the acoustic force density $\boldsymbol{f}_{\text{ac}}$ is zero in this case. What then generates a non-zero divergence $\boldsymbol{\nabla}\cdot\langle\boldsymbol{\Pi}_{\text{ac}}\rangle$ from which a force is derived?

The answer to this question is explored in the remaining of this chapter, which presents an overview of nonlinear acoustic forces and force densities including novel ideas developed in the enclosed Papers III, IV, and V [3, 4, 5]. Figure 4.1 presents a graphical summary of the findings, indicating the most important cases that give rise to a non-zero divergence $\boldsymbol{\nabla}\cdot\langle\boldsymbol{\Pi}_{\mathrm{ac}}\rangle$ and thus a nonlinear acoustic force. Six different cases are illustrated in (a)-(f), and their relation to the theory outlined above is briefly described in Section 4.3 to 4.7. The six cases are,

(a) The acoustic radiation force per area $\boldsymbol{F}_{\mathrm{rad}}/A$ acting on a straight interface in 1D. The notion of acoustic radiation pressure is discussed based on this example; Section 4.3.

(b) The acoustic radiation force $\boldsymbol{F}_{\mathrm{rad}}$ acting on a particle; Section 4.4. Thermoviscous corrections to this force are studied in Paper I [1].

(c) The non-dissipative acoustic force density $\boldsymbol{f}_{\mathrm{ac}}^{\mathrm{invisc}}$ acting on an inhomogeneous inviscid fluid with variations in $\rho_0(\boldsymbol{r})$ and $\kappa_0(\boldsymbol{r})$, which relocates and stabilizes inhomogeneities; Section 4.5. A novel theory is developed and validated experimentally in Paper III [3], explored further in Paper IV [4], and the phenomenon is used to develop the cell-handling method of iso-acoustic focusing in Paper II [2].

(d) The dissipative acoustic force density in a homogeneous viscous fluid $\boldsymbol{f}_{\mathrm{ac}}^{\mathrm{hom}}$, which drives acoustic streaming flows; Section 4.6.

(e) The dissipative acoustic force density $\boldsymbol{f}_{\mathrm{ac}}^{\mathrm{hom\text{-}bulk}}$, which is the part of $\boldsymbol{f}_{\mathrm{ac}}^{\mathrm{hom}}$ that drives bulk Eckart streaming; Section 4.6.1.

(e) The generalized acoustic force density $\boldsymbol{f}_{\mathrm{ac}}$ valid in viscous and inhomogeneous fluids including non-dissipative and dissipative forces, which drives a new class of altered and suppressed streaming flows; Section 4.7. Novel theoretical and experimental results are presented in Paper V [5].

Note again, that the phenomena themselves are not studied in this chapter – only their origins, as explained by the principal equation Eq. (4.5).

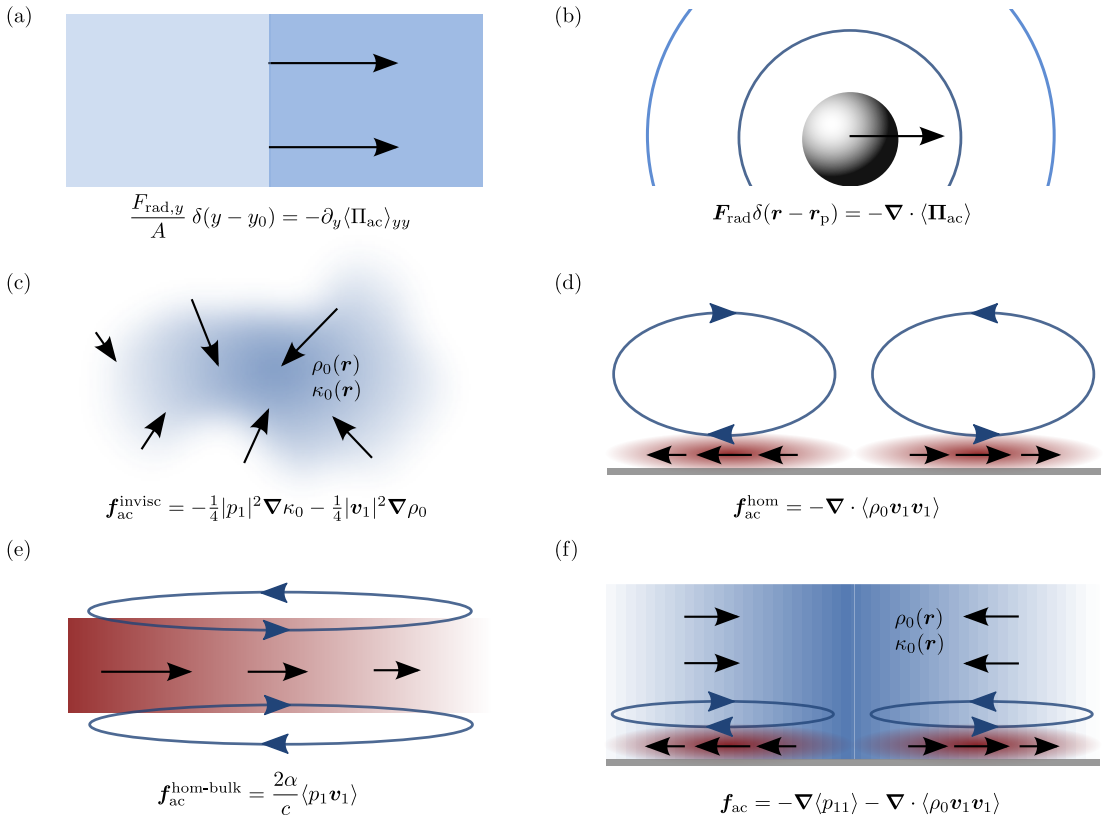

Figure 4.1: Sketches of the nonlinear acoustic force densities described in Section 4.3 to 4.7, each being responsible for a different nonlinear acoustics phenomenon. Black arrows indicate the acoustic force density. Blue shading indicates that the force density is non-dissipative, while red shading indicates a dissipative force densities. The acoustic force densities, given in the equations below each sketch, are all obtained from a divergence in the time-averaged acoustic momentum-flux density tensor, Eq. (4.5). **(a)** The acoustic radiation force per area $\boldsymbol{F}_{\mathrm{rad}}/A$ acting on an interface in 1D (non-dissipative origin). The force density has a singularity at the interface in $y = y_0$. **(b)** The acoustic radiation force $\boldsymbol{F}_{\mathrm{rad}}$ acting on a particle (non-dissipative origin). Seen from the far-field, the force density has a singularity at the particle position in $\boldsymbol{r} = \boldsymbol{r}_{\mathrm{p}}$. **(c)** The non-dissipative acoustic force density $\boldsymbol{f}_{\mathrm{ac}}^{\mathrm{invisc}}$ acting on an inhomogeneous fluid with variations in $\rho_0(\boldsymbol{r})$ and $\kappa_0(\boldsymbol{r})$, which may lead to relocation flows and stabilization of certain inhomogeneity configurations. **(d)** The dissipative acoustic force density $\boldsymbol{f}_{\mathrm{ac}}^{\mathrm{hom}}$ in a homogeneous viscous fluid. Boundary-layer dissipation yields Rayleigh streaming (blue loops). **(e)** The dissipative acoustic force density $\boldsymbol{f}_{\mathrm{ac}}^{\text{hom-bulk}}$ (part of $\boldsymbol{f}_{\mathrm{ac}}^{\mathrm{hom}}$), which drives bulk Eckart streaming (blue loops), proportional to the attenuation coefficient α, Eq. (2.21). **(f)** The generalized acoustic force density $\boldsymbol{f}_{\mathrm{ac}}$ in an inhomogeneous viscous fluid, including inhomogeneity-induced non-dissipative forces that may stabilize certain inhomogeneity configurations, as well as dissipative forces from boundary-layer and bulk attenuation that may drive streaming.

4.3 Acoustic radiation force on an interface in 1D

Consider the one-dimensional problem of a straight interface in $y = y_0$ between two immiscible fluids a ($y < y_0$) and b ($y > y_0$), with a traveling plane wave propagating in the y-direction normally incident from fluid a to fluid b, $\boldsymbol{v}_1 = v_1 \boldsymbol{e}_y$. In general, this yields an acoustic radiation force acting on the interface. The time-averaged acoustic momentum-flux-density, calculated from Eq. (4.4), becomes [43]

$$\langle \boldsymbol{\Pi}_{\mathrm{ac}} \rangle \cdot \boldsymbol{e}_y = \Big\langle \frac{1}{2}\kappa_0 p_1^2 + \frac{1}{2}\rho_0 v_1^2 \Big\rangle \boldsymbol{e}_y = \langle E_{\mathrm{ac}} \rangle \boldsymbol{e}_y = \frac{\langle \boldsymbol{S} \rangle}{c}, \tag{4.7}$$

Hence, in the case of a 1D traveling plane wave, the time-averaged momentum-flux-density equals the time-averaged Poynting vector $\langle \boldsymbol{S} \rangle = \langle p_1 \boldsymbol{v}_1 \rangle$ divided by the phase velocity c, or alternatively, the energy density $\langle E_{\mathrm{ac}} \rangle \boldsymbol{e}_y$ [43].

The radiation force $\boldsymbol{F}_{\mathrm{rad}}$ per area A on the interface is calculated from Eq. (4.6) by integrating the acoustic force density $\boldsymbol{f}_{\mathrm{ac}} = -\boldsymbol{\nabla} \cdot \langle \boldsymbol{\Pi}_{\mathrm{ac}} \rangle = -\partial_y \langle E_{\mathrm{ac}} \rangle \, \boldsymbol{e}_y$ across the interface. Defining the difference Δ in the fluid property q across the interface as $\Delta q = q_b - q_a$, one obtains

$$\frac{\boldsymbol{F}_{\mathrm{rad}}}{A} = -\boldsymbol{e}_y \int_{y_0-}^{y_0+} \partial_y \langle E_{\mathrm{ac}} \rangle \mathrm{d}y = -\Delta \langle E_{\mathrm{ac}} \rangle \boldsymbol{e}_y = -\frac{1}{4}\big[|p_1|^2 \Delta\kappa_0 + |v_1|^2 \Delta\rho_0 \big] \boldsymbol{e}_y, \tag{4.8}$$

where, in the last step, the time-averaging has been carried out, and the continuity of the acoustic fields p_1 and v_1 evaluated in $y = y_0$ has been used. The result is in agreement with that given in Ref. [149]. It is furthermore obtained as a special case in the study of the acoustic force density acting on inhomogeneous fluids in Paper III [3], as demonstrated later in Section 4.5.1.

Formally, the connection between the force per area $\boldsymbol{F}_{\mathrm{rad}}/A$ on the interface in $y = y_0$ and the divergence in the acoustic momentum-flux-density tensor $\boldsymbol{\nabla} \cdot \langle \boldsymbol{\Pi}_{\mathrm{ac}} \rangle$ may be written in terms of the Dirac delta-function. In the 1D case under consideration,

$$\frac{F_{\mathrm{rad},y}(y)}{A} \, \delta(y - y_0) = -\partial_y \langle \Pi_{\mathrm{ac}} \rangle_{yy}. \tag{4.9}$$

4.3.1 Acoustic radiation pressure

The quantity sometimes referred to as the acoustic radiation pressure may be extracted from the example above in the case of a 1D traveling wave normally incident on an interface. Indeed, if one interprets the radiation force Eq. (4.8) as being derived from the (negative) gradient of an acoustic radiation pressure p_{rad}, this pressure is

$$p_{\mathrm{rad}} = \langle E_{\mathrm{ac}} \rangle = \Big\langle \frac{1}{2}\kappa_0 p_1^2 + \frac{1}{2}\rho_0 v_1^2 \Big\rangle = \big\langle p_{11}^{\mathrm{L}} \big\rangle, \tag{4.10}$$

In the 1D example, the radiation pressure happens to be equal to the time-averaged acoustic energy density $\langle E_{\mathrm{ac}} \rangle$ [43], or equivalently, the second-order mean Lagrangian pressure $\langle p_{11}^{\mathrm{L}} \rangle$ [149]. However, this is not generally true in 2D and 3D [149]. Hence, the tensorial description of acoustic radiation forces must be employed [152]. In my opinion one should refrain from the concept of acoustic radiation pressure unless clearly tying it to the acoustic momentum-flux-density tensor $\langle \boldsymbol{\Pi}_{\mathrm{ac}} \rangle$.

4.4 Acoustic radiation force on a particle

Consider the acoustic radiation force $\boldsymbol{F}_{\mathrm{rad}}$ acting on a particle of radius a placed in $\boldsymbol{r} = \boldsymbol{r}_{\mathrm{p}}$ in a time-harmonic acoustic field in a homogeneous fluid, as introduced in Chapter 2, Section 2.4. Based on the conservation of the total momentum $\boldsymbol{P}$ in the fluid, Eq. (2.30), and the choice of placing the integration surface in the inviscid far-field, the expression Eq. (2.34) for $\boldsymbol{F}_{\mathrm{rad}}$ was derived. Introducing the momentum-flux-density tensor $\langle \boldsymbol{\Pi}_{\mathrm{ac}} \rangle$ into Eq. (2.34), the expression for $\boldsymbol{F}_{\mathrm{rad}}$ becomes identical to that given in Eq. (4.6), as expected. Hence, the evaluation of $\boldsymbol{F}_{\mathrm{rad}}$ once again comes down to the evaluation of $\boldsymbol{\nabla} \cdot \langle \boldsymbol{\Pi}_{\mathrm{ac}} \rangle$.

Note that, treating the particle as a point particle in the far-field, $\boldsymbol{\nabla} \cdot \langle \boldsymbol{\Pi}_{\mathrm{ac}} \rangle$ is non-zero only at the singularity in the particle position $\boldsymbol{r} = \boldsymbol{r}_{\mathrm{p}}$ introduced by the scattered field [119, 153]. Indeed, $\boldsymbol{\nabla} \cdot \langle \boldsymbol{\Pi}_{\mathrm{ac}} \rangle = \boldsymbol{0}$ remains true everywhere else. From the time-average of the momentum equation (4.3) (with $\eta_0 = 0$), one finds to second order

$$\begin{aligned} \boldsymbol{\nabla} \cdot \langle \boldsymbol{\Pi}_{\mathrm{ac}} \rangle &= -\langle \boldsymbol{v}_1 \partial_t \rho_1 \rangle - \langle \rho_1 \partial_t \boldsymbol{v}_1 \rangle, \\ &= \rho_0 \langle \boldsymbol{v}_1 (\boldsymbol{\nabla} \cdot \boldsymbol{v}_1) \rangle + \langle \boldsymbol{v}_1 \partial_t \rho_1 \rangle, \\ &= \rho_0 \Big\langle \boldsymbol{v}_1 \Big(\nabla^2 - \frac{1}{c^2} \partial_t^2 \Big) \phi \Big\rangle. \end{aligned} \tag{4.11}$$

where, in the first step the vanishing of time averages of first-order fields is used, in the second step, the first and second term is rewritten using, respectively, the mass equation $\partial_t \rho_1 = -\rho_0 \boldsymbol{\nabla} \cdot \boldsymbol{v}_1$, and the exchange of time-derivatives in a time-averaged product of time-harmonic fields $\langle \rho_1 \partial_t \boldsymbol{v}_1 \rangle = -\langle \boldsymbol{v}_1 \partial_t \rho_1 \rangle$. Finally, in the third step, the velocity potential ϕ is used to write $\boldsymbol{v}_1 = \boldsymbol{\nabla} \phi$ and $\rho_1 = -(\rho_0 / c^2) \partial_t \phi$, see Eq. (2.25).

Resolving the first-order fields in incident and scattered fields $\boldsymbol{v}_1 = \boldsymbol{v}_{\mathrm{in}} + \boldsymbol{v}_{\mathrm{sc}}$ and $\phi = \phi_{\mathrm{in}} + \phi_{\mathrm{sc}}$, the incident field is without singularities, so the d'Alembert operator acting on ϕ_{in} vanishes. Consequently, by Eq. (4.11) the expression for $\boldsymbol{F}_{\mathrm{rad}}$ becomes

$$\boldsymbol{F}_{\mathrm{rad}} = -\int_{\Omega_1} \boldsymbol{\nabla} \cdot \langle \boldsymbol{\Pi}_{\mathrm{ac}} \rangle \, \mathrm{d}\boldsymbol{r} = -\int_{\Omega_1} \rho_0 \Big\langle \boldsymbol{v}_1 \Big(\nabla^2 - \frac{1}{c^2} \partial_t^2 \Big) \phi_{\mathrm{sc}} \Big\rangle \, \mathrm{d}\boldsymbol{r}, \tag{4.12}$$

The d'Alembert operator acting on ϕ_{sc}, on the other hand, can be shown to yield a delta-function distribution [119]. Using the appropriate form of ϕ_{sc} in the far-field $r \gg \lambda$ in the long-wavelength limit $a \ll \lambda$, it was thus shown in Ref. [119] that the integral Eq. (4.12) yields Eq. (2.35) for $\boldsymbol{F}_{\mathrm{rad}}$, expressed in terms of the incident field p_{in} and $\boldsymbol{v}_{\mathrm{in}}$ and the monopole and dipole scattering coefficients f_0 and f_1.

In the business of understanding acoustic forces acting on particles and fluids from the divergence in the acoustic momentum-flux-density tensor, it is now clear how, and why, $\boldsymbol{F}_{\mathrm{rad}}$ and $\boldsymbol{\nabla} \cdot \langle \boldsymbol{\Pi}_{\mathrm{ac}} \rangle$ are related,

$$\boldsymbol{F}_{\mathrm{rad}}(\boldsymbol{r}) \, \delta(\boldsymbol{r} - \boldsymbol{r}_{\mathrm{p}}) = -\boldsymbol{\nabla} \cdot \langle \boldsymbol{\Pi}_{\mathrm{ac}} \rangle. \tag{4.13}$$

4.5 Acoustic force density acting on inhomogeneous fluids

Consider an inhomogeneous fluid with variations in the density ρ_0, the compressibility κ_0, and the viscosity η_0, caused by a solute concentration field $\zeta(\boldsymbol{r}, \tau)$ that varies on the slow

hydrodynamic time scale $\tau \sim 10$ ms by diffusion and advection, Eq. (2.5). Another cause of inhomogeneities could be variations in the mean temperature T_0. In the former case,

$$\rho_0 = \rho_0[\zeta(\boldsymbol{r},\tau)], \quad \kappa_0 = \kappa_0[\zeta(\boldsymbol{r},\tau)], \quad \eta_0 = \eta_0[\zeta(\boldsymbol{r},\tau)], \tag{4.14}$$

with the exact dependencies known from measurements for a particular solute, e.g., iodixanol, for which the fitted polynomials are given in Papers II and III [2, 3]. The energy density E_{ac} in a 1D standing plane wave in such an inhomogeneous fluid is no longer constant as in a homogeneous fluid. This suggests an imbalance in the momentum-flux-density and the presence of an acoustic force density acting on the fluid.

To be specific, it is shown in the enclosed Paper III that the negative divergence of the acoustic momentum-flux-density tensor, Eq. (4.5), evaluated under the assumption of inviscid acoustics in inhomogeneous fluids, i.e., $\eta_0 = 0$ while $\rho_0 = \rho_0(\boldsymbol{r})$ and $\kappa_0 = \kappa_0(\boldsymbol{r})$ in the acoustics, yields the force density [3],

$$\boldsymbol{f}_{\text{ac}}^{\text{invisc}} = -\frac{1}{4}|p_1|^2\boldsymbol{\nabla}\kappa_0 - \frac{1}{4}|\boldsymbol{v}_1|^2\boldsymbol{\nabla}\rho_0. \tag{4.15}$$

Hence, an acoustic force density acts on the inhomogeneous fluid in every point where there is a gradient in the continuous material parameters $\rho_0(\boldsymbol{r})$ or $\kappa_0(\boldsymbol{r})$.

This remarkably simple result Eq. (4.15) is derived from the principal equation Eq. (4.5), considering the mean Eulerian excess pressure $\langle p_{11}\rangle$ as an input in the second-order of approximation. It is further assumed that the expression for $\langle p_{11}\rangle$, Eq. (4.4), holds true locally in an inhomogeneous fluid, as discussed in Section 4.1.

A few pitfalls to the successful derivation of Eq. (4.15) should be pointed out. First, note that Eq. (4.15) is derived from the principal equation Eq. (4.5), namely

$$\boldsymbol{f}_{\text{ac}}^{\text{invisc}} = -\boldsymbol{\nabla}\cdot\langle\boldsymbol{\Pi}_{\text{ac}}\rangle = -\boldsymbol{\nabla}\langle p_{11}\rangle - \boldsymbol{\nabla}\cdot\langle\rho_0\boldsymbol{v}_1\boldsymbol{v}_1\rangle \quad \text{with} \quad \eta_0 = 0. \tag{4.16}$$

and that this force density enters a system of equations describing the slow-time-scale hydrodymamics [3, 4, 5]. Indeed, the idea of splitting the problem into a fast acoustic time scale $t \sim 0.1$ µs, and a slow hydrodynamic time scale $\tau \sim 10$ ms, developed in Paper III [3] and further used in Papers IV and V [4, 5] is what makes it possible to study the dynamics of inhomogeneities in acoustic fields under the combined actions of the acoustic force density, gravity, and diffusion-advection, as well as viscous stresses. Introducing the gravitational acceleration $\boldsymbol{g}$, the slow-time-scale hydrodynamics takes the form [3, 4, 5],

$$\partial_\tau(\rho_0\boldsymbol{v}) = \boldsymbol{\nabla}\cdot\big[\boldsymbol{\tau} - \rho_0\boldsymbol{v}\boldsymbol{v}\big] - \boldsymbol{\nabla}p + \boldsymbol{f}_{\text{ac}}^{\text{invisc}} + \rho_0\boldsymbol{g}, \tag{4.17a}$$

$$\partial_\tau\rho_0 = \boldsymbol{\nabla}\cdot\big[-\rho_0\boldsymbol{v}\big], \tag{4.17b}$$

$$\partial_\tau\zeta = \boldsymbol{\nabla}\cdot\big[D\boldsymbol{\nabla}\zeta - \boldsymbol{v}\zeta\big]. \tag{4.17c}$$

Note that the equations couple through the specific dependence of $\rho_0(\zeta)$, $\kappa_0(\zeta)$, and $\eta_0(\zeta)$, Eq. (4.14). Hence, only p, $\boldsymbol{v}$ and ζ are independent variabes solved for. It is crucial to realize that $\boldsymbol{f}_{\text{ac}}^{\text{invisc}}$, including its gradient term $-\boldsymbol{\nabla}\langle p_{11}\rangle$, is a function of the dynamical variable ζ through Eqs. (4.14) and (4.16).

Here comes the pitfall. Because $\langle p_{11} \rangle = \langle p_{11}(\zeta) \rangle$, the gradient term $-\boldsymbol{\nabla}\langle p_{11} \rangle$ from $\boldsymbol{f}_{\mathrm{ac}}^{\mathrm{invisc}}$ *cannot* be absorbed into the pressure gradient $-\boldsymbol{\nabla} p$ in the momentum equation Eq. (4.17a) simply by redefining the pressure from p to $\tilde{p} = p + \langle p_{11} \rangle$, because then its explicit dependence on the dynamical variable ζ would be lost. Indeed, such a redefinition is possible from a mathematical standpoint, however, because $\tilde{p} = \tilde{p}(\zeta)$, the new variables $\tilde{p}$, $\boldsymbol{v}$, and ζ are not adequately coupled unless one finds and inserts the explicit inverse expression for $\zeta = \zeta(\tilde{p})$ in the system of equations, thereby introducing $\tilde{p}$ in all of Eqs. (4.17a)-(4.17c). In conclusion, one must keep the gradient term in Eq. (4.16) when evaluating the expression.

In order to correctly evaluate the expression Eq. (4.16) to the result Eq. (4.15), one must furthermore consider inhomogeneous-fluid wave dynamics, as the wave equation for homogeneous fluids no longer applies. As noted in Paper III, the curl of $\boldsymbol{v}_1$ is not zero in an inhomogeneous fluid as it is in a homogeneous fluid, but instead the curl of $\rho_0 \boldsymbol{v}_1$ is zero. Hence, acoustics in inhomogeneous fluids should be formulated in terms of the mass current potential ϕ_ρ instead of the usual velocity potential ϕ [3],

$$\rho_0 \boldsymbol{v}_1 = \boldsymbol{\nabla}\phi_\rho, \qquad p_1 = -\partial_t \phi_\rho. \tag{4.18}$$

Keeping this in mind, the expression Eq. (4.16) yields the result given in Eq. (4.15) as shown in Paper III after some algebra [3]. The conclusion is that inhomogeneities in $\rho_0(\boldsymbol{r})$ and $\kappa_0(\boldsymbol{r})$ result in a divergence in the time-averaged momentum-flux density tensor, and that this yields a non-dissipative acoustic force density that acts on inhomogeneous fluids to relocate and stabilize certain inhomogeneity configuration, see Paper III and IV [3, 4]. As such, the acoustic force density $\boldsymbol{f}_{\mathrm{ac}}^{\mathrm{invisc}}$ shows more similarity to the acoustic radiation force than to the dissipative force densities that drive streaming.

4.5.1 Acoustic radiation force on an interface in 1D revisited

Revisiting the 1D example of Section 4.3, a straight interface in $y = y_0$ between two immiscible fluids a ($y < y_0$) and b ($y > y_0$) is considered from the perspective of the novel theory of the acoustic force density $\boldsymbol{f}_{\mathrm{ac}}^{\mathrm{invisc}}$ [3]. Writing the fluid property q using the Heaviside step-function $H(y)$ as $q(y) = q_a + \Delta q\, H(y - y_0)$, where $\Delta q = q_b - q_a$, the gradients become $\boldsymbol{\nabla}\rho_0 = \Delta\rho_0 \delta(y - y_0)\boldsymbol{e}_y$ and $\boldsymbol{\nabla}\rho_0 = \Delta\kappa_0 \delta(y - y_0)\boldsymbol{e}_y$. Integrating $\boldsymbol{f}_{\mathrm{ac}}^{\mathrm{invisc}}$, Eq. (4.15), across the interface yields the force per area $\boldsymbol{F}_{\mathrm{ac}}/A$ on the interface. Using that the fields p_1 and $\boldsymbol{v}_1$ are continuous, one finds,

$$\frac{\boldsymbol{F}_{\mathrm{ac}}}{A} = -\frac{1}{4}\left[|p_1|^2 \Delta\kappa_0 + |\boldsymbol{v}_1|^2 \Delta\rho_0\right]\boldsymbol{e}_y = -\Delta\langle E_{\mathrm{ac}} \rangle \boldsymbol{e}_y, \tag{4.19}$$

in agreement with the previously derived expression Eq. (4.8), and the literature in general [149, 43].

4.6 Acoustic streaming in a homogeneous fluid

Acoustic streaming in a viscous homogeneous fluid was introduced in Chapter 2, Section 2.3. It has been the subject of several important classical studies [77, 81, 83, 84], as

well as more recent studies [79, 82]. Common to these studies is that the driving term is always derived from the force density,

$$\boldsymbol{f}_{\mathrm{ac}}^{\mathrm{hom}} = -\boldsymbol{\nabla}\cdot\langle\rho_0\boldsymbol{v}_1\boldsymbol{v}_1\rangle. \tag{4.20}$$

This acoustic force density can also be inferred from the principal equation Eq. (4.5). Indeed, in a viscous homogeneous fluid $\langle p_{11}\rangle$ is independent of the hydrodynamic dynamical variables (in contrast to the inhomogeneous case, where $\langle p_{11}\rangle = \langle p_{11}(\zeta)\rangle$), so $\boldsymbol{\nabla}\langle p_{11}\rangle$ can be absorbed into the hydrodynamic pressure gradient $\boldsymbol{\nabla}p$ by redefining the pressure from p to $\tilde{p} = p + \langle p_{11}\rangle$, without further consequences. The implication is that the form of the principal equation Eq. (4.5) may indeed be reduced to $\boldsymbol{f}_{\mathrm{ac}}^{\mathrm{hom}}$ in Eq. (4.20) for studies of acoustic streaming in homogeneous fluids.

This form of the acoustic force density Eq. (4.20) may be used directly in numerical studies of boundary-driven acoustic streaming in a homogeneous fluid [5, 134, 79, 99]. However, $\boldsymbol{f}_{\mathrm{ac}}^{\mathrm{hom}}$ in the form Eq. (4.20) typically contains additional conservative force terms that can be written as gradients, and hence also absorbed into the pressure.

4.6.1 Attenuation-driven bulk acoustic streaming

Considering attenuation-driven bulk Eckart streaming [81], where the non-conservative force that drives the streaming is often much smaller than the conservative forces, it is practical to absorb all the conservative force terms in $\boldsymbol{f}_{\mathrm{ac}}^{\mathrm{hom}}$ into the pressure to avoid numerical noise in simulations. This approach was taken in a particularly thorough recent investigation of Eckart streaming by Riaud *et al.* [82]. The part of $\boldsymbol{f}_{\mathrm{ac}}^{\mathrm{hom}}$ thus responsible for attenuation-driven bulk Eckart streaming is,

$$\boldsymbol{f}_{\mathrm{ac}}^{\text{hom-bulk}} = \frac{2\alpha}{c}\langle p_1\boldsymbol{v}_1\rangle, \tag{4.21}$$

where the expression by Riaud *et al.* [82] has been modified to include thermal damping by substituting the viscous bulk damping factor Γ_{s} with $\Gamma_{\mathrm{s}}+(\gamma-1)\Gamma_{\mathrm{t}}$, Eqs. (2.17a) and (2.19), and finally written in terms of the attenuation coefficient α, Eq. (2.21), to highlight the connection to bulk attenuation.

4.7 Acoustic streaming in an inhomogeneous fluid

Finally, acoustic streaming may be studied in the general case of viscous and inhomogeneous fluids, where both viscosity and inhomogeneities are taken into account in the acoustics, as done in Paper V [5]. The generalized acoustic force density $\boldsymbol{f}_{\mathrm{ac}}$ thus contains both the non-dissipative force density due to gradients in the fluid density ρ_0 and compressibility κ_0 (Eq. (4.15)), and the dissipative force density due to viscous dissipation in boundary layers and in the bulk (Eq. (4.20)). In general, however, the two contributions are difficult to separate analytically, and hence the expression for the generalized acoustic force density is not reduced from that in the principal equation Eq. (4.5), namely

$$\boldsymbol{f}_{\mathrm{ac}} = -\boldsymbol{\nabla}\langle p_{11}\rangle - \boldsymbol{\nabla}\cdot\langle\rho_0\boldsymbol{v}_1\boldsymbol{v}_1\rangle. \tag{4.22}$$

As discussed in Section 4.5, one cannot absorb the gradient term $-\boldsymbol{\nabla}\langle p_{11}\rangle$ in an inhomogeneous fluid into the hydrodynamic pressure gradient in the momentum equation.

The expression in Eq. (4.22) is used in the enclosed Paper V [5] to develop a multiple-time-scale numerical model that simulates the dynamics and interactions on both the fast acoustic time scale (viscous inhomogeneous acoustics) and the slow hydrodynamic time scale (advection-diffusion with external forcing by $\boldsymbol{f}_{\mathrm{ac}}$ and $\rho_0\boldsymbol{g}$). The fast-time-scale dynamics gives rise to the acoustic force density $\boldsymbol{f}_{\mathrm{ac}}$ driving the slow-time-scale hydrodynamics, the non-dissipative part of which stabilizes a particular inhomogeneity configuration, and the dissipative part which attempts to set up a boundary-driven streaming flow. The balance between the two gives rise to a new class of altered and suppressed acoustic streaming flows, see Paper V [5] enclosed in Chapter 10.

4.8 Concluding remarks

This chapter was written to give a theoretical overview of the origins of nonlinear acoustic forces acting on fluids and particles, and to demonstrate that all nonlinear acoustic force densities derive from a divergence in the acoustic momentum-flux-density tensor, dependent only on first-order acoustic fields. The acoustic force densities can be classified as being either non-dissipative or dissipative in origin. Acoustic radiation forces resulting from scattering at interfaces or particles are non-dissipative in origin. While scattering generally has a dissipative component (Paper I), the force density associated with scattering does not vanish in the limit of zero dissipation. This thesis introduces the non-dissipative acoustic force density acting on inhomogeneous fluids with variations in the continuous fluid parameters of density and compressibility, Eq. (4.15), e.g., due to a solute concentration field (Paper III). This force density may relocate and stabilize certain inhomogeneity configurations (Paper III and IV), and its existence makes possible the cell-handling method of iso-acoustic focusing (Paper II). The dissipative acoustic force densities are associated with boundary-driven Rayleigh streaming and bulk-driven Eckart streaming in homogeneous fluids, and these force densities vanish in the limit of zero dissipation. The generalized acoustic force density $\boldsymbol{f}_{\mathrm{ac}}$ in Eq. (4.22) describes both non-dissipative and dissipative forces acting on inhomogeneous viscous fluids. It is emphasized that the gradient term in $\boldsymbol{f}_{\mathrm{ac}}$ cannot be absorbed into the hydrodynamic pressure in an inhomogeneous fluid. Using the generalized acoustic force density in simulations, this thesis reports novel theoretical and experimental results on boundary-driven acoustic streaming and its suppression in inhomogeneous fluids (Paper V).

The nonlinear acoustics phenomena themselves were not studied in this chapter – only their origins. The following Chapter 5 contains a brief summary of the main result of each of the Papers I to V. Following the short summary, Chapters 6 to 10 contain the main part of this thesis work, namely the published Papers I to V, where the nonlinear acoustics phenomena are studied in more detail [1, 2, 3, 4, 5].

Chapter 5

Summary of the results

This chapter presents a brief summary of the main result in each of the published Papers I to V [1, 2, 3, 4, 5]. Explicit reference to important figures, tables, and equations in the papers, indicated by square brackets [•], are intended to provide a brief overview of the most important parts of the papers. Two questions are answered for each paper: (i) What motivated the study? and (ii) What is the main result of the study?

5.1 Paper I: Forces acting on a small particle in an acoustical field in a thermoviscous fluid

The literature contains a startling number of studies of the acoustic radiation force acting on a particle in an acoustical field, however, with most of the studies limited to particles in ideal fluids. The ideal-fluid assumption is approximately upheld for particles of radius a much larger than the boundary layer thicknesses $\delta_\mathrm{s}, \delta_\mathrm{t}$ [118, 119]. Analytical closed-form expressions including thermoviscous effects are available only in the limits of $\delta_\mathrm{s}, \delta_\mathrm{t} \ll a \ll \lambda$ and $a \ll \delta_\mathrm{s}, \delta_\mathrm{t} \ll \lambda$ [117, 123, 124]. However, in water at 2 MHz, $\delta_\mathrm{s} = 0.4$ μm and $\delta_\mathrm{t} = 0.2$ μm, while in air at 50 kHz, $\delta_\mathrm{s} = 10$ μm and $\delta_\mathrm{t} = 12$ μm. Consequently, the acoustic radiation force on nanometer- and micrometer-sized particles is not well-described by the limited analytical expressions found in the literature, since $\delta_\mathrm{s}, \delta_\mathrm{t} \sim a \ll \lambda$ in many practical applications.

Closing this gap, Paper I [1] presents an analysis, based on the succesful ECAH scattering theory [63, 64], of the acoustic radiation force acting on droplets and elastic particles in thermoviscous fluids in the limit of $\delta_\mathrm{s}, \delta_\mathrm{t}, a \ll \lambda$ with no further restrictions between $\delta_\mathrm{s}, \delta_\mathrm{t}$ and a [1]. The results are reported in the style of Gorkov [103] and Settnes and Bruus [119], as corrected thermoviscous expressions for the monopole- and dipole-scattering coefficients f_0 and f_1, allowing the acoustic radiation force to be evaluated analytically [Eq. (5)] for any incident acoustic field p_in and $\boldsymbol{v}_\mathrm{in}$ [Table I]. Thermoviscous effects are shown to render the acoustic contrast factor Φ_ac [Eq. (79b)] a function of particle size, and a remarkable prediction of the analytical theory is that forces on small dense particles in gases may be orders of magnitude larger than predicted by ideal-fluid theory [Fig. 4], and that a sign-change in the force can happen at a critical particle size due to thermal effects, e.g.,

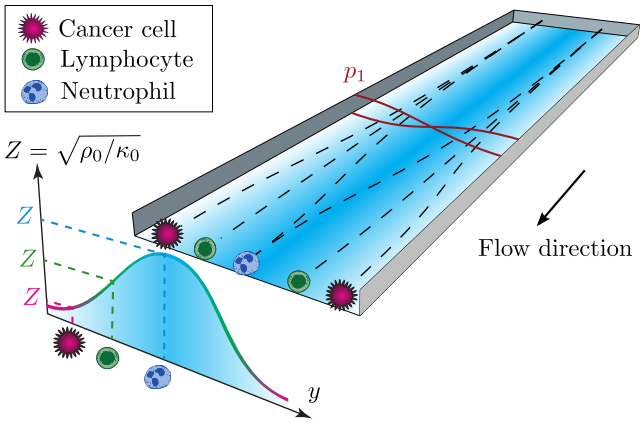

Figure 5.1: Schematic of iso-acoustic focusing for size-insensitive acousto-mechanical phenotyping of single cells, e.g., cancer cells and white blood cells. Cells flow through a channel and an acoustic pressure field p_1 (red half-wave) forces them sideways into media of gradually increasing or decreasing acoustic impedance Z (blue shading, Gaussian curve). Near the end, the sideways position of each cell depends on its phenotype-specific acoustic impedance, since it is focused in the position for which $Z_{\text{cell}} = Z_{\text{fluid}}$. Courtesy of Per Augustsson, Lund University.

for sufficiently small water droplets in air [Fig. 4(b)].

5.2 Paper II: Iso-acoustic focusing of cells for size-insensitive acousto-mechanical phenotyping

Mechanical phenotyping of single cells is an emerging tool for cell classification, enabled by the assessment of effective parameters that relate to differences or changes in the interior structure of a cell [154]. The hypothesis is that the mechanical properties of a cell reveals its phenotype as well as changes in cell-state and disease progress [155, 156].

In Paper II [2], the size-insensitive method of iso-acoustic focusing of cells is developed, allowing analysis of the effective acoustic impedance Z of single cells in continuous flow. A schematic of the principle of operation is shown in Fig. 5.1. While flowing through a microchannel, cells migrate sideways, influenced by the acoustic radiation force from a transverse pressure resonance p_1, into streams of increasing acoustic impedance in an inhomogeneous fluid, until reaching their cell-type-specific iso-acoustic point ($\Phi_{\text{ac}} \approx 0$ for $Z_{\text{cell}} = Z_{\text{fluid}}$), at which the radiation force becomes zero and the sideways displacement ceases. Cell-specific differences in the effective acoustic impedance Z thereby translate into a spatial dispersion of the cell population transverse to the flow, as indicated in Fig. 5.1, enabling continuous label-free analysis of individual cells. As such, the method can be considered a microfluidic analog to density-gradient centrifugation, with the control parameter being the acoustic impedance $Z = \sqrt{\rho_0/\kappa_0}$ instead of the density ρ_0. The method relies on the ability to tailor smooth acoustic impedance gradients by means of an acous-

tically stabilized iodixanol concentration gradient [Fig. 3], and the ability to optically measure the cell positions in the gradient [Fig. 4]. Iso-acoustic focusing is demonstrated in measurements of the effective acoustic impedance of monocytes, lymphocytes, neutrophils, BA-F3 and MCF7 cells [Fig. 5], and thousands of individual suspension cells are measured in just a few minutes. The method is analyzed by simple physical scaling arguments, and by numerical computations of the trajectories of cells migrating in a diffusing iodixanol gradient under the action of the acoustic radition force [Supplementary Notes 1-4, Supplementary Fig. 6].

5.3 Paper III: Acoustic force density acting on inhomogeneous fluids in acoustic fields

The study was motivated by the findings in Paper II [2], where experiments as well as simple physical scaling arguments indicated that acoustic forces act on and stabilize fluid inhomogeneities against gravity. The first observation of this phenomenon was made by Deshmukh *et al.* in 2014, discovering that acoustic fields may relocate inhomogeneous aqueous salt solutions and stabilize particular inhomogeneity profiles against gravity in microchannels [157].

The achievement of Paper III [3] is to provide a fundamental theoretical understanding of this phenomenon. The main result is the derivation of the non-dissipative acoustic force density $\boldsymbol{f}_{\rm ac}$ (denoted $\boldsymbol{f}_{\rm ac}^{\rm invisc}$ in this thesis) acting on inhomogeneous fluids with variations in density $\rho_0(\boldsymbol{r})$ and compressibility $\kappa_0(\boldsymbol{r})$ [Eq. (13)]. Care must be taken in the derivation of this result, as already outlined in Chapter 4, Section 4.5. Paper III furthermore utilizes the large separation in time scales between the fast-time-scale acoustics $t \sim 0.1$ µs [Eq. (1)], and the slow-time-scale hydrodynamics $\tau \sim 10$ ms [Eq. (2)] to simulate the slow-time-scale hydrodynamic advection-diffusion problem describing the relocation flows driven by the acoustic and gravitational force densities [Eq. (18), Fig. 3]. Compared to a separation into orders in a strict perturbation expansion, the separation in time scales makes the coupling between the acoustic and hydrodynamic degrees of freedom more apparent, and the modeling approach more transparent, and this is perhaps the second-most important contribution of Paper III. In the limit of weak density inhomogeneities it is shown that $\boldsymbol{f}_{\rm ac}$ can be evaluated from the homogeneous-fluid acoustic fields [Eq. (15)], that are known analytically, which allows the hydrodynamic time scale to be simulated without resolving the fast-time-scale acoustics. Last but not least, predictions of the theoretical model are validated experimentally using confocal imaging of aqueous iodixanol solutions in a glass-silicon acoustofluidic microchip [Fig. 2].

The results described in Paper III opens up a branch of research into a new class of nonlinear acoustics phenomena in inhomogeneous fluids, and in the author's opinion this constitutes the most important contribution of this thesis to nonlinear acoustics.

5.4 Paper IV: Acoustic tweezing and patterning of concentration fields in microfluidics

Experimental methods developed for dynamical particle-handling applications allow the precise control of ultrasound acoustic fields at the microscale [45], e.g., using surface acoustic waves [53], transducer arrays [54], or bulk acoustic waves [128]. The application of these methods allow particles and cells to be concentrated, trapped, separated, or patterned [9]. Interestingly, the results of Paper III [3] suggest that these methods can be extended to the manipulation of inhomogeneous fluids, or concentration fields, as long as the concentration field introduces inhomogeneities in the density ρ_0 or compressibility κ_0.

Paper IV [4] can be considered a natural extension of Paper III [3], applying the theory to develop the concept of manipulation of concentration fields using acoustic fields. The main result of Paper IV is the prediction that concentration fields (or miscible fluids) can be actively manipulated by acoustic fields with a high level of spatio-temporal control. This allows the patterning of concentration fields [Figs. 1-4], or the use of an acoustic tweezers system to "grab and move" a region of high-concentration fluid in a lower-concentration medium [Fig. 5]. This remarkable theoretical prediction [Fig. 5] suggests that the applicability of existing acoustic tweezers systems can be extended beyond particle manipulation to include manipulation of concentration fields, although limited by diffusion.

A theoretical framework, derived in the weakly inhomogeneous limit, is presented and exploited to develop an intuition for the dynamics of inhomogeneous fluids in acoustic fields. The acoustic field-shape functions R and C, dependent on the shape of the homogeneous-fluid acoustic field, controlling the acoustic force densities derived from gradients in the density ρ_0 and the speed of sound c_0, respectively, turn out to be useful in predicting the acoustic forces acting on inhomogeneities, as well as the quasi-stable resultant focusing of the inhomogeneities in the acoustic field [Eq. (10)]. Density-inhomogeneities thus tend to focus in the minima of R, however, with variations in the final inhomogeneity profile caused by the initial conditions that affect the time-dependent dynamics driven by the non-conservative acoustic force density [Fig. 2].

5.5 Paper V: Acoustic streaming and its suppression in inhomogeneous fluids

Historically, the subject of acoustic streaming, as studied by Rayleigh [77], Eckart [81], and Nyborg [83, 84], to mention a few, has been limited to homogeneous fluids. In homogeneous fluids, the force densities that drive streaming are dissipative in origin, caused by boundary-layer dissipation or bulk attenuation. Considering inhomogeneous fluids, the experiments in Papers II and III [2, 3] suggest that acoustic streaming is absent or suppressed in inhomogeneous fluids, since the inhomogeneities are not advected by a flow, but remain stabilized at the center of the channel.

Paper V [5] presents a theoretical, numerical, and experimental study of the evolution of boundary-driven acoustic streaming in an inhomogeneous fluid, as the acoustically sta-

bilized inhomogeneity profile in a microchannel evolves by diffusion and advection towards homogeneity on a one-minute time scale [Fig. 2]. The main findings are (i) that the competition between the boundary-induced streaming stresses and the inhomogeneity-induced acoustic force density introduces a dynamic length scale Δ of the streaming vortex size, (ii) that initially $\Delta \ll \Delta_{\mathrm{hom}}$, where Δ_{hom} is the vortex size in a homogeneous fluid, and (iii) that in the bulk farther than Δ from the boundaries, the streaming flow is suppressed. The vortex size Δ increases in time, as diffusion and advection flatten the inhomogeneity, and the vortices eventually expand into the bulk to yield homogeneous-fluid streaming [Fig. 3]. The length scale Δ is rationalized by a simple scaling argument [Eq. (10)].

From a theory perspective, the model of Paper V [5] extends the previous model [3, 4] from a hydrodynamic slow-time-scale model into a multiple-time-scale model that computes both the fast-time-scale acoustics (viscous inhomogeneous acoustics computed in the frequency domain [Eq. (2)]) and the slow-time-scale hydrodynamics (time-dependent advection-diffusion problem [Eq. (4)]). The numerical solution of the fast-timescale viscous acoustics in the inhomogeneous medium is carried out to accurately evaluate the generalized acoustic force density $\boldsymbol{f}_{\mathrm{ac}}$ [Eq. (7)] including both the dissipative forces in the boundary layers, and the non-dissipative inhomogeneity-induced forces.

From an applications perspective, the demonstrated suppression of acoustic streaming in inhomogeneous fluids may possibly enable nanoparticle manipulation. Indeed, as shown in the introductory Section 2.5.3, trajectories of particles smaller than ~ 1 μm are streaming-dominated and cannot in general be focused by the radiation force [134, 93]. However, in the absence of acoustic streaming, Eq. (2.43) no longer sets the lower size limit, and thus manipulation of nanoparticles such as bacteria, exosomes, and viruses may become feasible.

Chapter 6

Paper I in Physical Review E

Forces acting on a small particle in an acoustical field in a thermoviscous fluid

DOI: 10.1103/PhysRevE.92.043010.

Authors: J.T. Karlsen and H. Bruus.
Journal: Phys. Rev. E **92**, 043010 (2015).

Remarks: Featured as an Editors' Suggestion in Physical Review E. This paper has some overlap with work presented in my MSc thesis [158], however, the analysis and the results have been significantly extended.

PHYSICAL REVIEW E **92**, 043010 (2015)

Forces acting on a small particle in an acoustical field in a thermoviscous fluid

Jonas T. Karlsen* and Henrik Bruus†

Department of Physics, Technical University of Denmark, DTU Physics Building 309, DK-2800 Kongens Lyngby, Denmark

(Received 3 July 2015; published 12 October 2015)

We present a theoretical analysis of the acoustic radiation force on a single small spherical particle, either a thermoviscous fluid droplet or a thermoelastic solid particle, suspended in a viscous and heat-conducting fluid medium. Within the perturbation assumptions, our analysis places no restrictions on the length scales of the viscous and thermal boundary-layer thicknesses δ_s and δ_t relative to the particle radius a, but it assumes the particle to be small in comparison to the acoustic wavelength λ. This is the limit relevant to scattering of ultrasound waves from nanometer- and micrometer-sized particles. For particles of size comparable to or smaller than the boundary layers, the thermoviscous theory leads to profound consequences for the acoustic radiation force. Not only do we predict forces orders of magnitude larger than expected from ideal-fluid theory, but for certain relevant choices of materials, we also find a sign change in the acoustic radiation force on different-sized but otherwise identical particles. These findings lead to the concept of a particle-size-dependent acoustophoretic contrast factor, highly relevant to acoustic separation of microparticles in gases, as well as to handling of nanoparticles in lab-on-a-chip systems.

DOI: 10.1103/PhysRevE.92.043010 PACS number(s): 47.35.Rs, 43.25.Qp, 43.20.Fn, 43.20.+g

I. INTRODUCTION

The acoustic radiation force is the time-averaged force exerted on a particle in an acoustical field due to scattering of the acoustic waves from the particle. Theoretical studies of the acoustic radiation force date back to King in 1934 [1] and Yosioka and Kawasima in 1955 [2], who considered the force on an incompressible and a compressible particle, respectively, in an inviscid ideal fluid. Their work was summarized and generalized in 1962 by Gorkov [3], with the analysis, however, still limited to ideal fluids and valid only for particles with a radius a much smaller than the acoustic wavelength λ.

In subsequent work, Doinikov developed general theoretical schemes for calculating acoustic radiation forces including viscous and thermoviscous effects [4–6]. The direct applicability of these studies is hampered by the generality of the developed formalism, and analytical expressions are given only in the special limits of $\delta \ll a \ll \lambda$ and $a \ll \delta \ll \lambda$, where δ is the boundary-layer thickness. Similarly, the work of Danilov and Mironov, including viscous effects, only provides analytical expressions in these two limits [7]. However, micrometer-sized particles in water at MHz frequency used in lab-on-a-chip systems for trapping [8–10] and separation [11–21], or in gases at kHz frequency used for separation [22–24] and levitation [25–28], often fall outside of these limits as $\delta \sim a \ll \lambda$. For example, in water at 2 MHz the viscous and thermal boundary layers are of thickness $\delta_s = 0.4\ \mu$m and $\delta_t = 0.2\ \mu$m, respectively, while in air at 50 kHz one finds $\delta_s = 10\ \mu$m and $\delta_t = 12\ \mu$m. Consequently, the acoustic radiation force on nanometer- and micrometer-sized particles is not well described by the limited expressions for small and large boundary layers. The more general case of arbitrary viscous boundary-layer thicknesses compared to the particle size was subsequently studied analytically by Settnes and Bruus in the adiabatic limit where thermal boundary layers are neglected [29]. Their asymptotic study demonstrated that small changes in the scattered field may significantly affect the acoustic radiation force exerted on the particle. Since a thermal boundary layer may also lead to such changes for physically relevant parameters, an extension of the theory in Ref. [29] to include nonadiabatic effects from heat conduction is desirable. Moreover, it is also of interest to extend the treatment of compressible solid particles in Ref. [29] to include droplets or elastic particles for which viscous or elastic shear must be taken into account.

In this work we extend the radiation force theory for droplets and elastic particles to include the effect of both viscosity and heat conduction, thus accounting for the viscous and thermal boundary layers of thicknesses δ_s and δ_t, respectively, and we give closed-form analytical expressions in the limit of $\delta_s, \delta_t, a \ll \lambda$ with no further restrictions between δ_s, δ_t, and a. Our approach to the full thermoviscous scattering problem follows that of Epstein and Carhart from 1953 [30]. The scope of their work was a theory for the absorption of sound in emulsions such as water fog in air. In 1972, Allegra and Hawley further developed the theory to include elastic solid particles suspended in a fluid in order to calculate the attenuation of sound in suspensions and emulsions [31]. The seminal work of those authors has become known as ECAH theory within the field of ultrasound characterization of emulsions and suspensions, and combined with the multiple wave scattering theories of Refs. [32,33] it has been applied to calculate homogenized complex wave numbers of suspensions and emulsions [34,35].

The field of ultrasound characterization driven by engineering applications and the field of acoustic radiation forces have developed in parallel with little overlap. Indeed, the scopes of the work in the two fields are very different. In the works of Epstein and Carhart and Allegra and Hawley, there is no mention of acoustic radiation forces [30,31]. However, the underlying scattering problem of a particle suspended in a fluid remains the same, and having once solved for the amplitude of the propagating scattered wave, the acoustic radiation force on the particle may be obtained from a far-field calculation.

*jonkar@fysik.dtu.dk
†bruus@fysik.dtu.dk

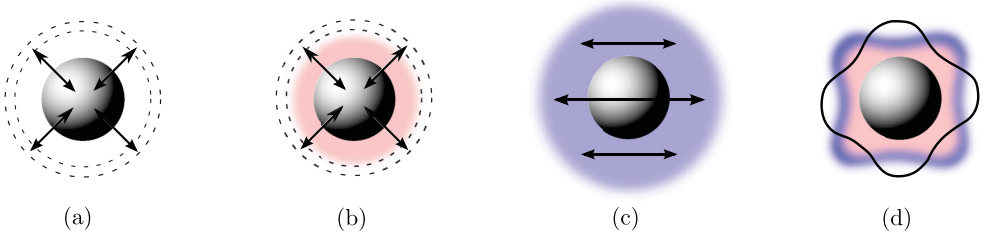

FIG. 1. (Color online) Sketches of the physical mechanisms responsible for various multipole components in the scattering of an incident acoustic wave on a particle. (a) Compressibility contrast: the incident periodic pressure field compresses the particle relative to the fluid, which leads to monopole radiation. (b) Thermal contrast: the incident periodic temperature field leads to thermal expansion of the particle relative to the fluid, which also gives rise to monopole radiation and the development of a diffusive thermal boundary layer (pink). (c) Density contrast: a difference in inertia between particle and fluid causes the particle to oscillate relative to the fluid, which gives rise to dipole radiation and the development of a viscous boundary layer (blue). (d) Particle resonances: acoustic wavelengths comparable to the particle size lead to complex shape changes, which give rise to multipole radiation and a complex thermoviscous boundary layer (pink and blue).

In the far field, the propagating scattered field changes when taking into account the thermoviscous scattering mechanisms, including boundary-layer losses and excitation of acoustic streaming in the vicinity of the particle. In this work we will elucidate this approach, as it leads to a particularly simple and valuable formulation for the acoustic radiation force in the long-wavelength limit [29].

Considering the success of the ECAH method to describe attenuation of sound in emulsions and suspensions, we can with great confidence apply the method to analyze the consequences of thermoviscous scattering on the acoustic radiation force. Nevertheless, we find a need to re-examine the problem of thermoviscous scattering in order to apply the theory to the problem of acoustic radiation forces in a clear and consistent manner. One point of clarification relates to an ambiguity in the thermoelastic solid theory presented by Allegra and Hawley [31], where no clear distinction is made between isothermal and adiabatic solid parameters, thus tacitly implying $\gamma = c_p/c_V = 1$ in solids. Here, we will provide a self-consistent treatment of thermoviscous scattering that clarifies this issue and allows easy comparison with existing acoustic radiation force theories.

Before proceeding with the mathematical treatment, we refer the reader to Fig. 1, which illustrates the physical mechanisms responsible for the monopole, dipole, and multipole scattering from a particle subject to a periodic acoustic field [35]. The final results for the acoustic radiation force are presented in terms of corrected expressions for the monopole and dipole scattering coefficients f_0 and f_1. This approach allows an easy comparison with ideal-fluid theory; moreover, as shown by Settnes and Bruus [29], it provides a simple way of evaluating acoustic radiation forces for any given incident acoustic field. To this end, Table I provides an overview of the equations needed to evaluate the thermoviscous acoustic radiation force on small droplets or solid particles.

TABLE I. References to analytical expressions derived in this paper for the monopole and dipole scattering coefficients f_0 and f_1 in the long-wavelength limit $\delta, a \ll \lambda$. For any given incident acoustic field, the acoustic radiation force $\boldsymbol{F}^{\mathrm{rad}}$ is calculated using Eq. (5) with these expressions for f_0 and f_1.

Size of particle and boundary layers	f_0	f_1
Thermoviscous droplet:		
Arbitrary-width boundary layers	Eq. (59)	Eq. (68)
Small-width boundary layers	Eq. (60)	Eq. (69)
Zero-width boundary layers	Eq. (61)	Eq. (72)
Point-particle limit	Eq. (62)	Eq. (73)
Thermoelastic particle:		
Arbitrary-width boundary layers	Eq. (64)	Eq. (70)
Small-width boundary layers	Eq. (66)	Eq. (71)
Zero-width boundary layers	Eq. (67)	Eq. (72)
Point-particle limit	Eq. (65)	Eq. (73)

II. BASIC CONSIDERATIONS ON THE ACOUSTIC RADIATION FORCE

We consider a single particle or droplet suspended in an infinite, quiescent fluid medium with no net body force, but perturbed by a time-harmonic acoustic field with angular frequency ω. The density, velocity, and stress of the perturbed fluid is denoted ρ, $\boldsymbol{v}$, and $\boldsymbol{\sigma}$, respectively. The region $\Omega(t)$ occupied by the particle, its surface $\partial\Omega(t)$, and the outward-pointing surface vector $\boldsymbol{n}$ depend on time due to the acoustic field. The instantaneous acoustic radiation force is given by the surface integral of the fluid stress $\boldsymbol{\sigma}$ acting on the particle surface. However, since the short time scale corresponding to the oscillation period τ is not resolved experimentally, we define the acoustic radiation force $\boldsymbol{F}^{\mathrm{rad}}$ in the conventional time-averaged sense [1–4,7,29],

$$\boldsymbol{F}^{\mathrm{rad}} = \left\langle \oint_{\partial\Omega(t)} \boldsymbol{\sigma}\cdot\boldsymbol{n}\,da \right\rangle, \tag{1}$$

where the angled bracket denotes the time average over one oscillation period. Notice that this definition includes the acoustic streaming generated locally near the particle, since the stresses leading to this streaming are contained in the fluid stress tensor $\boldsymbol{\sigma}$. In contrast, by considering an infinite domain, we are excluding effects of what Danilov and Mironov refer to as external streaming [7], which would be generated at the boundaries of any finite domain. For a given finite domain, the external streaming can be calculated [36], and the total force acting on a particle is the sum of the radiation force and the external-streaming-induced Stokes drag. This approach

has been used in studies of particle trajectories and has been validated experimentally [37,38].

We consider a state, which is periodic in the acoustic oscillation period τ, tantamount to requiring that any nonperiodic phenomenon, such as particle drift, is negligible within one oscillation period. Usually, this requirement is not very restrictive, as discussed in more detail in Sec. VII. For a time-periodic state, any field can be written as a Fourier series $f(\boldsymbol{r},t) = \sum_{n=0}^{\infty} f_n(\boldsymbol{r})\, e^{-\mathrm{i}n\omega t}$, with $\omega = 2\pi/\tau$, and the time average of any total time derivative is zero, $\langle \frac{d}{dt} f(\boldsymbol{r},t)\rangle = 0$.

A useful expression for $\boldsymbol{F}^{\mathrm{rad}}$ is obtained by considering the momentum flux density $\boldsymbol{\sigma} - \rho\boldsymbol{v}\boldsymbol{v}$ entering the fluid volume between the particle surface $\partial\Omega(t)$ and an arbitrary static surface $\partial\Omega_1$ enclosing the particle. The total momentum $\boldsymbol{P}$ of the fluid in this volume is the volume integral of $\rho\boldsymbol{v}$, and because the net body force on the fluid is zero, the time-averaged rate of change $\langle \frac{d}{dt}\boldsymbol{P}\rangle$ is

$$\left\langle \frac{d\boldsymbol{P}}{dt}\right\rangle = \left\langle \oint_{\partial\Omega_1} [\boldsymbol{\sigma} - \rho\boldsymbol{v}\boldsymbol{v}]\cdot\boldsymbol{n}\, da\right\rangle + \left\langle \oint_{\partial\Omega(t)} \boldsymbol{\sigma}\cdot(-\boldsymbol{n})\, da\right\rangle = \left\langle \oint_{\partial\Omega_1} [\boldsymbol{\sigma} - \rho\boldsymbol{v}\boldsymbol{v}]\cdot\boldsymbol{n}\, da\right\rangle - \boldsymbol{F}^{\mathrm{rad}}. \tag{2}$$

Here, $\boldsymbol{n}$ is the surface vector pointing out of $\partial\Omega_1$ (out of the fluid) and out of $\partial\Omega(t)$ (into the fluid). The advection term $\rho\boldsymbol{v}\boldsymbol{v}$ is zero at $\partial\Omega(t)$, since there is no advection of momentum through the interface of the particle. Finally, using that the time average of the total time derivative $\langle \frac{d\boldsymbol{P}}{dt}\rangle$ is zero in the time-periodic system, we obtain

$$\boldsymbol{F}^{\mathrm{rad}} = \left\langle \oint_{\partial\Omega_1} [\boldsymbol{\sigma} - \rho\boldsymbol{v}\boldsymbol{v}]\cdot\boldsymbol{n}\, da\right\rangle. \tag{3}$$

Thus, even before applying perturbation theory, the acoustic radiation force can be evaluated as the total momentum flux through any static surface $\partial\Omega_1$ enclosing the particle. To second order in the acoustic perturbation, using the expansions $\rho = \rho_0 + \rho_1 + \rho_2$, $\boldsymbol{v} = \boldsymbol{0} + \boldsymbol{v}_1 + \boldsymbol{v}_2$, and $\boldsymbol{\sigma} = \boldsymbol{\sigma}_0 + \boldsymbol{\sigma}_1 + \boldsymbol{\sigma}_2$, the radiation force (3) becomes

$$\boldsymbol{F}^{\mathrm{rad}} = \oint_{\partial\Omega_1} [\langle\boldsymbol{\sigma}_2\rangle - \rho_0\langle\boldsymbol{v}_1\boldsymbol{v}_1\rangle]\cdot\boldsymbol{n}\, da, \tag{4}$$

where we have used that the time average of the time-harmonic, first-order fields is zero.

In regions sufficiently far from acoustic boundary layers, the acoustic wave is a weakly damped propagating acoustic mode, for which viscous and thermal effects are negligible. Thus the result of Ref. [29], obtained by analytically integrating Eq. (4) by placing $\partial\Omega_1$ in the far field, remains valid in the thermoviscous case. In the long-wavelength limit, where the particle radius a is assumed much smaller than the wavelength λ, i.e., for $k_0 a \ll 1$ with $k_0 = 2\pi/\lambda$, it was shown that the acoustic radiation force may be evaluated directly from the incident first-order acoustic field and the expressions for the monopole and dipole scattering coefficients f_0 and f_1 for the suspended particle, as [29]

$$\boldsymbol{F}^{\mathrm{rad}} = -\pi a^3\left[\frac{2\kappa_s}{3}\mathrm{Re}[f_0^* p_{\mathrm{in}}^*\nabla p_{\mathrm{in}}] - \rho_0\mathrm{Re}[f_1^*\boldsymbol{v}_{\mathrm{in}}^*\cdot\nabla\boldsymbol{v}_{\mathrm{in}}]\right]. \tag{5}$$

Here, p_{in} and $\boldsymbol{v}_{\mathrm{in}}$ are the incident acoustic pressure and velocity fields evaluated at the particle position, the asterisk denotes complex conjugation, and κ_s and ρ_0 are the isentropic compressibility and the mass density of the fluid medium, respectively.

Equation (5) is valid for any incident time-harmonic acoustic field, and consequently the problem of calculating the radiation force on a small particle reduces to calculating the coefficients f_0 and f_1. Closed analytical expressions for these are given in the literature for small particles in the special cases of compressible particles in ideal fluids [2,3] and compressible particles in viscous fluids [29]. Moreover, f_0 and f_1 can be extracted from Refs. [5,6] for rigid spheres and liquid droplets in thermoviscous fluids for the limiting cases of very thin and very thick boundary layers. The main result of this paper is the derivation of analytical expressions for f_0 and f_1 for a spherical thermoviscous droplet and a thermoelastic particle suspended in a thermoviscous fluid without restrictions on the boundary-layer thicknesses, see Table I. Moreover, we provide an analysis of how $\boldsymbol{F}^{\mathrm{rad}}$ is affected by thermoviscous effects in these cases.

Finally, we note that since f_0 and f_1 depend only on frequency and material parameters, expression (5) for the radiation force remains valid for any incident wave composed of plane waves at the same frequency. In the case of a superposition $p_{\mathrm{in}}(\boldsymbol{r},t) = \sum_{n=1}^{N} p_n(\boldsymbol{r})e^{-i\omega_n t}$ of acoustic fields $p_n(\boldsymbol{r})$ (and similarly for $\boldsymbol{v}_{\mathrm{in}}$) at different frequencies ω_n, the resulting radiation force is obtained by summing over the forces obtained from Eq. (5) for each frequency,

$$\boldsymbol{F}^{\mathrm{rad}} = -\pi a^3\sum_{n=1}^{N}\left[\frac{2\kappa_s}{3}\mathrm{Re}[f_{0,n}^*\, p_n^*\nabla p_n] - \rho_0\,\mathrm{Re}[f_{1,n}^*\,\boldsymbol{v}_n^*\cdot\nabla\boldsymbol{v}_n]\right]. \tag{6}$$

This generalization of Eq. (5) provides a way to evaluate the acoustic radiation force on a single particle regardless of the complexity of the incident field.

III. THERMOVISCOUS PERTURBATION THEORY OF ACOUSTICS IN FLUIDS

The starting point of the theory is the first law of thermodynamics and the conservation of mass, momentum, and energy. Introducing the thermodynamic variables temperature T, pressure p, density ρ, internal energy ε per mass unit, entropy s per mass unit, and volume per mass unit $1/\rho$, the first law of thermodynamics with s and ρ as independent variables becomes

$$d\varepsilon = T\, ds - p\, d\left(\frac{1}{\rho}\right) = T\, ds + \frac{p}{\rho^2}\, d\rho. \tag{7}$$

For acoustic wave propagation it is often convenient to use T and p as independent thermodynamic variables. This is obtained by a Legendre transformation of the internal energy ε per unit mass to the Gibbs free energy g per unit mass, $g = \varepsilon - Ts + p\,\frac{1}{\rho}$.

Besides the first law of thermodynamics, the governing equations of thermoviscous acoustics require the introduction

of the velocity field $\boldsymbol{v}$ and the stress tensor $\boldsymbol{\sigma}$ of the fluid. The latter can be expressed in terms of $\boldsymbol{v}$, p, the dynamic shear viscosity η, the bulk viscosity η^{b}, and the viscosity ratio $\beta = \eta^{\mathrm{b}}/\eta + 1/3$, as

$$\boldsymbol{\sigma} = -p\,\mathbf{I} + \boldsymbol{\tau}, \tag{8a}$$

$$\boldsymbol{\tau} = \eta[\nabla\boldsymbol{v} + (\nabla\boldsymbol{v})^{\mathrm{T}}] + (\beta - 1)\eta(\nabla\cdot\boldsymbol{v})\,\mathbf{I}. \tag{8b}$$

Here, $\mathbf{I}$ is the unit tensor and the superscript "T" indicates tensor transposition. The tensor $\boldsymbol{\tau}$ is the viscous part of the stress tensor assuming a Newtonian fluid [39].

Considering the fluxes of mass, momentum, and energy into a small test volume, we use Gauss's theorem to formulate the general governing equations for conservation of mass, momentum, and energy in the fluid under the assumption of no net body forces and no heat sources,

$$\partial_t\rho = \nabla\cdot[-\rho\boldsymbol{v}], \tag{9a}$$

$$\partial_t(\rho\boldsymbol{v}) = \nabla\cdot[\boldsymbol{\sigma} - \rho\boldsymbol{v}\boldsymbol{v}], \tag{9b}$$

$$\partial_t\left(\rho\varepsilon + \tfrac{1}{2}\rho v^2\right) = \nabla\cdot\left[\boldsymbol{v}\cdot\boldsymbol{\sigma} + k_{\mathrm{th}}\nabla T - \rho\left(\varepsilon + \tfrac{1}{2}v^2\right)\boldsymbol{v}\right]. \tag{9c}$$

Here, we have introduced the thermal conductivity k_{th} assuming the usual linear form for the heat flux given by Fourier's law of heat conduction.

A. First-order equations for fluids

The zeroth-order state of the fluid is quiescent, homogeneous, and isotropic. Then, treating the acoustic field as a perturbation of this state in the acoustic perturbation parameter $\varepsilon_{\mathrm{ac}}$, given by

$$\varepsilon_{\mathrm{ac}} = \frac{|\rho_1|}{\rho_0} \ll 1, \tag{10}$$

we expand all fields as $g = g_0 + g_1$, but with $\boldsymbol{v}_0 = \mathbf{0}$. The zeroth-order terms drop out of the governing equations, while the first-order mass, momentum, and energy equations obtained from Eqs. (7) and (9) become

$$\partial_t\rho_1 = -\rho_0\nabla\cdot\boldsymbol{v}_1, \tag{11a}$$

$$\rho_0\partial_t\boldsymbol{v}_1 = -\nabla p_1 + \eta_0\nabla^2\boldsymbol{v}_1 + \beta\eta_0\nabla(\nabla\cdot\boldsymbol{v}_1), \tag{11b}$$

$$\rho_0 T_0\partial_t s_1 = k_{\mathrm{th}}\nabla^2 T_1. \tag{11c}$$

It will prove useful to eliminate the variables p_1, ρ_1, and s_1 to end up with only two equations for the variables $\boldsymbol{v}_1$ and T_1. To this end, we combine Eq. (11) with the two thermodynamic equations of state $\rho = \rho(p, T)$ and $s = s(p, T)$. The total differentials of ρ and s are

$$d\rho = \left(\frac{\partial\rho}{\partial p}\right)_T dp + \left(\frac{\partial\rho}{\partial T}\right)_p dT, \tag{12a}$$

$$ds = \left(\frac{\partial s}{\partial p}\right)_T dp + \left(\frac{\partial s}{\partial T}\right)_p dT, \tag{12b}$$

which may be linearized so that the partial derivatives of ρ and s refer to the unperturbed state of the fluid. This leads to the introduction of the isothermal compressibility κ_T, the isobaric thermal expansion coefficient α_p, and the specific heat capacity at constant pressure c_p,

$$\kappa_T = \frac{1}{\rho}\left(\frac{\partial\rho}{\partial p}\right)_T, \quad \alpha_p = -\frac{1}{\rho}\left(\frac{\partial\rho}{\partial T}\right)_p,$$

$$c_p = T\left(\frac{\partial s}{\partial T}\right)_p. \tag{13}$$

Moreover, $(\partial s/\partial p)_T = -\alpha_p/\rho$, which may be derived as a Maxwell relation differentiating g after p and T. Thus, the linearized form of Eq. (12) is

$$\rho_1 = \rho_0\,\kappa_T\,p_1 - \rho_0\,\alpha_p\,T_1, \tag{14a}$$

$$s_1 = \frac{c_p}{T_0}\,T_1 - \frac{\alpha_p}{\rho_0}\,p_1. \tag{14b}$$

We further introduce the isentropic compressibility κ_s and the specific heat capacity at constant volume c_V,

$$\kappa_s = \frac{1}{\rho}\left(\frac{\partial\rho}{\partial p}\right)_s, \quad c_V = T\left(\frac{\partial s}{\partial T}\right)_V. \tag{15}$$

Then the following two well-known thermodynamic identities may be derived [40]:

$$\kappa_T = \gamma\kappa_s, \quad \gamma \equiv \frac{c_p}{c_V} = 1 + \frac{\alpha_p^2 T_0}{\rho_0 c_p\kappa_s}. \tag{16}$$

To proceed with the reduction of Eq. (11), we first differentiate Eq. (11b) with respect to time and substitute $\nabla^2\boldsymbol{v}_1 = \nabla(\nabla\cdot\boldsymbol{v}_1) - \nabla\times\nabla\times\boldsymbol{v}_1$. Then, Eq. (14) is used to eliminate p_1 and s_1 in Eqs. (11b) and (11c), followed by elimination of $\partial_t\rho_1$ using Eq. (11a). The resulting equations for $\boldsymbol{v}_1$ and T_1 are

$$\partial_t^2\boldsymbol{v}_1 - \left(\frac{1}{\rho_0\kappa_T} + (1+\beta)\nu_0\partial_t\right)\nabla(\nabla\cdot\boldsymbol{v}_1) + \nu_0\partial_t\nabla\times\nabla\times\boldsymbol{v}_1 = -\frac{\alpha_p}{\rho_0\kappa_T}\partial_t\nabla T_1, \tag{17a}$$

$$\gamma D_{\mathrm{th}}\nabla^2 T_1 - \partial_t T_1 = \frac{\gamma - 1}{\alpha_p}\nabla\cdot\boldsymbol{v}_1, \tag{17b}$$

where we have introduced the momentum diffusion constant ν_0 and the thermal diffusion constant D_{th},

$$\nu_0 = \frac{\eta_0}{\rho_0}, \quad D_{\mathrm{th}} = \frac{k_{\mathrm{th}}}{\rho_0 c_p}. \tag{18}$$

B. Potential equations for fluids

The velocity field $\boldsymbol{v}_1$ is decomposed into the gradient of a scalar potential ϕ (the longitudinal component) and the rotation of a divergence-free vector potential $\boldsymbol{\psi}$ (the transverse component),

$$\boldsymbol{v}_1 = \nabla\phi + \nabla\times\boldsymbol{\psi}, \ \text{with}\ \nabla\cdot\boldsymbol{\psi} = 0. \tag{19}$$

Inserting this well-known Helmholtz decomposition into Eq. (17a) leads to the equation

$$\nabla\left[\partial_t^2\phi - \left(\frac{1}{\rho_0\kappa_T} + (1+\beta)\nu_0\partial_t\right)\nabla^2\phi + \frac{\alpha_p}{\rho_0\kappa_T}\partial_t T_1\right] = \nabla\times\left[-\partial_t^2\boldsymbol{\psi} + \nu_0\partial_t\nabla^2\boldsymbol{\psi}\right]. \tag{20}$$

In general, both sides of the equation must vanish separately, which leads to two equations. Combining these with Eq. (17b), into which Eq. (19) is inserted, leads to the following form of Eq. (17):

$$\partial_t^2\phi = \left(\frac{1}{\rho_0\kappa_T} + (1+\beta)\nu_0\partial_t\right)\nabla^2\phi - \frac{\alpha_p}{\rho_0\kappa_T}\partial_t T_1, \quad (21a)$$

$$\partial_t T_1 = \gamma D_{\rm th}\nabla^2 T_1 - \frac{\gamma-1}{\alpha_p}\nabla^2\phi, \quad (21b)$$

$$\partial_t \boldsymbol{\psi} = \nu_0\nabla^2\boldsymbol{\psi}. \quad (21c)$$

In the adiabatic limit, for which $D_{\rm th} = 0$, the well-known adiabatic wave equation for ϕ is obtained by inserting Eq. (21b) into (21a), from which the adiabatic speed of sound c for longitudinal waves is deduced,

$$c = \frac{1}{\sqrt{\rho_0\kappa_s}}. \quad (22)$$

In the isothermal case, for which $T_1 = 0$, the wave equation (21a) instead describes waves traveling at the isothermal speed of sound $c/\sqrt{\gamma} = 1/\sqrt{\rho_0\kappa_T}$. For ultrasound acoustics, sound propagation in the bulk of a fluid is generally very close to being adiabatic.

IV. THERMOELASTIC THEORY OF ACOUSTICS IN ISOTROPIC SOLIDS

A thermoelastic solid may be deformed by the action of applied forces or on account of thermal expansion. Following Landau and Lifshitz [41], we describe the deformation of a solid elastic body using the displacement field $\boldsymbol{u}$, which describes the displacement $\boldsymbol{u}(\boldsymbol{r},t)$ of a solid element away from its initial, undeformed position $\boldsymbol{r}$ to its new temporary position $\boldsymbol{r} + \boldsymbol{u}(\boldsymbol{r},t)$. Any displacement away from equilibrium gives rise to internal stresses tending to return the body to equilibrium. These forces are described using the stress tensor $\boldsymbol{\sigma}$, which leads to the force density $\boldsymbol{\nabla}\cdot\boldsymbol{\sigma}$. In the description of the thermodynamics of solids, it is advantageous to work with per-volume quantities denoted by uppercase letters, in contrast to the per-mass quantities given by lowercase letters. The first law of thermodynamics reads

$$d\mathcal{E} = TdS + \sigma_{ij}du_{ij}, \quad (23)$$

where $\mathcal{E}$ is the internal energy per unit volume, S is the entropy per unit volume, and T is the temperature. The work done by the internal stresses per unit volume is equal to $-\sigma_{ij}du_{ij}$, where we have introduced the strain tensor u_{ij}, which for small displacements is given by

$$u_{ij} = \tfrac{1}{2}[\partial_i u_j + \partial_j u_i]. \quad (24)$$

Transforming the internal energy per unit volume $\mathcal{E}$ to the Helmholtz free energy per unit volume $F = \mathcal{E} - TS$, where temperature T and strain u_{ij} are the independent variables, the first law becomes $dF = -SdT + \sigma_{ij}du_{ij}$.

Consider the undeformed state of an isotropic, thermoelastic solid at temperature T_0 in the absence of external forces. The free energy F is then given as an expansion in powers of the temperature difference $T - T_0$ and the strain tensor u_{ij}. To linear order, the stress tensor $\sigma_{ij} = (\frac{\partial F}{\partial u_{ij}})_T$ and the entropy $S = -(\frac{\partial F}{\partial T})_{u_{ij}}$ become

$$\sigma_{ij} = -\frac{\alpha_p(T-T_0)}{\kappa_T}\delta_{ij} + \frac{E}{1+\sigma}\left[u_{ij} + \frac{\sigma}{1-2\sigma}u_{kk}\delta_{ij}\right], \quad (25a)$$

$$S(T) = S_0(T) + \frac{\alpha_p}{\kappa_T}u_{kk}, \quad (25b)$$

where $S_0(T)$ is the entropy of the undeformed state at temperature T, while E and σ are the isothermal Young's modulus and Poisson's ratio, respectively. The isothermal compressibility κ_T of the solid is given in terms of E and σ as

$$\kappa_T = 3(1-2\sigma)\frac{1}{E}. \quad (26)$$

A. Linear equations for solids

In elastic solids, advection of momentum and heat cannot occur, so the momentum equation in the absence of body forces takes the linear form $\rho\partial_t^2\boldsymbol{u} = \boldsymbol{\nabla}\cdot\boldsymbol{\sigma}$. Assuming the material parameters α_p, κ_T, E, and σ to be constant, it becomes

$$\begin{aligned}\rho\partial_t^2\boldsymbol{u} &= -\frac{\alpha_p}{\kappa_T}\boldsymbol{\nabla}T + \frac{E}{2(1+\sigma)}\left[\nabla^2\boldsymbol{u} + \frac{1}{1-2\sigma}\boldsymbol{\nabla}(\boldsymbol{\nabla}\cdot\boldsymbol{u})\right]\\ &= -\frac{\alpha_p}{\rho\kappa_T}\boldsymbol{\nabla}T + c_{\rm T}^2\nabla^2\boldsymbol{u} + \left(c_{\rm L}^2 - c_{\rm T}^2\right)\boldsymbol{\nabla}(\boldsymbol{\nabla}\cdot\boldsymbol{u}), \quad (27)\end{aligned}$$

where we have introduced the isothermal speed of sound of longitudinal waves $c_{\rm L}$ and of transverse waves $c_{\rm T}$,

$$c_{\rm L}^2 = \frac{(1-\sigma)}{(1+\sigma)(1-2\sigma)}\frac{E}{\rho}, \quad c_{\rm T}^2 = \frac{1}{2(1+\sigma)}\frac{E}{\rho}. \quad (28a)$$

Using the decomposition $\boldsymbol{u} = \boldsymbol{u}_{\rm T} + \boldsymbol{u}_{\rm L}$ in the transverse and longitudinal displacements $\boldsymbol{u}_{\rm T}$ and $\boldsymbol{u}_{\rm L}$ with $\boldsymbol{\nabla}\cdot\boldsymbol{u}_{\rm T} = 0$ and $\boldsymbol{\nabla}\times\boldsymbol{u}_{\rm L} = \boldsymbol{0}$, respectively, it immediately follows from Eq. (27) that in the isothermal case, transverse and longitudinal waves travel at the speed $c_{\rm T}$ and $c_{\rm L}$, respectively. Combining Eqs. (26) and (28a) one obtains an important relation connecting the isothermal compressibility κ_T of the solid to the isothermal sound speeds $c_{\rm L}$ and $c_{\rm T}$,

$$\frac{1}{\rho\kappa_T} = c_{\rm L}^2 - \frac{4}{3}c_{\rm T}^2. \quad (28b)$$

Turning to the energy equation, the amount of heat absorbed per unit time per unit volume is $T(\partial_t S)$. If there are no heat sources in the bulk, the rate of heat absorbed is given by the influx $-k_{\rm th}\boldsymbol{\nabla}T$ of heat by conduction, and the heat equation thus becomes

$$T(\partial_t S) = -\boldsymbol{\nabla}\cdot[-k_{\rm th}\boldsymbol{\nabla}T] = k_{\rm th}\nabla^2 T, \quad (29)$$

where the heat conductivity $k_{\rm th}$ is taken to be constant. We rewrite this equation using expression (25b) for the entropy, and using that the time derivative of S_0 may be written as

$$\frac{\partial S_0}{\partial t} = \left(\frac{\partial S_0}{\partial T}\right)_V\frac{\partial T}{\partial t} = \frac{C_V}{T}\frac{\partial T}{\partial t}, \quad (30)$$

where the heat capacity C_V per unit volume at constant volume enters through the relation $C_V = T\,(\partial S_0/\partial T)_V$ with the

derivative taken for the undeformed state at constant volume, that is, for $u_{kk} = \nabla \cdot \boldsymbol{u} = 0$. Combining these considerations with the identity for γ equivalent to Eq. (16), the heat equation (29) becomes

$$C_V \partial_t T + \frac{(\gamma - 1)C_V}{\alpha_p} \partial_t \nabla \cdot \boldsymbol{u} = k_{\mathrm{th}} \nabla^2 T. \tag{31}$$

Finally, having eliminated all extensive thermodynamic variables, we return to per-mass quantities, such as $c_V = C_V/\rho$, and thus arrive at the coupled equations for thermoelastic solids,

$$\partial_t^2 \boldsymbol{u}_1 - c_{\mathrm{L}}^2 \nabla(\nabla \cdot \boldsymbol{u}_1) + c_{\mathrm{T}}^2 \nabla \times \nabla \times \boldsymbol{u}_1 = -\frac{\alpha_p}{\rho_0 \kappa_T} \nabla T_1, \tag{32a}$$

$$\gamma D_{\mathrm{th}} \nabla^2 T_1 - \partial_t T_1 = \frac{\gamma - 1}{\alpha_p} \partial_t \nabla \cdot \boldsymbol{u}_1, \tag{32b}$$

with γ and D_{th} defined in Eqs. (16) and (18), and the linearity emphasized by the addition of subscripts "1" to the field variables. In this form, the thermoelastic equations (32) correspond to the fluid equations (17).

B. Potential equations for solids

The time derivative $\partial_t \boldsymbol{u}_1$ of the displacement field $\boldsymbol{u}_1$ describes the velocity field in the solid. Analogous to the fluid case, we make a Helmholtz decomposition of this velocity field in terms of the velocity potentials ϕ and $\boldsymbol{\psi}$

$$\partial_t \boldsymbol{u}_1 = \nabla \phi + \nabla \times \boldsymbol{\psi}, \text{ with } \nabla \cdot \boldsymbol{\psi} = 0. \tag{33}$$

Inserting this into Eq. (32) and following the procedure leading to Eq. (21) for fluids, we obtain the corresponding three equations for solids:

$$\partial_t^2 \phi = c_{\mathrm{L}}^2 \nabla^2 \phi - \frac{\alpha_p}{\rho_0 \kappa_T} \partial_t T_1, \tag{34a}$$

$$\partial_t T_1 = \gamma D_{\mathrm{th}} \nabla^2 T_1 - \frac{\gamma - 1}{\alpha_p} \nabla^2 \phi, \tag{34b}$$

$$\partial_t^2 \boldsymbol{\psi} = c_{\mathrm{T}}^2 \nabla^2 \boldsymbol{\psi}. \tag{34c}$$

The main difference between the fluid and the solid case is in Eq. (34c) for the vector potential $\boldsymbol{\psi}$, which now takes the form of a wave equation describing transverse waves traveling at the transverse speed of sound c_{T} instead of the diffusion equation (21c).

The usual adiabatic wave equation for the scalar potential ϕ is obtained in the limit of $D_{\mathrm{th}} = 0$ combining Eqs. (34a) and (34b), and the speed c of adiabatic, longitudinal wave propagation in an elastic solid becomes

$$c^2 = c_{\mathrm{L}}^2 + \frac{\gamma - 1}{\rho_0 \kappa_T}. \tag{35}$$

For most solids, $\gamma - 1 \ll 1$, leading to a negligible difference between the isothermal c_{L} and the adiabatic c, the latter being closest to the actual speed of sound measured in ultrasonic experiments.

V. UNIFIED POTENTIAL THEORY OF ACOUSTICS IN FLUIDS AND SOLIDS

The similarity between the potential equations (21) and (34) allows us to write down a unified potential theory of acoustics in thermoviscous fluids and thermoelastic solids. The main result of this section is the derivation of three wave equations with three distinct wave numbers corresponding to three modes of wave propagation, namely, two longitudinal modes describing propagating compressional waves and damped thermal waves and one transverse mode describing a shear wave, which is damped in a fluid but propagating in a solid.

We work with the first-order fields in the frequency domain considering a single frequency ω. Using complex notation, we write any first-order field $g_1(\boldsymbol{r},t)$ as

$$g_1(\boldsymbol{r},t) = g_1(\boldsymbol{r})\, e^{-i\omega t}. \tag{36}$$

Assuming this form of time-harmonic first-order field, Eqs. (21a) and (34a) lead to expressions for the temperature field T_1 in a fluid (fl) and a solid (sl), respectively, in terms of the corresponding scalar potential ϕ

$$T_1^{\mathrm{fl}} = \frac{i\omega\rho_0\kappa_T}{\alpha_p}\left[\phi + \frac{c^2}{\omega^2}\frac{1 - i\gamma\Gamma_{\mathrm{s}}}{\gamma}\nabla^2\phi\right], \tag{37a}$$

$$T_1^{\mathrm{sl}} = \frac{i\omega\rho_0\kappa_T}{\alpha_p}\left[\phi + \frac{c_{\mathrm{L}}^2}{\omega^2}\nabla^2\phi\right]. \tag{37b}$$

Here, we have introduced the dimensionless bulk damping factor Γ_{s} accounting for viscous dissipation in the fluid. For convenience, we also introduce the thermal damping factor Γ_{t} accounting for dissipation due to heat conduction both in fluids and in solids. These two bulk damping factors are given by

$$\Gamma_{\mathrm{s}} = \frac{(1+\beta)\nu_0\omega}{c^2}, \quad \Gamma_{\mathrm{t}} = \frac{D_{\mathrm{th}}\omega}{c^2}. \tag{38}$$

Substituting expression (37a) for T_1^{fl} into Eq. (21b), or expression (37b) for T_1^{sl} into Eq. (34b), and assuming time-harmonic fields [Eq. (36)], we eliminate the temperature field and obtain a biharmonic equation for the scalar potential ϕ,

$$\alpha_{\mathrm{xl}}\nabla^2\nabla^2\phi + \beta_{\mathrm{xl}}k_0^2\nabla^2\phi + k_0^4\phi = 0, \quad \text{with} \quad k_0 = \frac{\omega}{c}, \tag{39a}$$

where we have introduced the undamped adiabatic wave number $k_0 = \omega/c$, and where the parameters α_{xl} and β_{xl} for fluids (xl = fl) and solids (xl = sl) are

$$\alpha_{\mathrm{fl}} = -i(1 - i\gamma\Gamma_{\mathrm{s}})\Gamma_{\mathrm{t}}, \quad \beta_{\mathrm{fl}} = 1 - i(\Gamma_{\mathrm{s}} + \gamma\Gamma_{\mathrm{t}}), \tag{39b}$$

$$\alpha_{\mathrm{sl}} = -i(1 + X)\Gamma_{\mathrm{t}}, \quad \beta_{\mathrm{sl}} = 1 - i\gamma\Gamma_{\mathrm{t}}. \tag{39c}$$

Here, we have used relation (35) for solids and further introduced the parameters X and χ,

$$X = (\gamma - 1)(1 - \chi), \tag{39d}$$

$$\chi = \frac{1}{\rho_0\kappa_s c^2} = 1 - \frac{4}{3}\frac{c_{\mathrm{T}}^2}{c^2}, \tag{39e}$$

the latter equality following from combining Eq. (35) with Eq. (28b) and using $\kappa_T = \gamma\kappa_s$ from Eq. (16). Note that for fluids, $\chi = 1$, $c_{\mathrm{T}} = 0$, and $X = 0$.

The biharmonic equation (39a) is factorized and written on the equivalent form

$$\left(\nabla^2 + k_c^2\right)\left(\nabla^2 + k_t^2\right)\phi = 0, \tag{40a}$$

and thus the wave numbers k_c and k_t are obtained from $k_c^2 + k_t^2 = \beta_{xl} k_0^2/\alpha_{xl}$ and $k_c^2 k_t^2 = k_0^4/\alpha_{xl}$, resulting in

$$k_c^2 = 2k_0^2\left[\beta_{xl} + \left(\beta_{xl}^2 - 4\alpha_{xl}\right)^{1/2}\right]^{-1}, \tag{40b}$$

$$k_t^2 = 2k_0^2\left[\beta_{xl} - \left(\beta_{xl}^2 - 4\alpha_{xl}\right)^{1/2}\right]^{-1}, \tag{40c}$$

with "xl" being either "fl" for fluids or "sl" for solids.

In the frequency domain, the equation for the vector potential $\boldsymbol{\psi}$, Eq. (21c) for fluids and Eq. (34c) for solids, can be written as $\nabla^2\boldsymbol{\psi} + k_s^2\boldsymbol{\psi} = \mathbf{0}$, which describes a transverse shear mode with shear wave number k_s. By introducing a shear constant η_0, which for a fluid is the dynamic viscosity, and for a solid is defined as

$$\eta_0 = i\,\frac{\rho_0 c_T^2}{\omega} \quad \text{(solid)}, \tag{41a}$$

the shear wave number k_s is given by the same expression for both fluids and solids,

$$k_s^2 = \frac{i\omega\rho_0}{\eta_0} \quad \text{(fluid and solid)}. \tag{41b}$$

A. Wave equations and modes

The general solution ϕ of the biharmonic equation (40a) is the sum

$$\phi = \phi_c + \phi_t \tag{42}$$

of the two potentials ϕ_c and ϕ_t, which satisfy the harmonic equations

$$\nabla^2\phi_c + k_c^2\phi_c = 0, \tag{43a}$$

$$\nabla^2\phi_t + k_t^2\phi_t = 0, \tag{43b}$$

where ϕ_c describes a compressional propagating mode with wave number k_c, while ϕ_t describes a thermal mode with wave number k_t. These two scalar wave equations together with the vector wave equation for $\boldsymbol{\psi}$, describing the shear mode with wave number k_s,

$$\nabla^2\boldsymbol{\psi} + k_s^2\boldsymbol{\psi} = \mathbf{0}, \tag{43c}$$

comprise the full set of first-order equations in potential theory. These wave equations, coupled through the boundary conditions, govern acoustics in thermoviscous fluids and thermoelastic solids. The distinction between fluids and solids is to be found solely in the wave numbers of the three modes.

1. Approximate wave numbers for fluids

For most systems of interest, $\Gamma_s, \Gamma_t \ll 1$ allowing a simplification of the expressions for k_c and k_t in Eq. (40). To first order in Γ_s and Γ_t one finds

$$k_c = \frac{\omega}{c}\left[1 + \frac{i}{2}[\Gamma_s + (\gamma - 1)\Gamma_t]\right], \tag{44a}$$

$$k_t = \frac{(1+i)}{\delta_t}\left[1 + \frac{i}{2}(\gamma - 1)(\Gamma_s - \Gamma_t)\right], \tag{44b}$$

$$k_s = \frac{(1+i)}{\delta_s}, \tag{44c}$$

where we have introduced the thermal diffusion length δ_t and the momentum diffusion length δ_s. Heat and momentum diffuses from boundaries, such that the characteristic thicknesses of the thermal and viscous boundary layers are δ_t and δ_s, respectively, given by

$$\delta_t = \sqrt{\frac{2D_{th}}{\omega}}, \quad \delta_s = \sqrt{\frac{2\nu_0}{\omega}}. \tag{45}$$

For water at room temperature and 2 MHz frequency, $\delta_s \simeq 0.4\ \mu$m, $\delta_t \simeq 0.2\ \mu$m, and $\lambda \simeq 760\ \mu$m. Consequently, the length scales of the thermal and viscous boundary-layer thicknesses are the same order of magnitude and much smaller than the acoustic wavelength. With $k_0 = \omega/c$ we note that

$$\Gamma_s = \tfrac{1}{2}(1+\beta)(k_0\delta_s)^2, \quad \Gamma_t = \tfrac{1}{2}(k_0\delta_t)^2, \tag{46}$$

and consequently

$$\Gamma_s \sim (k_0\delta_s)^2 \sim \left|\frac{k_c}{k_s}\right|^2 \ll 1, \tag{47a}$$

$$\Gamma_t \sim (k_0\delta_t)^2 \sim \left|\frac{k_c}{k_t}\right|^2 \ll 1. \tag{47b}$$

In the long-wavelength limit of the scattering theory to be developed, we expand to first order in $k_0\delta_s$ and $k_0\delta_t$, and thus neglect the second-order quantities Γ_s and Γ_t. For water at room temperature and MHz frequency one finds $k_0\delta_s \sim k_0\delta_t \sim 10^{-3}$, and $\Gamma_s \sim \Gamma_t \sim 10^{-6}$.

Clearly, the compressional mode with wave number k_c describes a weakly damped propagating wave with $\mathrm{Im}[k_c] \ll \mathrm{Re}[k_c] \simeq \omega/c$. In contrast, $\mathrm{Im}[k_t] \simeq \mathrm{Re}[k_t]$ for the thermal mode and $\mathrm{Im}[k_s] = \mathrm{Re}[k_s]$ for the shear mode, which correspond to waves that are damped within their respective wavelengths. Hence, these modes describe boundary layers near interfaces of walls and particles, which decay exponentially away from these interfaces on the length scales set by δ_t and δ_s.

2. Approximate wave numbers for solids

Similar to the fluid case, we use the smallness of the thermal damping factor, $\Gamma_t \ll 1$, to expand the exact wave numbers of Eq. (40). To first order we obtain

$$k_c = \frac{\omega}{c}\left[1 + \frac{i}{2}(\gamma - 1)\chi\Gamma_t\right], \tag{48a}$$

$$k_t = \frac{(1+i)}{\delta_t}\frac{1}{\sqrt{1-X}}\left[1 + \frac{i}{8}\frac{\gamma^2\Gamma_t}{(1-X)}\right], \tag{48b}$$

$$k_s = \frac{\omega}{c_T}. \tag{48c}$$

An important distinction between a fluid and a solid is that a solid allows propagating transverse waves while a fluid does not. This is evident from the shear mode wave number k_s, which for solids is purely real, $k_s = \omega/c_T$, while for fluids $\mathrm{Im}[k_s] = \mathrm{Re}[k_s] = 1/\delta_s$.

B. Acoustic fields from potentials

For a given thermoacoustic problem, the boundary conditions are imposed on the acoustic fields $\boldsymbol{v}_1$, T_1, and $\boldsymbol{\sigma}_1$ and not directly on the potentials ϕ_c, ϕ_t, and $\boldsymbol{\psi}$. We therefore need expressions for the acoustic fields in terms of the potentials in order to derive the boundary conditions for the latter.

The velocity fields follow trivially from the Helmholtz decompositions and are obtained from the same expression in both fluids and solids:

$$\boldsymbol{v}_1 = \boldsymbol{\nabla}(\phi_c + \phi_t) + \boldsymbol{\nabla} \times \boldsymbol{\psi}, \quad \text{where} \quad \boldsymbol{v}_1 = -i\omega \boldsymbol{u}_1 \text{ for solids.} \tag{49}$$

A single expression for T_1 in terms of ϕ_c and ϕ_t, valid for both fluids and solids, is obtained from Eq. (37) in combination with Eqs. (40)–(43) by introducing the material-dependent parameters b_c and b_t,

$$T_1 = b_c\phi_c + b_t\phi_t, \tag{50a}$$

$$b_c = \frac{i\omega(\gamma - 1)}{\alpha_p c^2}, \quad b_t = \frac{1}{\chi \alpha_p D_{th}}. \tag{50b}$$

Here, we have neglected Γ_s and Γ_t relative to unity. Note that the ratio $b_c/b_t \sim \Gamma_t \ll 1$.

In a fluid, the pressure field p_1 is obtained by inserting Eq. (19) into the momentum equation (11b) and using the wave equations (43),

$$p_1 = i\omega\rho_0(\phi_c + \phi_t) - (1 + \beta)\eta_0\left(k_c^2\phi_c + k_t^2\phi_t\right). \tag{51}$$

Inserting this expression into Eq. (8a), the stress tensor for fluids becomes

$$\boldsymbol{\sigma}_1 = \eta_0\left[\left(2k_c^2 - k_s^2\right)\phi_c + \left(2k_t^2 - k_s^2\right)\phi_t\right]\mathbf{I} + \eta_0[\boldsymbol{\nabla}\boldsymbol{v}_1 + (\boldsymbol{\nabla}\boldsymbol{v}_1)^{\mathrm{T}}], \tag{52}$$

where $\boldsymbol{v}_1$ can be expressed by the potentials through Eq. (49). This expression also holds true for the solid stress tensor in Eq. (25a) using the shear constant η_0, Eq. (41a), and the velocity field $\boldsymbol{v}_1 = -i\omega\boldsymbol{u}_1$, Eq. (33). This conclusion is obtained by inserting Eq. (37b) for T_1^{sl} into Eq. (25a) for $\boldsymbol{\sigma}_1$ and using the wave equations (43).

VI. SCATTERING FROM A SPHERE

The potential theory allows us in a unified manner to treat linear scattering of an acoustic wave on a spherical particle, consisting of either a thermoelastic solid or a thermoviscous fluid. The system of equations describing the general case of an arbitrary particle size is given, and analytical solutions are provided in the long-wavelength limit $a, \delta_s, \delta_t \ll \lambda$. In this limit, the particle and boundary layers are much smaller than the acoustic wavelength, but the ratios δ_s/a and δ_t/a are unrestricted. This is essential for applying our results to micro- and nanoparticle acoustophoresis. In particular, we derive analytical expressions for the monopole and dipole scattering coefficients f_0 and f_1, which together with the incident acoustic field serve to calculate the acoustic radiation force as shown in Sec. II and summarized in Table I.

A. System setup

We place the spherical particle of radius a at the center of the coordinate system and use spherical coordinates (r,θ,φ) with the radial distance r, the polar angle θ, and the azimuthal angle φ. We let unprimed variables and parameters characterize the region of the fluid medium, $r > a$, while primed variables and parameters characterize the region of the particle, $r < a$. For example, the parameter κ_s' is the compressibility of the particle, while κ_s is the compressibility of the fluid medium. Ratios of particle and fluid parameters are denoted by a tilde, e.g. $\tilde{\kappa}_s = \kappa_s'/\kappa_s$. Due to linearity, we can without loss of generality assume that in the vicinity of the particle, the incident wave is a plane wave propagating in the positive z direction, $\phi_i = \phi_0\, e^{ik_c z} = \phi_0\, e^{ik_c r\cos\theta}$. The fields do not depend on φ due to azimuthal symmetry.

B. Partial wave expansion

The solution to the scalar and the vector wave equations [Eq. (43)] with wave numbers k [Eqs. (44) and (48)] in spherical coordinates is standard textbook material. Avoiding singular solutions at $r = 0$ and considering outgoing scattered waves, the solution is written in terms of spherical Bessel functions $j_n(kr)$, outgoing spherical Hankel functions $h_n(kr)$, and Legendre polynomials $P_n(\cos\theta)$. As a consequence of azimuthal symmetry, only the φ component of the vector potential is nonzero, $\boldsymbol{\psi}(\boldsymbol{r}) = \psi_s(r,\theta)\,\boldsymbol{e}_\varphi$. The solution is written as a partial wave expansion of the incident propagating wave ϕ_i, the scattered reflected propagating wave ϕ_r, the scattered thermal wave ϕ_t, and the scattered shear wave ψ_s:

In the fluid medium, $r > a$

$$\phi_i = \phi_0 \sum_{n=0}^{\infty} i^n(2n+1) j_n(k_c r) P_n(\cos\theta), \tag{53a}$$

$$\phi_r = \phi_0 \sum_{n=0}^{\infty} i^n(2n+1) A_n h_n(k_c r) P_n(\cos\theta), \tag{53b}$$

$$\phi_t = \phi_0 \sum_{n=0}^{\infty} i^n(2n+1) B_n h_n(k_t r) P_n(\cos\theta), \tag{53c}$$

$$\psi_s = \phi_0 \sum_{n=0}^{\infty} i^n(2n+1) C_n h_n(k_s r) \partial_\theta P_n(\cos\theta). \tag{53d}$$

In the particle, $r < a$

$$\phi_c' = \phi_0 \sum_{n=0}^{\infty} i^n(2n+1) A_n' j_n(k_c' r) P_n(\cos\theta), \tag{53e}$$

$$\phi_t' = \phi_0 \sum_{n=0}^{\infty} i^n(2n+1) B_n' j_n(k_t' r) P_n(\cos\theta), \tag{53f}$$

$$\psi_s' = \phi_0 \sum_{n=0}^{\infty} i^n(2n+1) C_n' j_n(k_s' r) \partial_\theta P_n(\cos\theta), \tag{53g}$$

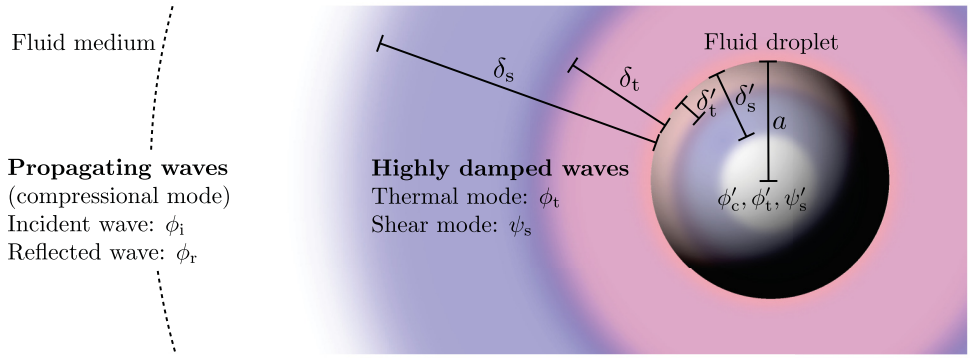

FIG. 2. (Color online) A compressional wave ϕ_i propagating in a thermoviscous fluid medium with parameters $\rho_0,\eta_0,\kappa_s,\alpha_p,c_p,\gamma$, and k_{th}, is incident on a thermoviscous fluid droplet with parameters $\rho'_0,\eta'_0,\kappa'_s,\alpha'_p,c'_p,\gamma'$, and k'_{th}, which results in a compressional scattered wave and highly damped thermal and shear waves both outside in the fluid medium (ϕ_r,ϕ_t,ψ_s) and inside in the fluid droplet $(\phi'_c,\phi'_t,\psi'_s)$. Viscous and thermal boundary layers are described by the highly damped waves both outside and inside the fluid droplet. In the long-wavelength limit the droplet radius a and the boundary-layer thicknesses $\delta_s,\delta_t,\delta'_s,\delta'_t$ are mutually unrestricted, but all much smaller than the acoustic wavelength λ. For a thermoelastic particle, the shear mode ψ'_s describes a propagating transverse wave instead of an internal viscous boundary layer.

where the parameter ϕ_0 is an arbitrary amplitude of the incident wave with unit $m^2\ s^{-1}$. The different components of the resulting acoustic field are illustrated in Fig. 2.

C. Boundary conditions

Neglecting surface tension, the appropriate boundary conditions at the particle surface are continuity of velocity, normal stress, temperature, and heat flux. Assuming sufficiently small oscillations, see Sec. VII C, the boundary conditions are imposed at $r = a$,

$$v_{1r} = v'_{1r}, \qquad v_{1\theta} = v'_{1\theta}, \qquad T_1 = T'_1, \tag{54a}$$

$$\sigma_{1rr} = \sigma'_{1rr}, \qquad \sigma_{1\theta r} = \sigma'_{1\theta r}, \qquad k_{th}\partial_r T_1 = k'_{th}\partial_r T'_1. \tag{54b}$$

The boundary conditions are expressed in terms of the potentials using Eqs. (49), (50), and (52). The components of velocity and stress in spherical coordinates are given in Appendix A.

It is convenient to introduce the nondimensionalized wave numbers x_c, x_t, and x_s for the medium, and x'_c, x'_t, and x'_s for the particle:

$$x_c = k_c a, \quad x_t = k_t a, \quad x_s = k_s a, \tag{55a}$$

$$x'_c = k'_c a, \quad x'_t = k'_t a, \quad x'_s = k'_s a. \tag{55b}$$

Inserting the expansion (53) into the boundary conditions (54), and making use of the Legendre equation (C1), we obtain the following system of coupled linear equations for the expansion coefficients in each order n:

$\underline{a v_{1r} = a v'_{1r}}$

$$\begin{aligned} &x_c j'_n(x_c) + A_n x_c h'_n(x_c) + B_n x_t h'_n(x_t) - C_n n(n+1) h_n(x_s) \\ &= A'_n x'_c j'_n(x'_c) + B'_n x'_t j'_n(x'_t) - C'_n n(n+1) j_n(x'_s), \end{aligned} \tag{56a}$$

$\underline{a v_{1\theta} = a v'_{1\theta}}$

$$\begin{aligned} &j_n(x_c) + A_n h_n(x_c) + B_n h_n(x_t) - C_n[x_s h'_n(x_s) + h_n(x_s)] \\ &= A'_n j_n(x'_c) + B'_n j_n(x'_t) - C'_n[x'_s j'_n(x'_s) + j_n(x'_s)], \end{aligned} \tag{56b}$$

$\underline{T_1 = T'_1}$

$$\begin{aligned} &b_c j_n(x_c) + A_n b_c h_n(x_c) + B_n b_t h_n(x_t) \\ &= A'_n b'_c j_n(x'_c) + B'_n b'_t j_n(x'_t), \end{aligned} \tag{56c}$$

$\underline{a k_{th}\partial_r T_1 = a k'_{th}\partial_r T'_1}$

$$\begin{aligned} &k_{th} b_c x_c j'_n(x_c) + A_n k_{th} b_c x_c h'_n(x_c) + B_n k_{th} b_t x_t h'_n(x_t) \\ &= A'_n k'_{th} b'_c x'_c j'_n(x'_c) + B'_n k'_{th} b'_t x'_t j'_n(x'_t), \end{aligned} \tag{56d}$$

$\underline{a^2\sigma_{1\theta r} = a^2\sigma'_{1\theta r}}$

$$\begin{aligned} &\eta_0[x_c j'_n(x_c) - j_n(x_c)] + A_n\eta_0[x_c h'_n(x_c) - h_n(x_c)] \\ &\quad + B_n\eta_0[x_t h'_n(x_t) - h_n(x_t)] \\ &\quad - \frac{1}{2}C_n\eta_0\left[x_s^2 h''_n(x_s) + (n^2+n-2)h_n(x_s)\right] \\ &= A'_n\eta'_0[x'_c j'_n(x'_c) - j_n(x'_c)] + B'_n\eta'_0[x'_t j'_n(x'_t) - j_n(x'_t)] \\ &\quad - \frac{1}{2}C'_n\eta'_0\left[x'^2_s j''_n(x'_s) + (n^2+n-2)j_n(x'_s)\right], \end{aligned} \tag{56e}$$

$\underline{a^2\sigma_{1rr} = a^2\sigma'_{1rr}}$

$$\begin{aligned} &\eta_0\left[\left(x_s^2 - 2x_c^2\right)j_n(x_c) - 2x_c^2 j''_n(x_c)\right] \\ &\quad + A_n\eta_0\left[\left(x_s^2 - 2x_c^2\right)h_n(x_c) - 2x_c^2 h''_n(x_c)\right] \\ &\quad + B_n\eta_0\left[\left(x_s^2 - 2x_t^2\right)h_n(x_t) - 2x_t^2 h''_n(x_t)\right] \\ &\quad + 2n(n+1)C_n\eta_0[x_s h'_n(x_s) - h_n(x_s)] \\ &= A'_n\eta'_0\left[\left(x'^2_s - 2x'^2_c\right)j_n(x'_c) - 2x'^2_c j''_n(x'_c)\right] \\ &\quad + B'_n\eta'_0\left[\left(x'^2_s - 2x'^2_t\right)j_n(x'_t) - 2x'^2_t j''_n(x'_t)\right] \\ &\quad + 2n(n+1)C'_n\eta'_0[x'_s j'_n(x'_s) - j_n(x'_s)]. \end{aligned} \tag{56f}$$

Here, primes on spherical Bessel and Hankel functions indicate derivatives with respect to the argument. The equations are valid for both a fluid and a solid particle, with η'_0 being the viscosity for a fluid particle and the shear constant [Eq. (41a)] for a solid particle.

For $n = 0$, the boundary conditions for $v_{1\theta}$ and $\sigma_{1\theta r}$ are trivially satisfied because there is no angular dependence in

the zeroth-order Legendre polynomial, $P_0(\cos\theta) = 1$. Consequently, $\psi_s = 0$, and we are left with four equations with four unknowns, namely, Eqs. (56a), (56c), (56d), and (56f) with $C_0 = C_0' = 0$.

The linear system of equations (56) may be solved for each order n yielding the scattered field with increasing accuracy as higher-order multipoles are taken into account, an approach referred to within the field of ultrasound characterization of emulsions and suspensions as ECAH theory after Epstein and Carhart [30] and Allegra and Hawley [31]. However, care must be taken due to the system matrix often being ill conditioned [42].

The long-wavelength limit is characterized by the small dimensionless parameter ε, given by

$$\varepsilon = k_0 a = 2\pi \frac{a}{\lambda} \ll 1. \tag{57}$$

In this limit, the dominant contributions to the scattered field are due to the $n = 0$ monopole and the $n = 1$ dipole terms, both proportional to ε^3, while the contribution of the nth-order multipole for $n > 1$ is proportional to $\varepsilon^{2n+1} \ll \varepsilon^3$.

D. Monopole scattering coefficient

To obtain the monopole scattering coefficient f_0 in Eq. (5), we solve for the expansion coefficient A_0 in Eq. (56) and use the identity $f_0 = 3i\, x_c^{-3} A_0$. The f_n coefficients are traditionally used in studies of acoustic radiation force, while the A_n coefficients are used in general scattering theory.

The solution to the inhomogeneous system of linear equations for $n = 0$ involves straightforward but lengthy algebra presented in Appendix B 1. In Eq. (B8) is given the general analytical expression for f_0 in the long-wavelength limit valid for any particle. In the following, this expression is given in explicit, simplified, closed analytical form for a thermoviscous droplet and a thermoelastic particle, respectively.

1. *Thermoviscous droplet in a fluid*

For a thermoviscous droplet in a fluid in the long-wavelength limit, the particle radius a and the viscous and thermal boundary layers both inside (δ_s', δ_t') and outside (δ_s, δ_t) the fluid droplet are all much smaller than the acoustic wavelength λ, while nothing is assumed about the relative magnitudes of a, δ_s, δ_s', δ_t, and δ_t'. Thus, using the nondimensionalized wave numbers of Eq. (55) and $\varepsilon = k_0 a$, the long-wavelength limit is defined as

$$|x_c|^2, |x_c'|^2 \sim \varepsilon^2 \ll 1 \quad \text{and} \tag{58a}$$

$$|x_c|^2, |x_c'|^2 \sim \varepsilon^2 \ll |x_s|^2, |x_s'|^2, |x_t|^2, |x_t'|^2, \tag{58b}$$

which implies

$$\Gamma_s, \Gamma_t, \frac{|b_c|}{|b_t|}, \frac{|b_c'|}{|b_t|} \sim \varepsilon^2 \ll 1. \tag{58c}$$

To first order in ε, the analytical result for the monopole scattering coefficient f_0^{fl} obtained from Eq. (B8) is most conveniently written as

$$f_0^{\mathrm{fl}} = 1 - \tilde{\kappa}_s + 3(\gamma - 1)\left(1 - \frac{\tilde{\alpha}_p}{\tilde{\rho}_0 \tilde{c}_p}\right)^2 H(x_t, x_t'), \tag{59a}$$

$$H(x_t, x_t') = \frac{1}{x_t^2}\left[\frac{1}{1 - i x_t} - \frac{1}{\tilde{k}_{\mathrm{th}}} \frac{\tan x_t'}{\tan x_t' - x_t'}\right]^{-1}, \tag{59b}$$

where $H(x_t, x_t')$ is a function of the particle radius a through the nondimensionalized thermal wave numbers x_t and x_t'. Epstein and Carhart obtained a corresponding result for A_0 but with a sign error in the thermal correction term [30], while the result of Allegra and Hawley [31] is in agreement with what we present here. The factor $(\gamma - 1)$ quantifies the coupling between heat and the mechanical pressure waves. This factor is multiplied by $[1 - \tilde{\alpha}_p/(\tilde{\rho}_0 \tilde{c}_p)]^2$, where the quantity $\xi_p = \alpha_p/(\rho_0 c_p)$, with unit m^3/J, may be interpreted as an isobaric expansion coefficient per added heat unit. The thermal correction can only be nonzero if there is a contrast $\tilde{\xi}_p \neq 1$ in this parameter.

In the weak dissipative limit of small boundary layers the function $H(x_t, x_t')$ is expanded to first order in δ_t/a and δ_t'/a, and using $\tan(x_t') \simeq i$, we obtain

$$f_0^{\mathrm{fl}} = 1 - \tilde{\kappa}_s - \frac{3}{2}\frac{(1+i)(\gamma - 1)}{1 + \tilde{D}_{\mathrm{th}}^{1/2} \tilde{k}_{\mathrm{th}}^{-1}}\left(1 - \frac{\tilde{\alpha}_p}{\tilde{\rho}_0 \tilde{c}_p}\right)^2 \frac{\delta_t}{a}$$

(small-width boundary layers). (60)

In the limit of zero boundary-layer thickness $\delta_t/a \to 0$, the thermal correction vanishes, and we obtain

$$f_0^{\mathrm{fl}} = 1 - \tilde{\kappa}_s \quad \text{(zero-width boundary layers)}, \tag{61}$$

which is the well-known result for a compressible sphere in an ideal [3] or a viscous [29] fluid.

In the opposite limit of a point particle, $a/\delta_t, a/\delta_t' \to 0$, we find $H(x_t, x_t') = -(1/3)\tilde{\rho}_0 \tilde{c}_p$, yielding

$$f_0^{\mathrm{fl}} = 1 - \tilde{\kappa}_s - (\gamma - 1)\tilde{\rho}_0 \tilde{c}_p \left(1 - \frac{\tilde{\alpha}_p}{\tilde{\rho}_0 \tilde{c}_p}\right)^2$$

(point-particle limit). (62)

Since $\gamma > 1$, the correction from thermal effects in the point-particle limit is negative. This implies that the thermal correction enhances the magnitude of f_0^{fl} for acoustically soft particles ($\tilde{\kappa}_s > 1$), while it diminishes the magnitude and eventually may reverse the sign of f_0^{fl} for acoustically hard particles ($\tilde{\kappa}_s < 1$).

Importantly, an inspection of the point-particle limit [Eq. (62)] leads to two noteworthy conclusions not previously discussed in the literature. First, the thermal contribution to f_0^{fl} allows a sign change of the acoustic radiation force for different-sized but otherwise identical particles. Second, the thermal contribution may result in forces that are orders of magnitude larger than expected from both ideal [3] and viscous [29] theory. For example, $\tilde{\rho}_0 \gg 1$ for particles or droplets in gases leads to a thermal contribution to f_0^{fl} two orders of magnitude larger than $1 - \tilde{\kappa}_s$. These predictions are discussed in more detail in Sec. VIII.

2. *Thermoelastic particle in a fluid*

For a thermoelastic particle in a fluid, the long-wavelength limit differs from that of a thermoviscous droplet [Eq. (58)] by the shear mode describing a propagating wave and not a viscous boundary layer. The wavelength of this transverse shear wave is comparable to that of the longitudinal compressional wave, and in the long-wavelength limit both are assumed to be large,

$$|x_c|^2, |x_c'|^2, |x_s'|^2 \sim \varepsilon^2 \ll 1 \quad \text{and} \tag{63a}$$

$$|x_c|^2, |x_c'|^2, |x_s'|^2 \sim \varepsilon^2 \ll |x_s|^2, |x_t|^2, |x_t'|^2, \tag{63b}$$

which implies

$$\Gamma_s, \Gamma_t, \frac{1}{|\tilde{\eta}_0|}, \frac{|b_c|}{|b_t|}, \frac{|b_c'|}{|b_t|} \sim \varepsilon^2 \ll 1. \tag{63c}$$

To first order in ε, the result Eq. (B8) for f_0^{sl} may be simplified as outlined in Appendix B, and one obtains after some manipulation

$$f_0^{\mathrm{sl}} = \frac{1 - \tilde{\kappa}_s + 3(\gamma-1)\left[\left(1 - \frac{\tilde{\alpha}_p}{\tilde{\rho}_0 \tilde{c}_p}\right)\left(1 - \frac{\chi' \tilde{\alpha}_p}{\tilde{\rho}_0 \tilde{c}_p}\right) - \frac{4}{3}\frac{\chi' \tilde{\alpha}_p \tilde{\kappa}_s}{\tilde{c}_p}\frac{c_T'^2}{c^2}\left(1 - \frac{\tilde{\alpha}_p}{\tilde{\rho}_0 \tilde{c}_p \tilde{\kappa}_s}\right)\right] H(x_t, x_t')}{1 + 4(\gamma-1)\frac{\chi' \tilde{\alpha}_p^2}{\tilde{\rho}_0 \tilde{c}_p^2}\frac{c_T'^2}{c^2} H(x_t, x_t')}, \tag{64}$$

where the function $H(x_t, x_t')$ is still given by the expression in Eq. (59b) with x_t' being the nondimensionalized thermal wave number in the solid particle obtained from Eq. (48b). In the limit of a point particle, $a/\delta_t, a/\delta_t' \to 0$, we find

$$f_0^{\mathrm{sl}} = \frac{1 - \tilde{\kappa}_s - \frac{(\gamma-1)\tilde{\rho}_0 \tilde{c}_p}{1 - X'}\left[\left(1 - \frac{\tilde{\alpha}_p}{\tilde{\rho}_0 \tilde{c}_p}\right)\left(1 - \frac{\chi' \tilde{\alpha}_p}{\tilde{\rho}_0 \tilde{c}_p}\right) - \frac{4}{3}\frac{\chi' \tilde{\alpha}_p \tilde{\kappa}_s}{\tilde{c}_p}\frac{c_T'^2}{c^2}\left(1 - \frac{\tilde{\alpha}_p}{\tilde{\rho}_0 \tilde{c}_p \tilde{\kappa}_s}\right)\right]}{1 - \frac{4}{3}\frac{\gamma - 1}{1 - X'}\frac{\chi' \tilde{\alpha}_p^2}{\tilde{c}_p}\frac{c_T'^2}{c^2}} \quad \text{(point-particle limit)}. \tag{65}$$

Remarkably, in the point-particle limit, f_0^{sl} and f_0^{fl} differ in general. However, as expected, letting $c_T' \to 0$ in Eq. (64), f_0^{sl} reduces to f_0^{fl} [Eq. (59)] for all particle sizes.

In the weak dissipative limit of small boundary layers, $\delta_t, \delta_t' \ll a$, the second term in the denominator of Eq. (64) is small for typical material parameters. An expansion in δ_t/a and δ_t'/a then yields in analogy with Eq. (60),

$$f_0^{\mathrm{sl}} = 1 - \tilde{\kappa}_s - \frac{3}{2}\frac{(1+i)(\gamma-1)}{1 + (1-X')^{1/2}\tilde{D}_{\mathrm{th}}^{1/2}\tilde{k}_{\mathrm{th}}^{-1}} \times \left(1 - \frac{\tilde{\alpha}_p}{\tilde{\rho}_0 \tilde{c}_p}\right)^2 \frac{\delta_t}{a} \quad \text{(small-width boundary layers)}, \tag{66}$$

simplified using Eq. (39e). In the limit $\delta_t/a \to 0$, the thermal correction term vanishes,

$$f_0^{\mathrm{sl}} = 1 - \tilde{\kappa}_s \quad \text{(zero-width boundary layers)}. \tag{67}$$

In this limit, where boundary-layer effects are negligible, f_0^{sl} and f_0^{fl} are identical and, as expected, equal to the ideal [3] and viscous [29] results.

E. Dipole scattering coefficient

To obtain the dipole scattering coefficient f_1 in Eq. (5), we solve for the expansion coefficient A_1 in Eq. (56) and use the identity $f_1 = -6i\, x_c^{-3} A_1$. In the long-wavelength limit, the terms involving the coefficients B_1 and B_1' are neglected to first order in ε. This reduces the system of equations (56) for $n = 1$ from six to four equations with the unknowns A_1, A_1', C_1, and C_1'. In Appendix B 2 we solve explicitly for A_1. Physically, the smallness of the B_1 and B_1' terms means that thermal effects are negligible compared to viscous effects. This is consistent with the dipole mode describing the center-of-mass oscillations of the undeformed particle.

1. *Thermoviscous droplet in a fluid*

The analytical expression for A_1 in the long-wavelength limit for a thermoviscous droplet in a fluid, as defined in Eq. (58), is given in Eq. (B23) of Appendix B 2. This expression for A_1 was also obtained by Allegra and Hawley [31] and, with a minor misprint, by Epstein and Carhart [30] in their studies of sound attenuation in emulsions and suspensions. We write the result for the dipole scattering coefficient f_1 in a form more suitable for comparison to the theory of acoustic radiation forces as presented by Gorkov [3] and Settnes and Bruus [29],

$$f_1^{\mathrm{fl}} = \frac{2(\tilde{\rho}_0 - 1)[1 + F(x_s, x_s') - G(x_s)]}{(2\tilde{\rho}_0 + 1)[1 + F(x_s, x_s')] - 3G(x_s)}, \tag{68a}$$

$$G(x_s) = \frac{3}{x_s}\left(\frac{1}{x_s} - i\right), \tag{68b}$$

$$F(x_s, x_s') = \frac{1 - i x_s}{2(1 - \tilde{\eta}_0) + \frac{\tilde{\eta}_0 x_s'^2(\tan x_s' - x_s')}{(3 - x_s'^2)\tan x_s' - 3x_s'}}. \tag{68c}$$

Even though no thermal effects are present in f_1^{fl}, Eq. (68) is nevertheless an extension of the result by Settnes and Bruus [29], since we have taken into account a finite viscosity in the droplet entering through the parameters $\tilde{\eta}_0$ and x_s'. In the limit $\tilde{\eta}_0 \to \infty$ of infinite droplet viscosity, the function $F(x_s, x_s')$ tends to zero, and we recover the result for f_1 obtained in Ref. [29].

In the weak dissipative limit of small boundary layers, $\delta_s, \delta_s' \ll a$, the dipole scattering coefficient for the thermoviscous droplet reduces to

$$f_1^{\mathrm{fl}} = \frac{2(\tilde{\rho}_0 - 1)}{2\tilde{\rho}_0 + 1}\left[1 + \frac{3(1+i)}{1 + \tilde{\nu}_0^{1/2}\tilde{\eta}_0^{-1}}\frac{\tilde{\rho}_0 - 1}{2\tilde{\rho}_0 + 1}\frac{\delta_s}{a}\right] \quad \text{(small-width boundary layers)}. \tag{69}$$

2. Thermoelastic particle in a fluid

In the long-wavelength limit Eq. (63) of a thermoelastic solid particle in a fluid, we obtain the result

$$f_1^{\mathrm{sl}} = \frac{2(\tilde{\rho}_0 - 1)[1 - G(x_s)]}{2\tilde{\rho}_0 + 1 - 3G(x_s)}, \tag{70}$$

with the function $G(x_s)$ given in Eq. (68). In this expression, the only particle-related parameters are density and radius, and it is identical to that derived by Settnes and Bruus [29], who included the same two parameters in their study of scattering from a compressible particle in a viscous fluid using asymptotic matching.

In the small-width boundary layer limit, $\delta_s \ll a$, the dipole scattering coefficient for the thermoelastic solid particle f_1^{sl} reduces to

$$f_1^{\mathrm{sl}} = \frac{2(\tilde{\rho}_0 - 1)}{2\tilde{\rho}_0 + 1}\left[1 + 3(1+i)\frac{\tilde{\rho}_0 - 1}{2\tilde{\rho}_0 + 1}\frac{\delta_s}{a}\right] \quad \text{(small-width boundary layers)}, \tag{71}$$

which closely resembles Eq. (69) for f_1^{fl}.

3. Asymptotic limits

In the zero-width boundary layer limit, the dipole scattering coefficients f_1^{fl} and f_1^{sl} both reduce to the ideal-fluid expression [3],

$$f_1^{\mathrm{fl}} = f_1^{\mathrm{sl}} = \frac{2(\tilde{\rho}_0 - 1)}{2\tilde{\rho}_0 + 1} \quad \text{(zero-width boundary layers)}. \tag{72}$$

In the opposite limit of a point particle, $F(x_s, x_s') = 1/(2 + 3\tilde{\eta}_0)$ is finite and the expression for f_0^{fl} and f_0^{sl} is dominated by the $G(x_s)$ terms, with both cases yielding the asymptotic result

$$f_1^{\mathrm{fl}} = f_1^{\mathrm{sl}} = \tfrac{2}{3}(\tilde{\rho}_0 - 1) \quad \text{(point-particle limit)}. \tag{73}$$

It is remarkable that for small particles suspended in a gas where $\tilde{\rho}_0 \gg 1$, the value of f_1 in Eq. (73) is three to five orders of magnitude larger than the value $f_1 = 1$ predicted by ideal-fluid theory [3].

VII. RANGE OF VALIDITY

Before turning to experimentally relevant predictions derived from our theory, we discuss the range of validity of our results imposed by the three main assumptions: the time periodicity of the total acoustic fields, the perturbation expansion of the acoustic fields, and the restrictions associated with size, shape, and motion of the suspended particle.

A. Time periodicity

The first fundamental assumption in our theory is the restriction to time-periodic total acoustic fields, which was used to obtain Eq. (3) for the acoustic radiation force evaluated at the static far-field surface $\partial\Omega_1$. Given a time-harmonic incident field, as studied in this work, a violation of time periodicity can only be caused by a nonzero time-averaged drift of the suspended particle. Denoting the speed of this drift by $v_p(t)$, we consider first the case of a steady particle drift. The assumption of time periodicity is then a good approximation if the displacement $\Delta\ell$ is small compared to the particle radius a during one acoustic oscillation cycle $\tau = 2\pi/\omega$ used in the time averaging. A nonzero, acoustically induced particle drift speed v_p must be of second or higher order in $\varepsilon_{\mathrm{ac}}$, $v_p/c \sim \varepsilon_{\mathrm{ac}}^2$, as all first-order fields have a zero time average. Thus

$$\frac{\Delta\ell}{a} \simeq \frac{v_p\tau}{a} = \frac{2\pi v_p}{\omega a} = \frac{2\pi}{k_0 a}\frac{v_p}{c} = \frac{\lambda}{a}\varepsilon_{\mathrm{ac}}^2 \ll 1, \tag{74}$$

and time periodicity is approximately upheld for reasonably small perturbation strengths $\varepsilon_{\mathrm{ac}} \ll \sqrt{a/\lambda}$, which is not a severe restriction in practice. In a given experimental situation, it is also easy to check if a measured nonzero drift velocity fulfills $v_p\tau \ll a$.

In the case of an unsteady drift speed $v_p(t)$, the time-averaged rate of change of momentum $\langle \frac{d\boldsymbol{P}}{dt} \rangle$ in the fluid volume bounded by $\partial\Omega_1$ in Eq. (2) is nonzero, thus violating the assumption $\langle \frac{d\boldsymbol{P}}{dt} \rangle = \boldsymbol{0}$ leading to Eq. (3). Only the unsteady growth of the viscous boundary layer in the fluid surrounding the accelerating particle contributes to $\langle \frac{d\boldsymbol{P}}{dt} \rangle$, since equal amounts of momentum are fluxed into and out of the static fluid volume in the steady problem. For Eq. (3) to remain approximately valid, we must require $\langle \frac{d\boldsymbol{P}}{dt} \rangle$ to be much smaller than $\boldsymbol{F}^{\mathrm{rad}}$. To check this requirement, we consider a constant radiation force accelerating the particle. When including the added mass from the fluid, this leads to the well-known time scale τ_p for the acceleration,

$$\tau_p = \frac{2\tilde{\rho}_0 + 1}{9\pi}\frac{a^2}{\delta_s^2}\,\tau. \tag{75}$$

Thus, small particles ($a \ll \delta_s$) are accelerated to their steady velocity in a time scale much shorter than the acoustic oscillation period ($\tau_p \ll \tau$), while the opposite ($\tau_p \gg \tau$) is the case for large particles ($a \gg \delta_s$). The unsteady momentum transfer to the fluid bounded by $\partial\Omega_1$ is obtained from the unsteady part $F_{\mathrm{drag}}^{\mathrm{unst}}(t)$ of the drag force on the particle as $\langle \frac{dP}{dt} \rangle = \frac{1}{\tau}\int_0^\tau F_{\mathrm{drag}}^{\mathrm{unst}}(t)\,dt$. Using the explicit expression for $F_{\mathrm{drag}}(t)$ given in problems 7 and 8 in §24 of Ref. [43], we obtain to leading order

$$\frac{1}{F^{\mathrm{rad}}}\left\langle \frac{dP}{dt} \right\rangle = \begin{cases} \dfrac{4}{2\tilde{\rho}_0 + 1}\dfrac{\delta_s}{a} \ll 1, & \text{for } a \gg \delta_s, \\ \dfrac{2}{\pi}\dfrac{a}{\delta_s} \ll 1, & \text{for } a \ll \delta_s. \end{cases} \tag{76}$$

We conclude that $\langle \frac{dP}{dt} \rangle \ll F^{\mathrm{rad}}$ in both the large and small particle limits, and hence the assumption of Eq. (3) is fulfilled in those limits.

Considering typical microparticle acoustophoresis experiments, the unsteady acceleration takes place on a time

scale between micro- and milliseconds, much shorter than the time of a full trajectory. Typically, the unsteady part of the trajectory is not resolved and it is not important to the experimentally observed quasisteady particle trajectory. In acoustic levitation [25–28], where there is no drift, the assumption of time periodicity is exact. We conclude that the assumption of time periodicity is not restricting practical applications of our theory.

B. Perturbation expansion and linearity

The second fundamental assumption of our theory is the validity of the perturbation expansion, which requires the acoustic perturbation parameter $\varepsilon_{\mathrm{ac}}$ of Eq. (10) to be much smaller than unity. For applications in particle handling in acoustophoretic microchips [12,14], this constraint is not very restrictive because typical resonant acoustic energy densities of 100 J/m^3 result in $\varepsilon_{\mathrm{ac}} \sim 10^{-4}$.

Given the validity of the linear first-order equations, the solutions we have obtained for f_0 and f_1 based on the particular incident plane wave $\phi_{\mathrm{i}} = \phi_0\, e^{ik_{\mathrm{c}}z}$ are general, since any incident wave at frequency ω can be written as a superposition of plane waves.

C. Oscillations of the suspended particle

The third fundamental assumption of our theory is the assumption of small particle oscillation amplitudes, allowing the boundary conditions to be evaluated at the fixed interface position $r = a$. In general, the oscillation amplitudes must be small in comparison to all other length scales. For small particles, $a \ll \delta_{\mathrm{s}},\delta_{\mathrm{t}}$, the smallest length scale is set by the particle radius a. In the opposite limit of small boundary layers, $a \gg \delta_{\mathrm{s}},\delta_{\mathrm{t}}$, thermoviscous theory reduces to ideal-fluid theory, and the boundary-layer length scales drop out of the equations, again leading to the smallest relevant length scale being the particle radius a. The assumption of small particle oscillation amplitudes leads to physical constraints on the volume oscillations, Figs. 1(a) and 1(b), and the center-of-mass oscillations, Fig. 1(c), discussed in the following.

The volume oscillations of the particle are due to mechanical and thermal expansion. From the definition of the compressibility κ_s' and the volumetric thermal expansion coefficient α_p', we estimate the maximum relative change in particle radius $\Delta a/a$ to be

$$\frac{\Delta a}{a} \simeq \frac{\kappa_s'}{3} p_1 = \frac{\tilde{\kappa}_s}{3}\varepsilon_{\mathrm{ac}} \ll 1, \tag{77a}$$

$$\frac{\Delta a}{a} \simeq \frac{\alpha_p'}{3} T_1 \simeq \frac{1}{3}\,(\gamma-1)\tilde{\alpha}_p\varepsilon_{\mathrm{ac}} \ll 1. \tag{77b}$$

Here, we have used $\kappa_s p_1 = \varepsilon_{\mathrm{ac}}$ and $T_1 = \frac{(\gamma-1)\kappa_s}{\alpha_p} p_1$ obtained from Eq. (14) in the adiabatic limit $s_1 = 0$ combined with Eq. (16). Except for gas bubbles in liquids, for which $\tilde{\kappa}_s \gg 1$, these inequalities are always fulfilled for small perturbation parameters $\varepsilon_{\mathrm{ac}}$.

The velocity of the center-of-mass oscillations is found from Eq. (37) of Ref. [29] to be $v_{\mathrm{p}}^{\mathrm{osc}} = \frac{3}{2}\frac{f_1}{\tilde{\rho}_0-1} v_{\mathrm{in}}$. In the large-particle limit, f_1 is given by Eq. (72), which implies $0 < v_{\mathrm{p}}^{\mathrm{osc}} < 3v_{\mathrm{in}}$, where the lower and the upper limit is for $\tilde{\rho}_0 \gg 1$ and $\tilde{\rho}_0 \ll 1$, respectively. In the point-particle limit, Eq. (73), $v_{\mathrm{p}}^{\mathrm{osc}} = v_{\mathrm{in}}$ independent of $\tilde{\rho}_0$. The relative displacement amplitude $\Delta\ell/a$ is hence estimated as

$$\frac{\Delta\ell}{a} \simeq \frac{v_{\mathrm{p}}^{\mathrm{osc}}}{\omega a} \simeq \begin{cases} \dfrac{3}{2\tilde{\rho}_0+1}\dfrac{\lambda}{2\pi a}\varepsilon_{\mathrm{ac}} \ll 1, & \text{for } a \gg \delta_{\mathrm{s}}, \\ \dfrac{\lambda}{2\pi a}\varepsilon_{\mathrm{ac}} \ll 1, & \text{for } a \ll \delta_{\mathrm{s}}, \end{cases} \tag{78}$$

and thus the general requirement is that $\varepsilon_{\mathrm{ac}} \ll 2\pi a/\lambda$. For large particles in typical experiments, this restriction is not severe. However, for small particles it can be restrictive. For example, to obtain $\Delta\ell/a < 0.05$, we find for particles of radius $a = 100$ nm in water at 1 MHz and particles of radius $a = 1\ \mu$m in air at 1 kHz, that $\varepsilon_{\mathrm{ac}} \lesssim 10^{-5}$ and $\varepsilon_{\mathrm{ac}} \lesssim 10^{-6}$, respectively.

VIII. MICROPARTICLES AND DROPLETS IN STANDING PLANE WAVES

The special case of a one-dimensional (1D) standing plane wave is widely used in practical applications of the acoustic radiation force in microchannel resonators [8–21] and acoustic levitators [25–28]. The many application examples as well as its relative simplicity make the 1D case an obvious and useful testing ground of our theory. In the following, we illustrate the main differences between our full thermoviscous treatment and the ideal-fluid or viscous-fluid models using the typical parameter values listed in Table II.

We consider a standing plane wave of the form $p_{\mathrm{in}} = p_{\mathrm{a}}\cos(k_0 y)$, $\boldsymbol{v}_{\mathrm{in}} = \frac{i}{\rho_0 c}\, p_{\mathrm{a}} \sin(k_0 y)\boldsymbol{e}_y$, with acoustic energy density $E_{\mathrm{ac}} = \frac{1}{4}\kappa_s p_{\mathrm{a}}^2 = \frac{1}{4}\rho_0 v_{\mathrm{a}}^2$, where p_{a} and v_{a} are the pressure and the velocity amplitude, respectively. Expression (5) for the radiation force then simplifies to

$$\boldsymbol{F}_{\mathrm{1D}}^{\mathrm{rad}} = 4\pi\ \Phi_{\mathrm{ac}} a^3 k_0 E_{\mathrm{ac}} \sin(2k_0 y)\boldsymbol{e}_y, \tag{79a}$$

$$\Phi_{\mathrm{ac}} = \tfrac{1}{3}\mathrm{Re}[f_0] + \tfrac{1}{2}\mathrm{Re}[f_1], \tag{79b}$$

where Φ_{ac} is the so-called acoustic contrast factor. The radiation force is thus proportional to Φ_{ac}, which contains the effects of thermoviscous scattering in f_0 and f_1. Note that for positive acoustic contrast factors, $\Phi_{\mathrm{ac}} > 0$, the force is directed towards the pressure nodes of the standing wave, while for negative acoustic contrast factors, $\Phi_{\mathrm{ac}} < 0$, it is directed towards the antinodes.

The acoustic contrast factor Φ_{ac} may be evaluated directly for an arbitrary particle size by using the expressions for the scattering coefficients, either f_0^{fl} and f_1^{fl} for a fluid droplet or f_0^{sl} and f_1^{sl} for a solid particle. For ease of comparison to the work of King [1], Yosioka and Kawasima [2], and Doinikov [4–6], we give the expression for the acoustic contrast factor $\Phi_{\mathrm{ac}}^{\mathrm{fl}}$ of a fluid droplet for small boundary layers and in the point-particle limit. In the small-width boundary layer limit one obtains

$$\Phi_{\mathrm{ac}}^{\mathrm{fl}} = \frac{1}{3}\left(\frac{5\tilde{\rho}_0-2}{2\tilde{\rho}_0+1} - \tilde{\kappa}_s\right) + \frac{3}{1+\tilde{\nu}_0^{1/2}\tilde{\eta}_0^{-1}}\left(\frac{\tilde{\rho}_0-1}{2\tilde{\rho}_0+1}\right)^2\frac{\delta_{\mathrm{s}}}{a} - \frac{1}{2}\frac{\gamma-1}{1+\tilde{D}_{\mathrm{th}}^{1/2}\tilde{k}_{\mathrm{th}}^{-1}}\left(1-\frac{\tilde{\alpha}_p}{\tilde{\rho}_0\tilde{c}_p}\right)\frac{\delta_{\mathrm{t}}}{a}$$

(small-width boundary layers). (80)

TABLE II. Material parameter values at ambient pressure 0.1 MPa and temperature 300 K used in this study, given for water (wa) [44–47], an average liquid food oil [48], air [49], and polystyrene (ps) [50–53]. Parameter values for water and oil at other temperatures are obtained from the fits in Refs. [44,48].

Parameter	Symbol	Value (wa)	Value (oil)	Value (air)	Value (ps)	Unit
Longitudinal speed of sound	c	1.502×10^3	1.445×10^3	3.474×10^2	2.40×10^3	$\mathrm{m\,s^{-1}}$
Transverse speed of sound	c_T				1.15×10^3	$\mathrm{m\,s^{-1}}$
Mass density	ρ_0	9.966×10^2	9.226×10^2	1.161×10^0	1.05×10^3	$\mathrm{kg\,m^{-3}}$
Compressibility	κ_s	4.451×10^{-10}	5.192×10^{-10}	7.137×10^{-6}	2.38×10^{-10}	$\mathrm{Pa^{-1}}$
Thermal expansion coefficient	α_p	2.748×10^{-4}	7.046×10^{-4}	3.345×10^{-3}	2.09×10^{-4}	$\mathrm{K^{-1}}$
Specific heat capacity	c_p	4.181×10^3	2.058×10^3	1.007×10^3	1.22×10^3	$\mathrm{J\,kg^{-1}K^{-1}}$
Heat capacity ratio	γ	1.012×10^0	1.151×10^0	1.402×10^0	1.04×10^0	1
Shear viscosity	η_0	8.538×10^{-4}	4.153×10^{-2}	1.854×10^{-5}		Pa s
Bulk viscosity[a]	η_0^b	2.4×10^{-3}	8.3×10^{-2}	1.1×10^{-5}		Pa s
Thermal conductivity	k_th	6.095×10^{-1}	1.660×10^{-1}	2.638×10^{-2}	1.54×10^{-1}	$\mathrm{W\,m^{-1}\,K^{-1}}$

[a]The bulk viscosity is negligible for scattering in the long-wavelength limit but has been included for completeness. Values for water, oil, and air are estimated from Refs. [54], [55], and [56], respectively. For oil, η_0^b is obtained from the attenuation constant α_0 at 298.15 K and 10 MHz [55] using $\alpha_0 = 2\pi^2 f^2/(\rho_0 c^3)[\eta_0^\mathrm{b} + (4/3)\eta_0 + (\gamma-1)k_\mathrm{th}/c_p]$.

The first term is the well-known result given by Yosioka and Kawasima [2], which reduces to that of King [1] for incompressible particles for which $\tilde{\kappa}_s = 0$. The second term is the viscous correction, which agrees with the result of Settnes and Bruus [29] for infinite particle viscosities, but extends it to finite particle viscosities. Note that the viscous correction yields a positive contribution to the acoustic contrast factor, while the thermal correction from the third term is negative. The result given in Eq. (80) is in agreement with the expression for the radiation force in a standing plane wave given by Doinikov [6] in the weak dissipative limit of small boundary layers. However, this is not seen without considerable effort combining and reducing a number of equations. Although we find Doinikov's approach rigorous, it lacks transparency and is difficult to apply with confidence.

In the point-particle limit of infinitely large boundary-layer thicknesses compared to the particle size, we obtain

$$\Phi_\mathrm{ac}^\mathrm{fl} = \frac{1}{3}\left[(1-\tilde{\kappa}_s) - (1-\tilde{\rho}_0) - (\gamma-1)\tilde{\rho}_0\tilde{c}_p\left(1-\frac{\tilde{\alpha}_p}{\tilde{\rho}_0\tilde{c}_p}\right)^2\right] \quad \text{(point-particle limit)}, \tag{81}$$

in agreement with the viscous result of Settnes and Bruus [29], when omitting the last term stemming from thermal effects. The result for $\Phi_\mathrm{ac}^\mathrm{fl}$ in Eq. (81) is written in a form which emphasizes how parameter contrasts between particle and fluid lead to scattering. As expected, for $\tilde{\kappa}_s = 1$ and $\tilde{\rho}_0 = 1$, the scattering due to compressibility and density (inertia) mechanisms vanishes. This is true for large particles [1–3,29], and it is reasonable that it remains true in the point-particle limit. The expressions for the acoustic radiation force on a point particle in a standing plane wave given by Doinikov [4–6] do not have this property, which is likely due to a sign error or a misprint in the term corresponding to our dipole scattering coefficient f_1 in the point-particle limit in Eq. (73), as was also suggested by Settnes and Bruus [29].

The small-width boundary layer limit and the point-particle limit are useful for analyzing consequences of thermoviscous scattering on the acoustic radiation force, but we emphasize that our theory is not restricted to these limits. In general, the scattering coefficients f_0 and f_1 are functions of the nondimensionalized wave numbers x_s, x_t, x_s', and x_t'. These may all be expressed in terms of the particle radius a normalized by the thickness of the viscous boundary layer in the medium δ_s,

$$x_\mathrm{s} = (1+i)\,\frac{a}{\delta_\mathrm{s}}, \qquad x_\mathrm{s}' = (1+i)\sqrt{\frac{\tilde{\rho}_0}{\tilde{\eta}_0}}\,\frac{a}{\delta_\mathrm{s}}, \tag{82a}$$

$$x_\mathrm{t} = (1+i)\sqrt{\mathrm{Pr}}\,\frac{a}{\delta_\mathrm{s}}, \quad x_\mathrm{t}' = \frac{(1+i)}{\sqrt{1-X'}}\sqrt{\frac{\mathrm{Pr}}{\tilde{D}_\mathrm{th}}}\,\frac{a}{\delta_\mathrm{s}} \tag{82b}$$

where we have used $\delta_\mathrm{s}' = \delta_\mathrm{s}\sqrt{\tilde{\eta}_0/\tilde{\rho}_0}$, $\delta_\mathrm{t} = \delta_\mathrm{s}\sqrt{1/\mathrm{Pr}}$, $\delta_\mathrm{t}' = \delta_\mathrm{s}\sqrt{[(1-X')\tilde{D}_\mathrm{th}]/\mathrm{Pr}}$, with $\mathrm{Pr} = \nu_0/D_\mathrm{th}$ being the Prandtl number of the fluid medium and X' set to zero for the fluid droplet case. Below, we investigate the thermoviscous effects on the acoustic radiation force by plotting the acoustic contrast factor Φ_ac as a function of δ_s/a, ranging from zero boundary-layer effects at $\delta_\mathrm{s}/a = 0$ to maximum effects in the limit $\delta_\mathrm{s}/a \to \infty$.

A. Oil droplets in water and water droplets in oil

We first consider the cases of water with a suspended oil droplet (wa-oil) and of oil with a suspended water droplet (oil-wa) using the parameters of a typical food oil given in Table II. Since the density contrast of water and oil is small, the dipole scattering with its viscous effects is small, while on the other hand the thermal effects in the monopole scattering are significant. This is clearly seen from Fig. 3, where the acoustic contrast factor Φ_ac is plotted for the two cases as a function of δ_s/a using ideal theory, viscous theory (obtained from our thermoviscous theory by setting $D_\mathrm{th} = 0$), and full thermoviscous theory. In Fig. 3, we see that for submicrometer droplets at MHz frequency the thermoviscous theory leads to corrections around 100% as compared to the ideal and the viscous theory, which manifestly demonstrates the importance of thermal effects in such systems.

We note from Fig. 3(a) that the acoustic contrast factor of oil droplets in water is negative, which means that oil droplets are focused at the pressure antinodes. Conversely, water droplets in oil are thus expected to be focused at the pressure nodes.

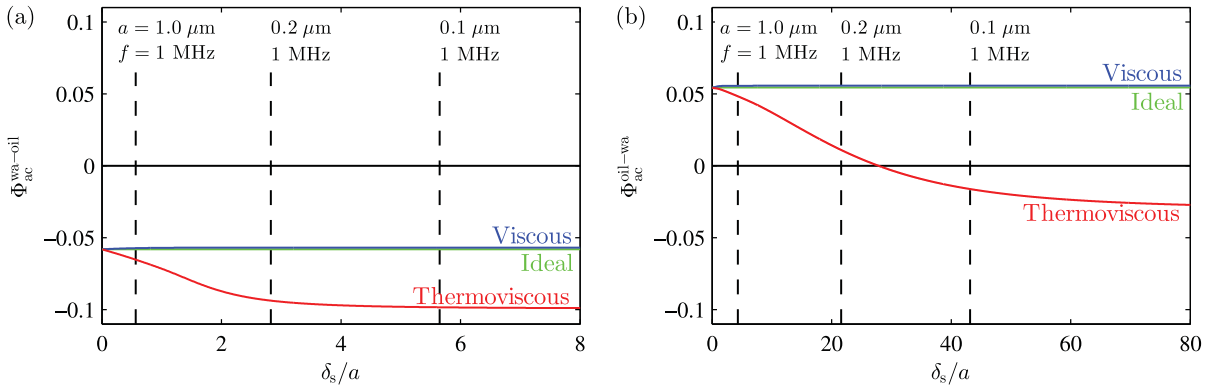

FIG. 3. (Color online) Acoustic contrast factor Φ_{ac} plotted as a function of δ_s/a, the viscous boundary-layer thickness in the medium normalized by particle radius. The curves are calculated using ideal theory (green), viscous theory (thermoviscous theory with $D_{th} = 0$, blue), and thermoviscous theory (red) for (a) an oil droplet in water (wa-oil) and (b) a water droplet in oil (oil-wa), both at 20 °C. Thermoviscous theory leads to corrections to the acoustic radiation force around 100%. The vertical dashed lines indicate examples of particle sizes corresponding to the given value of δ_s/a at $f = 1$ MHz. Note that the acoustic contrast factor changes sign at a critical particle radius for the case of water droplets in oil considered in (b).

However, in Fig. 3(b) we see that thermoviscous theory predicts a tunable sign change in the acoustic contrast factor as a result of the negative thermal corrections to the monopole scattering coefficient. This means that droplets above a critical size threshold experience a force directed towards the pressure nodes, while droplets smaller than the threshold experience a force towards the antinodes, even though the only distinction between the droplets is their size. This sign change in Φ_{ac} can also be achieved for elastic solid particles under properly tuned conditions. By changing, for example, the compressibility contrast $\tilde{\kappa}_s$, the curves for $\Phi_{ac}(\delta_s/a)$ may be shifted vertically and a possible size-threshold condition may be changed. Moreover, since $\delta_s = \sqrt{2\eta_0/(\rho_0\omega)}$ and $\delta_t = \sqrt{2k_{th}/(\rho_0 c_p \omega)}$, there are several direct ways of tuning a threshold value, e.g., by frequency or by changing the density of the medium.

B. Polystyrene particles and water droplets in air

Using the particular cases of a polystyrene particle and a water droplet suspended in air as main examples, we study the effects of a large density contrast $\tilde{\rho}_0 \gg 1$, for which our thermoviscous theory predicts much larger radiation forces on small particles than ideal-fluid theory, for which $\Phi_{ac}^{ideal} = 5/6$ independent of particle size. This is demonstrated in Fig. 4, where Φ_{ac} is plotted as a function of δ_s/a for the two particle types. In the large-particle limit $\delta_s/a = 0$, boundary-layer effects are negligible, and ideal, viscous ($D_{th} = 0$), and thermoviscous theories predict the same contrast factor $\Phi_{ac} = 5/6$, but as δ_s/a increases, the thermoviscous and viscous theories predict an increased value of Φ_{ac}, approximately $2\Phi_{ac}^{ideal}$ for $\delta_s/a = 1$ as seen in the insets of Figs. 4(a) and 4(b). Decreasing the particle size further, $\delta_s/a \gg 1$, the thermoviscous effects become more pronounced with $\Phi_{ac}/\Phi_{ac}^{ideal} \sim 10^2$. Choosing the frequency to be 1 kHz, this remarkable deviation from ideal-fluid theory is obtained for moderately-sized particles of radius $a \approx 2\,\mu$m.

While Φ_{ac}^{air-ps} in Fig. 4(a) for the polystyrene particle is a monotonically increasing function of δ_s/a, the Φ_{ac}^{air-wa} in Fig. 4(b) of a water droplet exhibits a nonmonotonic behavior. For small values of $\delta_s/a \lesssim 25$, the viscous dipole scattering dominates resulting in a positive contrast factor $\Phi_{ac}^{air-wa} \lesssim 10^2$. For larger values, $\delta_s/a \gtrsim 25$, thermal effects in the monopole scattering become dominant leading to a sign change in Φ_{ac}^{air-wa} and finally to large negative contrast factors approximately equal to -10^2 as the point-particle limit $\delta_s/a \gg 1$ is approached. This example clearly demonstrates how the acoustic contrast factor may exhibit a nontrivial size dependency with profound consequences for the acoustic radiation force on small particles. The detailed behavior depends on the specific materials but can be calculated using Eq. (79) and the expressions for f_0 and f_1 listed in Table I.

IX. CONCLUSION

Since the seminal work of Epstein and Carhart [30] and Allegra and Hawley [31], the effects of thermoviscous scattering have been known to be important for ultrasound attenuation in emulsions and suspensions of small particles. In this paper, we have by theoretical analysis shown that thermoviscous effects are equally important for the acoustic radiation force $\boldsymbol{F}^{rad}$ on a small particle. $\boldsymbol{F}^{rad}$ is evaluated from Eq. (5), or more generally from Eq. (6), using our analytical results for the thermoviscous scattering coefficients f_0 and f_1 summarized in Table I. Our analysis places no restrictions on the viscous and thermal boundary-layer thicknesses δ_s and δ_t relative to the particle radius a, a point which is essential to calculation of the acoustic radiation force on micrometer- and nanometer-sized particles.

The discussion in Sec. II leading to Eq. (5) for $\boldsymbol{F}^{rad}$ as well as the discussion of the range of validity presented in Sec. VII are intended to provide clarification and a deeper insight into the fundamental assumptions of the theory for the acoustic radiation force. Foremost, we have extended the discussions of the role of streaming, the fundamental assumption of time periodicity, and the trick of evaluating the radiation force in the far field, which led to the exact nonperturbative expression (3) for the radiation force evaluated in the far field.

For the simple case of a 1D standing plane wave at a single frequency, the expression (6) for $\boldsymbol{F}^{rad}$ simplifies to the useful expression given in Eq. (79), which involves the acoustic

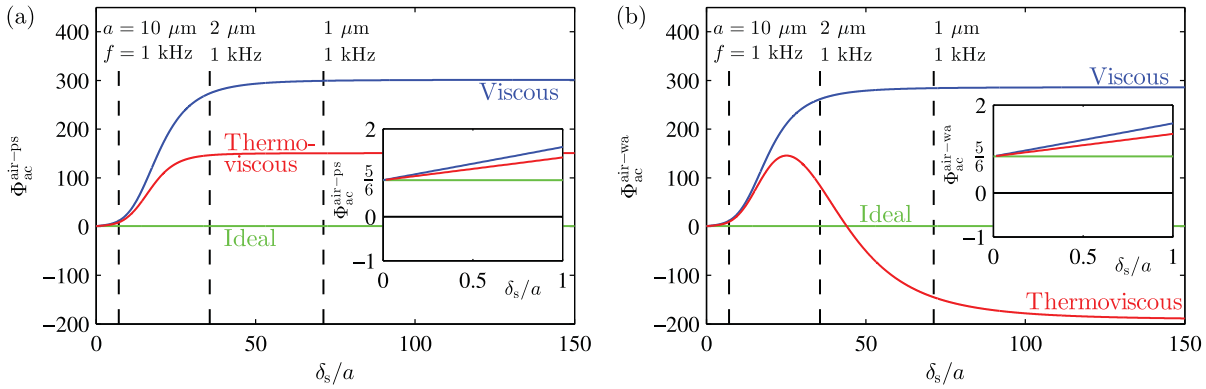

FIG. 4. (Color online) Acoustic contrast factor Φ_{ac} for particles in air plotted as a function of δ_s/a, the viscous boundary-layer thickness in the medium normalized by particle radius. The curves are calculated using ideal theory (green), viscous theory (thermoviscous theory with $D_{th} = 0$, blue), and thermoviscous theory (red) for (a) a polystyrene particle in air (air-ps) and (b) a water droplet in air (air-wa), both at 300 K. Ideal theory predicts a constant value of $\Phi_{ac} = 5/6$ independent of particle size. For particles much smaller than the boundary-layer thickness, however, thermoviscous theory predicts huge deviations from ideal theory leading to acoustic contrast factors two orders of magnitude larger than expected from ideal-fluid theory. The vertical dashed lines indicate examples of particle sizes corresponding to the given value of δ_s/a at $f = 1$ kHz.

contrast factor Φ_{ac}. Similar simplified expressions can be derived for other cases of interest such as that of a 1D traveling plane wave. An important result from the discussion of the simple 1D case in Sec. VIII is that we must abandon the notion of a purely material-dependent acoustic contrast factor Φ_{ac}. In general, Φ_{ac} also depends on the particle size, and in many cases this size dependency can even lead to a sign change in Φ_{ac} at a critical threshold. Recent acoustophoretic experiments on submicrometer-sized water droplets and smoke particles in air may provide the first evidence of this prediction [57]. Considering only viscous corrections, however, the authors could not fully explain their data. Our analysis suggests that thermoviscous effects must be taken into account when designing and analyzing such experiments.

Our results for the acoustic radiation force in a standing plane wave evaluated using Eq. (79) agree with the expressions obtained from the work of Doinikov [4–6] in the limit of small boundary layers, but not in the opposite limit of a point particle. In our theory both of these limits are evaluated directly using the derived analytical expressions valid for arbitrary boundary-layer thicknesses, and we have furthermore given a physical argument supporting our result in the point-particle limit. Considering the viscous theory of Danilov and Mironov [7], we remark that their result is based on the viscous reaction force on an oscillating rigid sphere [43] instead of a direct solution of the governing equations for an acoustic field scattering on a sphere.

Importantly, we have shown that the acoustic radiation force on a small particle including thermoviscous effects may deviate by orders of magnitude from the predictions of ideal-fluid theory when there is a large density contrast between the particle and the fluid. This result is particularly relevant for acoustic levitation and manipulation of small particles in gases [22–28]. Thermoviscous effects can also be significant in many lab-on-a-chip applications involving ultrasound handling of nanoparticles and nanodroplets. In general, acoustic boundary-layer effects should be expected for any type of submicrometer particle, including biological particles such as microvesicles, bacteria, and viruses [8,9,18]. A firm theoretical understanding of thermoviscous effects and of the particle-size-dependent sign change of the acoustic contrast factor could prove important for future applications relying on ultrasound manipulation of micrometer- and nanometer-sized particles.

APPENDIX A: VELOCITY AND NORMAL STRESS IN SPHERICAL COORDINATES

In spherical coordinates (r,θ,φ) with azimuthal symmetry, using that $\boldsymbol{v}_1 = \nabla\phi + \nabla\times\boldsymbol{\psi}$ with $\phi = \phi_c + \phi_t$ and $\boldsymbol{\psi} = \psi_s\,\boldsymbol{e}_\varphi$, the first-order velocity components are

$$v_{1r} = \partial_r\phi + \frac{1}{r\sin\theta}\partial_\theta[\sin\theta\,\psi_s], \tag{A1a}$$

$$v_{1\theta} = \frac{1}{r}\partial_\theta\phi - \frac{1}{r}\partial_r[r\,\psi_s]. \tag{A1b}$$

Inserting this into Eq. (52), we obtain the normal components of the first-order stress tensor

$$\sigma_{1rr} = \eta_0\left(2k_c^2 - k_s^2\right)\phi_c + \eta_0\left(2k_t^2 - k_s^2\right)\phi_t + 2\eta_0\partial_r^2\phi + \frac{2\eta_0}{\sin\theta}\partial_\theta\left[\sin\theta\left(\frac{1}{r}\partial_r\psi_s - \frac{1}{r^2}\psi_s\right)\right], \tag{A2a}$$

$$\sigma_{1\theta r} = 2\eta_0\partial_\theta\left(\frac{1}{r}\partial_r\phi - \frac{1}{r^2}\phi\right) - \eta_0\left(\partial_r^2\psi_s - \frac{2}{r^2}\psi_s\right) + \frac{\eta_0}{r^2}\partial_\theta\left[\frac{1}{\sin\theta}\partial_\theta(\sin\theta\,\psi_s)\right]. \tag{A2b}$$

APPENDIX B: SCATTERING COEFFICIENTS f_0 AND f_1

Here, we outline the calculation of the monopole and dipole scattering coefficients f_0 and f_1 in the long-wavelength limit where the particle radius and the boundary-layer thicknesses are assumed much smaller than the wavelength. Defining the small parameter $\varepsilon = k_0 a \ll 1$, we note that $k_0 a, k_0\delta_s, k_0\delta_t, k_0\delta_t'$, and for a fluid particle furthermore $k_0\delta_s'$, are all of order ε. The calculation is carried out to first order in ε.

1. Monopole scattering coefficient f_0

The monopole scattering coefficient f_0 may be obtained from Eqs. (56a), (56c), (56d), and (56f) setting $n = 0$ and $C_0 = C_0' = 0$. All Bessel functions of the small arguments $x_c, x_c' \sim \varepsilon \ll 1$ are expanded to first order in ε using Eq. (C5) of Appendix C, and in the (unprimed) fluid medium we neglect x_c^2 in comparison to x_s^2. Thus, we arrive at

$$A_0\frac{i}{x_c} + A_0'\frac{1}{3}x_c'^2 - B_0 x_t h_1(x_t) + B_0' x_t' j_1(x_t') = \frac{1}{3}x_c^2, \tag{B1a}$$

$$A_0 b_c\left(1 - \frac{i}{x_c}\right) - A_0' b_c' + B_0 b_t h_0(x_t) - B_0' b_t' j_0(x_t') = -b_c, \tag{B1b}$$

$$A_0 k_{th} b_c\frac{i}{x_c} + A_0'\frac{1}{3}k_{th}' b_c' x_c'^2 - B_0 k_{th} b_t x_t h_1(x_t) + B_0' k_{th}' b_t' x_t' j_1(x_t') = \frac{1}{3}k_{th} b_c x_c^2, \tag{B1c}$$

$$\begin{aligned} &A_0\eta_0\left[\left(4 - x_s^2\right)\frac{i}{x_c} + x_s^2\right] - A_0'\eta_0'\left[x_s'^2 - \frac{4}{3}x_c'^2\right] + B_0\eta_0\left[\left(x_s^2 - 2x_t^2\right)h_0(x_t) - 2x_t^2 h_0''(x_t)\right] \\ &\quad - B_0'\eta_0'\left[\left(x_s'^2 - 2x_t'^2\right)j_0(x_t') - 2x_t'^2 j_0''(x_t')\right] = -\eta_0 x_s^2, \end{aligned} \tag{B1d}$$

where Eq. (C3) is used to write $g_0'(x) = -g_1(x)$ for any spherical Bessel or Hankel function $g_0(x)$.

Multiplying Eq. (B1c) by $1/(k_{th} b_t)$ and using the ratios

$$\frac{b_c}{b_t} = -(\gamma - 1)\frac{x_c^2}{x_t^2}, \quad \frac{b_c'}{b_c} = \tilde{\chi}\frac{\tilde{\alpha}_p}{\tilde{c}_p}, \quad \frac{b_t'}{b_t} = \frac{1}{\tilde{\chi}\tilde{\alpha}_p\tilde{D}_{th}}, \quad \frac{b_c'}{b_t} = \frac{b_c}{b_t}\frac{b_c'}{b_c} = -\tilde{\chi}(\gamma - 1)\frac{\tilde{\alpha}_p}{\tilde{c}_p}\frac{x_c^2}{x_t^2}, \tag{B2}$$

of the b coefficients defined in Eq. (50) [here, $\tilde{\chi} = 1$ for a droplet and $\tilde{\chi} = \chi'$ for a solid particle, respectively, while Eqs. (16), (22), and (39e) are used to reduce b_c'/b_c], we note that the A_0 and A_0' terms can be neglected to order ε, and we obtain

$$B_0' = \frac{k_{th} b_t}{k_{th}' b_t'}\frac{x_t h_1(x_t)}{x_t' j_1(x_t')} B_0 = \tilde{\chi}\frac{\tilde{\alpha}_p}{\tilde{\rho}_0\tilde{c}_p}\frac{x_t h_1(x_t)}{x_t' j_1(x_t')} B_0. \tag{B3}$$

With this, we eliminate B_0' from the system of equations (B1), and the remaining three equations become

$$\begin{pmatrix} \frac{i}{x_c} & \frac{1}{3}x_c'^2 & -S_1 \\ \frac{b_c}{b_t}\left(\frac{i}{x_c} - 1\right) & \frac{b_c'}{b_t} & -\frac{S_2}{x_t^2} \\ \frac{i(x_s^2 - 4)}{x_c} - x_s^2 & \left(x_s'^2 - \frac{4}{3}x_c'^2\right)\tilde{\eta}_0 & -S_3 \end{pmatrix}\begin{pmatrix} A_0 \\ A_0' \\ B_0 \end{pmatrix} = \begin{pmatrix} \frac{x_c^2}{3} \\ \frac{b_c}{b_t} \\ x_s^2 \end{pmatrix}, \tag{B4}$$

where we have introduced the functions S_1, S_2, and S_3,

$$S_1 = \left[1 - \frac{1}{\tilde{k}_{th}}\frac{b_t}{b_t'}\right]x_t h_1(x_t), \tag{B5a}$$

$$S_2 = x_t^2\left[\frac{h_0(x_t)}{x_t h_1(x_t)} - \frac{1}{\tilde{k}_{th}}\frac{j_0(x_t')}{x_t' j_1(x_t')}\right]x_t h_1(x_t), \tag{B5b}$$

$$S_3 = \left[\frac{x_s^2 h_0(x_t)}{x_t h_1(x_t)} - 4\left(1 - \frac{\tilde{\eta}_0}{\tilde{k}_{th}}\frac{b_t}{b_t'}\right) - \frac{\tilde{\eta}_0}{\tilde{k}_{th}}\frac{b_t x_s'^2}{b_t' x_t'}\frac{j_0(x_t')}{j_1(x_t')}\right]x_t h_1(x_t), \tag{B5c}$$

and the relative shear constant $\tilde{\eta}_0$ obtained from Eq. (41b),

$$\tilde{\eta}_0 = \frac{\eta_0'}{\eta_0} = \tilde{\rho}_0\frac{x_s^2}{x_s'^2}. \tag{B6}$$

In obtaining the expression for S_3 we have used Eq. (C3) to substitute $g_0''(x) = -g_0(x) + (2/x)g_1(x)$ for any spherical Bessel or Hankel function $g(x)$. Using Eqs. (B2), (B6), and the explicit forms (C4) of the Bessel functions, the S functions are expressed

in terms of the dimensionless wave numbers as

$$S_1 = \left[1 - \tilde{\chi}\frac{\tilde{\alpha}_p}{\tilde{\rho}_0\tilde{c}_p}\right]x_\mathrm{t}h_1(x_\mathrm{t}), \tag{B7a}$$

$$S_2 = \frac{1}{H(x_\mathrm{t},x_\mathrm{t}')}\,x_\mathrm{t}h_1(x_\mathrm{t}), \tag{B7b}$$

$$S_3 = \left[\frac{x_\mathrm{s}^2}{1-ix_\mathrm{t}} - 4 + \frac{\tilde{\chi}\tilde{\alpha}_p}{\tilde{c}_p}\left(\frac{4x_\mathrm{s}^2}{x_\mathrm{s}'^2} - \frac{x_\mathrm{s}^2\tan x_\mathrm{t}'}{\tan x_\mathrm{t}' - x_\mathrm{t}'}\right)\right]x_\mathrm{t}h_1(x_\mathrm{t}), \tag{B7c}$$

where $H(x_\mathrm{t},x_\mathrm{t}')$ is given in Eq. (59b). The coefficient A_0 is now found from Eq. (B4) by the method of determinants (Cramer's rule) as $A_0 = D(A_0)/D$, where D is the determinant of the left-hand-side system matrix and $D(A_0)$ is the determinant of the system matrix in which the first column (the A_0 coefficients) are replaced by the right-hand-side column with the inhomogeneous terms. The monopole scattering coefficient f_0 in the long-wavelength limit can then be expressed as

$$f_0 = \frac{3i}{x_\mathrm{c}^3}\,A_0 = \frac{3i}{x_\mathrm{c}^3}\frac{D(A_0)}{D}, \tag{B8}$$

with the determinants D and $D(A_0)$ given by

$$\begin{aligned} D = -S_1\left[\tilde{\eta}_0\frac{b_\mathrm{c}}{b_\mathrm{t}}\left(\frac{i}{x_\mathrm{c}} - 1\right)\left(\frac{4}{3}x_\mathrm{c}'^2 - x_\mathrm{s}'^2\right) - \frac{b_\mathrm{c}'}{b_\mathrm{t}}\left(\left(4 - x_\mathrm{s}^2\right)\frac{i}{x_\mathrm{c}} + x_\mathrm{s}^2\right)\right] \\ - \frac{S_2}{x_\mathrm{t}^2}\left[\frac{x_\mathrm{c}'^2}{3}\left(\frac{i\left(4-x_\mathrm{s}^2\right)}{x_\mathrm{c}} + x_\mathrm{s}^2\right) - \frac{i\tilde{\eta}_0}{x_\mathrm{c}}\left(\frac{4}{3}x_\mathrm{c}'^2 - x_\mathrm{s}'^2\right)\right] - S_3\left[\frac{1}{3}x_\mathrm{c}'^2\frac{b_\mathrm{c}}{b_\mathrm{t}}\left(\frac{i}{x_\mathrm{c}} - 1\right) - \frac{i}{x_\mathrm{c}}\frac{b_\mathrm{c}'}{b_\mathrm{t}}\right], \end{aligned} \tag{B9a}$$

$$D(A_0) = -S_1\left[\tilde{\eta}_0\frac{b_\mathrm{c}}{b_\mathrm{t}}\left(\frac{4}{3}x_\mathrm{c}'^2 - x_\mathrm{s}'^2\right) + \frac{b_\mathrm{c}'}{b_\mathrm{t}}x_\mathrm{s}^2\right] - \frac{S_2}{3x_\mathrm{t}^2}\left[-\tilde{\eta}_0x_\mathrm{c}^2\left(\frac{4}{3}x_\mathrm{c}'^2 - x_\mathrm{s}'^2\right) - x_\mathrm{c}'^2x_\mathrm{s}^2\right] - \frac{S_3}{3}\left[\frac{b_\mathrm{c}}{b_\mathrm{t}}x_\mathrm{c}'^2 - \frac{b_\mathrm{c}'}{b_\mathrm{t}}x_\mathrm{c}^2\right]. \tag{B9b}$$

The solution $A_0 = D(A_0)/D$, though written somewhat differently, agrees with Allegra and Hawley's Eq. (10) of Ref. [31].

a. f_0 for a suspended thermoviscous droplet

For a suspended thermoviscous droplet, the precise definition of the long-wavelength limit is given in Eq. (58). In this case, the shear mode characterized by x_s' inside the droplet corresponds to a boundary layer, and consequently comparison to the compressional mode inside and outside the droplet yields $x_\mathrm{c}^2/x_\mathrm{s}'^2 \sim x_\mathrm{c}'^2/x_\mathrm{s}'^2 \sim \varepsilon^2 \ll 1$. This, combined with $b_\mathrm{c}/b_\mathrm{t} \sim b_\mathrm{c}'/b_\mathrm{t} \sim x_\mathrm{c}^2/x_\mathrm{t}^2 \sim \varepsilon^2 \ll 1$ from Eq. (B2), leads to the following simplification of Eq. (B9) to first order in ε,

$$D \simeq -\frac{i}{x_\mathrm{c}}\frac{x_\mathrm{s}^2}{x_\mathrm{t}^2}\tilde{\rho}_0S_2, \tag{B10a}$$

$$D(A_0) \simeq -\frac{\tilde{\rho}_0}{3}\frac{x_\mathrm{s}^2}{x_\mathrm{t}^2}\left(x_\mathrm{c}^2 - \frac{x_\mathrm{c}'^2}{\tilde{\rho}_0}\right)S_2 + \tilde{\rho}_0x_\mathrm{s}^2\frac{b_\mathrm{c}}{b_\mathrm{t}}\left(1 - \frac{\tilde{\alpha}_p}{\tilde{\rho}_0\tilde{c}_p}\right)S_1. \tag{B10b}$$

When inserting this into Eq. (B8), we obtain

$$f_0^\mathrm{fl} = 1 - \tilde{\kappa}_s + 3(\gamma - 1)\left(1 - \frac{\tilde{\alpha}_p}{\tilde{\rho}_0\tilde{c}_p}\right)\frac{S_1}{S_2}, \tag{B11}$$

which upon substitution with $\frac{S_1}{S_2} = (1 - \frac{\tilde{\alpha}_p}{\tilde{\rho}_0\tilde{c}_p})H(x_\mathrm{t},x_\mathrm{t}')$ from Eq. (B7) with $\tilde{\chi} = 1$, leads to the final analytical result for f_0^fl given in Eq. (59).

b. f_0 for a suspended thermoelastic particle

The qualitative change going from the thermoviscous droplet to the thermoelastic particle lies in the shear mode, which changes from a highly damped boundary-layer mode to a propagating transverse wave with $x_\mathrm{s}'^2 \sim \varepsilon^2$. A further implication is that the shear constant ratio of Eq. (B6) becomes large, $\tilde{\eta}_0 = \tilde{\rho}_0x_\mathrm{s}^2/x_\mathrm{s}'^2 \sim \varepsilon^{-2} \gg 1$; and the order of magnitude of the S functions of Eq. (B7) obey $S_1 \sim S_2 \sim \varepsilon^2S_3$. Combining this with the following expression derived from Eqs. (39e), (48), and (B6),

$$\tilde{\eta}_0\left(\frac{4}{3}x_\mathrm{c}'^2 - x_\mathrm{s}'^2\right) = -\chi'\tilde{\rho}_0x_\mathrm{s}^2, \tag{B12}$$

the leading-order expansions in ε of the determinants D and $D(A_0)$ in Eq. (B9) become

$$D = \frac{i}{x_c}\left(-\chi'\tilde{\rho}_0\frac{x_s^2}{x_t^2}S_2 + \frac{b_c'}{b_t}S_3\right), \tag{B13a}$$

$$D(A_0) = x_s^2\frac{b_c'}{b_t}\left(-1+\chi'\tilde{\rho}_0\frac{b_c}{b_c'}\right)S_1 + \frac{x_c^2}{3}\frac{x_s^2}{x_t^2}\left(\frac{x_c'^2}{x_c^2}-\chi'\tilde{\rho}_0\right)S_2 + \frac{x_c^2}{3}\frac{b_c'}{b_t}\left(1-\frac{b_c}{b_c'}\frac{x_c'^2}{x_c^2}\right)S_3. \tag{B13b}$$

From this and Eq. (B8), we obtain the monopole scattering coefficient f_0^{sl} for a thermoelastic particle suspended in a thermoviscous fluid,

$$f_0^{\mathrm{sl}} = \frac{3i}{x_c^3}A_0 = \frac{1-\frac{1}{\chi'\tilde{\rho}_0}\frac{x_c'^2}{x_c^2} - \frac{1}{\chi'\tilde{\rho}_0}\frac{b_c'}{b_t}\frac{x_t^2}{x_s^2}\left[\frac{3x_s^2}{x_c^2}\left(-1+\chi'\tilde{\rho}_0\frac{b_c}{b_c'}\right)\frac{S_1}{S_2} + \left(1-\frac{b_c}{b_c'}\frac{x_c'^2}{x_c^2}\right)\frac{S_3}{S_2}\right]}{1-\frac{1}{\chi'\tilde{\rho}_0}\frac{b_c'}{b_t}\frac{x_t^2}{x_s^2}\frac{S_3}{S_2}}. \tag{B14}$$

From Eq. (B7) we obtain the leading-order expansions in ε for the ratios S_1/S_2 and S_3/S_2,

$$\frac{S_1}{S_2} = \left(1-\frac{1}{\tilde{k}_{\mathrm{th}}}\frac{b_t}{b_t'}\right)H(x_t,x_t'), \quad \frac{S_3}{S_2} = 4\frac{\tilde{\eta}_0}{\tilde{k}_{\mathrm{th}}}\frac{b_t}{b_t'}H(x_t,x_t'), \tag{B15}$$

with the function $H(x_t,x_t')$ defined in Eq. (59b). Inserting this into Eq. (B14) and using Eqs. (B2) and (B6), and the expression (39e) for χ', we arrive at the final analytical form for f_0^{sl} given in Eq. (64).

2. Dipole scattering coefficient f_1

In the long-wavelength limit, for each order $n \geqslant 1$, the terms containing B_n and B_n', and thus the variables x_t and x_t', in the system of boundary equations (56) are of negligible order relative to the terms containing A_n, A_n', C_n, C_n', and the inhomogeneous terms. Formally, this is seen by writing up and inverting the entire 6-by-6 matrix equation for the six coefficients for a given $n \geqslant 1$. A quicker way to see this is to write Eqs. (56c) and (56d) as

$$\begin{pmatrix} h_n(x_t) & -j_n(x_t') \\ x_t h_n'(x_t) & -x_t' j_n'(x_t') \end{pmatrix}\begin{pmatrix} B_n \\ B_n' \end{pmatrix} \sim \varepsilon^2\begin{pmatrix} A_n' j_n(x_t') - A_n h_n(x_c) - j_n(x_c) \\ A_n' j_n(x_t') - A_n h_n(x_c) - j_n(x_c) \end{pmatrix}, \tag{B16}$$

where we have used $\frac{b_c}{b_t}, \frac{b_c'}{b_t} \sim \varepsilon^2$ and $\frac{b_t'}{b_t}, \frac{k_{\mathrm{th}}'}{k_{\mathrm{th}}} \sim 1$. Inserting the expressions for B_n and B_n' obtained by inversion of this equation into Eqs. (56a), (56b), (56e), and (56f), we see that due to the factor ε^2 all terms related to B_n or B_n' are negligible in all four equations. In treating Eq. (56e) it might be useful to use the Bessel's equation (C2). Consequently, returning to the dipole problem with $n = 1$, terms with B_1, B_1' are omitted and the system of equations reduces to four equations with four unknowns, namely, Eqs. (56a), (56b), (56e), and (56f) without the terms of B_1, B_1'. For $n = 1$ we thus obtain the simplified system of equations

$$x_c j_1'(x_c) + A_1 x_c h_1'(x_c) - 2C_1 h_1(x_s) = A_1' x_c' j_1'(x_c') - 2C_1' j_1(x_s'), \tag{B17a}$$

$$j_1(x_c) + A_1 h_1(x_c) - C_1[x_s h_1'(x_s) + h_1(x_s)] = A_1' j_1(x_c') - C_1'[x_s' j_1'(x_s') + j_1(x_s')], \tag{B17b}$$

$$\eta_0\left[x_c j_2(x_c) + A_1 x_c h_2(x_c) + \tfrac{1}{2}C_1 x_s^2 h_1''(x_s)\right] = \eta_0'\left[A_1' x_c' j_2(x_c') + \tfrac{1}{2}C_1' x_s'^2 j_1''(x_s')\right], \tag{B17c}$$

$$\eta_0\left[x_s^2 j_1(x_c) - 4x_c j_2(x_c)\right] - 4C_1\eta_0 x_s h_2(x_s) + A_1\eta_0\left[x_s^2 h_1(x_c) - 4x_c h_2(x_c)\right] = A_1'\eta_0'\left[x_s'^2 j_1(x_c') - 4x_c' j_2(x_c')\right] - 4C_1'\eta_0' x_s' j_2(x_s'), \tag{B17d}$$

where we have rewritten the last two equations using the recurrence relations obtained from Eq. (C3)

$$x g_1'(x) - g_1(x) = -x g_2(x), \tag{B18a}$$

$$g_1''(x) = -g_1(x) + \frac{2}{x}g_2(x), \tag{B18b}$$

valid for any spherical Bessel or Hankel function g.

Simplifying the system of equations we multiply Eq. (B17a) by (-1) and add to it Eq. (B17b), then use the recurrence relation (B18a). Equation (B17b) is multiplied by 2 and Eq. (B17a) is added while using the recurrence relation $x g_1'(x) + 2g_1(x) = x g_0(x)$. We leave Eq. (B17c) as it is. To Eq. (B17d) we add 4 times Eq. (B17c) and use the recurrence relation (B18b). With some

rearrangements, these manipulations give

$$A_1 x_c h_2(x_c) + C_1 x_s h_2(x_s) - A_1' x_c' j_2(x_c') - C_1' x_s' j_2(x_s') = -x_c j_2(x_c), \tag{B19a}$$

$$A_1 x_c h_0(x_c) - 2C_1 x_s h_0(x_s) - A_1' x_c' j_0(x_c') + 2C_1' x_s' j_0(x_s') = -x_c j_0(x_c), \tag{B19b}$$

$$A_1 x_c h_2(x_c) + \tfrac{1}{2} C_1 x_s^2 h_1''(x_s) - \tilde{\eta}_0 \big[A_1' x_c' j_2(x_c') + \tfrac{1}{2} C_1' x_s'^2 j_1''(x_s')\big] = -x_c j_2(x_c), \tag{B19c}$$

$$A_1 h_1(x_c) - 2C_1 h_1(x_s) - \tilde{\rho}_0 [A_1' j_1(x_c') - 2C_1' j_1(x_s')] = -j_1(x_c), \tag{B19d}$$

where $\tilde{\eta}_0 x_s'^2 = \tilde{\rho}_0 x_s^2$ was used to simplify the last equation. The equations may be further simplified using the relevant scalings in the long-wavelength limit for the fluid droplet and the solid particle, respectively.

a. f_1 for a suspended thermoviscous droplet

In the long-wavelength limit for the fluid droplet case the scalings of Eq. (58) apply. Using the approximate expressions for the spherical Bessel and Hankel functions [Eq. (C5)] applicable for small arguments and examining the resulting system of equations (B19) one finds that some terms may be omitted to first order in ε. The simplified system of equations (B19) for the fluid droplet case takes the form

$$-\frac{3i}{x_c^2} A_1 + C_1 x_s h_2(x_s) - C_1' x_s' j_2(x_s') = 0, \tag{B20a}$$

$$-2C_1 x_s h_0(x_s) - A_1' x_c' + 2C_1' x_s' j_0(x_s') = -x_c, \tag{B20b}$$

$$-\frac{3i}{x_c^2} A_1 + \frac{1}{2} C_1 x_s^2 h_1''(x_s) - \frac{1}{2} C_1' \tilde{\eta}_0 x_s'^2 j_1''(x_s') = 0, \tag{B20c}$$

$$\frac{3i}{x_c^2} A_1 + 6C_1 h_1(x_s) + A_1' \tilde{\rho}_0 x_c' - 6C_1' \tilde{\rho}_0 j_1(x_s') = x_c, \tag{B20d}$$

Subtracting Eq. (B20c) from Eq. (B20a) and using Eq. (B18b), we can express C_1' by C_1,

$$C_1' = \frac{x_s^2 h_1(x_s)}{\tilde{\eta}_0 x_s' Q(x_s')} C_1, \tag{B21a}$$

$$Q(x_s') = x_s' j_1(x_s') - 2\Big(1 - \tfrac{1}{\tilde{\eta}_0}\Big) j_2(x_s'). \tag{B21b}$$

Then, using this relation to eliminate C_1' in Eq. (B20a), we arrive at the first of the two equations in Eq. (B22). The second equation (B22b) is obtained by adding Eqs. (B20b) and (B20d) in order to eliminate A_1', then making use of the recurrence relation $3g_1(x) - x g_0(x) = x g_2(x)$. The resulting two equations for A_1 and C_1 are

$$\frac{3i}{x_c^2} A_1 - C_1 \left[x_s h_2(x_s) - \frac{x_s^2 h_1(x_s) j_2(x_s')}{\tilde{\eta}_0 Q(x_s')} \right] = 0, \tag{B22a}$$

$$\frac{3i}{x_c^2} A_1 + 2C_1 \tilde{\rho}_0 \left[\frac{3}{\tilde{\rho}_0} h_1(x_s) - x_s h_0(x_s) - \frac{x_s^2 h_1(x_s) j_2(x_s')}{\tilde{\eta}_0 Q(x_s')} \right] = (1 - \tilde{\rho}_0) x_c. \tag{B22b}$$

From this, and using again the relation $3g_1(x) - x g_0(x) = x g_2(x)$, we obtain the dipole expansion coefficient A_1,

$$A_1 = \frac{\frac{i}{3} x_c^3 (\tilde{\rho}_0 - 1)[h_2(x_s) \tilde{\eta}_0 Q(x_s') - x_s h_1(x_s) j_2(x_s')]}{[3h_2(x_s) - 2(\tilde{\rho}_0 - 1) h_0(x_s)] \tilde{\eta}_0 Q(x_s') - (2\tilde{\rho}_0 + 1) x_s h_1(x_s) j_2(x_s')}. \tag{B23}$$

This result, but with a small error in the numerator, was first obtained by Epstein and Carhart [30]. We reduce the fraction by $\tilde{\eta}_0 Q(x_s') h_0(x_s)$ and use the explicit expressions for the Bessel and Hankel functions in Eq. (C4) to introduce the functions $G(x_s)$ and $F(x_s, x_s')$ given explicitly in Eqs. (68b) and (68c), respectively,

$$G(x_s) = 1 + \frac{h_2(x_s)}{h_0(x_s)}, \tag{B24a}$$

$$F(x_s, x_s') = \frac{x_s h_1(x_s) j_2(x_s')}{\tilde{\eta}_0 h_0(x_s) Q(x_s')}. \tag{B24b}$$

Then, using that $f_1 = -6i\, x_c^{-3} A_1$, we arrive at the final expression (68a) for the dipole scattering coefficient f_1^{fl}.

b. f_1 for a suspended thermoelastic particle

In the long-wavelength limit for the solid particle the scalings of Eq. (63) apply. Using the approximate expressions for the spherical Bessel and Hankel functions [Eq. (C5)] applicable for small arguments and examining the resulting system of equations (B19) one finds that some terms may be omitted to first order in ε. The simplified system of equations (B19) in the solid particle case takes the form

$$-\frac{3i}{x_c^2}A_1 + C_1 x_s h_2(x_s) = 0, \tag{B25a}$$

$$-2C_1 x_s h_0(x_s) - A_1' x_c' + 2C_1' x_s' = -x_c, \tag{B25b}$$

$$-\frac{3i}{x_c^2}A_1 + \frac{1}{2}C_1 x_s^2 h_1''(x_s) - \frac{1}{15}A_1'\tilde{\eta}_0 x_c'^3 + \frac{1}{10}C_1'\tilde{\eta}_0 x_s'^3 = 0, \tag{B25c}$$

$$-\frac{3i}{x_c^2}A_1 - 6C_1 h_1(x_s) - A_1'\tilde{\rho}_0 x_c' + 2C_1'\tilde{\rho}_0 x_s' = -x_c, \tag{B25d}$$

Multiplying Eq. (B25b) by $(-\tilde{\rho}_0)$ and adding it to Eq. (B25d), then substituting C_1 using Eq. (B25a), and finally using the recurrence relation $3g_1(x) - xg_0(x) = xg_2(x)$ leads to the expansion coefficient A_1,

$$A_1 = \frac{\frac{i}{3}x_c^3(\tilde{\rho}_0 - 1)h_2(x_s)}{3h_2(x_s) - 2(\tilde{\rho}_0 - 1)h_0(x_s)}. \tag{B26}$$

Again, using that $f_1 = -6ix_c^{-3}\,A_1$ and introducing $G(x_s)$ as defined in Eq. (B24a), we obtain after some rearrangement the final result for f_1^{sl} given in Eq. (70).

APPENDIX C: SPECIAL FUNCTIONS

The Legendre differential equation solved by Legendre polynomials $P_n(\cos\theta)$ of order n is [58]

$$\frac{1}{\sin\theta}\frac{d}{d\theta}\left(\sin\theta\frac{d}{d\theta}P_n(\cos\theta)\right) + n(n+1)P_n(\cos\theta) = 0. \tag{C1}$$

The Bessel differential equation solved by spherical Bessel or Hankel functions $g_n(x)$ of order n is [58]

$$x^2[g_n''(x) + g_n(x)] = n(n+1)g_n(x) - 2xg_n'(x), \tag{C2}$$

with a prime indicating differentiation with respect to the argument. Useful recurrence relations for $g_n(x)$ are

$$\frac{d}{dx}[x^{-n}g_n(x)] = -x^{-n}g_{n+1}(x), \tag{C3a}$$

$$\frac{d}{dx}[x^{n+1}g_n(x)] = x^{n+1}g_{n-1}(x). \tag{C3b}$$

The lowest-order spherical Bessel functions $j_n(x)$ and Hankel functions of the first kind $h_n(x)$ are [58]

$$j_0(x) = \frac{\sin x}{x}, \quad j_1(x) = \frac{1}{x}\left(\frac{\sin x}{x} - \cos x\right), \tag{C4a}$$

$$j_2(x) = \frac{1}{x}\left[\left(\frac{3}{x^2} - 1\right)\sin x - \frac{3}{x}\cos x\right], \tag{C4b}$$

$$h_0(x) = -i\frac{e^{ix}}{x}, \quad h_1(x) = -\frac{e^{ix}}{x}\left(1 + \frac{i}{x}\right), \tag{C4c}$$

$$h_2(x) = i\frac{e^{ix}}{x}\left(1 + \frac{3i}{x} - \frac{3}{x^2}\right). \tag{C4d}$$

For small arguments, $x \ll 1$, to first order

$$j_0(x) \simeq 1, \quad j_0'(x) \simeq -\frac{x}{3}, \quad j_0''(x) \simeq -\frac{1}{3}, \tag{C5a}$$

$$h_0(x) \simeq 1 - \frac{i}{x}, \quad h_0'(x) \simeq \frac{i}{x^2}, \quad h_0''(x) \simeq -\frac{2i}{x^3}, \tag{C5b}$$

$$j_1(x) \simeq \frac{x}{3}, \quad j_2(x) \simeq \frac{x^2}{15}, \tag{C5c}$$

$$h_1(x) \simeq -\frac{i}{x^2}, \quad h_2(x) \simeq -\frac{3i}{x^3}. \tag{C5d}$$

[1] L. V. King, Proc. R. Soc. London, Ser. A **147**, 212 (1934).
[2] K. Yosioka and Y. Kawasima, Acustica **5**, 167 (1955).
[3] L. P. Gorkov, Sov. Phys. Dokl. **6**, 773 (1962) [Doklady Akademii Nauk SSSR **140**, 88 (1961)].
[4] A. A. Doinikov, J. Acoust. Soc. Am. **101**, 713 (1997).
[5] A. A. Doinikov, J. Acoust. Soc. Am. **101**, 722 (1997).
[6] A. A. Doinikov, J. Acoust. Soc. Am. **101**, 731 (1997).
[7] S. D. Danilov and M. A. Mironov, J. Acoust. Soc. Am. **107**, 143 (2000).
[8] B. Hammarström, T. Laurell, and J. Nilsson, Lab Chip **12**, 4296 (2012).
[9] M. Evander, O. Gidlof, B. Olde, D. Erlinge, and T. Laurell, Lab Chip **15**, 2588 (2015).
[10] I. Leibacher, P. Hahn, and J. Dual, Microfluid Nanofluid **19**, 923 (2015).
[11] H. Bruus, Lab Chip **11**, 3742 (2011).
[12] R. Barnkob, P. Augustsson, T. Laurell, and H. Bruus, Lab Chip **10**, 563 (2010).
[13] P. Thevoz, J. D. Adams, H. Shea, H. Bruus, and H. T. Soh, Anal. Chem. **82**, 3094 (2010).
[14] P. Augustsson, R. Barnkob, S. T. Wereley, H. Bruus, and T. Laurell, Lab Chip **11**, 4152 (2011).
[15] C. Grenvall, P. Augustsson, J. R. Folkenberg, and T. Laurell, Anal. Chem. **81**, 6195 (2009).
[16] Y. Liu, D. Hartono, and K.-M. Lim, Biomicrofluidics **6**, 012802 (2012).
[17] L. Schmid, D. A. Weitz, and T. Franke, Lab Chip **14**, 3710 (2014).
[18] M. Antfolk, P. B. Muller, P. Augustsson, H. Bruus, and T. Laurell, Lab Chip **14**, 2791 (2014).
[19] D. Carugo, T. Octon, W. Messaoudi, A. L. Fisher, M. Carboni, N. R. Harris, M. Hill, and P. Glynne-Jones, Lab Chip **14**, 3830 (2014).
[20] C. W. Shields, L. M. Johnson, L. Gao, and G. P. Lopez, Langmuir **30**, 3923 (2014).
[21] P. Li, Z. Mao, Z. Peng, L. Zhou, Y. Chen, P.-H. Huang, C. I. Truica, J. J. Drabick, W. S. El-Deiry, M. Dao, S. Suresh, and T. J. Huang, PNAS **112**, 4970 (2015).
[22] R. J. Imani and E. Robert, Ultrasonics **63**, 135 (2015).
[23] R. S. Budwig, M. J. Anderson, G. Putnam, and C. Manning, Ultrasonics **50**, 26 (2010).
[24] M. J. Anderson, R. S. Budwig, K. S. Line, and J. G. Frankel, Proc. IEEE Ultrasonics Symp. **1**, 481 (2002).
[25] E. H. Brandt, Nature **413**, 474 (2001).
[26] W. Xie and B. Wei, Appl. Phys. Lett. **79**, 881 (2001).
[27] V. Vandaele, P. Lambert, and A. Delchambre, Precis. Eng. **29**, 491 (2005).
[28] D. Foresti and D. Poulikakos, Phys. Rev. Lett. **112**, 024301 (2014).
[29] M. Settnes and H. Bruus, Phys. Rev. E **85**, 016327 (2012).
[30] P. S. Epstein and R. R. Carhart, J. Acoust. Soc. Am. **25**, 553 (1953).
[31] J. Allegra and S. Hawley, J. Acoust. Soc. Am. **51**, 1545 (1972).
[32] L. L. Foldy, Phys. Rev. **67**, 107 (1945).
[33] P. Lloyd and M. V. Berry, Proc. Phys. Soc. **91**, 678 (1967).
[34] D. J. McClements and M. J. W. Povey, J. Phys. D **22**, 38 (1989).
[35] R. E. Challis, M. J. W. Povey, M. L. Mather, and A. K. Holmes, Rep. Prog. Phys. **68**, 1541 (2005).
[36] P. B. Muller, R. Barnkob, M. J. H. Jensen, and H. Bruus, Lab Chip **12**, 4617 (2012).
[37] R. Barnkob, P. Augustsson, T. Laurell, and H. Bruus, Phys. Rev. E **86**, 056307 (2012).
[38] P. B. Muller, M. Rossi, A. G. Marin, R. Barnkob, P. Augustsson, T. Laurell, C. J. Kaehler, and H. Bruus, Phys. Rev. E **88**, 023006 (2013).
[39] H. Bruus, *Theoretical Microfluidics* (Oxford University Press, Oxford, 2008).
[40] L. D. Landau and E. M. Lifshitz, *Statistical Physics, Part 1*, 3rd ed., Vol. 5 (Butterworth-Heinemann, Oxford, 1980).
[41] L. D. Landau and E. M. Lifshitz, *Theory of Elasticity. Course of Theoretical Physics*, 3rd ed., Vol. 7 (Pergamon Press, Oxford, 1986).
[42] V. J. Pinfield, J. Acoust. Soc. Am. **122**, 205 (2007).
[43] L. D. Landau and E. M. Lifshitz, *Fluid Mechanics*, 2nd ed., Vol. 6 (Pergamon Press, Oxford, 1993).
[44] P. B. Muller and H. Bruus, Phys. Rev. E **90**, 043016 (2014).
[45] W. Wagner and A. Pruss, J. Phys. Chem. Ref. Data **31**, 387 (2002).
[46] M. L. Huber, R. A. Perkins, A. Laesecke, D. G. Friend, J. V. Sengers, M. J. Assael, I. N. Metaxa, E. Vogel, R. Mares, and K. Miyagawa, J. Phys. Chem. Ref. Data **38**, 101 (2009).
[47] M. L. Huber, R. A. Perkins, D. G. Friend, J. V. Sengers, M. J. Assael, I. N. Metaxa, K. Miyagawa, R. Hellmann, and E. Vogel, J. Phys. Chem. Ref. Data **41**, 033102 (2012).
[48] J. N. Coupland and D. J. McClements, J. Am. Oil Chem. Soc. **74**, 1559 (1997).
[49] *CRC Handbook of Chemistry and Physics*, 95th ed. (CRC Press, Boca Raton, FL, 2014).
[50] *Tables of Acoustic Properties of Materials: Plastics* (Onda Corporation, www.ondacorp.com/tecref_acoustictable.shtml, 2015).
[51] *CRC Polymers: A Properties Database* (CRC Press, Boca Raton, FL, 2014).
[52] E. S. Domalski and E. D. Hearing, J. Phys. Chem. Ref. Data **25**, 1 (1996).
[53] S. S. Chang and A. B. Bestul, J. Polym. Sci. A-2 Polym. Phys. **6**, 849 (1968).
[54] M. J. Holmes, N. G. Parker, and M. J. W. Povey, J. Phys. Conf. Ser. **269**, 012011 (2011).
[55] R. Chanamai and D. J. McClements, J. Am. Oil Chem. Soc. **75**, 1447 (1998).
[56] G. Prangsma, A. Alberga, and J. Beenakker, Physica **64**, 278 (1973).
[57] W. Ran and J. R. Saylor, J. Acoust. Soc. Am. **137**, 3288 (2015).
[58] G. B. Arfken and H. J. Weber, *Mathematical Methods for Physicists*, 6th ed. (Elsevier, New York, 2005).

Chapter 7

Paper II in Nature Communications

Iso-acoustic focusing of cells for size-insensitive acousto-mechanical phenotyping

DOI: 10.1038/ncomms11556.

Authors: P. Augustsson, J.T. Karlsen, H.-W. Su, H. Bruus, and J. Voldman.
Journal: Nat. Commun. **7**, 11556 (2016).

Remarks: Supplementary Figures 1-11 and Supplementary Notes 1-4, as made available online, are included immediately after the paper. Excuse the poor formatting. Supplementary Movies 1-3 are available online: https://www.nature.com/articles/ncomms11556#supplementary-information.

nature COMMUNICATIONS

ARTICLE

Received 22 Jan 2016 | Accepted 7 Apr 2016 | Published 16 May 2016

DOI: 10.1038/ncomms11556 OPEN

Iso-acoustic focusing of cells for size-insensitive acousto-mechanical phenotyping

Per Augustsson[1,2], Jonas T. Karlsen[3], Hao-Wei Su[1], Henrik Bruus[3] & Joel Voldman[1]

Mechanical phenotyping of single cells is an emerging tool for cell classification, enabling assessment of effective parameters relating to cells' interior molecular content and structure. Here, we present iso-acoustic focusing, an equilibrium method to analyze the effective acoustic impedance of single cells in continuous flow. While flowing through a microchannel, cells migrate sideways, influenced by an acoustic field, into streams of increasing acoustic impedance, until reaching their cell-type specific point of zero acoustic contrast. We establish an experimental procedure and provide theoretical justifications and models for iso-acoustic focusing. We describe a method for providing a suitable acoustic contrast gradient in a cell-friendly medium, and use acoustic forces to maintain that gradient in the presence of destabilizing forces. Applying this method we demonstrate iso-acoustic focusing of cell lines and leukocytes, showing that acoustic properties provide phenotypic information independent of size.

[1] Department of Electrical Engineering and Computer Science, Massachusetts Institute of Technology, 77 Massachusetts Avenue, Cambridge, MA 02139, USA. [2] Department of Biomedical Engineering, Lund University, Ole Römers väg 3, 22363, Lund, Sweden. [3] Department of Physics, Technical University of Denmark, DTU Physics Bldg 309, DK-2800 Kongens Lyngby, Denmark. Correspondence and requests for materials should be addressed to P.A. (email: per.augustsson@bme.lth.se).

Microfluidic methods to position, separate, and analyze cells hold promise to shorten the time from sample to answer in cell-based assays in health care and basic biology[1,2]. In particular, phenotyping of single cells based on their cell-intrinsic biophysical properties is an emerging tool for classification of cells that relates to differences or changes in their molecular and architectural structure[3]. To date the palette of cell properties made available for analysis in microfluidic systems include size[4], density[5], deformability[1,6,7], electrical[8,9], and optical[10] properties.

Acoustic characterization of tissue has tremendous value in medicine through various forms of medical ultrasound imaging applications such as sound scattering, attenuation and elasticity[11,12]. It is therefore reasonable to assume that acoustic properties of individual cells, which include mass density and adiabatic compressibility, are meaningfully related to their biological phenotype. Mapping of sound velocity and attenuation at sub-cellular resolution has been demonstrated for adherent cells using acoustic microscopy[13–16] indicating that the acoustic properties are related to the interior content and structure of a cell. While the population average of the acoustic properties of cells in suspension can be deduced from measurements using standard density and sound velocity meters[13–17] the acoustic properties of single suspension cells are largely unknown.

Acoustophoresis[18], relying on acoustic radiation forces, has emerged as a gentle[19,20] and robust method for concentrating[21,22], trapping[23,24], washing[25], aligning[26] and separating cells[27–29]. However, the strong size dependency in acoustophoresis has hampered the development of cell analyzers based on measuring the underlying properties of cell density and compressibility, a shortcoming shared by all volumetric force-based methods. Although examples exist of canceling the first-order size dependency via balancing against gravity,[30] loading cells with immuno-affinity microbeads[31,32], or by estimating and adjusting for cell size,[33] no acoustophoretic method exist today that allows size-independent cell analysis of individual cells in suspension.

Here we introduce a size-insensitive method, iso-acoustic focusing (IAF), that can analyze cells based on the previously uncharted parameter of effective acoustic impedance. This equilibrium method can be viewed as a microfluidic analog to density gradient centrifugation or iso-electric focusing. Cells flowing through a microchannel migrate sideways, influenced by an acoustic field, into flow streams of ever increasing acoustic impedance. Finally, the individual cells reach their iso-acoustic point (IAP), at which the acoustic contrast between the cell and the surrounding liquid becomes zero, and the sideways displacement ceases. Cell-specific differences in effective acoustic impedance translate to a spatial dispersion of the cell population transverse to the flow, enabling continuous label-free analysis of individual cells. To develop this method, we have first identified a suitable molecule (iodixanol) to alter the acoustic properties of the cell-culture medium such that cells can have positive, zero or negative acoustic contrast depending on the molecular concentration. We utilize here a recent finding that acoustic impedance gradients are self-stabilized in resonant acoustic fields, which counteracts any gravitational relocation of the laminated liquids due to density differences[34].

We lay out a simple theoretical model of the acoustofluidic system describing the shaping of a smooth impedance gradient through interactions of diffusion, gravity and acoustic radiation, and compute the trajectories of cell migration in the resulting acoustofluidic field. We then characterize the IAF system using cell lines and apply it to measuring the effective acoustic impedance of white blood cells.

Results

IAF Principle. In IAF, cells are deflected sideways by a half-wavelength resonant acoustic pressure field $p(y, t)$,[35–37] oriented orthogonal to the flow (Methods—Measuring the acoustic field, Supplementary Fig. 1), in a laminar flow microchannel (Fig. 1a). Cells suspended in a standard cell-culture medium are injected near both side walls of the channel and cell-free liquid of higher acoustic impedance Z_{med} is injected in a central inlet to occupy the central part of the flow. The flow velocity of the channel is tailored such that a smooth profile $Z_{med}(y)$ with an associated acoustic impedance gradient forms by way of molecular diffusion. The transverse acoustic radiation force F_{rad} on a given cell stems from momentum transfer to the cell from the sound wave due to scattering. Because this scattering is governed by differences in mass density ρ and adiabatic compressibility κ between the cell and the surrounding medium, there exists a medium condition for which the acoustic contrast Φ and force F_{rad} are zero, and thus the acoustically induced sideways velocity u_{rad} vanishes. This condition we refer to as the iso-acoustic point (IAP), (Fig. 1b). To a good approximation the IAP is the location at which Z_{med} equals the effective acoustic impedance Z_{cell} of the cell (Supplementary Note 1). Since the sound wavelength is in IAF much longer than the size of a single cell the effective acoustic impedance can be interpreted as a measure of the integral of the interior variations in acoustic properties that has been previously mapped using acoustic microscopy[14–16].

A cell initially near a wall at $y = 0$ will migrate toward the channel center due to a positive acoustic contrast. Upon traversing up the concentration or impedance gradient of the medium, the acoustic contrast eventually becomes zero at the IAP, preventing the cell from moving any further. The configuration is stable in the sense that if the cell starts out in the channel center, it will instead move out towards the walls, down the impedance gradient, until reaching the same IAP. When reaching the end of the microfluidic channel, the sideways position of individual cells can be recorded and then translated to an effective cell acoustic impedance, since at the IAP $Z_{cell} = Z_{med}$.

Tuning the acoustic contrast between medium and cells. Critical to IAF is the ability to prepare separation media of acoustic impedance higher and lower than that of the cells, thus

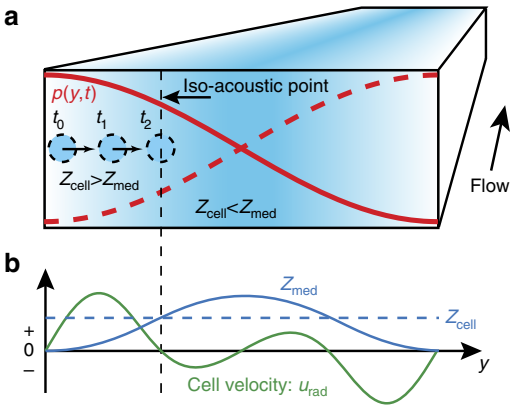

Figure 1 | The IAF principle. (**a**) Cells (circles) flowing in a microchannel are deflected sideways towards the node of an acoustic resonant pressure field p (red curves) in a medium of position-dependent acoustic impedance Z_{med} (color plot from low (white) to high (blue)). (**b**) Conceptual plot showing that when the acoustic impedance Z_{cell} (dashed blue line) of a given cell matches Z_{med} (full blue line) at the IAP, its transverse velocity u_{rad} (green line) becomes zero so that its position along y reflects its individual effective acoustic impedance.

enabling a transition from positive to negative acoustic contrast. The vast majority of cells have positive acoustic contrast in standard cell-culture media (a notable exception being adipocytes[38]). To increase the acoustic impedance of the medium, OptiPrep, a standard isotonic gradient centrifugation medium that contains iodixanol, was added. Iodixanol was chosen by virtue of its high acoustic impedance to viscosity ratio (Supplementary Fig. 2c and 2e), allowing substantial changes in acoustic impedance with only modest changes in viscosity. The acoustic impedance of iodixanol solutions increases monotonically with concentration when using isotonic serum-supplemented saline solutions as a diluent, such that the cells are expected to have positive acoustic contrast when suspended in low-concentration iodixanol and to have negative contrast for high-concentration iodixanol.

To demonstrate that the acoustic contrast of cells can be modulated by altering the properties of the medium we suspended murine BA-F3 pro B cells in a range of iodixanol concentrations, and observed their trajectories when exposed to a resonant sound field. Cells were injected in the acoustic microfluidic channel, the flow was stopped, and the sound was turned on while recording the trajectories of the cells (Supplementary Movies 1-3). The trajectories were then analyzed and classified (Methods—Stop flow trajectory classification, Supplementary Fig. 3) as having positive contrast if they moved to the central node and negative if they moved to either side-wall. 96% of cells suspended in 10% iodixanol had positive contrast, whereas most cells (83%) in 25% iodixanol had negative contrast (Fig. 2). For intermediate concentrations, many cells display oscillatory motion patterns (zero contrast), which indicates that the cells are predominantly influenced by acoustic streaming rather than acoustic radiation. Acoustic streaming is a phenomenon associated with acoustic fields in fluids that here induces a slow rotation of the bulk liquid[39–41]. Cells having zero acoustic contrast will experience a drag force from the rotating liquid exceeding that of the acoustic radiation force acting directly on the cell while cells of positive and negative contrast will be radiation dominated.

These results show that one can create both positive and negative acoustic contrast by tuning medium properties with iodixanol. Additionally, by assuming $Z_{cell} = Z_{med}$ at zero acoustic contrast, we can further conclude that these BA-F3 cells have acoustic impedances between 1.6 MPa s m^{-1} and 1.7 MPa s m^{-1}.

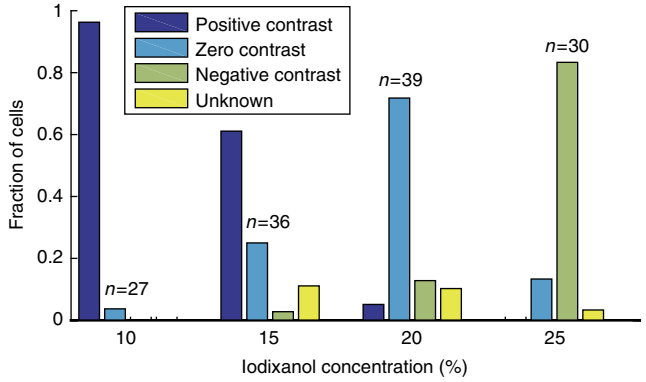

Figure 2 | Controlling the acoustic contrast of BA-F3 cells by altering the acoustic properties of the suspending medium. Fraction of cells exhibiting *Positive, Negative or Zero contrast* based on multi frame trajectory analysis. *Unknown* refers to cell trajectories that did not match any of the other categories. *n* refers to number of cell tracks, with a minimum five onsets of sound.

Creating an acoustic impedance gradient. To separate cells of different acoustic properties to distinct, stable locations in the acoustic field, the acoustic impedance of the liquid must form a spatial gradient that is monotonically increasing toward the channel center. We achieve this by laminating high acoustic impedance media containing iodixanol side by side with standard cell media of lower acoustic impedance. The steep acoustic impedance gradient at the inlet becomes flattened by diffusion of the iodixanol molecules during the flow through the channel. Injecting a fluorescent dextran (MW 3000 Da) tracer of similar molecular diffusion constant ($D_{dex} \approx 2.2 \times 10^{-10}$ m^2 s^{-1})[42] as iodixanol ($D_{ix} \approx 2.5 \times 10^{-10}$ m^2 s^{-1})[43] allows indirect visualization of the iodixanol concentration profile.

First consider a homogeneous solution (20% iodixanol) with no density gradient. A dilute fluorescent tracer gradient is created by injecting different concentrations of tracer in the central versus side inlets. It broadens due to molecular diffusion and flattens in more than 68 s (Supplementary Fig. 4c). Repeating this experiment, but increasing the concentration of iodixanol to 30% in the center layer while reducing the concentration to 10% in the side inlets induces ~30-fold faster flattening of the fluorescent tracer profile (~2 s, Supplementary Fig. 4b). This is caused by gravitational collapse of the high-density central liquid layer, which ends up in a stable configuration along the channel floor as confirmed by confocal imaging (Fig. 3a). Finally, repeating the latter experiment, but with ultrasound on, acoustic radiation forces act on the central liquid layer and stabilize it against gravitational collapse (Fig. 3b), an effect previously observed by confocal microscopy[34]. The condition for stability is that the acoustic energy density is larger than the hydrostatic pressure (Supplementary Note 2). The acoustically stabilized concentration profile still broadens over more than 34 s due to diffusion (Supplementary Fig. 4a) similar to the homogeneous-density system without ultrasound (Supplementary Fig. 4c).

As was pointed out in the previous section, acoustic streaming is observed for cells of zero acoustic contrast in the case of homogeneous medium. In the inhomogeneous system we observed an iodixanol concentration profile that evolved over more than 34 s (Supplementary Fig. 4a) which indicates that acoustic streaming is not present in the bulk to the extent that it affects the acoustic impedance gradient. We explain this absence of streaming in the bulk by a scaling argument presented in Supplementary Note 2. In essence, the acoustic force density stabilizing the gradient can be shown to be orders of magnitude larger than the shear-force density associated with the boundary-driven acoustic streaming. We can make the stabilized acoustic impedance gradient steeper or shallower by tuning the overall volume flow rate in the channel and thereby controlling the time available for diffusion of the iodixanol and the fluorescent tracer before the downstream imaging region is reached (Fig. 3c). This allows tuning of the range and resolution of the system so as to maximize the spatial spread of cells' IAP for a given input sample. Further, the position of a cell's IAP can be controlled by varying the relative flow rates of the side and central inlet streams (Fig. 3d).

In summary, we can create smooth acoustic impedance gradients and tailor their range according to the anticipated IAP of different cells. Remarkably, the same acoustic field that stabilizes these gradients also drives the cells towards their IAP.

Measuring the effective acoustic impedance of cells. To measure the acoustic impedance of individual cells in continuous flow, fluorescently labeled cells were resuspended in low-impedance medium (10% iodixanol) and injected into the side inlets while high-impedance media (iodixanol 36 %) containing dextran

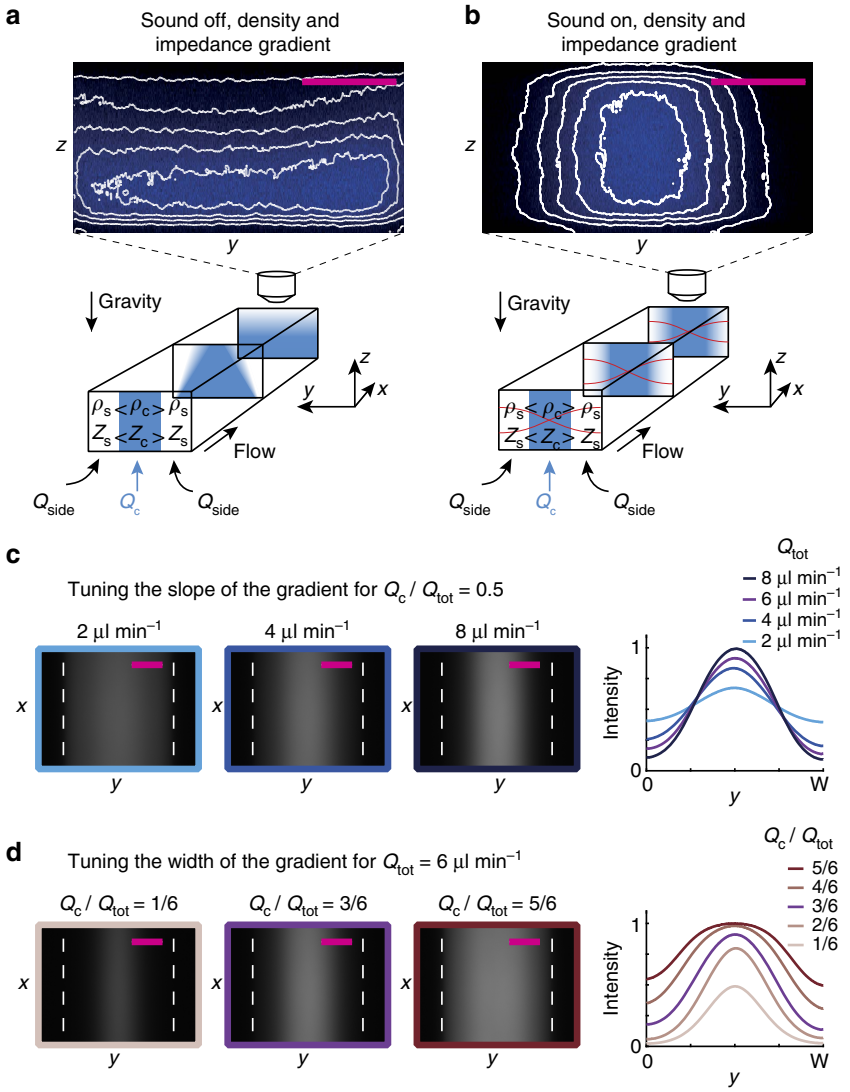

Figure 3 | Tailoring smooth acoustic impedance gradients. (**a** and **b**) Confocal cross sectional *y*-*z* scans recorded 20 mm downstream from the inlet, of the fluorescent dextran tracer gradient (blue color plot) in the case of (**a**) an iodixanol gradient and no sound, and (**b**) an iodixanol gradient and sound (red lines), along with schematic interpretations of the data. (**c**) Top views of the fluorescent dextran tracer gradient imaged with epifluorescence microscopy at different volume flow rates Q_{tot}. The graph shows the corresponding normalized fluorescence intensity profiles versus *y* averaged along the flow direction *x*. (**d**) Top view epifluorescence images when varying the relative flow rate in the central Q_c and side inlets while maintaining a constant overall flow rate Q_{tot} and the corresponding normalized fluorescence intensity profiles. Scale bars (magenta) are 100 µm.

tracer was injected through the central inlet (Fig. 4a). The resonant acoustic field pushes cells towards higher acoustic impedance in the self-forming concentration profile until they reach their respective IAP. At the end of the channel, by repeatedly imaging the dextran tracer gradient and then the cells, we could infer the cells' IAP from the local dextran fluorescence intensity—and thus the concomitant iodixanol concentration and acoustic impedance Z_{med} (Fig. 4b-e). The method is described in more detail in Methods—Method to measure cell IAP.

We introduced BA-F3 cells into the device and measured their IAP and inferred their acoustic impedances Z_{cell} (Fig. 4e). We found that the measured acoustic impedance $Z_{cell} = 1.68$ MPa · s m^{-1} was stable over time with no significant drift (Fig. 4f, slope = 3.04 Pa m^{-1}, correlation coefficient r = 0.039, CI_{95}: −0.013, 0.090, $P = 0.14$ computed with t-statistic). Comparing the populations of cells measured on the right and left hand side of the channel reveals a small difference of the means of 0.005 MPa s m^{-1} (CI_{95}: 0.0040, 0.0069) which is less than half the sample standard deviation 0.014 MPa s m^{-1} and thus insignificant.

To verify that the cells have reached their IAP upon entering the imaging region, the flow was kept constant while varying the piezoceramic actuator voltage amplitude U and thereby the acoustic energy density E_{ac} and acoustic pressure amplitude p_a ($E_{ac} \propto p_a^2 \propto U^2$, Methods—Measuring the acoustic field, Supplementary Fig. 5). Measurements of the apparent cell effective acoustic impedance distributions showed that the distributions narrowed and approached the same median value (Fig. 4g) at acoustic energy densities above $E_{ac} = 11$ J m^{-3}. This behavior is consistent with an equilibrium separation method. In addition, reducing the overall flow rate from 8 µl min^{-1} to 4 µl min^{-1} while maintaining the same actuation settings does not alter the measured distributions markedly (Fig. 4h), which shows that the method is insensitive to flow variations, again consistent with an equilibrium method. The inferred acoustic impedances of BA-F3 cells range from 1.66 MPa s m^{-1} to

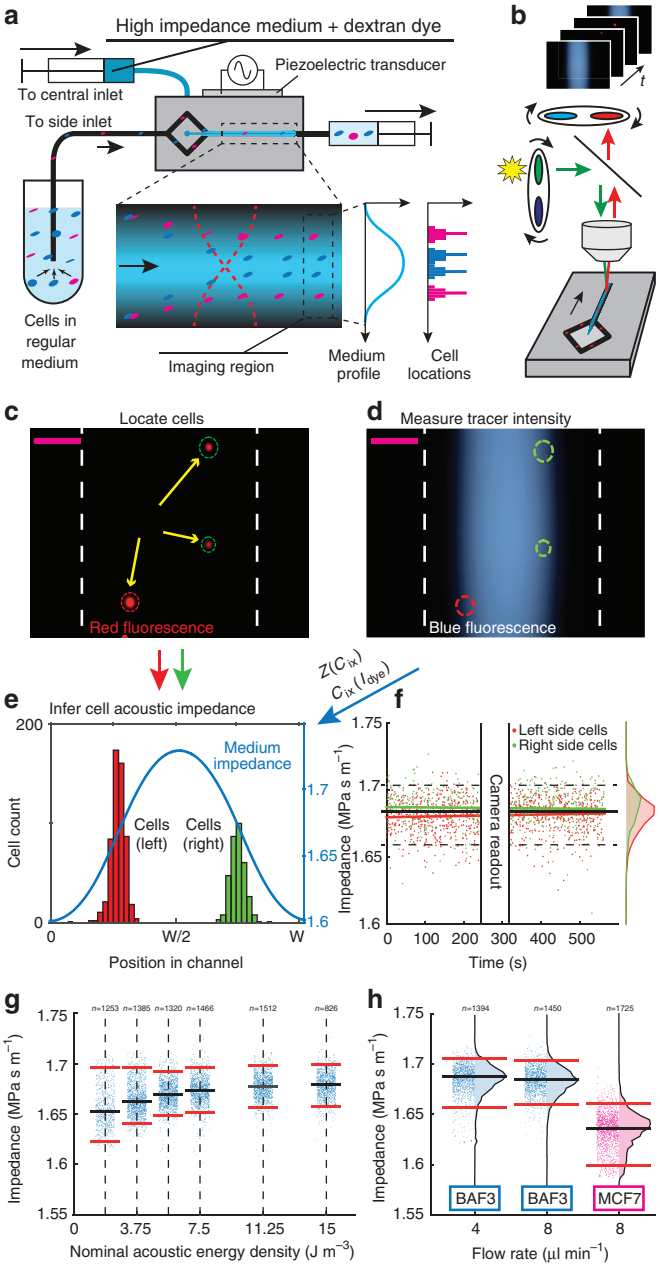

Figure 4 | IAF cell measurements. (**a**) Schematic of the system. (**b-e**) The acoustic impedance gradient is inferred via (**b**) sequential imaging at the end of the channel of (**c**) cells and (**d**) the fluorescent dextran tracer gradient. Scale bars (magenta) are 100 µm. (**e**) Standard solutions of iodixanol and dextran dye were analyzed to convert from fluorescence intensity to acoustic impedance. (**f**) Scatter plot during 500 s of the inferred acoustic impedance Z_{cell} of BA-F3 cells ($n=1,450$) passing the imaging region in both sides of the device. The red and green lines show the linear least square fits. The solid black horizontal line shows the median of all cells and the dashed lines show the 5th and 95th percentiles. (**g**) Scatter plots of Z_{cell} for BA-F3 ($n=7,762$) for six values of the acoustic energy density. (**h**) Scatter plots of Z_{cell} for BA-F3 cells at flow rates 4 µl min^{-1} ($n=1,394$) and 8 µl min^{-1} ($n=1,450$) and for MCF7 cells at 8 µl min^{-1} ($n=1,725$). Black horizontal lines show median and red lines show the 5th and 95th percentiles.

1.70 MPa s m^{-1} (5th to 95th percentile), which is within the range found by the stop-flow experiments in Fig. 2.

To see if the IAP is cell-type specific, we measured human breast cancer cell line MCF7 cells (Fig. 4h) and found that the measured acoustic impedance was lower than for the BA-F3 cells with only a minimal overlap of the two populations such that only 6.07% of the MCF7 cells were found above the 5th percentile of the BA-F3 cells. Because the diameter of MCF7 cells is ~1.5 times larger than that of BA-F3, and, in this system, lower acoustic impedance implies that cells are detected closer to the channel walls; this result also underpins the size insensitivity of IAF in being an equilibrium method. In traditional non-equilibrium acoustophoresis cell separation, where larger cells move faster than smaller cells, the MCF7 cells would end up closer to the channel center for a given time of exposure to sound.

To validate that cells indeed reach and stay in their IAP given the transit time through the IAF channel, and to illustrate the method in more detail, we implemented a simple numerical model of cells migrating in acoustic fields in diffusing iodixanol gradients (Supplementary Note 3, Supplementary Fig. 6). We modeled the trajectories of a BA-F3 cell and a MCF7 cell based on the measured effective acoustic impedances from the experiments, the literature values for density, and their sizes from Coulter counter measurements. We also performed a time-scale analysis of the process to give analytical estimates for deciding experimental design parameters (Supplementary Note 4). In brief, both cells reach their respective IAP within the first 5.7 s and stay there for up to 51 s after entering the channel, which corresponds to flow rates ranging from 1.3 µl min^{-1} to 12 µl min^{-1}. The diffusing gradient causes the position of the BA-F3 cell's IAP to approach the channel center over time while the MCF7 cell eventually ends up near a wall. The diffusing gradient narrows the measurement range leading to finer resolution in the IAP measurement as the profile evolves. A cell reaching the channel center or a wall indicates that the cell has an effective acoustic impedance that is higher or lower, respectively, than the upper or lower bounds on the measurement range.

Blood cell characterization. To understand to what extent acoustic impedance can discriminate cells from mixed populations, we analyzed primary human monocytes, lymphocytes and neutrophils purified from whole blood by negative selection (Fig. 5a). Lymphocytes (red) and monocytes (blue) have partly overlapping acoustic impedance distributions, whereas neutrophils (gray) have substantially higher acoustic impedance. The results suggest that neutrophils can be distinguished from lymphocytes and monocytes purely based on their location in an acoustic impedance gradient. Since lymphocytes and monocytes have substantially different sizes (~7.5 µm and ~9.0 µm, respectively, Fig. 5e) but similar acoustic impedance (~1.69 MPa s m^{-1}, Fig. 5c), whereas neutrophils and monocytes have similar sizes (~9.0 µm, Fig. 5e) but differing acoustic impedances (~1.73 MPa s m^{-1} and ~1.69 MPa s m^{-1}, respectively, Fig. 5c), these results further illustrate the size-independence of the IAF method.

To highlight how acoustic properties combined with optical measurements can form a two-parameter classification analogous to flow cytometry, without using cell type-specific labels, we point to the scatter plot and the associated distributions in Fig. 5b-d of the effective acoustic impedance vs the total cell fluorescence intensity. Even though the total intensity is not a true measure of cell volume, the scatter plot allows us to distinguish monocytes from lymphocytes based on an optical measurement, while the assessment of the effective acoustic impedance enables identification of neutrophils.

Furthermore, the sensitivity of IAF is high enough to detect alterations in mechanical properties of cells. Analysis of RBC-lysed human blood reveals a distinct peak (purple) corresponding to neutrophils, which are normally the most

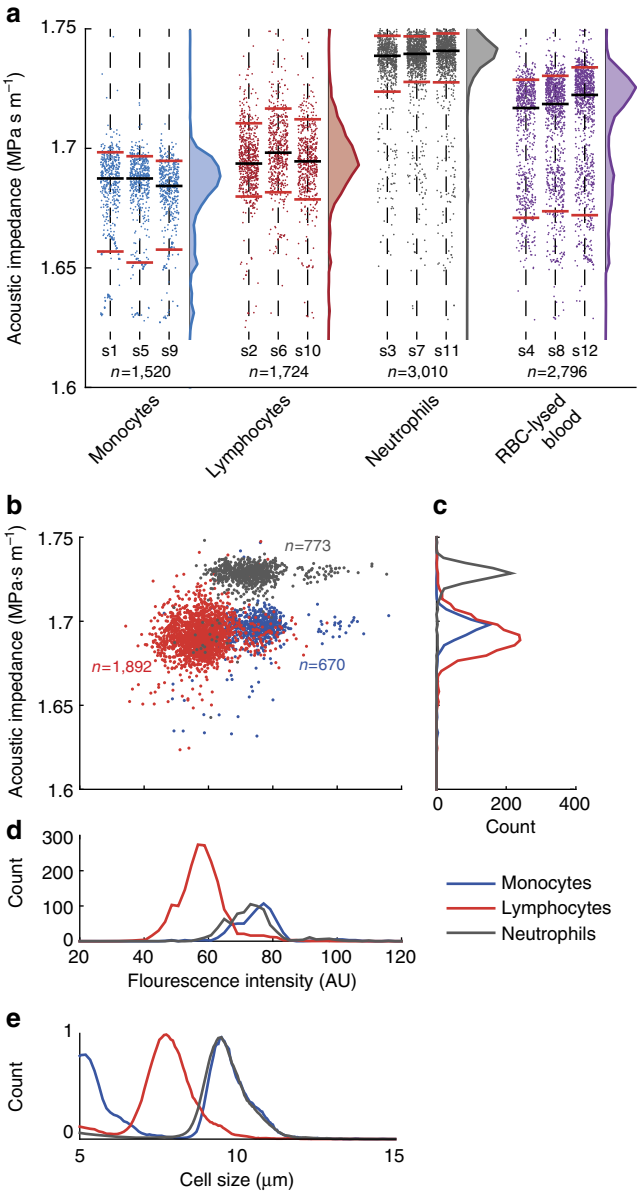

Figure 5 | The effective acoustic impedance of white blood cells as measured by their IAP in an iodixanol gradient. (**a**) Scatter plots containing 9050 data points of subsequent measurements of pre-enriched monocytes (blue), lymphocytes (red) and neutrophils (gray) isolated by negative depletion, and of white blood cells isolated by RBC-lysis of whole blood from a single donor. Labels s1 to s12 indicate the order of the sample analysis. Distributions show the sum of all measured cells for the three repeats. Black horizontal lines show the median and red lines show the 5th and 95th percentiles. (**b**) Scatter plots of the measured effective acoustic impedance vs fluorescence intensity of pre-enriched monocytes, lymphocytes and neutrophils from a second donor, and the distributions of (**c**) the effective acoustic impedance and (**d**) fluorescence intensity. (**e**) Size distributions of monocytes, lymphocytes and neutrophils as measured independently based on electrical resistance sizing (Coulter-counter).

abundant of the white blood cells (~60%), Fig. 5a. We find that this peak is shifted towards lower effective acoustic impedance compared to the peak (gray) of the neutrophils purified directly from whole blood. It is reasonable to assume that this shift is due to altered physical properties of the white blood cells when exposed to the RBC-lysis and subsequent centrifugation steps.

Discussion

We have presented and provided experimental and theoretical validations of the iso-acoustic focusing (IAF) equilibrium method for measuring the effective acoustic impedance of individual cells in continuous flow. IAF was applied to measure the effective acoustic impedance of monocytes, lymphocytes, neutrophils, BA-F3 and MCF7 cells. The IAPs of thousands of individual suspension cells were measured in just a few minutes and we could load and run up to 12 sequential samples within 3 hours, which make this a suitable method for high throughput intrinsic phenotyping of cells.

While cell size is an important parameter for categorizing and separating cells, it displays large variations across cell types. We have demonstrated in several experiments that IAF is size insensitive. For instance, the populations of monocytes and neutrophils differ markedly in acoustic impedance (Fig. 5a) despite almost completely overlapping size distributions (Fig. 5e).

We find it relevant to further investigate cell IAP as a potential biomarker since it was found to be cell-type specific with measured effective acoustic impedances ranging from 1.55 MPa s m^{-1} to 1.75 MPa s m^{-1} (Fig. 4h and Fig. 5a). Although organs and tissue typically consist of multiple cell types which can in turn have fundamentally different internal structure than the cells under investigation here we find it interesting to note the close correspondence to literature values for measured acoustic impedances of various tissues (fat 1.38 MPa s m^{-1}, brain 1.60 MPa s m^{-1}, heart 1.45 MPa s m^{-1}, kidney 1.65 MPa s m^{-1}, blood 1.66 MPa s m^{-1}, liver 1.69 MPa s m^{-1}, skin 1.99 MPa s m^{-1})[44] with fat, heart and skin being outside our established range. Further, the measurements on white blood cells (Fig. 5a) and the MCF7 cancer cells (Fig. 4h) indicate that these cancer cell line cells can be separated from blood cells with high purity based on their lower IAP. While no clinical samples has been analyzed in this study, this suggests that IAF can potentially be employed to isolate circulating tumor cells from cancer patient blood.

The acoustic properties of suspended MCF7 cells have previously been measured, by tracking individual cells in an acoustic field in stopped-flow homogeneous media[33], to have an effective acoustic impedance of 1.59 MPa s m^{-1}, and for adherent cells using acoustic microscopy[15], to 1.56 MPa s m^{-1}, both of which are in the lower range of the IAP_{MCF7} (1σ and 2σ below the mean, respectively) shown in Fig. 4h. Previously acoustic levitation against gravity has enabled measurement of the acoustic impedance of RBCs (1.81 MPa s m^{-1})[30], just above the IAP of neutrophils (Fig. 5a) which is not surprising given the slightly higher density of RBCs compared to neutrophils.

Cell deformability has been extensively studied for suspension cells as well as adherent cells and is informative about interior structure[3]. In contrast, IAF relates to the whole–cell, or effective, compressibility and density, and we believe it renders complementary acousto-mechanical information. As we have seen the effective impedance of neutrophils was dependent on exposure to lysis buffer and we can therefore speculate that IAF can be useful for assessing cell state and disease progress. Microfluidic single cell density measurements have been previously demonstrated to enable sensitive monitoring of yeast growth cycle[45] and altered cell state resulting from environmental perturbations[5]. We envision that IAF can be informative in a similar way but benefit from higher throughput and flexibility in terms of sample preparation and integration with complementary microfluidic operations. IAF could for instance be combined with label-free or label-based optical analysis enabling an iso-acoustic

tunable band-pass gate within which we interrogate cells of interest.

The results show that, in IAF, stratified liquids and suspended cells arrange themselves in a way that can be predicted from their effective acoustic impedances. This rearrangement and process is analogous to another well-established equilibrium method, density gradient centrifugation, but IAF has the benefit of being straightforwardly implemented in microfluidic systems. The precise spatiotemporal control offered by microfluidics[46,47] leads us to envision that the IAF method can be developed into a tunable cell profiling method as well as a new tool for size-insensitive label-free cell separation.

Methods

Device fabrication. The IAF chip was fabricated by UV-lithography and anisotropic KOH wet etching a channel structure in <100> silicon rendering a rectangular cross-section acoustic resonator channel (25 mm long, 375 μm wide, 150 μm deep), Supplementary Fig. 7a. The channel has a trifurcation inlet where cell-free media can be introduced through a central branch and cell suspension can be introduced via a common side inlet port that bifurcates to either side of the central branch. Fluid access holes were etched from the back side of the chip. Borosilica glass was anodically bonded to the silicon to seal the channel structure[48].

Acoustic actuation. A piezo-ceramic actuator was bonded to the back of the chip (Supplementary Fig. 7b) and connected to a function generator. In the blood cell experiments, to further increase the ultrasound intensity, a radio frequency amplifier (TVA-R5-13, Mini-Circuits, Brooklyn NY, USA) was connected in series with the output of the function generator. The resulting transducer amplitude peak to peak was measured with an oscilloscope to be 6.0 V (leading to an acoustic field amplitude in the channel of $E_{ac} = 43\,\mathrm{J\,m^{-3}}$, $p_a = 0.66$ MPa) in the blood cell measurements and 3.5 V (leading to an acoustic field amplitude in the channel of $E_{ac} = 15\,\mathrm{J\,m^{-3}}$, $p_a = 0.39$ MPa) in the cell line experiments. The function generator was set to make repeated linear sweeps in frequency from 1.900 MHz to 2.100 MHz over periods of 1 ms. This leads to stable operation and a more even acoustic field along the length of the device[49].

Flow setup. Liquid to the central inlet was pumped from a glass syringe mounted in a syringe pump and cell suspension was pushed into the side inlet port from the bottom of a pressurized test tube (10 psi). The outlet flow from the acoustic channel was controlled by a syringe pump (Fig. 4a). In all cell measurements a 1:1 flow ratio was maintained between the central and side inlet flow streams.

Medium to alter acoustic impedance. A stock solution of 20% iodixanol was prepared from 1 ml OptiPrep (contains 60% iodixanol) by addition of 2 × 1 ml of DPBS supplemented with 2 % fetal bovine serum (FBS) by reversed pipetting.

A stock solution containing 36 % iodixanol was prepared in the same manner by adding 3 × 1 ml OptiPrep and 2 × 1 ml DPBS with 2 % FBS, using reversed pipetting. 3 μg ml^{-1} fluorescent tracer molecules, Dextran Cascade Blue 3000 Da, was added.

Cell culture. The cells were cultured using standard protocols at 37 °C in a humidified atmosphere with 5% CO_2. All media were supplemented with 10% fetal bovine serum (FBS) and Penicillin 100 U ml^{-1}, Streptomycin 100 μg ml^{-1}.

BA-F3 murine pro B cells (Deutsche Sammlung von Mikroorganismen und Zellkulturen) were grown in a cell culture flask in RPMI 1640 media supplemented with Interleukin-3 (1 ng ml^{-1}) and L-glutamine (2 mM).

MCF7 human breast cancer cells (American Type Culture Collection) were grown in a cell culture dish in low glucose DMEM (Life Technologies). Cells were detached by trypsin/EDTA treatment and subsequent resuspension in DPBS supplemented with 2 mM ethylenediaminetetraacetic acid (EDTA).

Blood cell sample preparation. Blood was obtained from healthy volunteers with informed consent and was kept at room temperature in test tubes containing (EDTA) as anticoagulant. Sample preparation was initiated within 2 hours from blood draw.

Monocytes from 2 ml whole blood were isolated by immunomagnetic negative selection using the Direct Human Monocyte Isolation Kit (EasySep, Stemcell technolgies) according to the manufacturer instructions. Similarly, lymphocytes and neutrophils were isolated from aliquots of 1 ml whole blood using the Direct Human Total Lymphocyte Isolation Kit and the Direct Human Neutrophil Isolation Kit, respectively.

Leukocytes were prepared from 500 μl whole blood by standard isotonic lysing of RBCs based on ammonium chloride according to the manufacturer instructions. To remove platelets, cells were resuspended two times in DPBS supplemented with 2 mM containing EDTA.

Size distributions of cells from each fraction was measured based on electrical impedance measurements (Multisizer II, Beckman Coulter), Fig. 5e. Cells from each fraction were stained for CD45, CD66B, CD14 and CD3 and analyzed in a flow cytometer (Accuri C6, BD Biosciences) to assert purities: monocytes with 89.9 % purity, granulocytes with 94.1 % purity, and lymphocytes with 82.8 % purity (Supplementary Fig. 8).

Cells were resuspended in 1 ml DPBS supplemented with 2 mM containing EDTA and incubated for 20 min with Calecein AM orange red (2 μg ml^{-1}). Cells were then resuspended two times in 1 ml DPBS supplemented with 2 mM EDTA and 2 % Fetal Bovine Serum and kept on ice until the introduction into the acoustic chip.

Measuring the acoustic field. To measure the shape of the local acoustic field along a 1 mm segment of the IAF channel, fluorescent polystyrene microbeads (radius 2.23 μm) were investigated using micro particle image velocimetry (PIV). Particles were suspended in 10 % iodixanol (homogeneous) and injected in the IAF channel and the flow was stopped before turning on the acoustic field for a transducer voltage of 3.5 V. Image sequences were acquired at 4 Hz capturing the motion of the microbeads in the acoustic field and commercial PIV software (Dynamic studio, Dantec Dynamics, Denmark) was used to extract velocity information from the images (Supplementary Fig. 1a) using the method of adaptive correlation. The y-components (transverse to the channel) of the velocity vectors from 5 consecutive frames for three repeated acoustic actuation experiments are plotted in Supplementary Fig. 1b. Data was fitted (black dashed line) to the expression $u_{rad} = u_0 + \partial_t y$ following Eq. (12) in Supplementary Note 3, using u_0, E_{ac} and k_y as fitting parameters for a spherical polystyrene particle of radius 2.23 μm, density 1050 kg m^{-3} and compressibility 1.65×10^{-10} Pa^{-1}. Medium properties for 10% iodixanol (Supplementary Fig. 2) were used to calculate that the acoustic contrast factor $\Phi = 0.199$. The fit resulted in $u_0 = -3.557 \times 10^{-7}$ m s^{-1} (CI$_{95}$: -8.014×10^{-7}, 9.004×10^{-8}), $E_{ac} = 16.27\,\mathrm{J\,m^{-3}}$ (CI$_{95}$: 16.16, 16.39), and $k_y = 8315\,\mathrm{m^{-1}}$ (CI$_{95}$: 8293, 8336). The fitted acoustic wave vector k_y corresponds to a sound wavelength $\lambda = 2\pi/k_y = 756$ μm which is indicative of a half wavelength resonance in the 375 μm wide IAF channel. The fitted local acoustic energy density at 3.5 V actuation corresponds to a local pressure amplitude within the field of view of $p_a = 0.39$ MPa.

To estimate the acoustic pressure amplitude and the average acoustic energy density along the whole length of the acoustic resonator channel, as a function of the transducer voltage amplitude, microbeads suspended in 10% iodixanol were injected through a single inlet at constant flow rate. The final position of the microbeads as they arrive at the end of the channel depends on the acoustic energy density, the size and acoustic properties of the particle, and the viscosity, the flow profile and the acoustic properties of the liquid[39]. The trajectories of polystyrene microparticles in acoustic fields are well characterized in earlier work[35,36], and by comparing simulation to experiment we could estimate the average acoustic energy density. The beads were imaged 20 mm downstream from the inlet with the microscope focus set at the mid height of the channel. From a sequence of such images, we estimated how far into the channel the outermost beads had moved when entering the interrogation region, Supplementary Fig. 5a-e. Then we ran the script iteratively and updated the acoustic energies for each voltage setting until the simulations for each case matched the experimental observations, Supplementary Fig. 5f. Thereafter we made a fit for $E_{ac} = \frac{1}{4}\kappa_m p_a^2 = kU^2$, Supplementary Fig. 5g, and concluded that $k = 1.2\,\mathrm{J\,m^{-3}\,V^{-2}}$ and that $E_{ac}^{3.5V} = 15\,\mathrm{J\,m^{-3}}$ for a transducer voltage amplitude of 3.5 V.

Stop-flow cell trajectory classification. Images of 30 consecutive frames were analyzed, tracking the cell positions using the video analysis tool Tracker (http://physlets.org/tracker/). Supplementary Figure 3a-c show the cell images from all the frames in the repeated experiments projected onto a single image for three different concentrations of iodixanol. Only tracks of 20 frames or longer were analyzed.

First a cell was classified to have *zero* acoustic contrast if it displayed a track that is indicative of following the acoustic streaming of the bulk liquid rather than migrating to either the channel center or towards the side walls. This means the velocity changes sign or the cell flow past the channel center but do not stop there. Specifically, the starting position is away from the channel center and the channel walls and one of the following is true: The velocity changes sign and the ratio of minimal to maximal velocity is greater than 20%, or the cell crosses over the central region but does not stop within the central region.

Second, a cell of *positive* acoustic contrast was any cell that had not been classified as having *zero* acoustic contrast, and that starts out away from the channel center but ends up within the central region.

Third, a cell of *negative* acoustic contrast was any cell that had not been classified as having *zero* acoustic contrast, and that starts out away from the channel walls but ends up near either wall.

Cells that were not classified as any of the above were classified as *unknown*.

Method to measure cell IAP. Prior to each IAP measurement 100 μl of cell suspension was mixed with 100 μl of 20% iodixanol stock solution to a final concentration of 10% iodixanol in a test tube that was connected to the side inlet of

the acoustic microchannel. High acoustic impedance medium containing 36% iodixanol and fluorescent dextran tracer was loaded in a syringe connected to the central inlet, Fig. 4a.

The channel was imaged 20 mm downstream from the inlet alternating between two filter sets (Excitation/Emission: Violet/Blue and Green/Red, respectively) in a fluorescence microscope with the focus set to the channel mid height, Fig. 4a-b. First an image of the dextran dye concentration profile (blue) was acquired after which the filter set was changed and a sequence of 10 cell images (red) was recorded with <5 millisecond exposure time, each image containing up to 10 cells. The filter was then switched back to record a second gradient image to observe potential temporal fluctuations in the gradient. The process of recording gradient and cell images was then repeated 10 to 20 times capturing images of >1000 individual cells at a rate of 1–10 cells per second. The capture rate of the camera was set to 1 Hz to ensure that a cell was only measured once given the flow rate during the measurement.

To read out the acoustic impedance of a cell it was first located in the cell image, Fig. 4c and thereafter the dextran dye intensity was read off the gradient images at the corresponding position, Fig. 4d. The gradient images (I) were background-subtracted using images of a channel filled with side-inlet-medium (10% iodixanol and no fluorescent tracer) and then normalized with respect to background-subtracted reference images (I_{max}) of a channel completely filled with central inlet medium (36% iodixanol and 3 $\mu g\,ml^{-1}$ fluorescent dextran) such that the ratio (I/I_{max}) is a number from 0 to 1. The dextran dye intensity was taken to be linear with the iodixanol concentration (Supplementary Fig. 9) for which the acoustofluidic properties are known (Supplementary Fig. 2) and could be calculated through a 2nd degree polynomial (Fig. 4d). After determining the acoustic impedance of the liquid at the cell's iso-acoustic point we assigned that value to the effective acoustic impedance of the cell (Supplementary Note 1, Eq. 5).

Code availability. The custom computer code that support the findings of this study are available from the corresponding author upon request.

Data availability. The data that support the findings of this study are available from the corresponding author upon request.

References

1. Otto, O. *et al.* Real-time deformability cytometry: on-the-fly cell mechanical phenotyping. *Nat. Methods* **12,** 199–202 (2015).
2. Ozkumur, E. *et al.* Inertial focusing for tumor antigen-dependent and -independent sorting of rare circulating tumor cells. *Sci. Transl. Med.* **5,** 179ra147 (2013).
3. Darling, E. M. & Di Carlo, D. High-throughput assessment of cellular mechanical properties. *Annu. Rev. Biomed. Eng.* **17,** 35–62 (2015).
4. Davis, J. A. *et al.* Deterministic hydrodynamics: taking blood apart. *Proc. Natl Acad. Sci. USA* **103,** 14779–14784 (2006).
5. Grover, W. H. *et al.* Measuring single-cell density. *Proc. Natl Acad. Sci. USA* **108,** 10992–10996 (2011).
6. Beech, J. P., Holm, S. H., Adolfsson, K. & Tegenfeldt, J. O. Sorting cells by size, shape and deformability. *Lab Chip* **12,** 1048–1051 (2012).
7. Tse, H. T. *et al.* Quantitative diagnosis of malignant pleural effusions by single-cell mechanophenotyping. *Sci. Transl. Med.* **5,** 212ra163 (2013).
8. Vahey, M. D. & Voldman, J. An equilibrium method for continuous-flow cell sorting using dielectrophoresis. *Anal. Chem.* **80,** 3135–3143 (2008).
9. Holmes, D. *et al.* Leukocyte analysis and differentiation using high speed microfluidic single cell impedance cytometry. *Lab Chip* **9,** 2881–2889 (2009).
10. Vercruysse, D. *et al.* Three-part differential of unlabeled leukocytes with a compact lens-free imaging flow cytometer. *Lab Chip* **15,** 1123–1132 (2015).
11. Greenleaf, J. F., Fatemi, M. & Insana, M. Selected methods for imaging elastic properties of biological tissues. *Annu. Rev. Biomed. Eng.* **5,** 57–78 (2003).
12. Nightingale, K. Acoustic radiation force impulse (ARFI) imaging: a review. *Curr. Med. Imaging Rev.* **7,** 328–339 (2011).
13. Hildebrand, J. A., Rugar, D., Johnston, R. N. & Quate, C. F. Acoustic microscopy of living cells. *Proc. Natl Acad. Sci. Biol. USA* **78,** 1656–1660 (1981).
14. Kundu, T., Bereiter-Hahn, J. & Karl, I. Cell property determination from the acoustic microscope generated voltage versus frequency curves. *Biophys. J.* **78,** 2270–2279 (2000).
15. Strohm, E. M., Czarnota, G. J. & Kolios, M. C. Quantitative measurements of apoptotic cell properties using acoustic microscopy. *IEEE Trans Ultrason Ferroelectr. Freq. Control* **57,** 2293–2304 (2010).
16. Weiss, E., Anastasiadis, P., Pilarczyk, G., Lemor, R. & Zinin, P. Mechanical properties of single cells by high-frequency time-resolved acoustic microscopy. *IEEE Trans. Ultrason. Ferroelectr. Freq. Control* **54,** 2257–2271 (2007).
17. Challis, R. E., Povey, M. J. W., Mather, M. L. & Holmes, A. K. Ultrasound techniques for characterizing colloidal dispersions. *Rep. Prog. Phys.* **68,** 1541–1637 (2005).
18. Bruus, H. *et al.* Forthcoming Lab on a Chip tutorial series on acoustofluidics: acoustofluidics-exploiting ultrasonic standing wave forces and acoustic streaming in microfluidic systems for cell and particle manipulation. *Lab Chip* **11,** 3579–3580 (2011).
19. Burguillos, M. A. *et al.* Microchannel acoustophoresis does not impact survival or function of microglia, leukocytes or tumor cells. *PLoS One* **8** (2013).
20. Wiklund, M. Acoustofluidics 12: biocompatibility and cell viability in microfluidic acoustic resonators. *Lab Chip* **12,** 2018–2028 (2012).
21. Nordin, M. & Laurell, T. Two-hundredfold volume concentration of dilute cell and particle suspensions using chip integrated multistage acoustophoresis. *Lab Chip* **12,** 4610–4616 (2012).
22. Carugo, D. *et al.* A thin-reflector microfluidic resonator for continuous-flow concentration of microorganisms: a new approach to water quality analysis using acoustofluidics. *Lab Chip* **14,** 3830–3842 (2014).
23. Evander, M. & Nilsson, J. Acoustofluidics 20: applications in acoustic trapping. *Lab Chip* **12,** 4667–4676 (2012).
24. Collins, D. J. *et al.* Two-dimensional single-cell patterning with one cell per well driven by surface acoustic waves. *Nat. Commun.* **6,** 8686 (2015).
25. Augustsson, P. & Laurell, T. Acoustofluidics 11: affinity specific extraction and sample decomplexing using continuous flow acoustophoresis. *Lab Chip* **12,** 1742–1752 (2012).
26. Manneberg, O., Svennebring, J., Hertz, H. M. & Wiklund, M. Wedge transducer design for two-dimensional ultrasonic manipulation in a microfluidic chip. *J. Micromech. Microeng.* **18** (2008).
27. Augustsson, P., Magnusson, C., Nordin, M., Lilja, H. & Laurell, T. Microfluidic, label-free enrichment of prostate cancer cells in blood based on acoustophoresis. *Anal. Chem.* **84,** 7954–7962 (2012).
28. Ding, X. *et al.* Cell separation using tilted-angle standing surface acoustic waves. *Proc. Natl Acad. Sci. USA* **111,** 12992–12997 (2014).
29. Petersson, F., Åberg, L., Swärd-Nilsson, A. M. & Laurell, T. Free flow acoustophoresis: microfluidic-based mode of particle and cell separation. *Anal. Chem.* **79,** 5117–5123 (2007).
30. Weiser, M. A. H. & Apfel, R. E. Extension of acoustic levitation to include the study of micron-size particles in a more compressible host liquid. *J. Acoust. Soc. Am.* **71,** 1261–1268 (1982).
31. Dykes, J., Lenshof, A., Åstrand-Grundström, I. B., Laurell, T. & Scheding, S. Efficient removal of platelets from peripheral blood progenitor cell products using a novel micro-chip based acoustophoretic platform. *PLos One* **6,** e23074 (2011).
32. Shields, C.W., Johnson, L. M., Gao, L. & Lopez, G. P. Elastomeric negative acoustic contrast particles for capture, acoustophoretic transport, and confinement of cells in microfluidic systems. *Langmuir* **30,** 3923–3927 (2014).
33. Hartono, D. *et al.* On-chip measurements of cell compressibility via acoustic radiation. *Lab Chip* **11,** 4072–4080 (2011).
34. Deshmukh, S., Brzozka, Z., Laurell, T. & Augustsson, P. Acoustic radiation forces at liquid interfaces impact the performance of acoustophoresis. *Lab Chip* **14,** 3394–3400 (2014).
35. Augustsson, P., Barnkob, R., Wereley, S. T., Bruus, H. & Laurell, T. Automated and temperature-controlled micro-PIV measurements enabling long-term-stable microchannel acoustophoresis characterization. *Lab Chip* **11,** 4152–4164 (2011).
36. Barnkob, R., Augustsson, P., Laurell, T. & Bruus, H. Measuring the local pressure amplitude in microchannel acoustophoresis. *Lab Chip* **10,** 563–570 (2010).
37. Yosioka, K. & Kawasima, Y. Acoustic radiation pressure on a compressible sphere. *Acustica* **5,** 167–173 (1955).
38. Petersson, F., Nilsson, A., Holm, C., Jönsson, H. & Laurell, T. Separation of lipids from blood utilizing ultrasonic standing waves in microfluidic channels. *Analyst* **129,** 938–943 (2004).
39. Barnkob, R., Augustsson, P., Laurell, T. & Bruus, H. Acoustic radiation- and streaming-induced microparticle velocities determined by microparticle image velocimetry in an ultrasound symmetry plane. *Phys. Rev. E* **86** (2012).
40. Muller, P. B. *et al.* Ultrasound-induced acoustophoretic motion of microparticles in three dimensions. *Phys. Rev. E* **88** (2013).
41. Rayleigh, L On the circulation of air observed in Kundt's tubes, and on some allied acoustical problems. *Philos. Trans. R. Soc. Lond.* **175,** 1–21 (1884).
42. Thorne, R. G. & Nicholson, C. In vivo diffusion analysis with quantum dots and dextrans predicts the width of brain extracellular space. *Proc. Natl Acad. Sci. USA* **103,** 5567–5572 (2006).
43. Nair, N., Kim, W. J., Braatz, R. D. & Strano, M. S. Dynamics of surfactant-suspended single-walled carbon nanotubes in a centrifugal field. *Langmuir* **24,** 1790–1795 (2008).
44. Azhari, H. *Basics of biomedical ultrasound for engineers* (Wiley: IEEE, 2010).
45. Bryan, A. K., Goranov, A., Amon, A. & Manalis, S. R. Measurement of mass, density, and volume during the cell cycle of yeast. *Proc. Natl Acad. Sci. USA* **107,** 999–1004 (2010).
46. Squires, T. M. & Quake, S. R. Microfluidics: fluid physics at the nanoliter scale. *Rev. Mod. Phys.* **77,** 977–1026 (2005).
47. Toner, M. & Irimia, D. Blood-on-a-chip. *Annu. Rev. Biomed. Eng.* **7,** 77–103 (2005).
48. Nilsson, A., Petersson, F., Jönsson, H. & Laurell, T. Acoustic control of suspended particles in micro fluidic chips. *Lab Chip* **4,** 131–135 (2004).

49. Manneberg, O., Vanherberghen, B., Önfelt, B. & Wiklund, M. Flow-free transport of cells in microchannels by frequency-modulated ultrasound. *Lab Chip* **9,** 833–837 (2009).

Acknowledgements

The authors are grateful for assistance with experiments by Mads Givskov Senstius (Technical University of Denmark), Louise Gren (Lund University) and Filip Sköld (Lund University), for valuable comments from Peter Muller (Technical University of Denmark) and Pelle Ohlsson (Lund University, Sweden), for chip fabrication by Andreas Lenshof (Lund Univesity, Sweden) and for accessing measurement apparatus from Thomas Laurell (Lund University, Sweden). The study was carried out with financial support from the Swedish Research Council (grant no. 2012-6708), the Royal Physiographic Society, Lund, Sweden and the Birgit and Hellmuth Hertz' Foundation, Lund, Sweden.

Author contribution

P.A. H.-W.S. and J.V. did the experimental design. P.A. and H.-W.S. performed and analyzed the experiments. P.A., J.T.K. and H.B. made the physical interpretations. J.T.K. and H.B. derived the physical scaling arguments. P.A. and J.T.K. performed numerical modelling. P.A. prepared the manuscript. J.V. and H.B. supervised the project. P.A., J.T.K., H.B. and J.V. edited the manuscript.

Additional information

Supplementary Information accompanies this paper at http://www.nature.com/naturecommunications

Competing financial interests: Although not closely related to the herein presented results P.A. declares part-time activity as a consultant in acoustofluidic research and development.

Reprints and permission information is available online at http://npg.nature.com/reprintsandpermissions/

How to cite this article: Augustsson, P. *et al.* Iso-acoustic focusing of cells for size-insensitive acousto-mechanical phenotyping. *Nat. Commun.* 7:11556 doi: 10.1038/ncomms11556 (2016).

Supplementary Figure 1: Mapping the local acoustic field

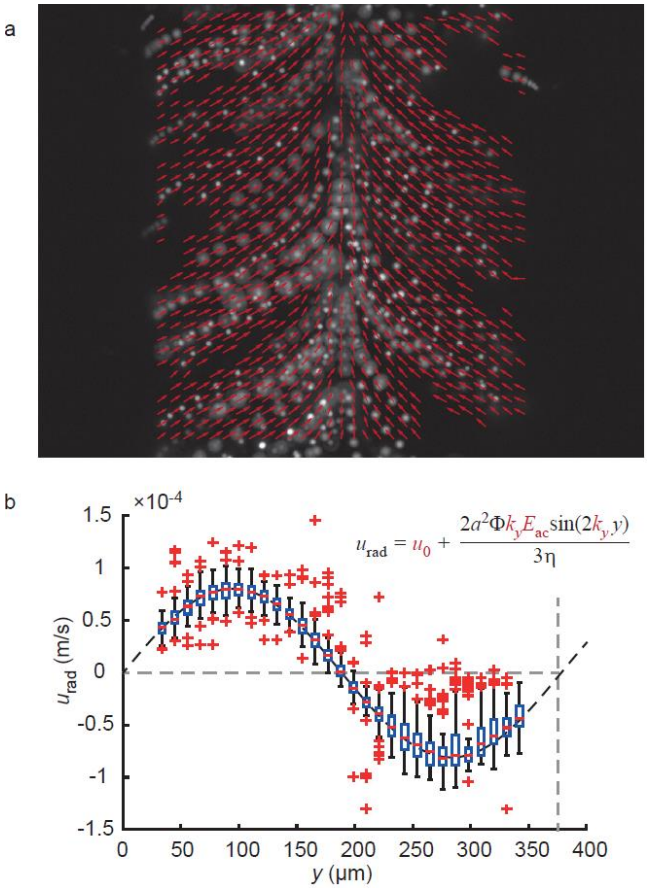

(**a**) Overlay of six consecutive frames of an image sequence of fluorescent microparticles (gray) submerged in 10 % iodixanol acquired immediately after turning on the acoustic actuation. Red arrows show velocity vectors from particle imaging velocimetry analysis of repeated onsets of sound. (**b**) Box plots of the *y*-components (u_{rad}), of the measured velocities vs position. For each box, the central mark (red) is the median, the edges of the box (blue) are the 25th and 75th percentiles, the whiskers extend to the most extreme data points not considered outliers, and outliers (red plus-sign) are defined as larger than $q_3 + 1.5(q_3 - q_1)$ or smaller than $q_1 - 1.5(q_3 - q_1)$, where q_1 and q_3 are the 25th and 75th percentiles, respectively. Data was fitted to a one-dimensional model $\underline{u}_{rad}$ of the acoustic field (black dashed line) with fitting parameters highlighted in red.

Supplementary Figure 2: **Acoustofluidic properties of iodixanol *versus* concentration**

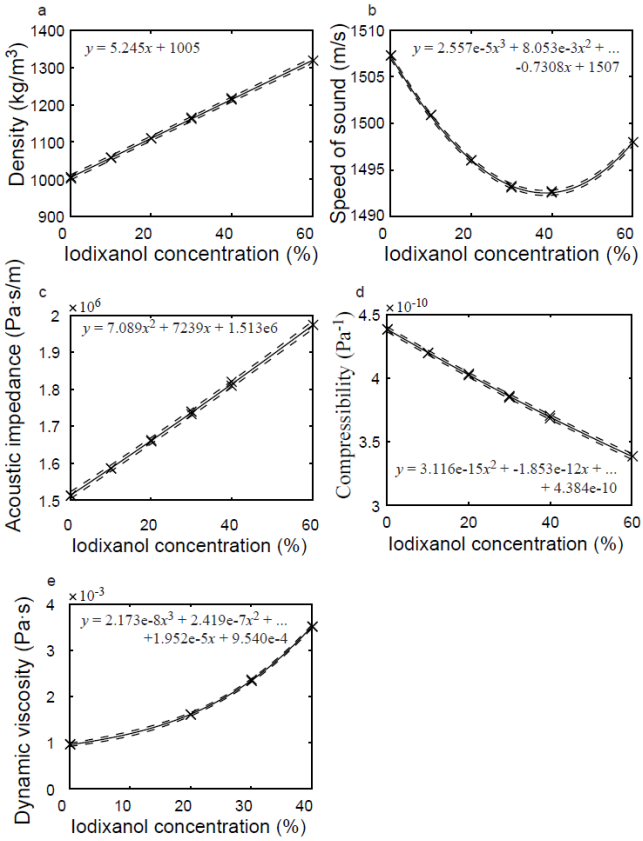

(**a**) Density ρ and (**b**) speed of sound c_s were measured simultaneously using a density and sound-velocity meter based on oscillating U-tube and ultrasound pulse echo respectively. (**c**) Compressibility ($\kappa = 1/\rho c_s^2$) and (**d**) acoustic impedance ($Z = \rho c_s = \sqrt{\rho/\kappa}$) were derived from the individual measurements of ρ and c_s. (**e**) Viscosity η was measured using a falling-ball viscometer. (**a-e**) Data was fitted to polynomials (solid lines). Dashed lines show the upper and lower 99% prediction bounds.

Supplementary Figure 3: Stop flow cell trajectories

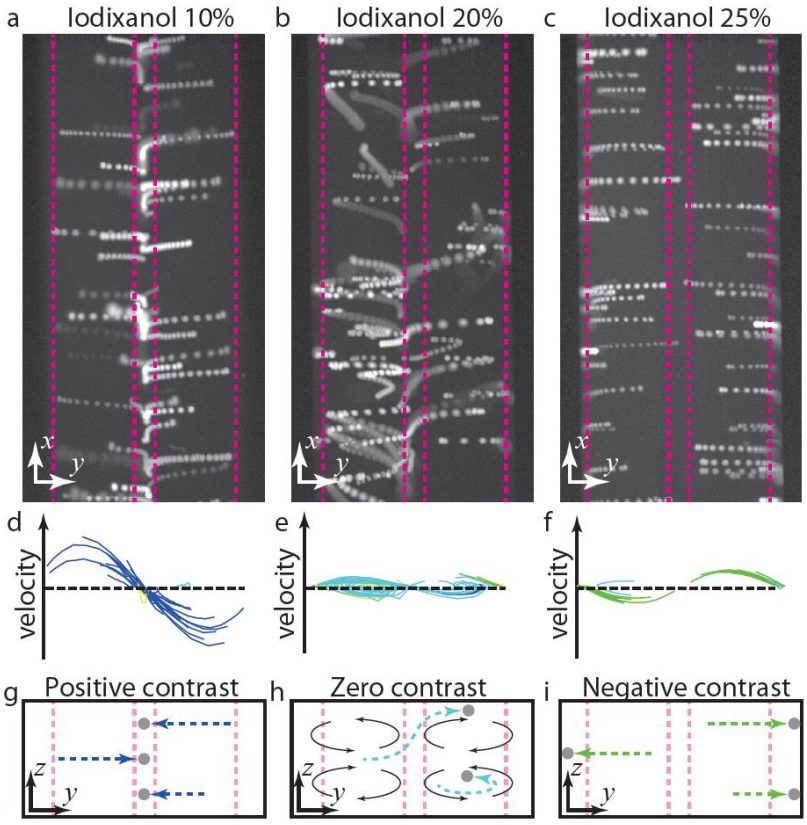

(**a-c**) Projection of cell images from 30 sequential frames for BA-F3 cells suspended in (**a**) 10 %, (**b**) 20 % and (**c**) 25 % iodixanol. Magenta dashed lines indicate the limits for the central region and the near-wall regions. (**d-f**) The corresponding cell velocities vs *y*-position corresponding to the tracks of cells in (**a-c**). Tracks are color coded based on the classification such that (**g**) blue indicate positive acoustic contrast, (**h**) cyan indicate zero acoustic contrast and (**i**) green indicate negative acoustic contrast. Yellow indicate unknown cells.

Supplementary Figure 4: Measured fluorescence intensity profiles for dextran dye.

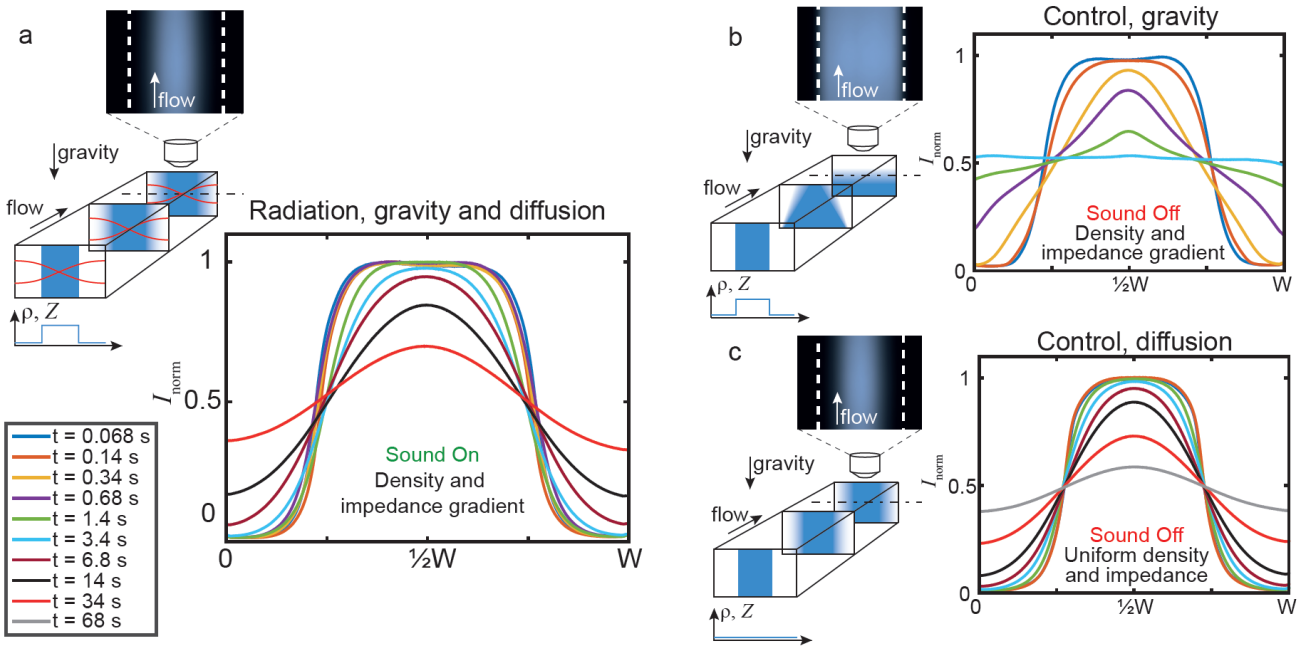

Fluorescence profiles imaged 20 mm downstream the trifurcation inlet for different retention times t obtained from Eq. (11) by varying the overall flow rate Q. (**a**) A density and acoustic impedance gradient is setup by an initial central and side inlet iodixanol concentration of 30% and 10%, respectively. The gradient is stabilized by the ultrasound, which counteracts both gravitational relocation and acoustic streaming in the bulk, such that the profile evolution is governed by diffusion. (**b**) Control experiment for gravitational relocation with the sound turned off. The profiles indicate that the central liquid reaches a stable position at the bottom of the channel within a few seconds. (**c**) Control experiment for diffusion only. The ultrasound is turned off and the iodixanol concentration was 20% in both center and side inlets so there is no density and acoustic impedance gradient present in the channel.

Supplementary Figure 5: Estimating the average acoustic energy density

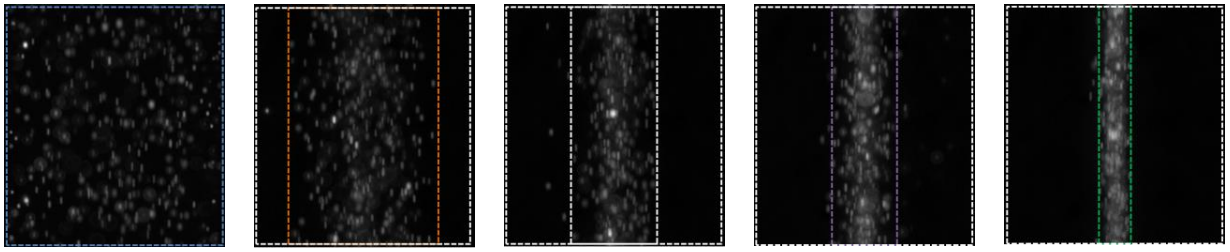

a 0 V b 1.4 V c 1.8 V d 2.1 V e 2.5 V

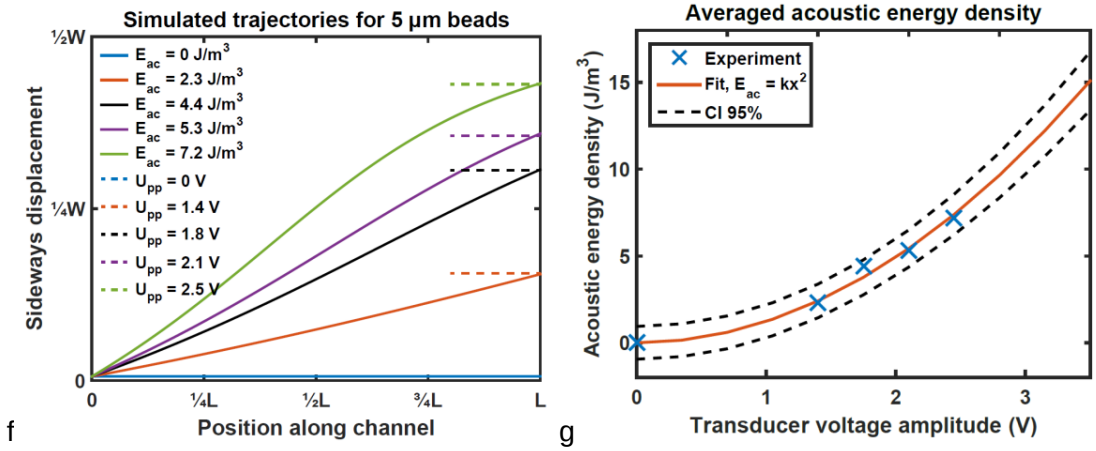

f g

(**a-e**) Beads focusing in flow for increasing piezo actuator voltage amplitude. Regions (colored dashed lines) are chosen manually to encompass all beads except for some outliers. (**f**) Simulated trajectories of 5-µm-beads in a rectangular microchannel. Beads start near a wall and migrate towards $y = W/2$. Dashed lines show the position of the outermost observed beads from (**a-e**) at the end of the channel. Values for E_{ac} were adjusted iteratively in the simulation to match the observations. (**g**) Fit of E_{ac} versus U assuming a power 2 dependence.

Supplementary Figure 6: Time-dependent simulations of IAF cell trajectories in a diffusing iodixanol gradient

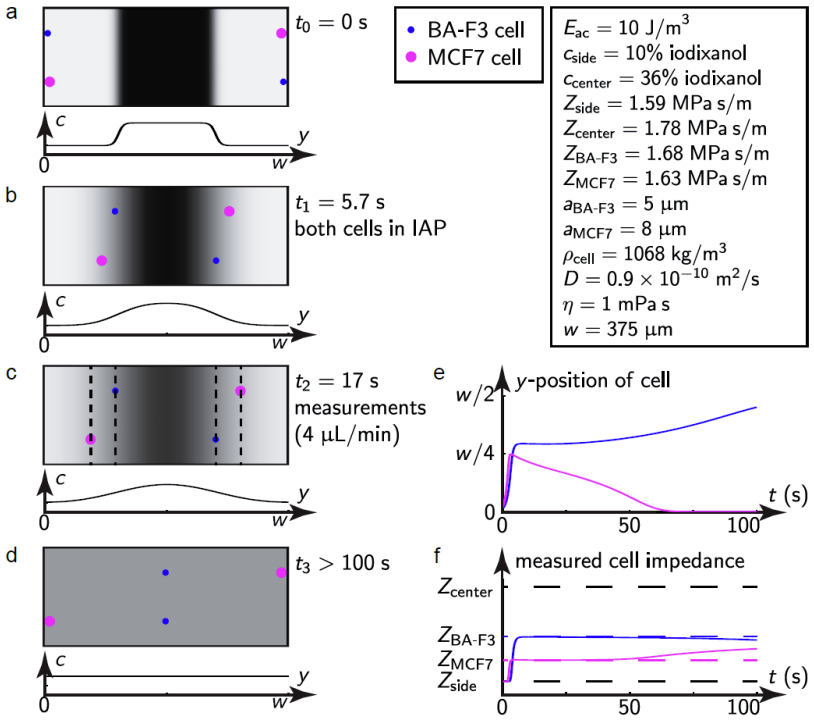

(**a**) Cells are introduced at time t_0 near the side walls at the inlet cross-section. (**b**) After initial migration caused by the acoustic force, the cells have reached their respective IAP at time t_1. (**c**) In the experiment, images are recorded at time t_2 with cells residing in their respective IAP. The cells stay in their diffusing IAP until diffusion has flattened the gradient. (**d**) At times longer than the diffusion time t_3, the gradient has vanished leaving the cells either at the center (postive contrast Φ) or at the walls (negative contrast Φ). (**e**) The transverse cell positions as function of time. (**f**) The measured cell impedances assuming $Z_{\mathrm{cell}} = Z_{\mathrm{med}}$ as a function of time. Accurate measurements with a relative error less than 0.3% are obtained at times t between 5.7 s and 51 s.

Supplementary Figure 7: Photo of the microfluidic chip and holder

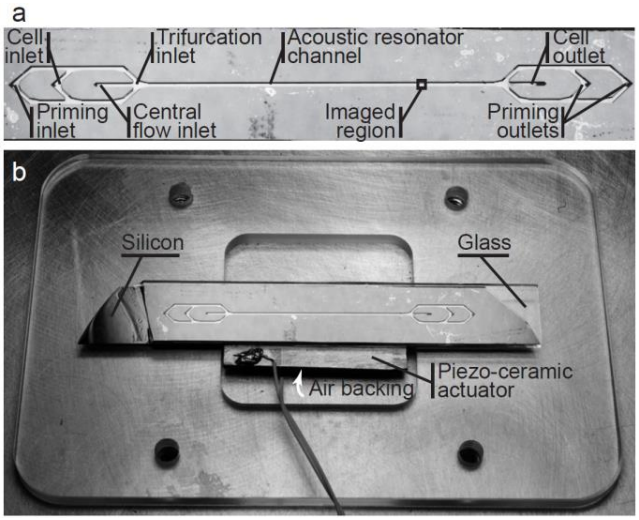

(**a**) Photo of the chip. (**b**) Photo of the chip in its holder with the piezoceramic actuator glued underneath.

Supplementary Figure 8: Flow cytometry of lymphocyte, granulocyte and monocyte preparations

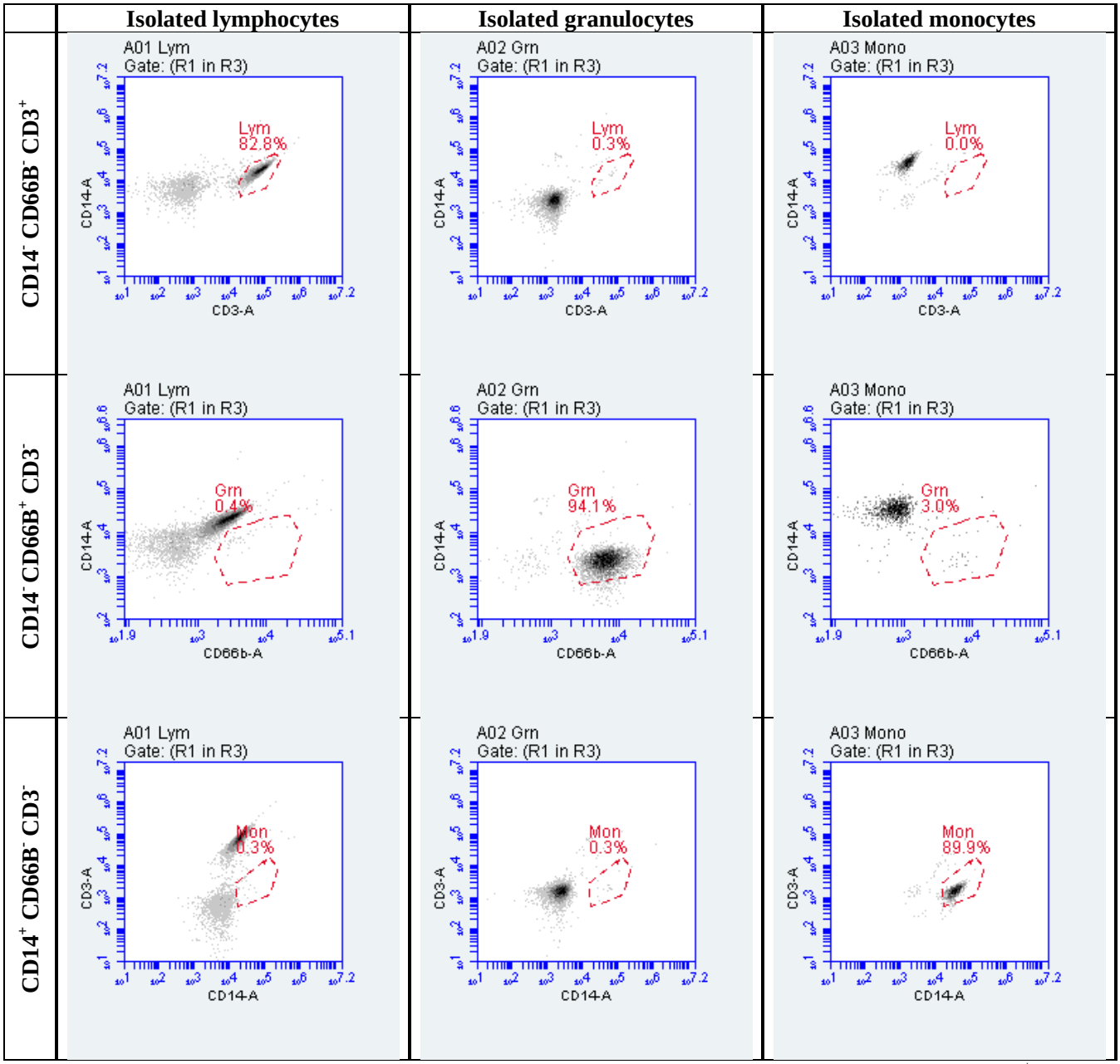

The purities of lymphocytes, granulocytes and monocytes are 82.8 %, 94.1%, and 89.9 % (gated on $CD45^+$), respectively. The purity of lymphocytes was underestimated given there were $CD3^-$ lymphocytes in the sample. According to the manufacturer manual (EasySep™ Direct Human Total Lymphocyte Isolation Kit, Stemcell Technologies), the percentage of CD3- lymphocyte can be around 9%.

Supplementary Figure 9: Standard curve for Dextran Cascade Blue fluorescence intensity in iodixanol

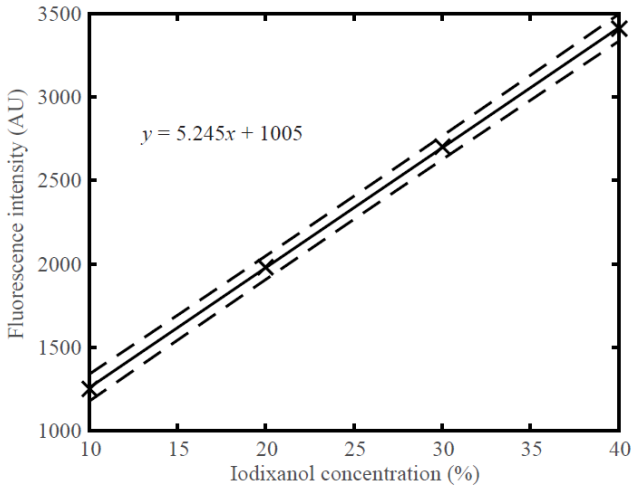

Fluorescence intensity of Dextran Cascade Blue as a function of iodixanol concentration. Solid line show linear fit and dashed lines show 99% prediction bounds.

Supplementary Figure 10: Relative impedance difference between the medium and the cell at the true IAP

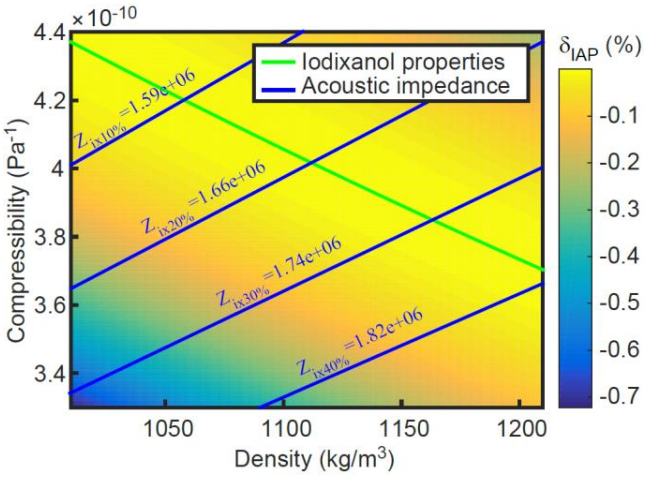

Color plot of the relative deviation $\delta_{\mathrm{IAP}} = (Z_{\mathrm{med}} - Z_{\mathrm{cell}})/Z_{\mathrm{cell}}$ at the true IAP ($\Phi = 0$) between the approximate cell impedance $Z_{\mathrm{cell}}^{\mathrm{approx}} \approx Z_{\mathrm{med}}$ and the actual value Z_{cell} as a function of cell density ρ_{c} compressibility κ_{c}. The green line represents the density and compressibility of iodixanol as a function of concentration. The four blue contour lines trace out the combinations of hypothetical cell properties (ρ_{c}, κ_{c}) that lead to the same acoustic impedance as iodixanol at concentrations of 10%, 20%, 30%, and 40%, respectively.

Supplementary Figure 11: Comparison of the temporal evolution of dextran dye concentration profiles in simulations and experiments.

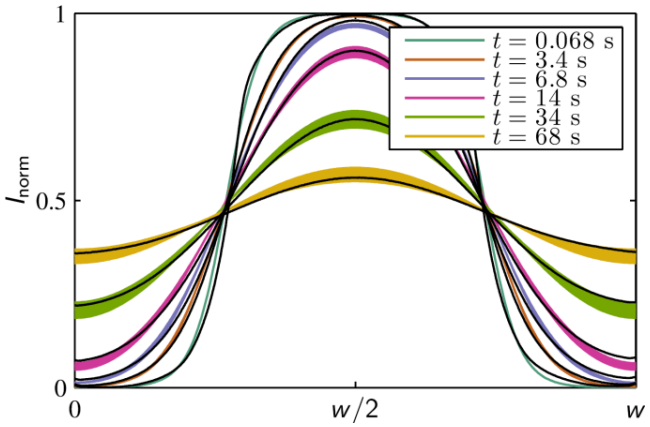

Concentration profiles at different times t. The colored bands show simulation results for the diffusivity D between 0.8×10^{-10} m^2 s^{-1} and 1×10^{-10} m^2 s^{-1} overlaid by black curves showing the normalized measured fluorescence intensity of dextran dye in 20% iodixanol (**Supplementary Fig. 4c**).

Supplementary Note 1: Basic theory of iso-acoustic focusing (IAF)

Consider the acoustic cavity in **Fig. 1a** of width w bounded by acoustically hard walls at $y = 0$ and $y = w$. By adjusting the sound frequency such that half the acoustic wavelength λ matches the width w, a standing wave builds up in the acoustically soft liquid. The resulting time-harmonic resonant pressure field p of amplitude p_a has an anti-node at each wall and a node at the channel center. Considering first the case of a homogeneous medium the field is given by $p = p_\mathrm{a}\cos(k_y y)$, where $k_y = 2\pi/\lambda$ is the wavenumber and $\lambda = 2w$. A small particle or cell of radius $a \ll \lambda$ suspended in this sound field will experience the acoustic radiation force $\boldsymbol{F}_\mathrm{rad}$ given by[1, 2],

$$\boldsymbol{F}_\mathrm{rad} = 4\pi a^3 \Phi k_y E_\mathrm{ac} \sin\big(2k_y y\big)\boldsymbol{e}_y \,, \quad (1)$$

where $E_\mathrm{ac} = \frac{1}{4}\kappa_\mathrm{m} p_\mathrm{a}^2$ is the time-averaged acoustic energy density and Φ is the acoustic contrast factor given by

$$\Phi = \frac{1-\tilde{\kappa}}{3} + \frac{\tilde{\rho}-1}{2\tilde{\rho}+1}. \quad (2)$$

Φ depends on the ratios of cell-to-medium densities $\tilde{\rho} = \rho_\mathrm{c}/\rho_\mathrm{m}$ and adiabatic compressibilities $\tilde{\kappa} = \kappa_\mathrm{c}/\kappa_\mathrm{m}$, with the subscripts (c) and (m) denoting cell and medium, respectively. In general, Φ thus depends on four parameters.

In this work we deal with a medium stratified by the added iodixanol concentration c, which perturbs the density and compressibility across the y-direction. Hence, the contrast factor Φ depends on c through the concentration-dependent medium density $\rho_\mathrm{m}(c)$ and compressibility $\kappa_\mathrm{m}(c)$. These have been obtained from measurements of density and speed of sound as functions of iodixanol concentration, (**Supplementary Fig. 2**). The actual $\boldsymbol{F}_\mathrm{rad}$ is modeled by inserting $\Phi(c)$ in Eq. (1).

In IAF, cells move to the IAP of zero acoustic contrast defined by the iodixanol concentration c_IAP for which $\Phi(c_\mathrm{IAP}) = 0$. In general, the IAP of a cell thus depends on the two cell parameters ρ_c and κ_c. It would be valuable for the IAF method to allow identification of the IAP in terms of a single parameter. Here, we show that the acoustic impedance $Z = \sqrt{\rho/\kappa}$ may be used to quantify the IAP. We find, that in the IAP the effective acoustic impedance of the cell Z_cell equals that of the surrounding medium Z_med to within 0.8% for all combinations of cells with ρ_c ranging from 1000 kg m^{-3} to 1200 kg m^{-3} and κ_c ranging from 3.4 ×10^{-10} Pa^{-1} to 4.4 ×10^{-10} Pa^{-1}. To arrive at this conclusion, we input the cell parameters ρ_c and κ_c into the expression for the contrast factor in Eq. (2), then, using the fitted polynomials for $\rho_\mathrm{m}(c)$ and $\kappa_\mathrm{m}(c)$, we solve for the iodixanol concentration c_IAP satisfying $\Phi(c_\mathrm{IAP}) = 0$, which defines the true IAP. In **Supplementary Fig. 10** we then plot the relative impedance difference ($\delta_\mathrm{IAP} = (Z_\mathrm{med} - Z_\mathrm{cell})/Z_\mathrm{cell}$) between the medium and the cell at the true IAP as functions of cell density and compressibility. As can be anticipated, the error is zero for cells that have combinations of ρ_c and κ_c that exactly match the properties of the medium (the green contour line). For all other combinations in the experimentally relevant range, the error stays below 0.8%, demonstrating that the IAP is well-described by the simple impedance condition $Z_\mathrm{cell} = Z_\mathrm{med}$.

We can obtain the result more formally by writing Φ in terms of the relative compressibility and impedance. Extending the fraction in the second term of Eq. (2) by $1/\tilde{\kappa}$, we find in terms of $\tilde{Z} = Z_\mathrm{cell}/Z_\mathrm{med}$ that

$$\Phi = \frac{1-\tilde{\kappa}}{3} + \frac{\tilde{Z}^2 - 1/\tilde{\kappa}}{2\tilde{Z}^2 + 1/\tilde{\kappa}} \quad . \quad (3)$$

In the true IAP where $\Phi = 0$, we may then solve for $\tilde{Z}$,

$$\tilde{Z} = \sqrt{\frac{2+\tilde{\kappa}}{(5-2\tilde{\kappa})\tilde{\kappa}}}, \quad \text{for } \Phi = 0\,. \quad (4)$$

For the relative compressibility we further write $\tilde{\kappa} = 1 + \Delta\tilde{\kappa}$ and Taylor expand to lowest order in $\Delta\tilde{\kappa} \ll 1$. One finds

$$\tilde{Z} = 1 + \frac{1}{3}(\Delta\tilde{\kappa})^2\,, \quad \text{for } \Phi = 0\,, \quad (5)$$

which shows that the leading error in assuming $Z_{\mathrm{cell}} = Z_{\mathrm{med}}$ (or $\tilde{Z} = 1$) is $\frac{1}{3}(\Delta\tilde{\kappa})^2$ and of second order in the relative compressibility difference $\Delta\tilde{\kappa}$. A relative difference of 30% thus gives an error of 3%. However, even with the full parameter range of **Supplementary Fig. 10**, the relative compressibility difference in the IAP never exceeds 15%, and thus the error is less than 0.8% for the full range of experimental conditions considered.

Supplementary Note 2: A scaling analysis of the acoustic stabilization of inhomogeneous liquids

In a homogeneous fluid the time-averaged acoustic energy density E_{ac} of the standing wave is constant across the channel width, and as a result there are no time-averaged net forces acting on the fluid due to the acoustic field. This is no longer the case in an inhomogeneous fluid, where gradients in density and compressibility lead to spatial inhomogeneities in the acoustic energy density. Since the relative change in the speed of sound of iodixanol concentrations is small in comparison to the relative change in the density (**Supplementary Fig. 2a-b**), we consider a fluid of density $\rho_{\mathrm{m}}(y) = [1 + \delta(y)]\rho_{\mathrm{m0}}$, where $\delta(y)$ is the position-dependent relative density variation (of the order 0.1) and ρ_{m0} is a constant reference density. The order-of-magnitude of the acoustic body force f_{ac} acting on the fluid can then be estimated as,

$$|f_{\mathrm{ac}}| \approx \partial_y E_{\mathrm{ac}} \approx \frac{\partial E_{\mathrm{ac}}}{\partial \rho_{\mathrm{m}}} \partial_y \rho_{\mathrm{m}} \approx E_{\mathrm{ac}}\, \partial_y \delta \,. \qquad (6)$$

In the channel of height h with horizontal walls at $z = 0$ and $z = h$, the hydrostatic pressure in the fluid is given by $p_{\mathrm{hyd}} = g(h - z)\rho_{\mathrm{m}}(y)$, where $g = 9.8\ \mathrm{m\ s^{-2}}$ is the acceleration due to gravity. Consequently, the force on the fluid along the y-direction due to hydrostatic pressure is

$$f_{\mathrm{hyd}} = -\partial_y p_{\mathrm{hyd}} = -g(h - z)\rho_{\mathrm{m0}}\, \partial_y \delta \,, \qquad (7)$$

with the maximum force at the bottom of the channel in $z = 0$. We obtain the estimated condition for the fluid to be stable against gravity from the requirement that the magnitude of the acoustic force $|f_{\mathrm{ac}}|$ is everywhere greater than $|f_{\mathrm{hyd}}|$. Since both f_{ac} and f_{hyd} are proportional to the gradient $\partial_y \delta$ the condition simply becomes

$$E_{\mathrm{ac}} > \rho_{\mathrm{m0}} g h \approx 2\ \mathrm{J\ m^{-3}} \,. \qquad (8)$$

The numerical value is calculated for our typical experimental conditions, $\rho_{\mathrm{m0}} = 1.1 \times 10^3\ \mathrm{kg\ m^{-3}}$ and $h = 150\ \mu\mathrm{m}$, and it is in agreement with our experimental measurements.

The experiments show that boundary-driven acoustic streaming in the bulk (Rayleigh streaming) is suppressed in an inhomogeneous fluid. This can be understood by a scaling argument comparing f_{ac} to the magnitude f_{str} of the shear-force density associated with the streaming flow rolls driven by the usual slip-velocity $v_{\mathrm{str}} = \Psi \frac{v_{\mathrm{a}}^2}{c_s}$ at the walls. Here, v_{a} is the amplitude of the acoustic velocity field, c_s is the speed of sound, and Ψ is a geometrical prefactor, which is equal to 3/8 for a planar wall[3]. A scaling estimate for the shear-force density is then,

$$|f_{\mathrm{str}}| \approx \eta \nabla^2 v_{\mathrm{str}} \approx \eta \frac{1}{L^2} \Psi \frac{v_{\mathrm{a}}^2}{c_s} \approx \frac{4\Psi\eta}{\rho_{\mathrm{m0}} c_s L^2} E_{\mathrm{ac}} \,, \qquad (9)$$

where L is the characteristic length scale, and it has been used that $E_{\mathrm{ac}} \approx \frac{1}{4}\rho_{\mathrm{m0}} v_{\mathrm{a}}^2$. The ratio of the destabilizing streaming force $|f_{\mathrm{str}}|$ in Eq. (9) and the stabilizing acoustic force $|f_{\mathrm{ac}}|$ in Eq. (8) using $L = h/4$ becomes

$$\frac{|f_{\mathrm{str}}|}{|f_{\mathrm{ac}}|} \approx \frac{|f_{\mathrm{str}}|}{E_{\mathrm{ac}}\delta/L} \approx \frac{4\Psi\eta}{\rho_{\mathrm{m0}} c_s L \delta} \approx \frac{16\Psi\eta}{\rho_{\mathrm{m0}} c_s h \delta} \approx 10^{-4} \,. \qquad (10)$$

Thus the scaling calculation shows that acoustic streaming is suppressed in the bulk of inhomogeneous fluids due to the density-gradient-induced acoustic force f_{ac}.

Supplementary Note 3: Numerical model of cell trajectories in diffusing iodixanol gradients

To confirm that our measurements at flow rates 4 µL min^{-1} and 8 µL min^{-1} do indeed yield the correct acoustic impedances Z_{cell} of the cells, we solve a simple numerical model of cell trajectories in the diffusing iodixanol gradient. An important question we address, is whether the acoustic force on the cell, which approaches zero near the IAP, is able to keep the cell in its IAP at intermediate time scales where the IAP moves due to diffusion.

Because the molecular diffusivity of the fluorescent dextran tracer and the iodixanol are nearly identical, we assume, as discussed in the main text (**Main article, Creating an acoustic impedance gradient**), that the measured fluorescence signal is proportional to the iodixanol concentration as it evolves in time. The experimentally measured diffusive evolution of the fluorescence profile in 20% iodixanol (**Supplementary Fig. 4c**) is well described by Fickean diffusion of the concentration c,

$$\partial_t c = D\nabla^2 c, \quad (11)$$

with zero flux at the channel walls. Treating the diffusivity D as a free parameter in our numerical model, we obtain the best agreement with experiments using the value $D = 0.9 \times 10^{-10}$ m^2 s^{-1} (**Supplementary Fig. 11**).

Considering the cell trajectories, we solve for the transverse dynamics along the y-direction neglecting effects of inertia (Reynolds number $\sim 10^{-3}$), gravitational sedimentation and acoustic streaming. The dynamical equation for the cell then takes the form $F_{\text{rad}} + F_{\text{drag}} = 0$, with F_{rad} given by Eq. (1) and the Stokes drag given by $F_{\text{drag}} = -6\pi\eta a\, \partial_t y$, where η is the dynamic viscosity of the medium. This leads to the following equation for the cell position y

$$\partial_t y = \frac{2k_y a^2 E_{\text{ac}}}{3\eta} \Phi(c(y)) \sin(2k_y y). \quad (12)$$

Note that the contrast factor $\Phi = \Phi(c(y))$ is a function of y through the diffusing iodixanol concentration c. It is calculated from Eq. (2) using the measured polynomials for $\kappa_{\text{m}}(c)$ and $\rho_{\text{m}}(c)$, **Supplementary Fig. 2**. The time-dependent solution of Eqs. (11) and (12) was carried out in COMSOL Multiphysics using the Particle Tracing Module to integrate the cell trajectory.

Using this model, we simulated cell trajectories of BA-F3 and MCF7 cells starting at time $t = 0$ a radius a from the sidewall in $y = 0$. The side and central streams were of initial iodixanol concentration 10% and 36%, respectively. The cell densities were set to $\rho_{\text{c}} = 1068$ kg m^{-3} as previously reported for MCF7 cells[4], while the compressibilities κ_{c} were calculated from the measured cell impedances Z_{c}.

The simulation results (**Supplementary Fig. 6**) summarize the IAF method: In IAF, cells are introduced near the sides of the channel walls in a low acoustic-impedance medium (**Supplementary Fig. 6a**). When subject to the acoustic field in the cavity, the cells migrate rapidly to reach their IAP in the initially steep impedance gradient at the border of the central flow stream (**Supplementary Fig. 6b**). The gradient decreases slowly over time due to molecular diffusion of the iodixanol. During this process, the acoustic force maintains the cells at their respective IAP's allowing accurate measurements of the cell impedances (**Supplementary Fig. 6c**). Finally, when diffusion has eliminated all gradients, the cells are located either at a channel wall or at the channel center depending on their acoustic impedance relative to the acoustic impedance of the homogenized medium (**Supplementary Fig. 6d**).

The transverse cell position as a function of time is plotted in **Supplementary Fig. 6e** and shows the rapid migration in the first few seconds followed by slower migration as the IAP changes due to diffusion. Combining the cell positions with the temporal development of the acoustic impedance profile of the medium gives the apparent IAP and cell impedance versus time plotted in **Supplementary Fig. 6f**. Clearly, there exists a temporal window $t_1 < t < t_3$ during which accurate measurements of the cell impedance Z_{cell} of both BA-F3 and MCF7

can be obtained. Tolerating a relative impedance error between the cell and the medium of maximum 0.3% we obtain the lower bound $t_{1,\mathrm{BA-F3}} = 5.7$ s and $t_{1,\mathrm{MCF7}} = 3.0$ s. For the upper bound we find $t_{3,\mathrm{BA-F3}} = 79$ s and $t_{3,\mathrm{MCF7}} = 51$ s. Consequently, accurate measurement of the acoustic impedance of both BA-F3 and MCF7 cells can be obtained for $5.7\ \mathrm{s} < t < 51\ \mathrm{s}$ corresponding to flow rates between 1.3 µL min^{-1} and 12 µL min^{-1}.

In conclusion, the simulations have shown that the IAF method represents a robust method of obtaining the acoustic impedance of the cells in our experiments. The experimental flow rates of 4 µL min^{-1} and 8 µL min^{-1} ensure that the cells are indeed located in their IAP at the time of measurement.

Supplementary Note 4: Time-scale analysis of iso-acoustic focusing

As demonstrated by the simulation results in **Supplementary Fig. 6**, IAF involves three time scales. First, there is the time scale t_1 of the initial migration to the IAP due to the acoustic radiation force (**Supplementary Fig. 6b**). Second, there is the retention time t_2 of a cell in the channel set by the flow rate Q. Finally, there is the diffusion time t_3 over which the impedance gradient is flattened (**Supplementary Fig. 6d**). For the IAF method to work properly the time scales must be ordered $t_1 < t_2 < t_3$ such that cells are in their IAP when imaged near the outlet (**Supplementary Fig. 6c**). Below we give simple analytical estimates for these three time scales useful for deciding experimental design parameters such as channel dimensions and flow rates for various cell types.

The initial migration time scale t_1 can be estimated by integration of Eq. (12) from $t = 0$ to $t = t_1$ assuming a constant contrast factor Φ. Starting from an initial position $0 < y_0 < w/2$ and migrating to a final position y_1 at $y_0 < y_1 < w/2$ takes a time[1]

$$t_1 \approx \frac{3\eta}{4\Phi(k_y a)^2}\frac{1}{E_{\mathrm{ac}}}\ln\left[\frac{\tan[k_y y_1]}{\tan[k_y y_0]}\right] = 3.1\ \mathrm{s}, \qquad (13)$$

where the numeric value is calculated for an MCF7 cell with the parameters given in **Supplementary Fig. 6** assuming a side inlet stream of 10% iodixanol and using $y_0 = a$ and $y_1 = w/3$.

The characteristic diffusion time t_3 for diffusion over one third of the channel is

$$t_3 \approx \frac{(w/3)^2}{2D} = \frac{w^2}{18D} = 87 \text{ s}, \qquad (14)$$

again with the numeric value calculated using the parameters given in **Supplementary Fig. 6**.

The retention time t_2 is obtained from the flow rate as

$$t_2 = \frac{w \cdot h \cdot l}{Q} = 17 \text{ s}, \qquad (15)$$

where the numeric value is calculated for a flow rate of 4 µL min^{-1} and l = 20 mm is the downstream distance from the inlet to the imaging region. These simple estimates are in agreement with the simulation results of **Supplementary Fig. 6**.

Supplementary References

1. Barnkob R, Augustsson P, Laurell T, Bruus H. Measuring the local pressure amplitude in microchannel acoustophoresis. *Lab Chip* **10**, 563-570 (2010).

2. Yosioka K, Kawasima Y. Acoustic radiation pressure on a compressible sphere. *Acustica* **5**, 167-173 (1955).

3. Lord Rayleigh. On the circulation of air observed in Kundt's tubes, and on some allied acoustical problems. *Philosophical Transactions of the Royal Society of London* **175**, 1-21 (1884).

4. Hartono D, Liu Y, Tan PL, Then XYS, Yung L-YL, Lim K-M. On-chip measurements of cell compressibility via acoustic radiation. *Lab Chip*, (2011).

5. Barnkob R, Augustsson P, Laurell T, Bruus H. Acoustic radiation- and streaming-induced microparticle velocities determined by microparticle image velocimetry in an ultrasound symmetry plane. *Phys Rev E* **86**, (2012).

6. Augustsson P, Barnkob R, Wereley ST, Bruus H, Laurell T. Automated and temperature-controlled micro-PIV measurements enabling long-term-stable microchannel acoustophoresis characterization. *Lab Chip* **11**, 4152-4164 (2011).

Chapter 8

Paper III in Physical Review Letters

Acoustic force density acting on inhomogeneous fluids in acoustic fields

DOI: 10.1103/PhysRevLett.117.114504.

Authors: J.T. Karlsen, P. Augustsson, and H. Bruus.
Journal: Phys. Rev. Lett. **117**, 114504 (2016).

Remarks: Featured as an Editors' Suggestion in Physical Review Letters. Supplemental Movies are available online: http://link.aps.org/supplemental/10.1103/PhysRevLett.117.114504.

Acoustic Force Density Acting on Inhomogeneous Fluids in Acoustic Fields

Jonas T. Karlsen,[1,*] Per Augustsson,[2] and Henrik Bruus[1,†]
[1]Department of Physics, Technical University of Denmark, DTU Physics Building 309, DK-2800 Kongens Lyngby, Denmark
[2]Department of Biomedical Engineering, Lund University, Ole Römers väg 3, 22363 Lund, Sweden
(Received 22 April 2016; revised manuscript received 24 June 2016; published 9 September 2016)

We present a theory for the acoustic force density acting on inhomogeneous fluids in acoustic fields on time scales that are slow compared to the acoustic oscillation period. The acoustic force density depends on gradients in the density and compressibility of the fluid. For microfluidic systems, the theory predicts a relocation of the inhomogeneities into stable field-dependent configurations, which are qualitatively different from the horizontally layered configurations due to gravity. Experimental validation is obtained by confocal imaging of aqueous solutions in a glass-silicon microchip.

DOI: 10.1103/PhysRevLett.117.114504

The physics of acoustic forces on fluids and suspensions has a long and rich history including early work on fundamental phenomena such as acoustic streaming [1–4], the acoustic radiation force acting on a particle [5,6] or an interface of two immiscible fluids [7], and acoustic levitation [8,9]. Driven by applications related to particle and droplet handling, the field continues to be active with recent advanced studies of acoustic levitators [10–12], acoustic tweezers and tractor beams [13–15], thermoviscous effects [16–18], and, in general, rapid advances within the field of microscale acoustofluidics [19]. In the latter, acoustic radiation forces are used to confine, separate, sort, or probe particles such as microvesicles [20,21], cells [22–26], bacteria [27,28], and biomolecules [29]. Biomedical applications include the early detection of circulating tumor cells in blood [30,31] and the diagnosis of bloodstream infections [32].

The theoretical treatment of acoustic forces involves nonlinear models including multiple length and time scales [33]. Steady acoustic streaming [34] describes a steady swirling fluid motion, spawned by fast-time-scale acoustic dissipation either in boundary layers [2] or in the bulk [3]. Similarly, the acoustic radiation force acting on a particle [18] or an interface of two immiscible fluids [35,36] is due to interactions between the incident and the scattered acoustic waves. This force derives from a divergence in the time-averaged momentum-flux-density tensor, which is nonzero only at the position of the particle or the interface.

Recently, in microchannel acoustofluidics experiments, it was discovered that acoustic forces can relocate inhomogeneous aqueous salt solutions and stabilize the resulting density profiles against hydrostatic pressure gradients [37]. Building on this discovery, isoacoustic focusing was subsequently introduced as an equilibrium cell-handling method that overcomes the central issue of cell-size dependency in acoustophoresis [38]. The method can be considered a microfluidic analog to density gradient centrifugation, achieving spatial separation of different cell types based on differences in their acoustomechanical properties. Not surprisingly, the subtle nonlinear acoustic phenomenon of relocation and stabilization of inhomogeneous fluids was discovered in the realm of microfluidics, where typical hydrostatic pressure differences ($\sim$1 Pa) are comparable to, or less than, the acoustic energy densities (1–100 Pa) obtained in typical microchannel resonators [38–40].

The main goal of this Letter is to provide a theoretical explanation of this phenomenon. To this end, we extend acoustic radiation force theory beyond the requirement of immiscible phases, and we present a general theory for the time-averaged acoustic force density acting on a fluid with a continuous spatial variation in density and compressibility. The starting point of our treatment is to identify and exploit the separation in time scales between the fast time scale of acoustic oscillations and the slow time scale of the oscillation-time-averaged fluid motion. We show that gradients in density and compressibility result in a divergence in the time-averaged momentum-flux-density tensor, which, in contrast to the case of immiscible phases, is generally nonzero everywhere in space. Our theory explains the observed relocation and stabilization of inhomogeneous fluids. Furthermore, we present an experimental validation of our theory obtained by confocal imaging in an acoustofluidic glass-silicon microchip.

Characteristic time scales.—Consider the sketch in Fig. 1 of a long, straight microchannel of cross-sectional width $W = 375\ \mu$m and height $H = 150\ \mu$m filled with a fluid of inhomogeneous density $\rho_0(\boldsymbol{r}) = [1 + \hat{\rho}(\boldsymbol{r})]\rho_0^{(0)}$, adiabatic compressibility $\kappa_0(\boldsymbol{r})$, and dynamic viscosity $\eta_0(\boldsymbol{r})$. Here, $\hat{\rho}(\boldsymbol{r})$ is the relative deviation away from the reference density $\rho_0^{(0)}$. Assuming an acoustic standing half-wave resonance at angular frequency ω, the wave number is $k = \omega/c = \pi/W$, where $c = 1/\sqrt{\rho_0\kappa_0}$ is the speed of sound. In terms of the parameters of the microchannel and of water at ambient conditions, the fast acoustic oscillation time scale t is

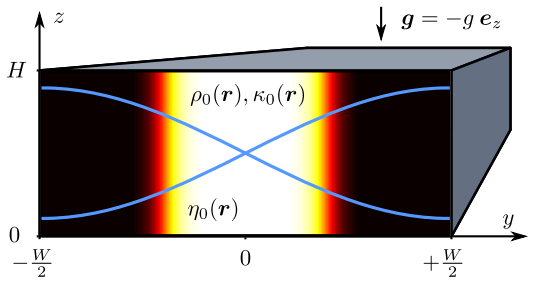

FIG. 1. Sketch of a long, straight acoustofluidic microchannel of length $L = 40$ mm along x, width $W = 375$ μm and height $H = 150$ μm with an imposed half-wave acoustic pressure resonance (sinusoidal curves) inside a glass-silicon chip. A salt concentration (black, low; white, high) leads to an inhomogeneous-fluid density $\rho_0(\boldsymbol{r})$, compressibility $\kappa_0(\boldsymbol{r})$, and dynamic viscosity $\eta_0(\boldsymbol{r})$. The gravitational acceleration is $\boldsymbol{g} = -g\boldsymbol{e}_z$.

$$t \sim \frac{1}{\omega} = \frac{1}{kc} = \frac{1}{\pi} W\sqrt{\rho_0\kappa_0} \sim 0.1\ \mu\text{s}. \tag{1}$$

In contrast, the time scales associated with flows driven by hydrostatic pressure gradients are much slower. Given the length scale H, the gravitational acceleration g, and the kinematic viscosity $\nu_0 = \eta_0/\rho_0$, we estimate the time scale of inertia $t_{\text{inertia}} \sim \sqrt{H/(g\hat{\rho})}$, of viscous relaxation $t_{\text{relax}} \sim H^2/\nu_0$, and of steady shear motion $t_{\text{shear}} \sim \nu_0/(Hg\hat{\rho})$, with the latter being obtained by balancing the shear stress η_0/t_{shear} with the hydrostatic pressure difference $H\rho_0 g\hat{\rho}$. Remarkably, in our system with $\hat{\rho} \approx 0.1$, all time scales are of the order of 10 ms, henceforth denoted as the slow time scale τ,

$$\tau \sim t_{\text{inertia}} \sim t_{\text{relax}} \sim t_{\text{shear}} \sim 10\ \text{ms}. \tag{2}$$

Furthermore, for acoustic energy densities E_{ac} of the order $\rho_0 gH$, the time scale of flows driven by time-averaged acoustic forces is also τ. Hence, we have identified a separation of time scales into a fast acoustic time scale t and a slow time scale $\tau \sim 10^5 t$. This separation is sufficient to ensure $\tau \gg t$ in general, even for large variations in parameter values.

Fast-time-scale dynamics.—The dynamics at the fast time scale t describes acoustics for which viscosity may be neglected [41–43]. On this time scale ρ_0, κ_0, and η_0 can be assumed to be stationary, and the acoustic fields are treated as time-harmonic perturbations at the angular frequency ω [43]. The perturbation expansion for the density ρ thus takes the form

$$\rho = \rho_0(\boldsymbol{r}, \tau) + \rho_1(\boldsymbol{r}, \tau)e^{-i\omega t}, \tag{3}$$

and likewise for the pressure p and the velocity $\boldsymbol{v}$. In terms of the material derivative $(d/dt) = \partial_t + (\boldsymbol{v}\cdot\boldsymbol{\nabla})$, the density-pressure relation for a fluid particle is

$$\frac{d\rho}{dt} = \frac{1}{c^2}\frac{dp}{dt}, \quad \text{where } \frac{1}{c^2} = \left(\frac{\partial\rho}{\partial p}\right)_S = \rho_0\kappa_0. \tag{4}$$

Here, c is the adiabatic local speed of sound, which depends on the position through the inhomogeneity in κ_0 and ρ_0. Combining Eqs. (3) and (4) leads to the first-order relation

$$\partial_t\rho_1 + (\boldsymbol{v}_1\cdot\boldsymbol{\nabla})\rho_0 = \rho_0\kappa_0[\partial_t p_1 + (\boldsymbol{v}_1\cdot\boldsymbol{\nabla})p_0], \tag{5}$$

where we have discarded terms involving $\boldsymbol{v}_0$, as they are negligible for $|\boldsymbol{v}_0| \ll c$. From the governing equations for mass and momentum [41–43] follows $|\boldsymbol{\nabla}p_0| \ll c^2|\boldsymbol{\nabla}\rho_0|$, and the term involving $\boldsymbol{\nabla}p_0$ in Eq. (5) is also negligible. This results in the first-order equations

$$\kappa_0\partial_t p_1 = -\boldsymbol{\nabla}\cdot\boldsymbol{v}_1, \tag{6a}$$

$$\rho_0\partial_t\boldsymbol{v}_1 = -\boldsymbol{\nabla}p_1, \tag{6b}$$

and the wave equation for the acoustic pressure p_1 in an inhomogeneous fluid [42,44],

$$\frac{1}{c^2}\partial_t^2 p_1 = \rho_0\boldsymbol{\nabla}\cdot\left[\frac{1}{\rho_0}\boldsymbol{\nabla}p_1\right]. \tag{7}$$

Note that the curl of Eq. (6b) yields $\boldsymbol{\nabla}\times(\rho_0\boldsymbol{v}_1) = \boldsymbol{0}$, which implies that acoustics in inhomogeneous fluids should be formulated in terms of the mass current potential ϕ_ρ instead of the usual velocity potential,

$$\rho_0\boldsymbol{v}_1 = \boldsymbol{\nabla}\phi_\rho \quad \text{and} \quad p_1 = -\partial_t\phi_\rho. \tag{8}$$

Combining Eqs. (6a) and (8) reveals that the mass current potential ϕ_ρ fulfills the same wave equation as p_1.

The acoustic force density.—The first-order acoustic fields lead to no net fluid displacement since the time average $\langle g_1\rangle = (1/T)\int_0^T g_1 dt$ over one oscillation period T of any time-harmonic first-order field g_1 is zero. The description of time-averaged effects thus requires the solution of the time-averaged second-order equations, and the introduction of the time-averaged acoustic momentum-flux-density tensor $\langle\boldsymbol{\Pi}\rangle$ [41],

$$\langle\boldsymbol{\Pi}\rangle = \langle p_2\rangle\mathbf{I} + \langle\rho_0\boldsymbol{v}_1\boldsymbol{v}_1\rangle. \tag{9}$$

Here, $\mathbf{I}$ is the unit tensor, and the second-order mean Eulerian excess pressure $\langle p_2\rangle$ is given by the difference between the time-averaged acoustic potential and kinetic energy densities [45–47],

$$\langle p_2\rangle = \langle E_{\text{pot}}\rangle - \langle E_{\text{kin}}\rangle = \frac{1}{2}\kappa_0\langle|p_1|^2\rangle - \frac{1}{2}\rho_0\langle|\boldsymbol{v}_1|^2\rangle. \tag{10}$$

In the well-known case of a particle suspended in a homogeneous fluid in an acoustic field, the deviation in density and compressibility introduced by the particle leads to a scattered acoustic wave, which induces a divergence $\boldsymbol{\nabla}\cdot\langle\boldsymbol{\Pi}\rangle$ in $\langle\boldsymbol{\Pi}\rangle$. The radiation force exerted on the particle

may then be obtained by integrating the force density $-\boldsymbol{\nabla}\cdot\langle\boldsymbol{\Pi}\rangle$ over a volume enclosing the particle, thereby picking out the divergence at the particle position [18,48].

In the case of an inhomogeneous fluid, the gradient in the continuous material parameters $\rho_0(\boldsymbol{r})$ and $\kappa_0(\boldsymbol{r})$ will likewise lead to a nonzero divergence in $\langle\boldsymbol{\Pi}\rangle$. This is the origin of the acoustic force density $\boldsymbol{f}_{\mathrm{ac}}$ acting on the inhomogeneous fluid at the slow time scale. Consequently, we introduce $\boldsymbol{f}_{\mathrm{ac}}$ as

$$\boldsymbol{f}_{\mathrm{ac}} = -\boldsymbol{\nabla}\cdot\langle\boldsymbol{\Pi}\rangle = -\boldsymbol{\nabla}\langle p_2\rangle - \boldsymbol{\nabla}\cdot\langle\rho_0\boldsymbol{v}_1\boldsymbol{v}_1\rangle. \tag{11}$$

Here, $\langle p_2\rangle$ is given by the local expression (10), which remains true in an inhomogeneous fluid, while the divergence term is rewritten using Eq. (6a) for $\boldsymbol{\nabla}\cdot\boldsymbol{v}_1$ and Eq. (8) defining the mass current potential ϕ_ρ,

$$\boldsymbol{\nabla}\cdot\langle\rho_0\boldsymbol{v}_1\boldsymbol{v}_1\rangle = \langle\boldsymbol{v}_1\cdot\boldsymbol{\nabla}(\rho_0\boldsymbol{v}_1)\rangle + \langle\rho_0\boldsymbol{v}_1(\boldsymbol{\nabla}\cdot\boldsymbol{v}_1)\rangle, \tag{12a}$$

$$= \left\langle\left(\frac{1}{\rho_0}\boldsymbol{\nabla}\phi_\rho\right)\cdot\boldsymbol{\nabla}(\boldsymbol{\nabla}\phi_\rho)\right\rangle + \langle(\boldsymbol{\nabla}\phi_\rho)(\kappa_0\partial_t^2\phi_\rho)\rangle, \tag{12b}$$

$$= \frac{1}{2\rho_0}\boldsymbol{\nabla}\langle|\boldsymbol{\nabla}\phi_\rho|^2\rangle - \kappa_0\langle(\boldsymbol{\nabla}\partial_t\phi_\rho)(\partial_t\phi_\rho)\rangle, \tag{12c}$$

$$= \frac{1}{2\rho_0}\boldsymbol{\nabla}\langle|\boldsymbol{\nabla}\phi_\rho|^2\rangle - \frac{1}{2}\kappa_0\boldsymbol{\nabla}\langle|\partial_t\phi_\rho|^2\rangle, \tag{12d}$$

$$= \frac{1}{2\rho_0}\boldsymbol{\nabla}\langle|\rho_0\boldsymbol{v}_1|^2\rangle - \frac{1}{2}\kappa_0\boldsymbol{\nabla}\langle|p_1|^2\rangle. \tag{12e}$$

In Eq. (12c) we have used $\langle f_1(\partial_t g_1)\rangle = -\langle(\partial_t f_1)g_1\rangle$, valid for time-harmonic fields f_1 and g_1.

Combining Eqs. (9)–(12) and evaluating the time averages [49], we arrive at our final expression for the acoustic force density $\boldsymbol{f}_{\mathrm{ac}}$ acting on an inhomogeneous fluid,

$$\boldsymbol{f}_{\mathrm{ac}} = -\frac{1}{4}|p_1|^2\boldsymbol{\nabla}\kappa_0 - \frac{1}{4}|\boldsymbol{v}_1|^2\boldsymbol{\nabla}\rho_0. \tag{13}$$

This main result, obtained in part by using the mass current potential ϕ_ρ, demonstrates that gradients in compressibility and density lead to a time-averaged acoustic force density acting on an inhomogeneous fluid.

Our theory is consistent with the classical expression for the radiation pressure on an immiscible fluid interface given by the difference in the mean Lagrangian pressure $\langle p_2^L\rangle = \langle E_{\mathrm{pot}}\rangle + \langle E_{\mathrm{kin}}\rangle$ (not the Eulerian pressure $\langle p_2\rangle$) across the interface [45]. Considering a straight interface at $y = 0$ between two immiscible fluids a and b, we may write the fluid property q (either ρ_0 or κ_0) using the Heaviside step function $H(y)$ as $q(y) = q_a + \Delta q H(y)$, where $\Delta q = q_b - q_a$. Integrating $\boldsymbol{f}_{\mathrm{ac}}$ across the interface then yields the force per area $\boldsymbol{F}_{\mathrm{ac}}/A$ on the interface,

$$\frac{\boldsymbol{F}_{\mathrm{ac}}}{A} = -\frac{1}{4}[|p_1|^2\Delta\kappa_0 + |\boldsymbol{v}_1|^2\Delta\rho_0]\boldsymbol{n} = -\Delta\langle p_2^L\rangle\boldsymbol{n}, \tag{14}$$

where $\boldsymbol{n}$ is the normal vector pointing from fluid a to b, and the continuous acoustic fields p_1 and $\boldsymbol{v}_1$ are evaluated at the interface. Inserting into Eq. (14) the explicit expressions for p_1 and $\boldsymbol{v}_1$ in the case of a normally incident wave being partially transmitted from fluid a to fluid b, we recover the radiation pressure given by Lee and Wang [45] in their Eq. (109).

Analytical approximation for $|\hat{\rho}| \ll 1$.—We can obtain analytical results that provide physical insight into the experimentally relevant limit of fluids with a constant speed of sound c and a weakly varying density [37,38]. Writing the latter as $\rho_0(\boldsymbol{r},\tau) = \rho_0^{(0)}[1+\hat{\rho}(\boldsymbol{r},\tau)]$, where $|\hat{\rho}(\boldsymbol{r},\tau)| \ll 1$ and the superscript (0) indicates zeroth-order in $\hat{\rho}$, we obtain $\boldsymbol{\nabla}\kappa_0 = \frac{1}{c^2}\boldsymbol{\nabla}(1/\rho_0) = -(\kappa_0/\rho_0)\boldsymbol{\nabla}\rho_0$. To first order in $\hat{\rho}$, $\boldsymbol{f}_{\mathrm{ac}}$ in Eq. (13) thus becomes

$$\boldsymbol{f}_{\mathrm{ac}}^{(1)} = \left[\frac{1}{4}\kappa_0^{(0)}|p_1^{(0)}|^2 - \frac{1}{4}\rho_0^{(0)}|\boldsymbol{v}_1^{(0)}|^2\right]\boldsymbol{\nabla}\hat{\rho}. \tag{15}$$

Compared to Eq. (13), this expression constitutes a major simplification since it is linear in $\boldsymbol{\nabla}\hat{\rho}$ and it employs the $\hat{\rho}$-independent homogeneous-fluid fields $p_1^{(0)}$ and $\boldsymbol{v}_1^{(0)}$.

Based on Eq. (15), we demonstrate analytically that our theory is capable of explaining recent experimental results [37,38]. For the system in Fig. 1, with a horizontal acoustic half-wave pressure resonance of amplitude p_{a}, the homogeneous-fluid field solution takes the form,

$$p_1^{(0)} = p_{\mathrm{a}}\sin(ky) \quad \text{with} \quad k = \frac{\pi}{W}, \tag{16a}$$

$$\boldsymbol{v}_1^{(0)} = \frac{p_{\mathrm{a}}}{i\rho_0^{(0)}c}\cos(ky)\boldsymbol{e}_y. \tag{16b}$$

In this case Eq. (15) reduces to

$$\boldsymbol{f}_{\mathrm{ac}}^{(1)} = -\cos(2ky)E_{\mathrm{ac}}^{(0)}\boldsymbol{\nabla}\hat{\rho}, \tag{17}$$

where $E_{\mathrm{ac}}^{(0)} = \frac{1}{4}\kappa_0^{(0)}p_{\mathrm{a}}^2$ is the homogeneous-fluid time-averaged acoustic energy density. Consider a fluid that is initially stratified in horizontal density layers $\hat{\rho}(\boldsymbol{r},0) = \hat{\rho}(z)$ (not the vertical layers seen in Fig. 1), with the dense fluid occupying the floor of the channel ($\partial_z\hat{\rho} < 0$). Equation (17) then predicts that the fluid layers will be pushed downwards near the channel sides, but upwards in the center. This explains the initial phase in the slow-time-scale relocation of the denser fluid to the center of the channel observed experimentally [37].

Slow-time-scale dynamics.—Our experiments confirm the observation [38] that acoustic streaming is suppressed in the bulk of an inhomogeneous fluid. On the slow time scale τ, the dynamics is therefore governed by the acoustic

force density $\boldsymbol{f}_{\mathrm{ac}}$, the gravitational force density $\rho_0\boldsymbol{g}$, and the induced viscous stress, such that the Navier–Stokes equation and the continuity equation take the form

$$\partial_\tau(\rho_0\boldsymbol{v}) = \boldsymbol{\nabla}\cdot[\boldsymbol{\sigma} - \rho_0\boldsymbol{v}\boldsymbol{v}] + \boldsymbol{f}_{\mathrm{ac}} + \rho_0\boldsymbol{g}, \tag{18a}$$

$$\partial_\tau\rho_0 = -\boldsymbol{\nabla}\cdot(\rho_0\boldsymbol{v}), \tag{18b}$$

where $\boldsymbol{\sigma}$ is the stress tensor, given by

$$\boldsymbol{\sigma} = -p\mathbf{I} + \eta_0[\boldsymbol{\nabla}\boldsymbol{v} + (\boldsymbol{\nabla}\boldsymbol{v})^T] + \left(\eta_0^b - \frac{2}{3}\eta_0\right)(\boldsymbol{\nabla}\cdot\boldsymbol{v})\mathbf{I}.$$

Here, the superscript T indicates tensor transposition and η_0^b is the bulk viscosity, for which we use the value of water [17]. The inhomogeneity in the fluid parameters is assumed to be caused by a spatially varying concentration field $s(\boldsymbol{r},\tau)$ of a solute molecule with diffusivity D, satisfying the advection-diffusion equation

$$\partial_\tau s = -\boldsymbol{\nabla}\cdot[-D\boldsymbol{\nabla}s + \boldsymbol{v}s]. \tag{18c}$$

In our experimental setup, aqueous solutions of iodixanol are used to create inhomogeneities in density, while maintaining an approximately constant speed of sound. The relevant solution properties have been measured as functions of the iodixanol volume-fraction concentration s in our previous work [38]. For the density ρ_0 and viscosity η_0, the resulting fits, valid for $s \le 0.6$ and $s \le 0.4$, respectively, are $\rho_0 = \rho_0^{(0)}[1 + a_1 s]$ and $\eta_0 = \eta_0^{(0)}[1 + b_1 s + b_2 s^2 + b_3 s^3]$, with $\rho_0^{(0)} = 1005\ \mathrm{kg/m^3}$, $\eta_0^{(0)} = 0.954\ \mathrm{mPa\,s}$, and $a_1 = 0.522$, $b_1 = 2.05$, $b_2 = 2.54$, $b_3 = 22.8$. The diffusivity was measured *in situ* to be $D = 0.9 \times 10^{-10}\ \mathrm{m^2/s}$.

Comparison to experiments.—Our experimental setup is described in detail in Ref. [38]. The microchannel in the glass-silicon microchip has the dimensions given in Fig. 1. The horizontal half-wave resonance is excited by driving an attached piezoelectric transducer with an ac voltage U swept repeatedly in frequency from 1.9 to 2.1 MHz in cycles of 1 ms to ensure stable operation. The resulting average acoustic energy density is measured by observing the acoustic focusing of 5 μm beads [50]. The channel inlet conditions are illustrated in Fig. 1: a fluorescently marked 36% iodixanol solution (white) is laminated by 10% iodixanol solutions on either side (black) [51]. The corresponding density variation is 13%, with the maximum at the channel center. At the outlet, after a retention time of $\tau_{\mathrm{ret}} = 17$ s, the fluorescence profile is imaged using confocal microscopy in the channel cross section. The characteristic time for diffusion across one third of the channel width is $\tau_{\mathrm{diff}} = (1/2D)(W/3)^2 = 87$ s, so diffusion is important but not dominant in the experiment.

We simulate numerically the time evolution in the system using the finite-element solver COMSOL Multiphysics [52], by implementing Eqs. (17) and (18) with the measured dependencies of density $\rho_0(s)$ and viscosity $\eta_0(s)$ on concentration s. The initial concentration field $s(\boldsymbol{r},0)$ is set to the inlet conditions allowing the concentration field $s(\boldsymbol{r},\tau_{\mathrm{ret}})$ to be compared to the experimental images. The acoustic energy density E_{ac} entering the model is set to the measured experimental value, which leaves no free parameters. Concerning the validity of the numerical solutions, several convergence tests were performed [17], and the integral of s over the domain was conserved in time with a relative error of the order 10^{-3}.

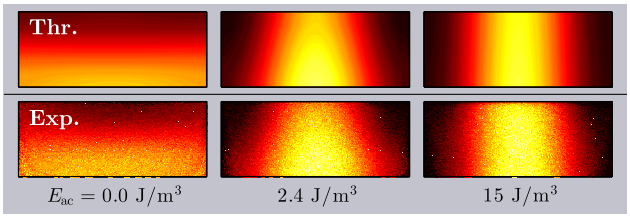

FIG. 2. Theoretical prediction from simulation (top row) and experimental confocal image (bottom row) of the cross-sectional concentration of iodixanol after 17 s retention time for three acoustic energy densities E_{ac}. Initially, the denser fluorescently marked fluid (36% iodixanol, white) is in the center and the less dense fluid (10% iodixanol, black) is at the sides; see Fig. 1. The stable configurations confirm the observation in Ref. [38] that acoustic streaming is suppressed in inhomogeneous fluids. There are no fitting parameters.

In Fig. 2 we compare the numerically simulated and experimentally measured concentration fields $s(\boldsymbol{r},\tau)$ at time $\tau_{\mathrm{ret}} = 17$ s for three acoustic energy densities E_{ac}. For $E_{\mathrm{ac}} = 0\ \mathrm{J/m^3}$, the initially vertical center fluid column of high density (Fig. 1, white) has collapsed and relocated to the channel bottom due to gravity. For $E_{\mathrm{ac}} = 15\ \mathrm{J/m^3}$, the acoustic force density stabilizes the denser vertical fluid

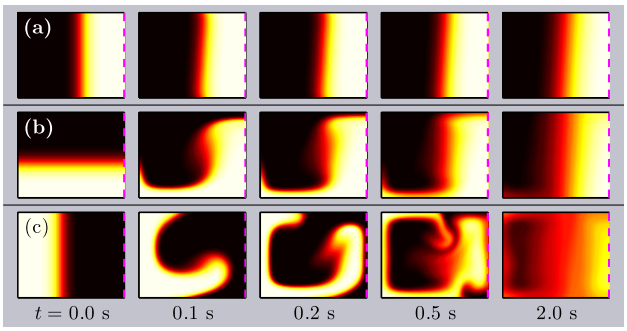

FIG. 3. Simulation for $E_{\mathrm{ac}} = 10\,\mathrm{J/m^3}$ of the time evolution of the iodixanol concentration profile in the vertical y-z plane symmetric around $y = 0$ (the dashed line), with only the left half, $-\frac{1}{2}W \le y \le 0$, shown. Three different initial configurations of the dense (36% iodixanol, white) and less dense (10% iodixanol, black) solution give rise to different time evolutions. (a) A vertical slab of the dense fluid in the center. (b) A horizontal slab of the dense fluid at the bottom. (c) Two vertical slabs of the dense fluid at the sides. All configurations develop towards a stable configuration, with the dense fluid located as a nearly vertical slab in the center.

column against gravity, such that it broadens only by diffusion. For the intermediate value $E_{ac} = 2.4\ \mathrm{J/m^3}$, where the gravitational and acoustic forces are comparable, the stable configuration has a triangular shape. Note that the good agreement between the simulated and measured concentration profiles has been obtained without fitting parameters.

In Fig. 3 we show time-resolved simulations obtained with $E_{ac} = 10\ \mathrm{J/m^3}$ for (a) the stable initial configuration with the denser fluid at the center, (b) the unstable initial configuration with the denser fluid at the bottom, and (c) the unstable initial configuration with the denser fluid at the sides. While the stable initial configuration (a) evolves only by diffusion, the unstable initial configurations (b) and (c) evolve by complex advection patterns into essentially the same stable configuration, with the denser fluid at the center. This fluid relocation is in full qualitative agreement with recent experiments [37]. Movies are provided in the Supplemental Material [53].

Discussion.—Our theory for the acoustic force density acting on an inhomogeneous fluid explains recent experimental observations [37,38] and agrees with our experimental validation without free parameters. The additional observation that steady acoustic streaming, driven by dissipation in the acoustic boundary layers, is suppressed in the bulk of an inhomogeneous fluid [38] has not been treated in this Letter. However, Figs. 2 and 3 demonstrate that the acoustic force density stabilizes a particular inhomogeneous configuration, which suggests that there is a competition between the inhomogeneity-induced acoustic force density (13) and the boundary-driven shear-force density associated with acoustic streaming. The experimental observation of stable inhomogeneous configurations further suggests that the latter is negligible. By adding acoustic boundary layers to our model, we are currently investigating this hypothesis. The extension of acoustic radiation force theory to include inhomogeneous fluids through the introduction of the acoustic force density (13) represents an increased understanding of acoustofluidics, in general, and further has the potential to open up new ways for microscale handling of fluids and particles using acoustic fields.

We thank Mads Givskov Senstius, Technical University of Denmark, for assistance with the experiments. P. A. had financial support from the Swedish Research Council (Grant No. 2012-6708), the Royal Physiographic Society, and the Birgit and Hellmuth Hertz Foundation.

*jonkar@fysik.dtu.dk
†bruus@fysik.dtu.dk

[1] L. Rayleigh, Philos. Trans. R. Soc. London **175**, 1 (1884).
[2] H. Schlichting, Phys. Z. **33**, 327 (1932).
[3] C. Eckart, Phys. Rev. **73**, 68 (1948).
[4] W. L. Nyborg, J. Acoust. Soc. Am. **30**, 329 (1958).
[5] L. V. King, Proc. R. Soc. A **147**, 212 (1934).
[6] K. Yosioka and Y. Kawasima, Acustica **5**, 167 (1955).
[7] G. Hertz and H. Mende, Z. Phys. **114**, 354 (1939).
[8] K. Bücks and H. Müller, Z. Phys. **84**, 75 (1933).
[9] A. Hanson, E. Domich, and H. Adams, Rev. Sci. Instrum. **35**, 1031 (1964).
[10] D. Foresti, M. Nabavi, M. Klingauf, A. Ferrari, and D. Poulikakos, Proc. Natl. Acad. Sci. U.S.A. **110**, 12549 (2013).
[11] D. Foresti and D. Poulikakos, Phys. Rev. Lett. **112**, 024301 (2014).
[12] A. Marzo, S. A. Seah, B. W. Drinkwater, D. R. Sahoo, B. Long, and S. Subramanian, Nat. Commun. **6**, 8661 (2015).
[13] C. R. P. Courtney, C. E. M. Demore, H. Wu, A. Grinenko, P. D. Wilcox, S. Cochran, and B. W. Drinkwater, Appl. Phys. Lett. **104**, 154103 (2014).
[14] D. Baresch, J.-L. Thomas, and R. Marchiano, Phys. Rev. Lett. **116**, 024301 (2016).
[15] C. E. M. Démoré, P. M. Dahl, Z. Yang, P. Glynne-Jones, A. Melzer, S. Cochran, M. P. MacDonald, and G. C. Spalding, Phys. Rev. Lett. **112**, 174302 (2014).
[16] A. Y. Rednikov and S. S. Sadhal, J. Fluid Mech. **667**, 426 (2011).
[17] P. B. Muller and H. Bruus, Phys. Rev. E **90**, 043016 (2014).
[18] J. T. Karlsen and H. Bruus, Phys. Rev. E **92**, 043010 (2015).
[19] H. Bruus, J. Dual, J. Hawkes, M. Hill, T. Laurell, J. Nilsson, S. Radel, S. Sadhal, and M. Wiklund, Lab Chip **11**, 3579 (2011).
[20] M. Evander, O. Gidlof, B. Olde, D. Erlinge, and T. Laurell, Lab Chip **15**, 2588 (2015).
[21] K. Lee, H. Shao, R. Weissleder, and H. Lee, ACS Nano **9**, 2321 (2015).
[22] F. Petersson, L. Åberg, A. M. Sward-Nilsson, and T. Laurell, Anal. Chem. **79**, 5117 (2007).
[23] M. Wiklund, Lab Chip **12**, 2018 (2012).
[24] D. J. Collins, B. Morahan, J. Garcia-Bustos, C. Doerig, M. Plebanski, and A. Neild, Nat. Commun. **6**, 8686 (2015).
[25] D. Ahmed, A. Ozcelik, N. Bojanala, N. Nama, A. Upadhyay, Y. Chen, W. Hanna-Rose, and T. J. Huang, Nat. Commun. **7**, 11085 (2016).
[26] F. Guo, Z. Mao, Y. Chen, Z. Xie, J. P. Lata, P. Li, L. Ren, J. Liu, J. Yang, M. Dao, S. Suresh, and T. J. Huang, Proc. Natl. Acad. Sci. U.S.A. **113**, 1522 (2016).
[27] B. Hammarström, T. Laurell, and J. Nilsson, Lab Chip **12**, 4296 (2012).
[28] D. Carugo, T. Octon, W. Messaoudi, A. L. Fisher, M. Carboni, N. R. Harris, M. Hill, and P. Glynne-Jones, Lab Chip **14**, 3830 (2014).
[29] G. Sitters, D. Kamsma, G. Thalhammer, M. Ritsch-Marte, E. J. G. Peterman, and G. J. L. Wuite, Nat. Methods **12**, 47 (2015).
[30] P. Augustsson, C. Magnusson, M. Nordin, H. Lilja, and T. Laurell, Anal. Chem. **84**, 7954 (2012).
[31] P. Li, Z. Mao, Z. Peng, L. Zhou, Y. Chen, P.-H. Huang, C. I. Truica, J. J. Drabick, W. S. El-Deiry, M. Dao, S. Suresh, and T. J. Huang, Proc. Natl. Acad. Sci. U.S.A. **112**, 4970 (2015).
[32] B. Hammarström, B. Nilson, T. Laurell, J. Nilsson, and S. Ekström, Anal. Chem. **86**, 10560 (2014).

[33] *Nonlinear Acoustics*, edited by M. F. Hamilton and D. T. Blackstock (Acoustical Society of America, Melville, NY, 2008).
[34] N. Riley, Annu. Rev. Fluid Mech. **33**, 43 (2001).
[35] M. J. Marr-Lyon, D. B. Thiessen, and P. L. Marston, Phys. Rev. Lett. **86**, 2293 (2001).
[36] N. Bertin, H. Chraïbi, R. Wunenburger, J.-P. Delville, and E. Brasselet, Phys. Rev. Lett. **109**, 244304 (2012).
[37] S. Deshmukh, Z. Brzozka, T. Laurell, and P. Augustsson, Lab Chip **14**, 3394 (2014).
[38] P. Augustsson, J. T. Karlsen, H.-W. Su, H. Bruus, and J. Voldman, Nat. Commun. **7**, 11556 (2016).
[39] R. Barnkob, P. Augustsson, T. Laurell, and H. Bruus, Lab Chip **10**, 563 (2010).
[40] P. Augustsson, R. Barnkob, S. T. Wereley, H. Bruus, and T. Laurell, Lab Chip **11**, 4152 (2011).
[41] L. D. Landau and E. M. Lifshitz, *Fluid Mechanics*, 2nd ed., Vol. 6 (Pergamon Press, Oxford, 1993).
[42] P. M. Morse and K. U. Ingard, *Theoretical Acoustics* (Princeton University Press, Princeton, NJ, 1986).
[43] H. Bruus, Lab Chip **12**, 20 (2012).
[44] P. G. Bergmann, J. Acoust. Soc. Am. **17**, 329 (1946).
[45] C. P. Lee and T. G. Wang, J. Acoust. Soc. Am. **94**, 1099 (1993).
[46] B. L. Smith and G. W. Swift, J. Acoust. Soc. Am. **110**, 717 (2001).
[47] L. Zhang and P. L. Marston, J. Acoust. Soc. Am. **129**, 1679 (2011).
[48] Z. Fan, D. Mei, K. Yang, and Z. Chen, J. Acoust. Soc. Am. **124**, 2727 (2008).
[49] The time average of the product of two time-harmonic complex-valued fields f_1 and g_1 is $\langle f_1 g_1 \rangle = \frac{1}{2}\mathrm{Re}[f_1^* g_1]$, where the asterisk denotes complex conjugation.
[50] The average acoustic energy density E_{ac} is estimated as a function of the piezoelectric-transducer voltage U by observing the focusing of 5 μm polystyrene particles in a homogeneous 10% iodixanol solution and comparing to theoretical models; see Refs. [39,40]. In our system, this yields $E_{\mathrm{ac}} = kU^2$, with $k = 1.2\ \mathrm{J\,m^{-3}\,V^{-2}}$ [38].
[51] We use a fluorescent dextran tracer with the molecular weight of 3000 Da and a diffusivity close to that of iodixanol, which allows indirect visualization of the iodixanol concentration profile; see Ref. [38].
[52] COMSOL Multiphysics 5.2, http://www.comsol.com (2015).
[53] See Supplemental Material at http://link.aps.org/supplemental/10.1103/PhysRevLett.117.114504 for movies of the time evolution of the concentration fields.

Chapter 9

Paper IV in Physical Review Applied

Acoustic tweezing and patterning of concentration fields in microfluidics

DOI: 10.1103/PhysRevApplied.7.034017.

Authors: J.T. Karlsen and H. Bruus.
Journal: Phys. Rev. Applied **7**, 034017 (2017).

Remarks: Supplemental Movies are available online: http://link.aps.org/supplemental/10.1103/PhysRevApplied.7.034017.

Acoustic Tweezing and Patterning of Concentration Fields in Microfluidics

Jonas T. Karlsen* and Henrik Bruus†

Department of Physics, Technical University of Denmark, DTU Physics Building 309, DK-2800 Kongens Lyngby, Denmark

(Received 5 December 2016; published 24 March 2017)

We demonstrate theoretically that acoustic forces acting on inhomogeneous fluids can be used to pattern and manipulate solute concentration fields into spatiotemporally controllable configurations stabilized against gravity. A theoretical framework describing the dynamics of concentration fields that weakly perturb the fluid density and speed of sound is presented and applied to study manipulation of concentration fields in rectangular-channel acoustic eigenmodes and in Bessel-function acoustic vortices. In the first example, methods to obtain horizontal and vertical multilayer stratification of the concentration field at the end of a flow-through channel are presented. In the second example, we demonstrate acoustic tweezing and spatiotemporal manipulation of a local high-concentration region in a lower-concentration medium, thereby extending the realm of acoustic tweezing to include concentration fields.

DOI: 10.1103/PhysRevApplied.7.034017

I. INTRODUCTION

Sparked by the ambition to dynamically manipulate microparticles in solution, there have been major advances in the development of experimental methods to control ultrasound acoustic fields at the microscale [1,2]: for example, using bulk acoustic waves [3–5], surface acoustic waves [6–9], transducer arrays [10–12], and 3D-printed transmission holograms [13]. The acoustic radiation force acting on particles in acoustic fields is used in these systems to manipulate particles and cells, thereby concentrating [14], trapping [15,16], separating [17], and sorting [18] bioparticles and cells based on their acoustomechanical properties. It would be of considerable interest if these methods could be extended to the manipulation of solute concentration fields in microfluidic systems. Indeed, the ability to pattern and manipulate molecular concentration fields plays an essential role in several lab-on-a-chip applications and in controlled studies of biological processes such as development, inflammation, wound healing, and cancer, for which biomolecule gradients act as cellular signaling mechanisms [19]. The standard approach to precisely generate specified concentration gradients is to use microfluidic networks [20,21]—with limited temporal control, however.

Here, we present a theoretical analysis of acoustic tweezing, patterning, and manipulation of solute concentration fields in microfluidics. We predict that acoustics will offer a high degree of spatiotemporal control in these dynamical operations. Our study is predominantly motivated by the recent development of isoacoustophoresis [22], a microfluidic analog to density-gradient centrifugation. In isoacoustophoresis, cells are differentiated by their phenotype-specific acoustic impedance by observing their equilibrium position in an acoustically stabilized concentration gradient. The physics of this stabilization has only recently been understood [23], and an increased understanding of the ability of acoustics to shape and manipulate a concentration field is important to further develop the method.

In this work, we explore the consequences of our recent theory of the acoustic force density acting on inhomogeneous fluids in acoustic fields [23], a theory successfully validated by experiments, which explains the acoustic stabilization and relocation of inhomogeneous fluids observed in microchannels [24]. We define an inhomogeneous fluid as a fluid with spatial variations in density and speed of sound caused by a varying concentration of a solute. Consequently, there is a direct correspondence between fluid inhomogeneities and solute concentration. We present a theoretical framework for analyzing acoustic manipulation of such concentration fields, and we apply it to the special cases of rectangular-channel eigenmodes and Bessel-function acoustic vortices. In the former system, we present methods to obtain stable horizontal and vertical multilayer stratification of the concentration field at the end of a flow-through channel starting from typical inlet conditions. In the latter system, we demonstrate acoustic tweezing and spatiotemporal manipulation of a local high-concentration region in a lower-concentration medium. This result extends the realm of acoustic tweezing to include concentration fields.

II. MODEL SYSTEMS

In Fig. 1, the two typical model systems are introduced to provide the context necessary to appreciate the ensuing theoretical development. The implementation and design of

*jonkar@fysik.dtu.dk
†bruus@fysik.dtu.dk

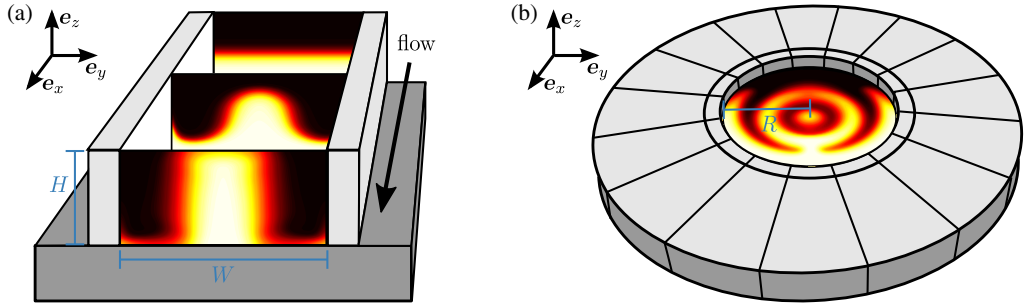

FIG. 1. Sketches of the two model systems considered in this work for the controlled ultrasound manipulation of inhomogeneous fluids at the microscale. The concentration fields (white, high; black, low) are manipulated by the acoustic field excited in the fluid domain by the attached piezoelectric transducers. (a) Acoustic eigenmodes in the two-dimensional cross section of a rectangular microchannel of width W and height H in the y-z plane. (b) Acoustic Bessel-function vortices in the two-dimensional x-y plane generated by a circular 16-element phased transducer array of inner radius R. Gravity acts in the negative z direction.

the numerical model and how it corresponds to experimental conditions is discussed in more detail in Sec. IV.

The first model system, shown in Fig. 1(a), is a long, straight, rectangular glass-silicon microchannel, placed along the x axis, with a piezoelectric transducer glued underneath. By actuating the transducer at a resonance frequency of the cavity, an acoustic standing-wave field can be established in the channel cross section in the y-z plane, which is typically a few hundred micrometers in the width W and height H, leading to fundamental resonance frequencies on the order of 1–10 MHz. These systems are well characterized [4,25–28] and are used in various biomedical applications, for example, the enrichment of circulating tumor cells in blood [14,29].

The second model system, shown in Fig. 1(b), consists of a transducer array with 16 elements enclosing a circular fluid chamber. It is inspired by, and closely resembles, the experimental systems in Refs. [9,10,30–32]. The radius of these chambers is typically around 1 mm, and the chambers may have between 8 and 64 transducer elements operating at MHz frequency. By controlling the amplitude and phase of each transducer, approximate Bessel-function acoustic vortices may be generated by a superposition of waves, then used to trap and move microparticles [10,31].

III. THEORY

The recently developed theory for the acoustic force density acting on inhomogeneous fluids in acoustic fields [23] is based on the separation of time scales between the fast acoustic time scale t and the slow hydrodynamic time scale τ. In general, the large separation of time scales ($\tau \sim 10^5 t$) allows the acoustic fields, oscillating at the fast time scale t, to be solved for while keeping the hydrodynamic degrees of freedom fixed at each instance in time τ on the slow time scale. Because of the inhomogeneity in the fluid medium, the resulting acoustic field yields a divergence in the time-averaged acoustic momentum-flux-density tensor [23], and this is the origin of the acoustic force density $\boldsymbol{f}_{\mathrm{ac}}$, which enters the slow-time-scale hydrodynamics as an external driving force.

The inhomogeneity in the fluid medium is caused by the solute concentration field $s(\boldsymbol{r},\tau)$. The fluid density ρ_0, compressibility κ_0, and dynamic viscosity η_0 are all functions of the solute concentration s, and thus functions of space and time as the concentration field evolves by advection and diffusion,

$$\rho_0 = \rho_0[s(\boldsymbol{r},\tau)], \quad \kappa_0 = \kappa_0[s(\boldsymbol{r},\tau)], \quad \eta_0 = \eta_0[s(\boldsymbol{r},\tau)]. \tag{1}$$

The specific dependences of ρ_0, κ_0, and η_0 on concentration s depend on the solute used to establish the inhomogeneity, e.g., iodixanol (OptiPrep), polysucrose (Ficoll), or colloidal nanoparticles (Percoll) as commonly used in density-gradient centrifugation. In this work, we consider solutions of iodixanol, for which we have measured the fluid properties as functions of concentration [22].

A. Slow-time-scale hydrodynamics

The hydrodynamics on the slow time scale τ is governed by the momentum and mass-continuity equations for the fluid velocity $\boldsymbol{v}(\boldsymbol{r},\tau)$ and pressure $p(\boldsymbol{r},\tau)$, as well as the advection-diffusion equation for the solute concentration field $s(\boldsymbol{r},\tau)$ of the solute with diffusivity D,

$$\partial_\tau(\rho_0\boldsymbol{v}) = \boldsymbol{\nabla}\cdot[\boldsymbol{\sigma} - \rho_0\boldsymbol{v}\boldsymbol{v}] + \boldsymbol{f}_{\mathrm{ac}} + \rho_0\boldsymbol{g}, \tag{2a}$$

$$\partial_\tau\rho_0 = -\boldsymbol{\nabla}\cdot(\rho_0\boldsymbol{v}), \tag{2b}$$

$$\partial_\tau s = -\boldsymbol{\nabla}\cdot[-D\boldsymbol{\nabla}s + \boldsymbol{v}s]. \tag{2c}$$

Here, $\boldsymbol{g}$ is the acceleration due to gravity, and $\boldsymbol{\sigma}$ is the fluid stress tensor, given by

$$\boldsymbol{\sigma} = -p\mathbf{I} + \eta_0[\boldsymbol{\nabla}\boldsymbol{v} + (\boldsymbol{\nabla}\boldsymbol{v})^T] + \left(\eta_0^b - \frac{2}{3}\eta_0\right)(\boldsymbol{\nabla}\cdot\boldsymbol{v})\mathbf{I}, \tag{3}$$

where the superscript T indicates tensor transposition, and η_0 and η_0^b are the dynamic and bulk viscosities, respectively. The equations constitute an advection-diffusion flow problem with an external forcing due to the acoustic and gravitational force densities $\boldsymbol{f}_{\mathrm{ac}}$ and $\rho_0\boldsymbol{g}$, both appearing on the right-hand side of the momentum equation (2a).

B. The acoustic force density

The acoustic force density $\boldsymbol{f}_{\mathrm{ac}}$ acting on the fluid on the slow hydrodynamic time scale τ was derived in Ref. [23] from a divergence in the time-averaged acoustic momentum-flux-density tensor induced by continuous spatial variations in the fluid parameters of density ρ_0 and compressibility κ_0,

$$\boldsymbol{f}_{\mathrm{ac}} = -\frac{1}{4}|p_1|^2\boldsymbol{\nabla}\kappa_0 - \frac{1}{4}|\boldsymbol{v}_1|^2\boldsymbol{\nabla}\rho_0. \tag{4}$$

Here, p_1 and $\boldsymbol{v}_1$ are the acoustic pressure and the acoustic velocity field, respectively, assumed to be time-harmonic first-order perturbations of the hydrodynamic degrees of freedom.

Because the compressibility κ_0 is difficult to measure directly, it is often more convenient to work with the fluid density ρ_0 and speed of sound c_0, both of which are readily measured as functions of concentration. With $\kappa_0 = 1/(\rho_0 c_0^2)$, we find

$$\boldsymbol{\nabla}\kappa_0 = \boldsymbol{\nabla}\left(\frac{1}{\rho_0 c_0^2}\right) = -\kappa_0\frac{\boldsymbol{\nabla}\rho_0}{\rho_0} - 2\kappa_0\frac{\boldsymbol{\nabla}c_0}{c_0}, \tag{5}$$

and the expression (4) becomes

$$\boldsymbol{f}_{\mathrm{ac}} = \frac{1}{4}[\kappa_0|p_1|^2 - \rho_0|\boldsymbol{v}_1|^2]\frac{\boldsymbol{\nabla}\rho_0}{\rho_0} + \frac{1}{2}\kappa_0|p_1|^2\frac{\boldsymbol{\nabla}c_0}{c_0}. \tag{6}$$

In the weakly inhomogeneous limit where the variations in density ρ_0 and speed of sound c_0 are small, we introduce the dimensionless relative deviations $\hat{\rho}(\boldsymbol{r},\tau)$ and $\hat{c}(\boldsymbol{r},\tau)$ and write

$$\rho_0(\boldsymbol{r},\tau) = \rho_0^{(0)}[1+\hat{\rho}(\boldsymbol{r},\tau)], \qquad |\hat{\rho}(\boldsymbol{r},\tau)| \ll 1, \tag{7a}$$

$$c_0(\boldsymbol{r},\tau) = c_0^{(0)}[1+\hat{c}(\boldsymbol{r},\tau)], \qquad |\hat{c}(\boldsymbol{r},\tau)| \ll 1. \tag{7b}$$

Here, the superscript (0) indicates zeroth-order in the inhomogeneity $\hat{\rho}$ and $\hat{c}$. To first order in $\hat{\rho}$ and $\hat{c}$, the force density (6) then becomes

$$\boldsymbol{f}_{\mathrm{ac}}^{(1)} = \frac{1}{4}[\kappa_0^{(0)}|p_1^{(0)}|^2 - \rho_0^{(0)}|\boldsymbol{v}_1^{(0)}|^2]\boldsymbol{\nabla}\hat{\rho} + \frac{1}{2}\kappa_0^{(0)}|p_1^{(0)}|^2\boldsymbol{\nabla}\hat{c}. \tag{8}$$

In this expression, the acoustic fields $p_1^{(0)}$ and $\boldsymbol{v}_1^{(0)}$ are zeroth order in $\hat{\rho}$ and $\hat{c}$ and, consequently, the fields are obtained as solutions of the homogeneous-fluid wave equation. This constitutes a significant simplification in applications of the theory, as will be shown next.

Let p_a denote the acoustic pressure amplitude, ω the angular acoustic frequency, and $k_0^{(0)} = \omega/c_0^{(0)}$ the homogeneous-fluid wave number. The time-harmonic acoustic fields $p_1^{(0)}$ and $\boldsymbol{v}_1^{(0)}$ may then be written in terms of a nondimensionalized pressure field $\hat{p}_1^{(0)}(\boldsymbol{r},\tau)$ as

$$p_1^{(0)} = p_a\hat{p}_1^{(0)}e^{-i\omega t}, \quad \boldsymbol{v}_1^{(0)} = \frac{-ip_a}{k_0^{(0)}c_0^{(0)}\rho_0^{(0)}}\boldsymbol{\nabla}\hat{p}_1^{(0)}e^{-i\omega t}. \tag{9}$$

Inserting Eq. (9) into Eq. (8) and introducing the homogeneous-fluid oscillation-time-averaged acoustic energy density $E_{\mathrm{ac}}^{(0)} = \frac{1}{4}\kappa_0^{(0)}p_a^2$, the acoustic force density $\boldsymbol{f}_{\mathrm{ac}}^{(1)}$ can be rewritten as

$$\boldsymbol{f}_{\mathrm{ac}}^{(1)} = E_{\mathrm{ac}}^{(0)}[R(\boldsymbol{r},\tau)\boldsymbol{\nabla}\hat{\rho} + C(\boldsymbol{r},\tau)\boldsymbol{\nabla}\hat{c}], \tag{10a}$$

where we have introduced the dimensionless field-shape functions $R(\boldsymbol{r},\tau)$ and $C(\boldsymbol{r},\tau)$, given by

$$R(\boldsymbol{r},\tau) = |\hat{p}_1^{(0)}|^2 - (k_0^{(0)})^{-2}|\boldsymbol{\nabla}\hat{p}_1^{(0)}|^2, \tag{10b}$$

$$C(\boldsymbol{r},\tau) = 2|\hat{p}_1^{(0)}|^2. \tag{10c}$$

The field-shape functions $R(\boldsymbol{r},\tau)$ and $C(\boldsymbol{r},\tau)$ depend on the shape of the homogeneous-fluid acoustic pressure field $\hat{p}_1^{(0)}(\boldsymbol{r},\tau)$, often known analytically, and may thus be varied in space and time. Consequently, our theoretical framework suggests that a high level of spatiotemporal control of fluid inhomogeneities can be achieved.

C. Eigenmodes in a rectangular microchannel

Consider a long, straight, hard-walled microchannel of width W and height H, with the aspect ratio $\alpha = H/W$. The acoustic fields obtained at resonance conditions in the two-dimensional channel cross section take the form of eigenmode solutions to the Helmholtz wave equation with hard-wall boundary conditions. Choosing the fluid domain in the y-z plane defined by $0 < y < W$ and $0 < z < H$, and introducing the normalized coordinates $\hat{y} = (\pi/W)y$ and $\hat{z} = (\pi/H)z$, the eigenmodes $\hat{p}_1^{(0)}(\hat{y},\hat{z})$ are

$$\hat{p}_1^{(0)} = \cos(n\hat{y})\cos(m\hat{z}), \tag{11a}$$

$$\text{with} \quad f_{nm} = \frac{\omega_{nm}}{2\pi} = \frac{c}{2}\sqrt{\left(\frac{n}{W}\right)^2 + \left(\frac{m}{H}\right)^2}. \tag{11b}$$

Here, $n = 0, 1, 2, \ldots$ and $m = 0, 1, 2, \ldots$ are the mode numbers in the y and z directions, respectively, and f_{nm} is the resonance frequency of the nm mode.

Inserting the eigenmode solution (11) into Eq. (10), one obtains the acoustic force density acting on the fluid in the nm mode. After some algebra, the field-shape functions $R_{nm}(\hat{y},\hat{z})$ and $C_{nm}(\hat{y},\hat{z})$ take the form

$$R_{nm}(\hat{y},\hat{z}) = \frac{1}{2}\left\{\frac{n^2}{n^2+m^2\alpha^{-2}}[\cos(2n\hat{y})-\cos(2m\hat{z})] + \cos(2n\hat{y})\cos(2m\hat{z}) + \cos(2m\hat{z})\right\}, \quad (12a)$$

$$C_{nm}(\hat{y},\hat{z}) = \frac{1}{2}[1+\cos(2n\hat{y})][1+\cos(2m\hat{z})]. \quad (12b)$$

In the horizontal half-wave resonance $(n,m)=(1,0)$, we obtain $R_{10}=\cos(2\hat{y})$ and $C_{10}=1+\cos(2\hat{y})$, in agreement with Ref. [23], given an appropriate change of the coordinate system.

D. Bessel-function acoustic vortex fields

It has been demonstrated that transducer arrays can be used to generate acoustic vortices in fluid-filled chambers [10,31–33]. By controlling the amplitude and phase of each transducer in a circular array, one can generate approximate Bessel-function pressure fields of the form [31]

$$\hat{p}_1^{(0)} = J_l(k_0^{(0)}r)e^{il\theta}. \quad (13)$$

Here, we are using cylindrical polar coordinates (r,θ,z) with the origin at the center of the Bessel function. J_l is the lth-order Bessel function of the first kind, and l is the number of 2π phase shifts around the axis of the vortex, often referred to as the topological charge.

The acoustic force density acting on an inhomogeneous fluid in the acoustic vortex is obtained by inserting Eq. (13) into Eq. (10). Introducing the normalized radial coordinate $\hat{r}=k_0^{(0)}r$ and making use of the recurrence relations $(2n/r)J_n(\hat{r}) = J_{n-1}(\hat{r})+J_{n+1}(\hat{r})$ and $2J_n'(\hat{r}) = J_{n-1}(\hat{r})-J_{n+1}(\hat{r})$, the field-shape functions $R_l(\hat{r})$ and $C_l(\hat{r})$ of the lth-order vortex take the form

$$R_l(\hat{r}) = [J_l(\hat{r})]^2 - \frac{1}{2}[J_{l-1}(\hat{r})]^2 - \frac{1}{2}[J_{l+1}(\hat{r})]^2, \quad (14a)$$

$$C_l(\hat{r}) = 2[J_l(\hat{r})]^2. \quad (14b)$$

IV. NUMERICAL MODEL IN 2D

In this section, we present the implementation and design of our numerical models. Emphasis is put on the considerations that went into designing numerical models that describe experimental conditions that may be reproduced with the setups introduced in Sec. II and sketched in Fig. 1. In order to reduce computational complexity, we model only the 2D dynamics in the perpendicular planes specified for each model in Fig. 1.

A. Numerical implementation

In the numerical models of the slow-time-scale hydrodynamics, the coupled field equations (2) are implemented and solved on weak form using the finite-element solver COMSOL Multiphysics [34]. We consider the limit of weakly inhomogeneous fluids and use the analytical expression (10a) for the acoustic force density $\boldsymbol{f}_{\rm ac}^{(1)}$ with the field-shape functions given in the rectangular-channel eigenmodes and acoustic vortex fields, respectively, in Eqs. (12) and (14).

For numerical stability, a logarithmic concentration field $\hat{s}$, with $s=s_0\exp(\hat{s})$, is used as the independent concentration variable. A free triangular mesh with an element mesh size around $\Delta h = 2\ \mu$m is used. Lagrange shape functions are used with cubic-order elements in the velocity and concentration fields and quadratic-order elements in the pressure. A backward differentiation formula is used for the time stepping with an initial time step of 50 μs and a maximum time step of $\Delta t = 5$ ms in all of the simulations, except that of acoustic tweezing, where the maximum time step is reduced to $\Delta t = 0.5$ ms. These choices of parameters are motivated by the numerical stability criteria that the cell Péclet number $\mathrm{Pe} = U\Delta h/D$ and the Courant number $\mathrm{Co} = U\Delta t/\Delta h$, where U is a characteristic flow speed, should be on the order of unity or smaller.

The boundary conditions imposed on the slow-time-scale velocity and concentration fields $\boldsymbol{v}(\boldsymbol{r},\tau)$ and $s(\boldsymbol{r},\tau)$ at the boundary $\partial\Omega$ of the fluid domain Ω, with normal vector $\boldsymbol{n}$, are the standard no-slip and no-flux conditions,

$$\boldsymbol{v}=\boldsymbol{0}, \qquad \boldsymbol{n}\cdot\boldsymbol{\nabla}s = 0, \quad \text{for } \boldsymbol{r}\in\partial\Omega. \quad (15)$$

Several convergence tests are carried out to ensure numerical convergence. For example, the integrated concentration is conserved with a maximum relative error of 2×10^{-3} at all times.

B. Modeling the fluid inhomogeneity

We model aqueous solutions of iodixanol (OptiPrep), for which the fluid parameters have been measured experimentally as functions of the iodixanol volume-fraction concentration s [22]. OptiPrep is a cell-friendly medium that is used in density-gradient centrifugation and isoacoustic focusing. In the models, we consider initial concentration fields with iodixanol volume fractions ranging from $s_{\rm min}=0.1$ to $s_{\rm max}=0.3$, yielding a relative density difference of up to 10%, while the maximum relative variation in the speed of sound is 0.5%. Consequently, we neglect variations in c_0, which means that only gradients in ρ_0 contribute to the acoustic force density.

The polynomials fitting the measured density $\rho_0(s)$ and dynamic viscosity $\eta_0(s)$, as functions of the iodixanol volume-fraction concentration s, are [22]

$$\rho_0 = \rho_0^{(0)}[1+a_1 s], \quad (16a)$$

$$\eta_0 = \eta_0^{(0)}[1 + b_1 s + b_2 s^2 + b_3 s^3]. \quad (16b)$$

Here, $\rho_0^{(0)} = 1005$ kg/m^3 and $\eta_0^{(0)} = 0.954$ mPa s, and the dimensionless constants are $a_1 = 0.522$, $b_1 = 2.05$, $b_2 = 2.54$, and $b_3 = 22.8$. In Ref. [22], the diffusivity of iodixanol was measured to $D = 0.9 \times 10^{-10}$ m^2/s. For the bulk viscosity, we use the value of pure water [35].

C. Modeling the rectangular microchannel

In this model, we consider a long, straight, rectangular microchannel of width $W = 375\,\mu$m and height $H = 150\,\mu$m, as sketched in Fig. 1(a). In acoustophoresis experiments, acoustic eigenmodes of the two-dimensional channel cross section transverse to the flow are used extensively to manipulate and focus particles and cells based on their mechanical properties. Two notable advantages of using acoustic eigenmodes, or bulk acoustic waves, are that the eigenmodes are easily excited by an attached piezoceramic transducer actuated at the resonance frequency and that high acoustic energy densities can be obtained in the resonant modes. Typical quality factors in glass-silicon microchips are between 10^2 and 10^3, and typical measured acoustic energy densities are in the range 1–1000 J/m^3 [25,27]. We use $E_{\rm ac}^{(0)} = 10$ J/m^3, approximately an order of magnitude larger than the hydrostatic pressure difference across the channel height, ensuring that gravity plays only a minor role in the fluid relocation [23].

Referring again to Fig. 1(a), we are modeling a flow-through microchannel system where the flow rate can be controlled, thereby setting the retention time of the fluid in the channel. In our time-dependent model, the time τ can thus be translated into a downstream length L from the inlet. For example, in the system under consideration, a fluid retention time of $\tau_{\rm ret} = 1.0$ s over a length of $L = 5.0$ mm implies a flow rate of 17 μL/ min, all of which are realistic experimental parameters [22]. Diffusion generally plays a role in manipulating concentration fields. However, the time scale of diffusion across one third of the channel width is $\tau_{\rm diff} = (1/2D)(\frac{1}{3}W)^2 = 87$ s, leaving enough time to conduct typical steady-flow experiments at relevant flow rates without diffusion flattening the gradients.

The validity of this 2D model of the flow-through channel requires that the gradients of the concentration s in the axial direction $r_\parallel$ of the flow are small in comparison to the gradients in the transverse direction $r_\perp$, that is, $|\Delta s/\Delta r_\parallel| \ll |\Delta s/\Delta r_\perp|$. Because the length scales $\Delta r_\parallel$ and $\Delta r_\perp$ are set by the characteristic flow speeds, the condition is that the flow speed $U_\parallel$ in the axial direction should be much larger than the acoustically induced flow speed $U_\perp$ in the transverse plane, $U_\parallel \gg U_\perp$. In our simulations, considering typical experimental flow rates, $U_\parallel$ is approximately an order of magnitude larger than $U_\perp$.

D. Modeling the acoustic vortex field

In this model, we consider a circular fluid chamber, as sketched in Fig. 1(b), in which an acoustic vortex field of the form (13) is excited by the surrounding transducer array or by swirling surface acoustic waves [9,10,32]. Notice that, in contrast to the rectangular-microchannel acoustic fields, the acoustic vortices are nonresonant fields, and the center of the vortex can be moved relative to the chamber. In our model, we use a chamber of radius $R = 250\,\mu$m, an acoustic energy density of $E_{\rm ac}^{(0)} = 10$ J/m^3, and a frequency of $f = 7.5$ MHz.

V. SIMULATION RESULTS

We present a selection of simulation results demonstrating acoustics as a means to spatiotemporally control, manipulate, and relocate solute concentration fields in microsystems. Specifically, we demonstrate the manipulation of concentration fields in rectangular-channel eigenmodes and in acoustic vortex fields in circular chambers. In the former, we demonstrate the use of sequential eigenmode actuation to obtain horizontal or vertical multilayering of the fluid inhomogeneities. We further motivate and introduce the simple but useful concept of orthogonal relocation. In the circular chamber, we demonstrate the trapping and translation of a fluid inhomogeneity using Bessel-function acoustic tweezers.

A. Multilayering of concentration fields in rectangular-channel eigenmodes

We consider the patterning of concentration fields in the nm eigenmodes in the rectangular microchannel using the modes $(n, m) = (1, 0)$, (2,0), (0,1), (0,2), and (2,1) as examples. The resonance frequency f_{nm} of these eigenmodes is obtained from Eq. (11b), yielding $f_{10} = 2.0$ MHz, $f_{20} = 4.0$ MHz, $f_{01} = 5.0$ MHz, $f_{02} = 10$ MHz, and $f_{21} = 6.4$ MHz.

In Fig. 2, we consider three different initial conditions, a, b, and c (first column), on the concentration field $s(\boldsymbol{r}, 0)$. In the following columns are shown the concentration fields $s(\boldsymbol{r}, \tau)$ in the selected nm modes after a time $\tau = 1.0$ s for each of the three initial configurations, a, b, and c. The resulting configurations are denoted $i - nm$, with i indicating the initial configuration ($i = a$, b, or c) and nm denoting the mode of actuation. The top row shows the field-shape functions R_{nm} of the corresponding modes. In general, the denser high-concentration fluid (30% iodixanol, white) is relocated into the minima of R_{nm} appearing at pressure nodes, as one might anticipate from the analogy to the acoustic radiation force acting on a particle. It should be emphasized, however, that, in contrast to the acoustic radiation force acting on a particle in a standing wave, $\boldsymbol{f}_{\rm ac}$ is a nonconservative force and it cannot, in general, be written as the gradient of a potential. The acoustic force density $\boldsymbol{f}_{\rm ac}$, moreover, depends on the history of the system,

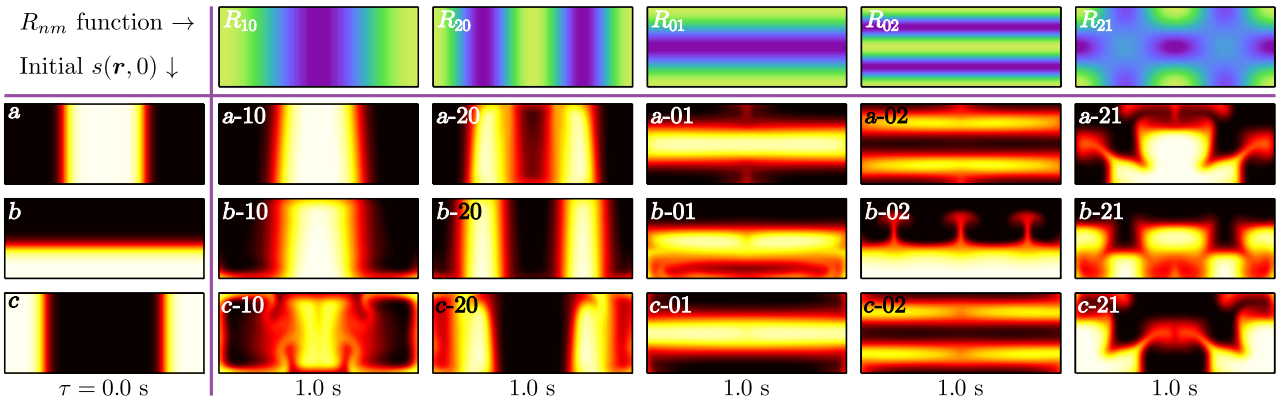

FIG. 2. Patterning of inhomogeneous iodixanol solutions in rectangular-channel eigenmodes. The top row shows the field-shape functions R_{nm} for each mode nm (min, dark blue; max, light green). Three different initial concentration fields $s(\boldsymbol{r},0)$ of the dense (30% iodixanol, white) and less dense (10% iodixanol, black) solutions are considered (first column, a, b, and c). The next columns show the resulting concentration fields $s(\boldsymbol{r},\tau)$ after a retention time of $\tau = 1.0$ s in either the 10 mode (second column), the 20 mode (third column), the 01 mode (fourth column), the 02 mode (fifth column), or the 21 mode (sixth column), starting from the initial condition a (second row), b (third row), or c (bottom row).

which is also in contrast to the particle force. For a given mode, the concentration fields tend to evolve towards the same quasistable equilibrium configuration; however, the different initial conditions generally influence the resulting configurations.

Inspecting Fig. 2, one finds that relocation of the inhomogeneity into vertical layers is obtained for $m = 0$, while horizontal layers are obtained for $n = 0$. This result is to be expected from the geometry of the acoustic field. However, comparing a-01, b-01, and c-01, it is evident that the concentration field after 1 s of actuation in the 01 mode depends strongly on the initial configuration (a, b, or c). Indeed, configurations a and c have been relocated into much "cleaner" 01-mode configurations with a single horizontal layer compared to configuration b. The reason is that the relocations $a \to a$-01 and $c \to c$-01 are orthogonal relocations, in the sense that the initial and final stratifications are orthogonal to one another. By contrast, the relocation $b \to b$-01 is a parallel relocation, where whole fluid layers are to be moved into new parallel positions, which can only proceed by an instability. The instability is particularly evident in the 02 mode comparing the orthogonally relocated configurations a-02 and c-02 to b-02, the latter for which the parallel relocation proceeds by a Rayleigh–Taylor-like instability, shooting up three streams that slowly feed the second horizontal layer.

These observations suggest that orthogonal relocation provides the most effective way of relocating and patterning concentration fields. In the event that a desired relocation is parallel, as in the example b-01 starting from the configuration b, the resulting horizontally layered 01-mode configuration is blurred because it proceeds by an instability. The solution to obtaining sharp horizontally layered 01- and 02-mode configurations starting from b is to go through a sequence of orthogonal relocations. By applying the sequence b-10-0m, the 10 mode being an intermediate, one can achieve sharp horizontally layered 0m-mode configurations from the initial configuration b. This operational principle is illustrated in Fig. 3, where the relocation dynamics is also indicated by showing

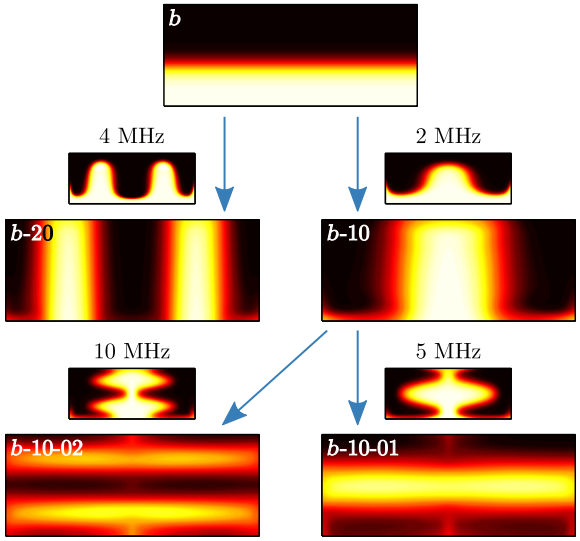

FIG. 3. Vertical and horizontal layering of iodixanol concentration fields $s(\boldsymbol{r},\tau)$ starting from the horizontally layered initial configuration b with the dense fluid (30% iodixanol, white) at the bottom of the channel and the less dense fluid (10% iodixanol, black) at the top (top row). Each arrow (blue) represents an orthogonal relocation obtained by exciting an nm eigenmode in the rectangular channel for 1 s, with the miniature showing the transition 50 ms after the mode shift. Vertical layering is obtained directly by actuation of the 10 or the 20 mode, yielding the configurations b-10 and b-20, respectively. Horizontal layering involves an intermediate step going through the 10 mode, yielding the b-10-01 and b-10-02 configurations.

intermediate configurations. A movie of the dynamics in the sequence *b*-10-01-20 can be found in the Supplemental Material [36].

In summary, starting from a single-layer configuration, one can achieve multilayering of concentration fields on a 1-s time scale in the rectangular-channel eigenmodes commonly employed in acoustophoresis. While we focus on the spatial patterning, the ability to switch between modes provides temporal control of the concentration field at the end of the flow-through channel. This type of acoustic fluid manipulation is best performed by orthogonal relocation, and a parallel relocation can always be substituted by two sequential orthogonal relocations.

B. Patterning and tweezing of concentration fields in acoustic vortex fields

Next, we demonstrate the patterning and spatiotemporal manipulation of concentration fields in Bessel-function acoustic vortex fields in circular fluid chambers. Starting from the initial concentration field $s(\boldsymbol{r},0)$, shown in Fig. 4(a), with the denser fluid (30% iodixanol, white) occupying half of the circular domain. Figures 4(b)–4(d) show the concentration fields $s(\boldsymbol{r},\tau)$ after $\tau = 3.0$ s of actuation in acoustic vortices of orders $l = 0$, $l = 1$, and $l = 2$, respectively. Again, it is observed that the denser fluid tends to be relocated into the minima of the field-shape functions R_l.

The central region of an acoustic vortex is of particular interest because it provides a trapping potential that can be used to trap and manipulate particles. Here, considering inhomogeneous fluid manipulation, we define the central region of the lth-order vortex from the condition $\hat{r} < \hat{r}_l^*$, where $\hat{r}_l^*$ is the first nonzero root of the field-shape function, $R_l(\hat{r}_l^*) = 0$. This condition yields the approximate values, $\hat{r}_0^* = 1.44$, $\hat{r}_1^* = 1.18$, and $\hat{r}_2^* = 2.26$. As demonstrated in Fig. 4, in the vortex with $l = 0$, the denser fluid (white) is forced outside of the central region, while in the vortices with $l = 1$ and $l = 2$, the denser fluid is forced into the central region. Mathematically, this result follows directly from Eq. (10a) (with $\boldsymbol{\nabla}\hat{c} = \boldsymbol{0}$) by inspecting the field-shape functions $R_l(r)$ shown in Fig. 4 because they indicate the initial radial distribution of the acoustic force density acting on the blurred interface. Physically, the acoustic pressure is maximum at the center for $l = 0$, while it is zero for $l > 0$. Note, furthermore, that, for $l > 0$, the central trapping region becomes larger for an increasing l. These findings for manipulation of inhomogeneous fluids are analogous to those of the acoustic tweezing of particles [10].

Acoustic tweezing of a high-concentration region in a lower-concentration medium can thus be realized in the central region of vortices with $l > 0$. Hence, the central region may be used to confine and translate a fluid inhomogeneity, as will be demonstrated next using the $l = 1$ vortex. We consider an initial concentration field $s(\boldsymbol{r},0)$ that has a Gaussian high-concentration region (30% iodixanol, white) centered at the position $(r,\theta) = (\frac{1}{2}R, \frac{1}{2}\pi)$, as given in polar coordinates, in the lower-concentration medium (10% iodixanol); see Fig. 5(a). The width (or standard deviation) of the Gaussian is set to $\sigma = 0.5\hat{r}_1^*$, half the width of the central trapping region. The acoustic vortex is initially centered at the position of the inhomogeneity, and it is then translated in a closed-loop equilateral triangle moving in straight lines from $(\frac{1}{2}R, \frac{1}{2}\pi)$ to $(\frac{1}{2}R, -\frac{1}{6}\pi)$ to $(\frac{1}{2}R, -\frac{5}{6}\pi)$, and finally back to the starting position in $(\frac{1}{2}R, \frac{1}{2}\pi)$. The translation speed $U = 0.7$ mm/s of the center of the vortex is chosen such that it takes 0.3 s to move the distance from one corner of the triangle to the next. The resulting concentration field $s(\boldsymbol{r},\tau)$ after $\tau = 0.3$, 0.6, and 0.9 s is shown in Figs. 5(b), 5(c), and 5(d), respectively, with the central region of the vortex indicated by the green circle, and the path of the center of the vortex

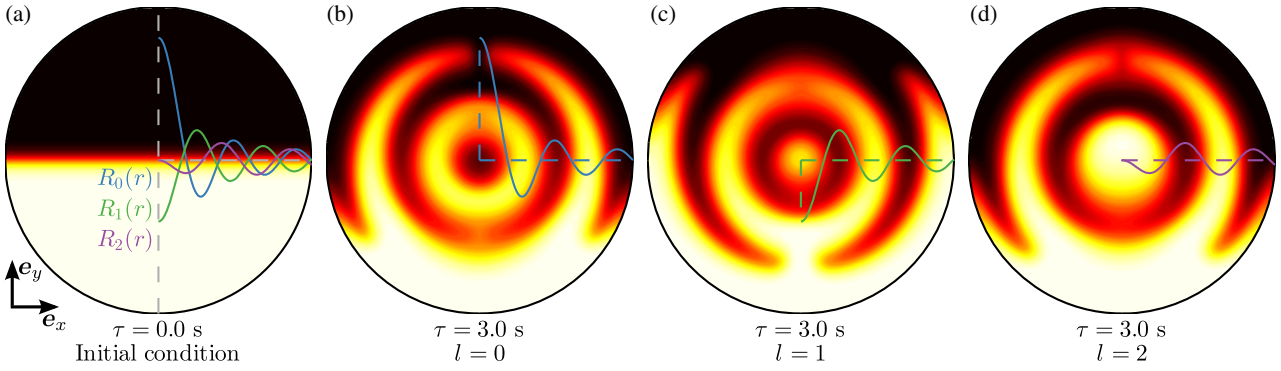

FIG. 4. Patterning of inhomogeneous iodixanol solutions in acoustic vortices of topological charge l. (a) Initial concentration field $s(\boldsymbol{r},0)$ with the dense (30% iodixanol, white) and less dense (10% iodixanol, black) solutions each occupying half of the circular domain. The radial field-shape function $R_l(r)$ is shown for $l = 0$ (blue), $l = 1$ (green), and $l = 2$ (violet), indicating the initial magnitude and (negative) direction of the acoustic force density acting on the blurred interface. (b)–(d) Resulting concentration fields $s(\boldsymbol{r},\tau)$ after $\tau = 3.0$ s in the acoustic vortex with $l = 0$, $l = 1$, and $l = 2$, respectively, with a central trapping region for $l > 0$. The denser fluid (white) is relocated into the minima of the field-shape functions R_l.

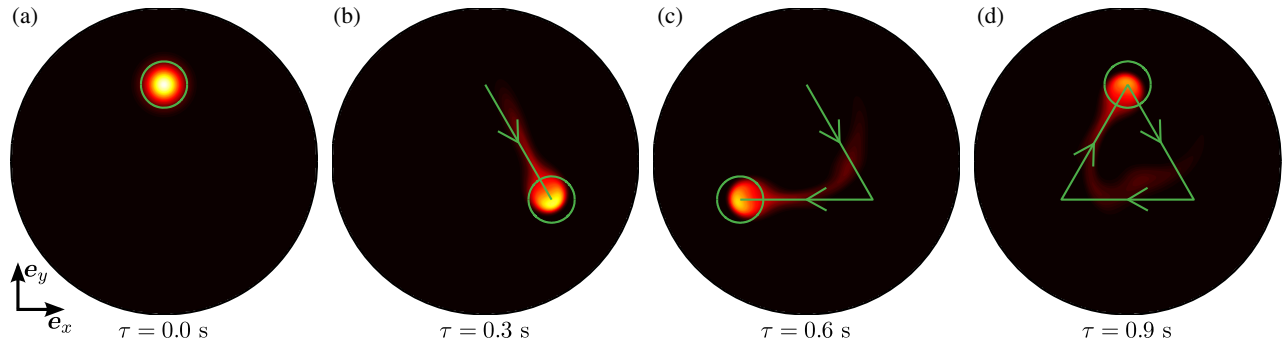

FIG. 5. Acoustic tweezing and translation of a local high-concentration region using an acoustic vortex with topological charge $l = 1$. (a) Initial concentration field $s(\boldsymbol{r}, 0)$ with a Gaussian high-concentration region (30% iodixanol, white) in a lower-concentration medium (10% iodixanol, black). Initially, the acoustic vortex is centered at the position of the inhomogeneity, with the green circle indicating the central region of the vortex. At time $\tau > 0.0$ s, the vortex is moved at constant speed $U = 0.7$ mm/s along the green path in a closed-loop triangle. The resulting concentration fields $s(\boldsymbol{r}, \tau)$ after $\tau = 0.3$, 0.6, and 0.9 s are shown in (b), (c), and (d), respectively.

by the straight green lines. To a good approximation, the high-concentration solution is kept within the central region of the vortex as it is translated in space, leaving only a trailing diffusive residue. Movies showing the manipulation in real time for two different translation speeds are available in the Supplemental Material [36]. We find that when the translation speed of the vortex is increased by a factor of 3, the inhomogeneity does not remain trapped at the center during the full loop. Conversely, for slower translation speeds, the inhomogeneity stays in the center of the vortex, but the increased loop time leads to a more pronounced diffusion broadening.

The results presented in this section provide theoretical evidence that the applicability of acoustic tweezers can be extended beyond particle manipulation to include manipulation of concentration fields—a phenomenon that has yet to be demonstrated experimentally.

VI. DISCUSSION

In this paper, we explore some consequences of our recent theory of the acoustic force density acting on inhomogeneous fluids [23]. For this purpose, a useful formulation of the theory is given in terms of the field-shape functions R and C in the experimentally relevant limit of weakly inhomogeneous fluids. The theory of the acoustic force density acting on inhomogeneous fluids show resemblance to the Gorkov theory of the acoustic radiation force acting on a particle [37], for example, by the tendency of dense fluids being focused at the pressure nodes. However, the two theories have important distinctions. (1) The theory of the acoustic force density acting on inhomogeneous fluids is a field theory with $\boldsymbol{f}_{\mathrm{ac}}$ generally acting on the fluid in every point in space, in contrast to the Newtonian theory for the radiation force acting on a point particle. (2) The acoustic force density $\boldsymbol{f}_{\mathrm{ac}}$ is a nonconservative force, and, in general, it cannot be written as the gradient of a potential, as can the radiation force on a particle in a standing wave [38,39]. Instead, one may use the field-shape functions to assess the direction and magnitude of the forces acting on the fluid for a given initial concentration field. For density inhomogeneities, the denser fluid tends to relocate to the minima of the field-shape function R. (3) Not unrelated, in the theory of the acoustic force density, the force density $\boldsymbol{f}_{\mathrm{ac}}$ depends on the history of the system and it evolves as the concentration field changes by advection and diffusion.

While the acoustic force density can stabilize a fluid inhomogeneity against destabilizing forces, such as gravity in the case of a density gradient, it cannot counteract molecular diffusion. Consequently, an inhomogeneity always has a finite lifetime set by the characteristic diffusion time, and it will broaden due to diffusion. Interestingly, diffusion is an advantage in isoacoustic focusing because it allows fine-tuning of the gradient at the end of a steady-flow-through channel by varying the flow rate [22]. In acoustic tweezing of a high-concentration region, diffusion limits the time that the inhomogeneity can be manipulated in a closed chamber. One can obtain longer diffusion times by going to larger scales or by using Ficoll or Percoll solutions with larger solute molecules that diffuse slower.

Importantly, the ability to manipulate concentration fields requires that the concentration field introduces inhomogeneities in the fluid density or the speed of sound. A weaker inhomogeneity will, in general, result in weaker acoustic forces acting on the fluid. This scaling sets a lower limit to the weakness of an inhomogeneity that can be manipulated because, at some point, the fluid manipulation speed U_{ac} becomes smaller than the speed U_{diff} of the diffusing concentration profile. One may estimate the critical density deviation $\hat{\rho}_{\mathrm{crit}}$ at which manipulation becomes impossible by the condition $U_{\mathrm{ac}} = U_{\mathrm{diff}}$. Balancing the magnitude of the acoustic force density with the viscous shear stress, one obtains $U_{\mathrm{ac}} \sim E_{\mathrm{ac}} \ell \hat{\rho} / \eta_0$, where ℓ is a characteristic length scale. Equating U_{ac} with the

characteristic diffusive speed $U_{\mathrm{diff}} \sim D/\ell$, one obtains the rough estimate $\hat{\rho}_{\mathrm{crit}} \sim \eta_0 D/(E_{\mathrm{ac}}\ell^2) \sim 10^{-4}$, where the number is for $\ell = 10$ μm. In practice, for the manipulation to be effective, the manipulation speed should be at least an order of magnitude larger than the diffusion speed. Consequently, for the parameters used in this study, the density deviation should be larger than 0.1% in order that the fluid can be manipulated. Note that, for concentrations of iodixanol (OptiPrep), polysucrose (Ficoll), or colloidal nanoparticles (Percoll), all used in density-gradient separation, this requirement is easily fulfilled. One can, in principle, enable manipulation of any specific solution of biomolecules at low concentration by adding a density modifier that increases the acoustic contrast to other fluids.

VII. CONCLUSION

Advances in the development of experimental methods to control acoustic fields for microparticle-manipulation purposes—for example, using transducer arrays, surface acoustic waves, and transmission holograms—allow spatiotemporal tailoring of acoustic fields. In this paper, we demonstrate theoretically that this tailoring provides dynamic control of solute concentration fields at the microscale. We can think of this as acoustic "landscaping" of concentration fields because of the ability to dynamically manipulate "hills" and "valleys" of high and low concentration. Using acoustic landscaping, one may relocate, shape, and pattern concentration fields with the methods already developed for particle handling as demonstrated by our two examples: First, in rectangular microchannels, we describe an operational principle for obtaining multilayer stratification of concentration fields using acoustic eigenmodes. Second, we demonstrate acoustic tweezing and manipulation of a high-concentration fluid region in a lower-concentration fluid medium using a Bessel-function acoustic vortex.

We envision that the insights obtained in this study will find applications in the further development of isoacoustophoresis and other gradient-based separation methods. Another use may be found in studies of biological processes with active spatiotemporal control of solute gradients. Finally, the ability to pattern fluid inhomogeneities using acoustics might also find applications in drug delivery, tissue engineering, and the 3D printing of microstructures.

[1] B. W. Drinkwater, Dynamic-field devices for the ultrasonic manipulation of microparticles, Lab Chip **16**, 2360 (2016).

[2] H. Bruus, J. Dual, J. Hawkes, M. Hill, T. Laurell, J. Nilsson, S. Radel, S. Sadhal, and M. Wiklund, Forthcoming lab on a chip tutorial series on acoustofluidics: Acoustofluidics-exploiting ultrasonic standing wave forces and acoustic streaming in microfluidic systems for cell and particle manipulation, Lab Chip **11**, 3579 (2011).

[3] T. Laurell, F. Petersson, and A. Nilsson, Chip integrated strategies for acoustic separation and manipulation of cells and particles, Chem. Soc. Rev. **36**, 492 (2007).

[4] P. Augustsson, R. Barnkob, S. T. Wereley, H. Bruus, and T. Laurell, Automated and temperature-controlled micro-PIV measurements enabling long-term-stable microchannel acoustophoresis characterization, Lab Chip **11**, 4152 (2011).

[5] I. Leibacher, S. Schatzer, and J. Dual, Impedance matched channel walls in acoustofluidic systems, Lab Chip **14**, 463 (2014).

[6] X. Ding, S.-C. S. Lin, B. Kiraly, H. Yue, S. Li, I.-K. Chiang, J. Shi, S. J. Benkovic, and T. J. Huang, On-chip manipulation of single microparticles, cells, and organisms using surface acoustic waves, Proc. Natl. Acad. Sci. U.S.A. **109**, 11105 (2012).

[7] S. B. Q. Tran, P. Marmottant, and P. Thibault, Fast acoustic tweezers for the two-dimensional manipulation of individual particles in microfluidic channels, Appl. Phys. Lett. **101**, 114103 (2012).

[8] A. Riaud, J.-L. Thomas, E. Charron, A. Bussonnière, O. Bou Matar, and M. Baudoin, Anisotropic Swirling Surface Acoustic Waves from Inverse Filtering for On-Chip Generation of Acoustic Vortices, Phys. Rev. Applied **4**, 034004 (2015).

[9] A. Riaud, M. Baudoin, O. Bou Matar, L. Becerra, and J.-L. Thomas, Selective Manipulation of Microscopic Particles with Precursor Swirling Rayleigh Waves, Phys. Rev. Applied **7**, 024007 (2017).

[10] C. R. P. Courtney, C. E. M. Demore, H. Wu, A. Grinenko, P. D. Wilcox, S. Cochran, and B. W. Drinkwater, Independent trapping and manipulation of microparticles using dexterous acoustic tweezers, Appl. Phys. Lett. **104**, 154103 (2014).

[11] A. Marzo, S. A. Seah, B. W. Drinkwater, D. R. Sahoo, B. Long, and S. Subramanian, Holographic acoustic elements for manipulation of levitated objects, Nat. Commun. **6**, 8661 (2015).

[12] D. Baresch, J.-L. Thomas, and R. Marchiano, Observation of a Single-Beam Gradient Force Acoustical Trap for Elastic Particles: Acoustical Tweezers, Phys. Rev. Lett. **116**, 024301 (2016).

[13] K. Melde, A. G. Mark, T. Qiu, and P. Fischer, Holograms for acoustics, Nature (London) **537**, 518 (2016).

[14] M. Antfolk, C. Magnusson, P. Augustsson, H. Lilja, and T. Laurell, Acoustofluidic, label-free separation and simultaneous concentration of rare tumor cells from white blood cells, Anal. Chem. **87**, 9322 (2015).

[15] M. Wiklund, A. E. Christakou, M. Ohlin, I. Iranmanesh, T. Frisk, B. Vanherberghen, and B. Önfelt, Ultrasound-induced cell-cell interaction studies in a multi-well microplate, Micromachines **5**, 27 (2014).

[16] D. J. Collins, B. Morahan, J. Garcia-Bustos, C. Doerig, M. Plebanski, and A. Neild, Two-dimensional single-cell patterning with one cell per well driven by surface acoustic waves, Nat. Commun. **6**, 8686 (2015).

[17] K. Lee, H. Shao, R. Weissleder, and H. Lee, Acoustic purification of extracellular microvesicles, ACS Nano **9**, 2321 (2015).

[18] C. Grenvall, C. Magnusson, H. Lilja, and T. Laurell, Concurrent isolation of lymphocytes and granulocytes using

prefocused free flow acoustophoresis, Anal. Chem. **87**, 5596 (2015).
[19] T. M. Keenan and A. Folch, Biomolecular gradients in cell culture systems, Lab Chip **8**, 34 (2008).
[20] S. Takayama, J. C. McDonald, E. Ostuni, M. N. Liang, P. J. A. Kenis, R. F. Ismagilov, and G. M. Whitesides, Patterning cells and their environments using multiple laminar fluid flows in capillary networks, Proc. Natl. Acad. Sci. U.S.A. **96**, 5545 (1999).
[21] S. K. W. Dertinger, D. T. Chiu, N. L. Jeon, and G. M. Whitesides, Generation of gradients having complex shapes using microfluidic networks, Anal. Chem. **73**, 1240 (2001).
[22] P. Augustsson, J. T. Karlsen, H.-W. Su, H. Bruus, and J. Voldman, Iso-acoustic focusing of cells for size-insensitive acousto-mechanical phenotyping, Nat. Commun. **7**, 11556 (2016).
[23] J. T. Karlsen, P. Augustsson, and H. Bruus, Acoustic Force Density Acting on Inhomogeneous Fluids in Acoustic Fields, Phys. Rev. Lett. **117**, 114504 (2016).
[24] S. Deshmukh, Z. Brzozka, T. Laurell, and P. Augustsson, Acoustic radiation forces at liquid interfaces impact the performance of acoustophoresis, Lab Chip **14**, 3394 (2014).
[25] R. Barnkob, P. Augustsson, T. Laurell, and H. Bruus, Measuring the local pressure amplitude in microchannel acoustophoresis, Lab Chip **10**, 563 (2010).
[26] P. B. Muller, M. Rossi, A. G. Marín, R. Barnkob, P. Augustsson, T. Laurell, C. J. Kähler, and H. Bruus, Ultrasound-induced acoustophoretic motion of microparticles in three dimensions, Phys. Rev. E **88**, 023006 (2013).
[27] J. van't Oever, R. Frentrop, D. Wijnperlé, H. Offerhaus, D. van den Ende, J. Herek, and F. Mugele, Imaging local acoustic pressure in microchannels, Appl. Opt. **54**, 6482 (2015).
[28] A. Lamprecht, S. Lakamper, T. Baasch, I. A. T. Schaap, and J. Dual, Imaging the position-dependent 3D force on microbeads subjected to acoustic radiation forces and streaming, Lab Chip **16**, 2682 (2016).
[29] P. Augustsson, C. Magnusson, M. Nordin, H. Lilja, and T. Laurell, Microfluidic, label-free enrichment of prostate cancer cells in blood based on acoustophoresis, Anal. Chem. **84**, 7954 (2012).
[30] A. L. Bernassau, C. R. P. Courtney, J. Beeley, B. W. Drinkwater, and D. R. S. Cumming, Interactive manipulation of microparticles in an octagonal sonotweezer, Appl. Phys. Lett. **102**, 164101 (2013).
[31] C. R. P. Courtney, B. W. Drinkwater, C. E. M. Demore, S. Cochran, A. Grinenko, and P. D. Wilcox, Dexterous manipulation of microparticles using Bessel-function acoustic pressure fields, Appl. Phys. Lett. **102**, 123508 (2013).
[32] A. Riaud, J.-L. Thomas, M. Baudoin, and O. Bou Matar, Taming the degeneration of Bessel beams at an anisotropic-isotropic interface: Toward three-dimensional control of confined vortical waves, Phys. Rev. E **92**, 063201 (2015).
[33] B. T. Hefner and P. L. Marston, An acoustical helicoidal wave transducer with applications for the alignment of ultrasonic and underwater systems, J. Acoust. Soc. Am. **106**, 3313 (1999).
[34] COMSOL Multiphysics 5.2, http://www.comsol.com (2015).
[35] P. B. Muller and H. Bruus, Numerical study of thermoviscous effects in ultrasound-induced acoustic streaming in microchannels, Phys. Rev. E **90**, 043016 (2014).
[36] See Supplemental Material at http://link.aps.org/supplemental/10.1103/PhysRevApplied.7.034017 for movies of the time evolution of the concentration fields.
[37] L. P. Gorkov, On the forces acting on a small particle in an acoustical field in an ideal fluid, Dokl. Akad. Nauk SSSR **140**, 88 (1961) [Sov. Phys. Dokl. **6**, 773 (1962)].
[38] M. Settnes and H. Bruus, Forces acting on a small particle in an acoustical field in a viscous fluid, Phys. Rev. E **85**, 016327 (2012).
[39] J. T. Karlsen and H. Bruus, Forces acting on a small particle in an acoustical field in a thermoviscous fluid, Phys. Rev. E **92**, 043010 (2015).

Chapter 10

Paper V in Physical Review Letters (in press)

Acoustic streaming and its suppression in inhomogeneous fluids

E-print: arXiv:1707.07369 (old version).

Authors: J.T. Karlsen, W. Qui, P. Augustsson, and H. Bruus.
Journal: Phys. Rev. Lett. **in press** (accepted 9 January 2018).

Remarks: The revised version accepted in Physical Review Letters is included in this chapter. The Supplemental Figure is included immediately after the paper. Supplemental Movies are not yet available online.

Acoustic Streaming and its Suppression in Inhomogeneous Fluids

Jonas T. Karlsen,[1,*] Wei Qiu,[1] Per Augustsson,[2] and Henrik Bruus[1,†]

[1] *Department of Physics, Technical University of Denmark, DTU Physics Building 309, DK-2800 Kongens Lyngby, Denmark*

[2] *Department of Biomedical Engineering, Lund University, Ole Römers väg 3, 22363, Lund, Sweden*

(Dated: 11 December 2017)

We present a theoretical and experimental study of boundary-driven acoustic streaming in an inhomogeneous fluid with variations in density and compressibility. In a homogeneous fluid this streaming results from dissipation in the boundary layers (Rayleigh streaming). We show that in an inhomogeneous fluid, an additional non-dissipative force density acts on the fluid to stabilize particular inhomogeneity configurations, which markedly alters and even suppresses the streaming flows. Our theoretical and numerical analysis of the phenomenon is supported by ultrasound experiments performed with inhomogeneous aqueous iodixanol solutions in a glass-silicon microchip.

Acoustic streaming is the steady vortical flow that accompanies the propagation of acoustic waves in viscous fluids. This ubiquitous phenomenon [1, 2], studied as early as 1831 by Faraday observing the motion of powder above a vibrating Chladni plate [3], is driven by a nonzero divergence in the nonlinear momentum-flux-density tensor. In a homogeneous fluid, this divergence is caused by two acoustic energy dissipation mechanisms. One mechanism is dissipation in the thin boundary layers, where the acoustic fluid velocity changes to match the velocity of the boundary. The resulting streaming, called boundary-driven Rayleigh streaming [4, 5], is typically observed in standing wave fields near walls [6] or suspended objects [7]. The other mechanism is the attenuation of acoustic waves in the bulk of the fluid, which produces streaming known as bulk-driven Eckart streaming [8], typically observed in systems much larger than the wavelength [9]. Both cases have been extensively studied theoretically [10–13], and the phenomenon continues to attract attention due to its importance in thermoacoustic engines [14–16], ultrasound contrast agents, sonoporation, and drug delivery [17–19], and the manipulation of particles and cells in microscale acoustofluidics [20–27].

Recent experiments on fluids have revealed that inhomogeneities in density ρ_0 and compressibility κ_0, introduced by a solute concentration field, can be acoustically relocated into stabilized configurations [28, 29]. In subsequent work [30, 31], we showed that fast-timescale acoustics in such inhomogeneous fluids spawns a time-averaged acoustic force density $\boldsymbol{f}_{\rm ac}$ acting on the fluid on the slower hydrodynamic timescale, and that $\boldsymbol{f}_{\rm ac}$ leads to the observed relocation and stabilization of inhomogeneities. The experiments also indicated that boundary-driven streaming is suppressed in inhomogeneous fluids [29], and we hypothesized that this hitherto unexplored phenomenon can be explained by $\boldsymbol{f}_{\rm ac}$.

In this Letter, we investigate this hypothesis by combining the theories of acoustic streaming [10–13] and the acoustic force density [30]. We verify analytically the limiting cases of the combined theory, and proceed to develop a full numerical model of boundary-driven acoustic streaming in inhomogeneous viscous fluids. We know of only one similar theoretical study, which however is limited to prescribed static inhomogeneities [32]. Using our dynamic theory, we simulate the evolution of acoustic streaming, as an acoustically stabilized density profile evolves by diffusion and advection. Experimentally, we measure this evolution in an inhomogeneous aqueous iodixanol solution in an ultrasound-activated glass-silicon microchannel, Fig. 1, that enables injection of layered fluids creating a density gradient across the channel width [29, 30].

Our main findings are (i) that the competition between the boundary-induced streaming stresses and the inhomogeneity-induced acoustic force density introduces a dynamic length scale Δ of the streaming vortex size, (ii) that initially $\Delta \ll \Delta_{\rm hom} \sim \min\{\frac{1}{8}\lambda, \frac{1}{4}H\}$, where $\Delta_{\rm hom}$ is the vortex size in a homogeneous fluid set by the acoustic wavelength λ or the channel height H, and (iii) that in the bulk farther than Δ from the boundaries, the streaming flow is suppressed. Δ increases in time, as diffusion and advection smear the inhomogeneity, and the vortices eventually expand into the bulk, similar to homogeneous

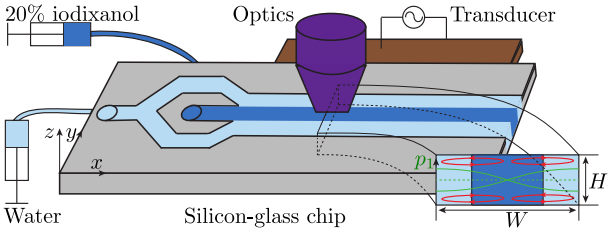

FIG. 1. (color online) Sketch of the acoustofluidic silicon chip (grey) sealed with a glass lid, that allows optical recording (purple) of the tracer bead motion (red trajectories) in the channel cross-section of width $W = 375$ μm and height $H = 130$ μm. A 20% iodixanol solution (dark blue) is injected in the center and laminated by pure water (light blue). The piezoelectric transducer (brown) excites the resonant half-wave pressure field p_1 (inset, green) at 2 MHz.

fluids. These findings are rationalized by simple scaling arguments.

Our analysis of acoustic streaming in inhomogeneous fluids elucidates fundamental physical aspects and further has potential applications in nanoparticle manipulation. Indeed, suppression of acoustic streaming may enable acoustophoretic manipulation of small bioparticles such as bacteria, exosomes, and viruses [33], that is otherwise hampered by the unfavorable scalings of the radiation force relative to the streaming-induced drag force with decreasing particle size [22, 34]. Nanoparticle manipulation has been attempted by suppressing streaming using pulsed actuation [35, 36], and by engineering streaming patterns in special geometries [37–39].

Separation of timescales.— Our analysis is based on the separation of timescales between the fast acoustics $t \sim 0.1$ µs and the slow hydrodynamics $\tau \sim 10$ ms [30]. Because $\tau \sim 10^5 t$, the acoustic fields can be computed while keeping the hydrodynamic degrees of freedom fixed at each instance in time τ. Assuming the system to be time-harmonically actuated at the angular frequency ω, the density ρ is written as

$$\rho = \rho_0(\boldsymbol{r},\tau) + \rho_1(\boldsymbol{r},\tau)\,\mathrm{e}^{-\mathrm{i}\omega t}. \tag{1}$$

Here, ρ_0 is the hydrodynamic density, and ρ_1 is the acoustic perturbation.

Fast-timescale acoustics.— Using perturbation expansions of the form Eq. (1) in the equations for conservation of fluid momentum and mass, the first-order equations for the acoustic perturbations in velocity $\boldsymbol{v}_1$, pressure p_1, and density ρ_1 become

$$-\mathrm{i}\omega\rho_0\boldsymbol{v}_1 = \boldsymbol{\nabla}\cdot\boldsymbol{\sigma}_1, \tag{2a}$$
$$-\mathrm{i}\omega\kappa_0 p_1 = -\boldsymbol{\nabla}\cdot\boldsymbol{v}_1, \tag{2b}$$
$$-\mathrm{i}\omega\rho_0\kappa_0 p_1 = -\mathrm{i}\omega\rho_1 + \boldsymbol{v}_1\cdot\boldsymbol{\nabla}\rho_0. \tag{2c}$$

Here, $\boldsymbol{\sigma}_1$ is the first-order fluid stress tensor, obtained by replacing p by p_1 and $\boldsymbol{v}$ by $\boldsymbol{v}_1$ in the usual fluid stress tensor $\boldsymbol{\sigma}$ [30]. The local speed of sound is $c_0 = 1/\sqrt{\rho_0\kappa_0}$.

In viscous acoustics, the oscillation velocity $\boldsymbol{v}_1$ attains the wall velocity on the length scale $\delta = \sqrt{2\nu_0/\omega}$ (≈ 0.4 µm for water at 2 MHz), where $\nu_0 = \eta_0/\rho_0$ with ν_0 and η_0 being the kinematic and dynamic viscosities, respectively. The time-averaged stress driving the streaming is generated within these narrow boundary layers. For inviscid acoustics, Eq. (2) reduces to the standard wave equation for inhomogeneous media [40, 41].

Slow-timescale dynamics.— The fluid inhomogeneity is caused by a solute concentration field $s(\boldsymbol{r},\tau)$, which is being transported on the slow timescale. This changes the hydrodynamic fluid density ρ_0, compressibility κ_0, and dynamic viscosity η_0,

$$\rho_0 = \rho_0\big[s(\boldsymbol{r},\tau)\big],\ \kappa_0 = \kappa_0\big[s(\boldsymbol{r},\tau)\big],\ \ \eta_0 = \eta_0\big[s(\boldsymbol{r},\tau)\big]. \tag{3}$$

For iodixanol, the specific dependencies in Eq. (3) are known experimentally, and c_0 is nearly independent of s, so that $\boldsymbol{\nabla}\kappa_0 \approx -(\rho_0 c_0)^{-2}\,\boldsymbol{\nabla}\rho_0$ [29, 30].

The hydrodynamics on the slow timescale τ is governed by the momentum- and mass-continuity equations for the fluid velocity $\boldsymbol{v}(\boldsymbol{r},\tau)$ and pressure $p(\boldsymbol{r},\tau)$, and by the advection-diffusion equation for the concentration $s(\boldsymbol{r},\tau)$ of the solute with diffusivity D, [30]

$$\partial_\tau(\rho_0\boldsymbol{v}) = \boldsymbol{\nabla}\cdot\big[\boldsymbol{\sigma} - \rho_0\boldsymbol{v}\boldsymbol{v}\big] + \boldsymbol{f}_{\mathrm{ac}} + \rho_0\boldsymbol{g}, \tag{4a}$$
$$\partial_\tau\rho_0 = -\boldsymbol{\nabla}\cdot\big(\rho_0\boldsymbol{v}\big), \tag{4b}$$
$$\partial_\tau s = -\boldsymbol{\nabla}\cdot\big[-D\boldsymbol{\nabla}s + \boldsymbol{v}s\big]. \tag{4c}$$

Here, $\boldsymbol{g}$ is the gravitational acceleration, $\boldsymbol{\sigma}$ is the fluid stress tensor, and $\boldsymbol{f}_{\mathrm{ac}}$ is the acoustic force density.

All types of time-averaged acoustic flows, such as Rayleigh and Eckart streaming [10–13] and the relocation flows in inhomogeneous fluids [30, 31], are driven by the divergence of the oscillation-time-averaged acoustic momentum-flux-density tensor $\langle\boldsymbol{\Pi}_{\mathrm{ac}}\rangle$. In particular [30],

$$\boldsymbol{f}_{\mathrm{ac}} = -\boldsymbol{\nabla}\cdot\langle\boldsymbol{\Pi}_{\mathrm{ac}}\rangle. \tag{5}$$

$\langle\boldsymbol{\Pi}_{\mathrm{ac}}\rangle$ is given by products of first-order acoustic fields,

$$\langle\boldsymbol{\Pi}_{\mathrm{ac}}\rangle = \langle p_{11}\rangle\mathbf{1} + \langle\rho_0\boldsymbol{v}_1\boldsymbol{v}_1\rangle, \tag{6a}$$
$$\langle p_{11}\rangle = \frac{1}{4}\kappa_0|p_1|^2 - \frac{1}{4}\rho_0|\boldsymbol{v}_1|^2, \tag{6b}$$

where $\langle p_{11}\rangle$ is a local oscillation-time-averaged acoustic pressure, which for an inhomogeneous fluid depends on the solute concentration s. Combining Eqs. (5) and (6), the general expression for $\boldsymbol{f}_{\mathrm{ac}}$ in viscous inhomogeneous acoustics becomes,

$$\boldsymbol{f}_{\mathrm{ac}} = -\boldsymbol{\nabla}\langle p_{11}\rangle - \boldsymbol{\nabla}\cdot\langle\rho_0\boldsymbol{v}_1\boldsymbol{v}_1\rangle. \tag{7}$$

Note that in Eq. (4a), $\boldsymbol{\nabla}\langle p_{11}\rangle$ from $\boldsymbol{f}_{\mathrm{ac}}$ cannot simply be absorbed in the pressure gradient $\boldsymbol{\nabla}p$ contained in $\boldsymbol{\nabla}\cdot\boldsymbol{\sigma}$, as its explicit dependence of the dynamical variable s, expressed in Eq. (6b), would be lost.

Expression (7) for $\boldsymbol{f}_{\mathrm{ac}}$ may be simplified in two special cases. First, in a viscous homogeneous fluid $\langle p_{11}\rangle$ is independent of s, so $\boldsymbol{\nabla}\langle p_{11}\rangle$ can be absorbed into $\boldsymbol{\nabla}p$ in Eq. (4a) by redefining the pressure from p to $\tilde{p} = p + \langle p_{11}\rangle$. Consequently,

$$\boldsymbol{f}_{\mathrm{ac}}^{\mathrm{hom}} = -\boldsymbol{\nabla}\cdot\langle\rho_0\boldsymbol{v}_1\boldsymbol{v}_1\rangle. \tag{8}$$

Indeed, this is how the driving terms are often presented in classical [10–12] and more recent [6, 9, 42] works on time-independent acoustic streaming.

In the second case of inhomogeneous but inviscid acoustics, we recently demonstrated that Eq. (7) yields

$$\boldsymbol{f}_{\mathrm{ac}}^{\mathrm{invisc}} = -\frac{1}{4}|p_1|^2\boldsymbol{\nabla}\kappa_0 - \frac{1}{4}|\boldsymbol{v}_1|^2\boldsymbol{\nabla}\rho_0, \tag{9}$$

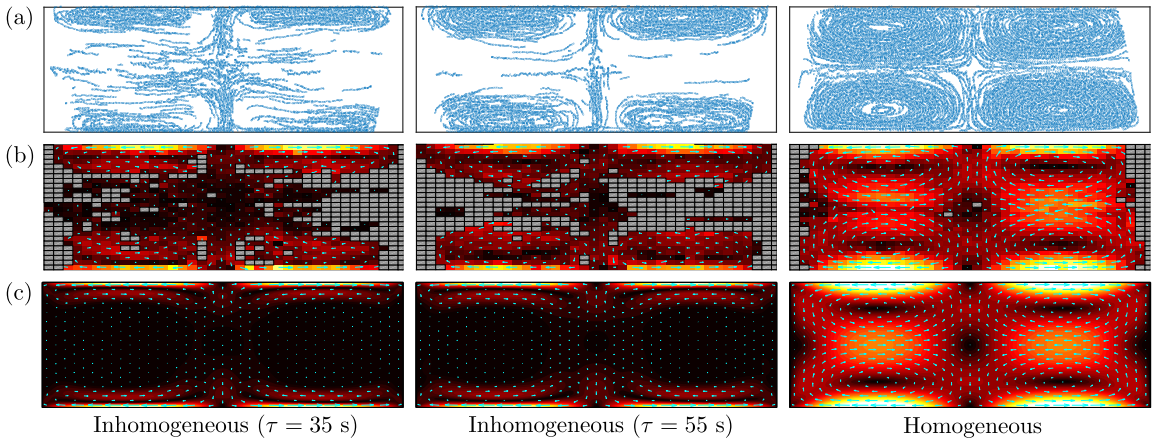

FIG. 2. (color online) Acoustic streaming in the inhomogeneous fluid at $\tau = 35$ s (column 1) and $\tau = 55$ s (column 2) and in the corresponding homogenized fluid (column 3). (a) Experimental particle positions (blue points). (b) Experimental streaming velocity amplitude $|\boldsymbol{v}|$ (0 μm/s, black; 35 μm/s, white) with the arrows (cyan) indicating the direction. Spatial bins with no data points are excluded (grey). (c) Simulated streaming velocity; same colors as (b).

and that this non-dissipative force density is driving the slow-timescale relocation of the fluid inhomogeneities into stable field-dependent configurations [30, 31].

In the context of boundary-driven acoustic streaming in inhomogeneous fluids, the content of Eqs. (7)-(9) is as follows: In the boundary layers, dissipation of acoustic energy leads to time-averaged stresses, confined on the length scale δ, that cause boundary-driven streaming flows. However, in the presence of gradients in the density and compressibility, the non-dissipative acoustic force density tends to stabilize the fluid (after initial focusing) in a certain static inhomogeneity configuration [30], thereby counteracting the advective streaming flow. While Eqs. (8) and (9) demonstrate that these two force densities are present in inhomogeneous viscous fluids, they cannot in general be separated analytically. The force density responsible for bulk-driven Eckart streaming is included in Eq. (7), but it is negligible in this study.

Numerical model in 2D.— The dynamics in the 2D channel cross-section is solved numerically, under stop-flow conditions with the initial condition sketched in Fig. 1, using a weak-form finite-element implementation in COMSOL Multiphysics [43] with regular rectangular mesh elements [44]. A segregated solver solves the time-dependent problem in two steps: (i) The fast-timescale acoustics Eq. (2) in the inhomogeneous medium is solved while keeping the hydrodynamic degrees of freedom fixed. This allows computation of the time-averaged acoustic force density $\boldsymbol{f}_{\rm ac}$, Eq. (7). (ii) The slow-timescale dynamics Eq. (4) is then integrated in time τ using a generalized alpha solver with a damping parameter of 0.25, and a maximum time step $\Delta\tau = 7.5$ ms, while keeping the acoustic energy density fixed at $E_{\rm ac} = 50$ Pa [45]. This model extends our previous model [30, 31] by explicitly solving for the fast-timescale viscous acoustics in the inhomogeneous medium, a necessity for computing the boundary-layer stresses that drive streaming.

Experimental method.— The experiments were performed using a long straight microchannel of height $H = 130$ μm and width $W = 375$ μm in a silicon-glass chip with an attached piezoelectric transducer. A laminated flow of water and an aqueous 20%-iodixanol solution (OptiPrep) was injected to form a concentration gradient with the denser fluid at the center, see Fig. 1. General Defocusing Particle Tracking (GDPT) [46] was used to record the motion of 1 μm-diameter polystyrene tracer beads. The fluid streaming velocity was computed by subtracting the radiation-force contribution from the bead veloicty [22, 47]. At time $\tau = 0$, the flow was stopped, and the GDPT measurements (10 fps) were conducted with the transducer driven at 2.0 V peak-to-peak voltage and the frequency swept from 1.95 to 2.05 MHz in cycles of 10 ms to produce a standing half-wave across the width [48] with $E_{\rm ac} = 52$ Pa [49]. The frequency sweep ensures that resonance conditions (1.96 and 1.97 MHz in pure water and in 20% iodixanol, respectively) are achieved throughout the experiment during the time-evolution of the concentration field. For each set of measurements, the particle motion was recorded for 160 s to observe the evolution of the acoustic streaming. The experiment was repeated 16 times to improve the statistics.

Results.— Experimental data and simulation results for the acoustic streaming in the channel cross-section are plotted in Fig. 2. Column-wise, the figure first shows the inhomogeneous-fluid streaming at $\tau = 35$ s and $\tau = 55$ s, and then the steady homogeneous-fluid streaming. In the rows are (a) the raw experimental particle positions, (b) the grid-interpolated experimental velocity field, and (c) the simulated velocity field. The acoustically stabilized inhomogeneity distribution remains almost one-

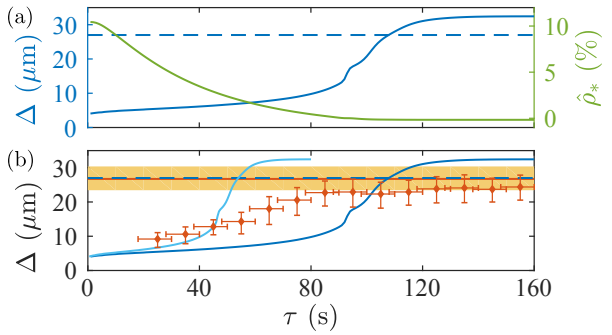

FIG. 3. (color online) (a) Simulation results for the vortex size Δ (left axis, blue curve), Δ_{hom} (left axis, dashed blue line), and the excess mass density $\hat{\rho}_*$ (right axis, green curve) as functions of time τ. (b) Experimental results for Δ (red dots with errorbars) and Δ_{hom} (red line with orange error-bar band), plotted with the simulation results for Δ (blue curve for unscaled time; light blue curve for rescaled time; see text) and Δ_{hom} (dashed blue line) as functions of time τ.

dimensional with the denser fluid at the center diffusing sidewards; see Supplemental Material [50]. Hence, recalling that for iodixanol $\boldsymbol{\nabla}\kappa_0 \approx -(\rho_0 c_0)^{-2}\,\boldsymbol{\nabla}\rho_0$, we may quantify the inhomogeneity with the single parameter of the excess mass density $\hat{\rho}_*$ at the center relative to the sides [51]. The experimental inhomogeneous-fluid streaming pattern evolves towards the homogeneous steady-state as diffusion (and, to a lesser extent, advection) diminish the initial $\hat{\rho}_*$ of 10% to 4% and 2% at $\tau = 35$ s and 55 s, respectively. We note that the timescale for the evolution of the inhomogeneous-fluid streaming (~ 10 s) is orders of magnitude larger than that for achieving steady-state streaming in a homogeneous fluid (~ 1 ms) [36].

Evidently, the inhomogeneous-fluid streaming is initially confined close to the boundaries and suppressed in the bulk as compared to homogeneous-fluid streaming. To quantify this suppression of streaming, we define the vortex size Δ as the orthogonal distance from the boundary to the vortex center, where $\boldsymbol{v} = \boldsymbol{0}$. In Fig. 3(a), the simulated vortex size Δ and the excess mass density $\hat{\rho}_*$ are plotted as functions of time. Δ increases slowly in time, as $\hat{\rho}_*$ decreases by diffusion, until a transition occurs when a critically weak inhomogeneity is reached. At this point the streaming expands into the bulk and becomes similar to homogeneous-fluid streaming. Figure 3(a) shows that Δ and $\hat{\rho}_*$ are inversely related, supporting the hypothesis that the inhomogeneity-induced part of $\boldsymbol{f}_{\mathrm{ac}}$ [Eq. (9)] suppresses the boundary-driven streaming.

We further assess the validity of the above-mentioned hypothesis by estimating Δ from a scaling argument. In a homogeneous fluid, being interested in the bulk length scale of the flow, the only relevant length scales are the channel dimensions H and W (given the half-wave resonance, $\lambda_0 = 2W$). In the shallow-channel limit, the explicit analytical solution yields $\Delta_{\mathrm{hom}} = (1 - 1/\sqrt{3})(H/2) = 28$ μm [6]. In a density-stratified medium, an additional relevant length scale is L_ρ of the density gradient $\nabla\rho_0 \approx \rho_0/L_\rho$. Writing $\rho_0 = \rho_0^{(0)}[1 + \hat{\rho}]$, the inhomogeneity-induced part of $\boldsymbol{f}_{\mathrm{ac}}$ [Eq. (9)] is of the order $f_{\mathrm{ac}} \approx E_{\mathrm{ac}}\nabla\hat{\rho}$. We may then estimate Δ as the length scale on which the shear stress $\eta_0\nabla^2 v_{\mathrm{R}} \approx \eta_0 v_{\mathrm{R}}/\Delta^2$, associated with the boundary-driven Rayleigh streaming velocity amplitude $v_{\mathrm{R}} = (3/2)E_{\mathrm{ac}}\rho_0^{-1}c_0^{-1}$ [4], is balanced by f_{ac}. Using the early-time values $\hat{\rho} \approx 0.1$ and $L_\rho \approx W/2$, we obtain

$$\Delta \approx \sqrt{\frac{3}{2}\frac{\nu_0}{c_0}\frac{1}{|\nabla\hat{\rho}|}} \approx \sqrt{\frac{3}{2}\frac{\nu_0}{c_0}\frac{L_\rho}{\hat{\rho}}} \approx 2\ \mu\mathrm{m}. \qquad (10)$$

This estimate is an order of magnitude smaller than Δ_{hom}, in good agreement with experiments and simulations. It supports the hypothesis that $\Delta \ll \Delta_{\mathrm{hom}}$ due to the inhomogeneity-induced acoustic force density. Equation (10) furthermore illustrates why Δ grows in time; as time progresses, the inhomogeneity weakens by diffusion, i.e. $|\nabla\hat{\rho}|$ decreases, and consequently Δ grows.

The timescale characterizing the growth of the vortex size Δ towards the value Δ_{hom} is consequently set by diffusion. In the 2D simulation, where the diffusion is essentially 1D (across the width), the timescale of diffusion across one third of the channel width is $\tau_{\mathrm{diff,1D}} = (2D)^{-1}(W/3)^2 = 87$ s. Figure 3(a) shows a rapid transition in the simulated vortex size occurring around $\tau \approx 90$ s, see also Supplemental Material [51]. However, experimentally we find that the transition occurs earlier and less rapid around $\tau \approx 60$ s, see Fig. 3(b). Because axial variations in the acoustic field cannot be avoided in the experiment [52], and because such variations destroy translational invariance, the axial concentration gradients tend to change the diffusion from 1D to 2D, which would halve the diffusion time, $\tau_{\mathrm{diff,2D}} = (4D)^{-1}(W/3)^2 = 43$ s. Most likely, the effective diffusion in the experiment is in between the idealized 1D and 2D diffusion. In Fig. 3(b), the experimental data for the vortex size Δ is plotted as a function of time τ, along with the simulation result for unscaled and rescaled time for 1D and 2D diffusion, respectively. The experimental data fall mostly between the two curves, and given that there are no free fitting parameters, the agreement between theory and experiment is reasonable.

The 2D simulation successfully captures the essential physics of the experiment, including the initial suppression of streaming followed by the growth of the vortex size and the transition to a steady state. However, Fig. 3(b) indicates that the simulation reaches a steady state that overestimates the long-time limit of Δ. Interestingly, this is caused by an imperfect homogenization in 2D due to a delicate balance between advective

flows and diffusive currents, leaving a slight steady-state over-concentration at the sidewalls (small negative $\hat{\rho}_*$; see Fig. 3(a) at $\tau = 160$ s) that speeds up the flow in the center. Experimentally, however, the lack of perfect translational symmetry leads to homogeneous-fluid streaming at long timescales in agreement with homogeneous-fluid simulations, see Fig. 3(b).

Conclusion.— Theoretically, numerically, and experimentally, we have investigated the problem of acoustic streaming in inhomogeneous fluids with acoustically stabilized inhomogeneities. We have combined the theories of acoustic streaming and the acoustic force density, and developed a numerical model that simulates viscous inhomogeneous acoustics (the fast-timescale dynamics) and the resulting flows due to the generalized acoustic force density (the slow-timescale dynamics), allowing the interpretation of our microfluidic experiments with aqueous iodixanol solutions. We find that acoustic streaming is markedly different in homogeneous and inhomogeneous fluids as summarized by the main findings (i) - (iii) in the introduction. Our study is fundamental in scope, but the suppression of acoustic streaming in inhomogeneous fluids may enable ultrasound handling of nanoparticles in standard acoustophoretic chips.

We are grateful to R. Barnkob and M. Rossi, Universität der Bundeswehr München, for providing the software GDPTlab [46]. WQ was supported by the People Programme (Marie Curie Actions) EC-FP7/2007-2013, REA grant 609405 (COFUNDPostdocDTU).

* jonkar@fysik.dtu.dk
† bruus@fysik.dtu.dk

[1] T. M. Squires and S. R. Quake, Microfluidics: Fluid physics at the nanoliter scale, Rev. Mod. Phys. **77**, 977 (2005).
[2] M. Wiklund, R. Green, and M. Ohlin, Acoustofluidics 14: Applications of acoustic streaming in microfluidic devices, Lab Chip **12**, 2438 (2012).
[3] M. Faraday, On a peculiar class of acoustical figures; and on certain forms assumed by groups of particles upon vibrating elastic surfaces, Philos. Trans. R. Soc. London **121**, 299 (1831).
[4] Lord Rayleigh, On the circulation of air observed in Kundt's tubes, and on some allied acoustical problems, Philos. Trans. R. Soc. London **175**, 1 (1884).
[5] H. Schlichting, Berechnung ebener periodischer grenzeschichtströmungen, Phys. Z. **33**, 327 (1932).
[6] P. B. Muller, M. Rossi, A. G. Marín, R. Barnkob, P. Augustsson, T. Laurell, C. J. Kähler, and H. Bruus, Ultrasound-induced acoustophoretic motion of microparticles in three dimensions, Phys. Rev. E **88**, 023006 (2013).
[7] P. Tho, R. Manasseh, and A. Ooi, Cavitation microstreaming patterns in single and multiple bubble systems, J. Fluid Mech. **576**, 191 (2007).
[8] C. Eckart, Vortices and streams caused by sound waves, Phys. Rev. **73**, 68 (1948).
[9] A. Riaud, M. Baudoin, O. Bou Matar, J.-L. Thomas, and P. Brunet, On the influence of viscosity and caustics on acoustic streaming in sessile droplets: anï¿½experimental and a numerical study with aï¿½cost-effective method, J. Fluid Mech. **821**, 384 (2017).
[10] W. L. Nyborg, Acoustic streaming due to attenuated plane waves, J. Acoust. Soc. Am. **25**, 68 (1953).
[11] W. L. Nyborg, Acoustic streaming near a boundary, J. Acoust. Soc. Am. **30**, 329 (1958).
[12] J. Lighthill, Acoustic streaming, J Sound Vibr **61**, 391 (1978).
[13] N. Riley, Steady streaming, Annu. Rev. Fluid Mech. **33**, 43 (2001).
[14] G. Swift, Thermoacoustic engines, J. Acoust. Soc. Am. **84**, 1145 (1988).
[15] M. Hamilton, Y. Ilinskii, and E. Zabolotskaya, Acoustic streaming generated by standing waves in two-dimensional channels of arbitrary width, J. Acoust. Soc. Am. **113**, 153 (2003).
[16] M. Hamilton, Y. Ilinskii, and E. Zabolotskaya, Thermal effects on acoustic streaming in standing waves, J. Acoust. Soc. Am. **114**, 3092 (2003).
[17] A. A. Doinikov and A. Bouakaz, Theoretical investigation of shear stress generated by a contrast microbubble on the cell membrane as a mechanism for sonoporation, J. Acoust. Soc. Am. **128**, 11 (2010).
[18] J. Wu and W. L. Nyborg, Ultrasound, cavitation bubbles and their interaction with cells, Adv. Drug Deliv. Rev. **60**, 1103 (2008).
[19] P. Marmottant and S. Hilgenfeldt, Controlled vesicle deformation and lysis by single oscillating bubbles, Nature **423**, 153 (2003).
[20] H. Bruus, J. Dual, J. Hawkes, M. Hill, T. Laurell, J. Nilsson, S. Radel, S. Sadhal, and M. Wiklund, Forthcoming lab on a chip tutorial series on acoustofluidics: Acoustofluidics-exploiting ultrasonic standing wave forces and acoustic streaming in microfluidic systems for cell and particle manipulation, Lab Chip **11**, 3579 (2011).
[21] J. Friend and L. Y. Yeo, Microscale acoustofluidics: Microfluidics driven via acoustics and ultrasonics, Rev. Mod. Phys. **83**, 647 (2011).
[22] R. Barnkob, P. Augustsson, T. Laurell, and H. Bruus, Acoustic radiation- and streaming-induced microparticle velocities determined by microparticle image velocimetry in an ultrasound symmetry plane, Phys. Rev. E **86**, 056307 (2012).
[23] B. Hammarström, T. Laurell, and J. Nilsson, Seed particle enabled acoustic trapping of bacteria and nanoparticles in continuous flow systems, Lab Chip **12**, 4296 (2012).
[24] D. J. Collins, B. Morahan, J. Garcia-Bustos, C. Doerig, M. Plebanski, and A. Neild, Two-dimensional single-cell patterning with one cell per well driven by surface acoustic waves, Nat. Commun. **6**, 8686 (2015).
[25] A. Marin, M. Rossi, B. Rallabandi, C. Wang, S. Hilgenfeldt, and C. J. Kähler, Three-dimensional phenomena in microbubble acoustic streaming, Phys. Rev. Applied **3**, 041001 (2015).
[26] P. Hahn, I. Leibacher, T. Baasch, and J. Dual, Numerical simulation of acoustofluidic manipulation by radiation forces and acoustic streaming for complex particles, Lab Chip **15**, 4302 (2015).

[27] F. Guo, Z. Mao, Y. Chen, Z. Xie, J. P. Lata, P. Li, L. Ren, J. Liu, J. Yang, M. Dao, S. Suresh, and T. J. Huang, Three-dimensional manipulation of single cells using surface acoustic waves, PNAS **113**, 1522 (2016).

[28] S. Deshmukh, Z. Brzozka, T. Laurell, and P. Augustsson, Acoustic radiation forces at liquid interfaces impact the performance of acoustophoresis, Lab Chip **14**, 3394 (2014).

[29] P. Augustsson, J. T. Karlsen, H.-W. Su, H. Bruus, and J. Voldman, Iso-acoustic focusing of cells for size-insensitive acousto-mechanical phenotyping, Nat. Commun. **7**, 11556 (2016).

[30] J. T. Karlsen, P. Augustsson, and H. Bruus, Acoustic force density acting on inhomogeneous fluids in acoustic fields, Phys. Rev. Lett. **117**, 114504 (2016).

[31] J. T. Karlsen and H. Bruus, Acoustic tweezing and patterning of concentration fields in microfluidics, Phys. Rev. Applied **7**, 034017 (2017).

[32] G. P. Chini, Z. Malecha, and T. D. Dreeben, Large-amplitude acoustic streaming, J. Fluid Mech. **744**, 329 (2014).

[33] M. Antfolk and T. Laurell, Continuous flow microfluidic separation and processing of rare cells and bioparticles found in blood - a review, Anal. Chim. Acta **965**, 9 (2017).

[34] P. B. Muller, R. Barnkob, M. J. H. Jensen, and H. Bruus, A numerical study of microparticle acoustophoresis driven by acoustic radiation forces and streaming-induced drag forces, Lab Chip **12**, 4617 (2012).

[35] M. Hoyos and A. Castro, Controlling the acoustic streaming by pulsed ultrasounds, Ultrasonics **53**, 70 (2013).

[36] P. B. Muller and H. Bruus, Theoretical study of time-dependent, ultrasound-induced acoustic streaming in microchannels, Phys. Rev. E **92**, 063018 (2015).

[37] M. Antfolk, P. B. Muller, P. Augustsson, H. Bruus, and T. Laurell, Focusing of sub-micrometer particles and bacteria enabled by two-dimensional acoustophoresis, Lab Chip **14**, 2791 (2014).

[38] Z. Mao, P. Li, M. Wu, H. Bachman, N. Mesyngier, X. Guo, S. Liu, F. Costanzo, and T. J. Huang, Enriching nanoparticles via acoustofluidics, ACS Nano **11**, 603 (2017).

[39] D. J. Collins, Z. Ma, J. Han, and Y. Ai, Continuous micro-vortex-based nanoparticle manipulation via focused surface acoustic waves, Lab Chip **17**, 91 (2017).

[40] P. G. Bergmann, The wave equation in a medium with a variable index of refraction, J. Acoust. Soc. Am. **17**, 329 (1946).

[41] P. M. Morse and K. U. Ingard, *Theoretical Acoustics* (Princeton University Press, Princeton NJ, 1986).

[42] J. Lei, P. Glynne-Jones, and M. Hill, Comparing methods for the modelling of boundary-driven streaming in acoustofluidic devices, Microfluidics and Nanofluidics **21**, 23 (2017).

[43] COMSOL Multiphysics 5.2, www.comsol.com, (2015).

[44] The mesh-element size grows from $\Delta h = 0.1$ μm in the boundary layers to $\Delta h = 1.3$ μm in the bulk. The order of the Lagrange shape functions is quadratic for p and cubic for s and $\boldsymbol{v}$.

[45] To fix E_{ac}, which varies due to small shifts in resonance frequency as $s(\boldsymbol{r}, \tau)$ evolves, we compensate by adjusting the sidewall actuation amplitude $d_0(\tau)$ iteratively; see also Ref. [34].

[46] R. Barnkob, C. J. Kahler, and M. Rossi, General defocusing particle tracking, Lab Chip **15**, 3556 (2015).

[47] J. T. Karlsen and H. Bruus, Forces acting on a small particle in an acoustical field in a thermoviscous fluid, Phys. Rev. E **92**, 043010 (2015).

[48] O. Manneberg, B. Vanherberghen, B. Onfelt, and M. Wiklund, Flow-free transport of cells in microchannels by frequency-modulated ultrasound, Lab Chip **9**, 833 (2009).

[49] We estimate $E_{\mathrm{ac}} = (E_{\mathrm{ac}}^{20\%} + E_{\mathrm{ac}}^{0\%})/2$, where $E_{\mathrm{ac}}^{20\%}$ and $E_{\mathrm{ac}}^{0\%}$ are measured in homogeneous 20% and 0% iodixanol solutions.

[50] See Supplemental Material at [URL] for simulation results of density evolution and particle trajectories.

[51] $\hat{\rho}_* = \rho_0^{\mathrm{center}}/\rho_0^{\mathrm{sidewall}} - 1$, evaluated numerically at mid-height.

[52] P. Augustsson, R. Barnkob, S. T. Wereley, H. Bruus, and T. Laurell, Automated and temperature-controlled micro-piv measurements enabling long-term-stable microchannel acoustophoresis characterization, Lab Chip **11**, 4152 (2011).

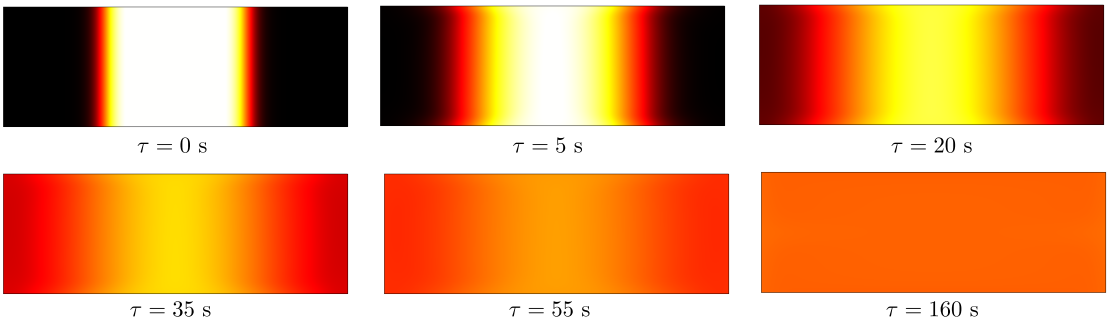

Supplemental Figure. Simulation results corresponding to those of Fig. 2(c). Relative density distribution $\hat{\rho} = \rho_0(s)/\rho_0^{\text{water}} - 1$ in percent (0%, black; 10%, white) in the vertical channel cross section as it evolves by diffusion and advection from the initial condition in $\tau = 0$ s to $\tau = 5$ s, 20 s, 35 s, 55 s, and 160 s. The stabilization of the denser fluid at the center is due to the inhomogeneity-induced acoustic force density.

Chapter 11

Experimental work in progress

This chapter presents a short description and a few preliminary results of experimental work in progress that the author is currently involved in together with collaborators at University of Lille, Section 11.1, and Lund University, Section 11.2, acknowledged in the appropriate sections.

11.1 Active manipulation of diffusive miscible fluid interfaces using ultrasound

This section presents an experimental work in progress initiated by the author in April-June 2017 during an external research stay in the group of Prof. Michaël Baudoin, Université Lille 1, IEMN, France. Collaborators on this project include Michaël Baudoin, Henrik Bruus, and Jean-Claude Gerbedoen, SATT du Nord, IEMN, who introduced me to the experimental lab facilities and assisted with the chip production. Initial experimental tests were carried out by visiting student Masakazu Muto from the group of Prof. Masahiro Motosuke, Tokyo University of Science, Japan. The acoustical tweezers system developed and produced by Antoine Riaud *et al.* [53] made the work possible. My time in Lille served as an interesting hands-on introduction to microfabrication and clean-room techniques as well as microfluidic experiments, with which I had no previous experience. Several microfluidic chips were produced, and broken, by my hands.

11.1.1 Motivation in microfluidics

In microfluidics, laminar-flow conditions make the diffusive interface between two miscible fluids evolve only by diffusion, and thus in a highly predictible and well-controlled manner [202]. Arguably, this realization is what prompted the development of microfluidics with the concepts of the H-filter [203, 204] and the T-sensor [205], which have found widespred applications, e.g., in immunoassays [206] and chemical assays [207]. Gradient-generation using microfluidic networks is another application relying on the passive combination of a large number of miscible fluid streams in order to generate predefined concentration gradients [197]. Indeed, diffusive interfaces between miscible fluids is at the heart of

microfluidics, and their passive manipulation is an ubiquitous part of almost any integrated microfluidic system. Remarkably, there exists no method to actively manipulate miscible fluid interfaces. The development of such a tool could potentially enable a new branch of microfluidic technologies, in the same way that active manipulation of *im*miscible fluids and droplets paved the way for the development of digital microfluidics [208].

11.1.2 Theoretical predictions

The experimental findings and theoretical results presented in Papers II, III, and IV suggest that gradients in density ρ_0 and compressibility κ_0, appearing in the diffusive interface between two miscible fluids, can be acted upon by a nonlinear acoustic force density, and that this generates laminar flows that relocate the inhomogeneities into patterns that can be predicted by the linear acoustic fields [2, 3, 4, 157]. In the enclosed Paper IV, Chapter 9, several remarkable theoretical predictions for the manipulation of inhomogeneous fluids using acoustic fields were made [4]. In particular, it was predicted that Bessel-function acoustic vortices, or acoustic tweezers [54, 56, 53], can be used to "grab and move" a local high-concentration fluid inhomogeneity. Theoretical predictions of the patterns of concentration fields in acoustic vortices, determined by the linear acoustic field as described by the field-shape functions R and C, were furthermore presented. The experimental work in progress aims at testing these theoretical predictions using an acoustical tweezers system.

11.1.3 Experimental setup

The integrated acoustical tweezers system developed and produced by Riaud *et al.* utilizes surface acoustic waves excited at 10 MHz by a single spiraling interdigitated transducer (IDT) on a piezo-electric lithium niobate substrate [53]. The microfluidic chip is placed on top of this substrate in a thin contact layer of olive oil. A number of different chips, designed to create different initial conditions for the interface between the two miscible fluids, are produced in PDMS using standard photolithography. A 150 µm thick glass-slide is bonded to make up the bottom of the microchannels that are of 50 µm height. The two miscible fluids are water dyed with methylene blue (non-transparent) and a 50 w/vol% aqueous Ficoll-PM400 solution (transparent), with a mass density 20% higher than water. Since all layers in the system are transparent except for the dyed water (and the IDT), the miscible fluid interface can be monitored directly by using an optical microscope. Photos of the experimental setup are shown in Fig. 11.1. In this description of the preliminary work, an overview of the experimental setup is all that is needed, and a detailed description of the setup will not be provided.

The integrated acoustical tweezers system is described in detail by Riaud *et al.* [53]. It is based on the generation of the so-called precursor swirling Rayleigh waves on the lithium-niobate substrate. These precursor waves are designed to degenerate into an acoustic vortex after passing through the glass-slide of the microfluidic chip and into the liquid [53, 52], and are obtained by solving the inverse problem with the output being the particular IDT pattern that should be deposited on the piezo-electric substrate. Different sets of IDTs allow the generation of both Bessel-0 and Bessel-1 vortices.

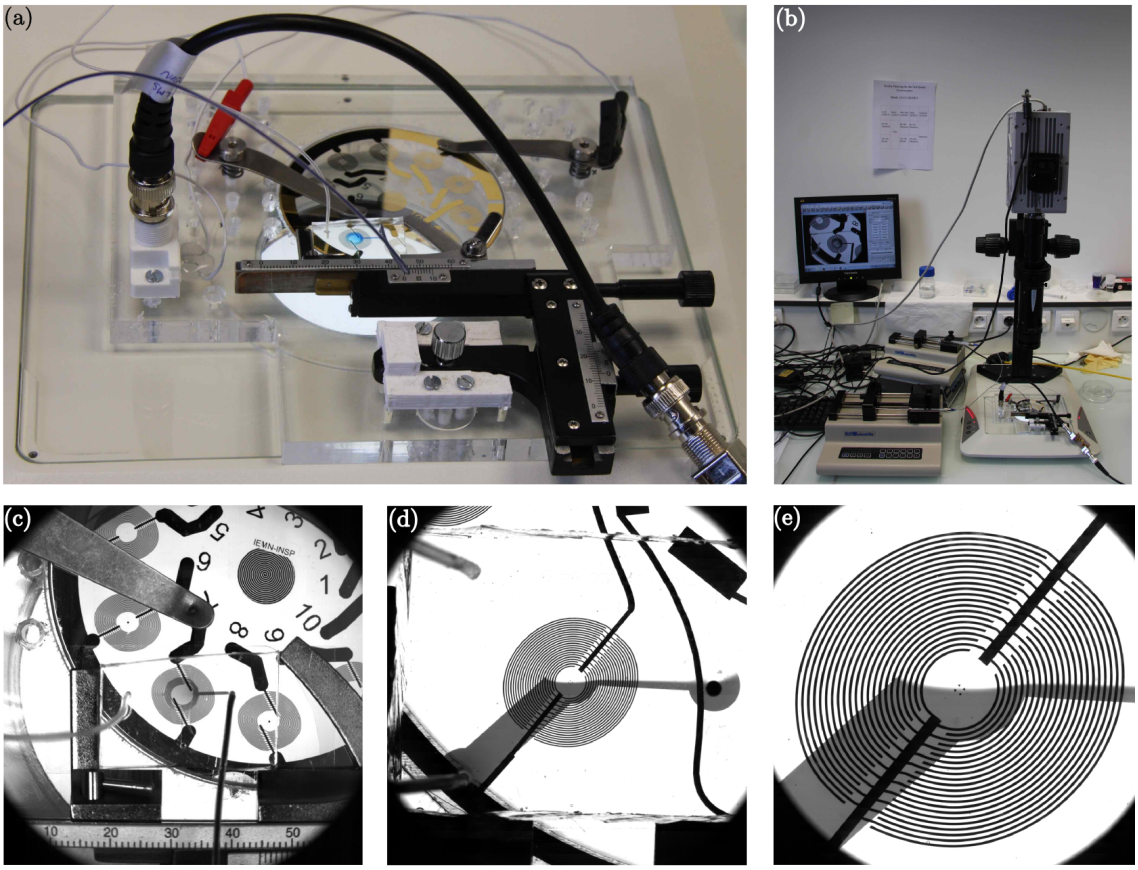

Figure 11.1: Photos of the experimental setup at Université Lille 1, IEMN, Group of Prof. Michaël Baudoin. **(a)** Circular acoustic tweezers piezo-electric substrate with golden electrodes, as placed in its holder in the microscope stage, with the microfluidic glass-PDMS chip on top of the substrate. **(b)** Zoom-out of the tweezers setup in the microscope stage. **(c)** Zoom-in of a microfluidic glass-PDMS chip placed on top of the tweezers substrate. **(d)** Zoom-in of a chip in which methylene-blue-dyed water (dark) is in contact with aqueous Ficoll solution (transparent). **(e)** Zoom-in of the interface between the two fluids, with the the spiraling IDTs clearly visible in the background.

11.1.4 Preliminary results

Using the acoustic tweezers system, the following three proof-of-concept experimental studies are performed: (i) the patterning of miscible fluids starting from simple layered configurations into a pattern predicted from the linear acoustic field, (ii) the trapping and moving of a high-concentration miscible-fluid "island" in a medium of lower concentration, and (iii) the study of the dissolution of such a trapped "island" in flow as a function of flow speed and acoustic energy density. In all three cases, the experimental results are compared against the predictive theoretical framework [4], and simulations of the framework allow for a quantitative comparison between theory and experiment.

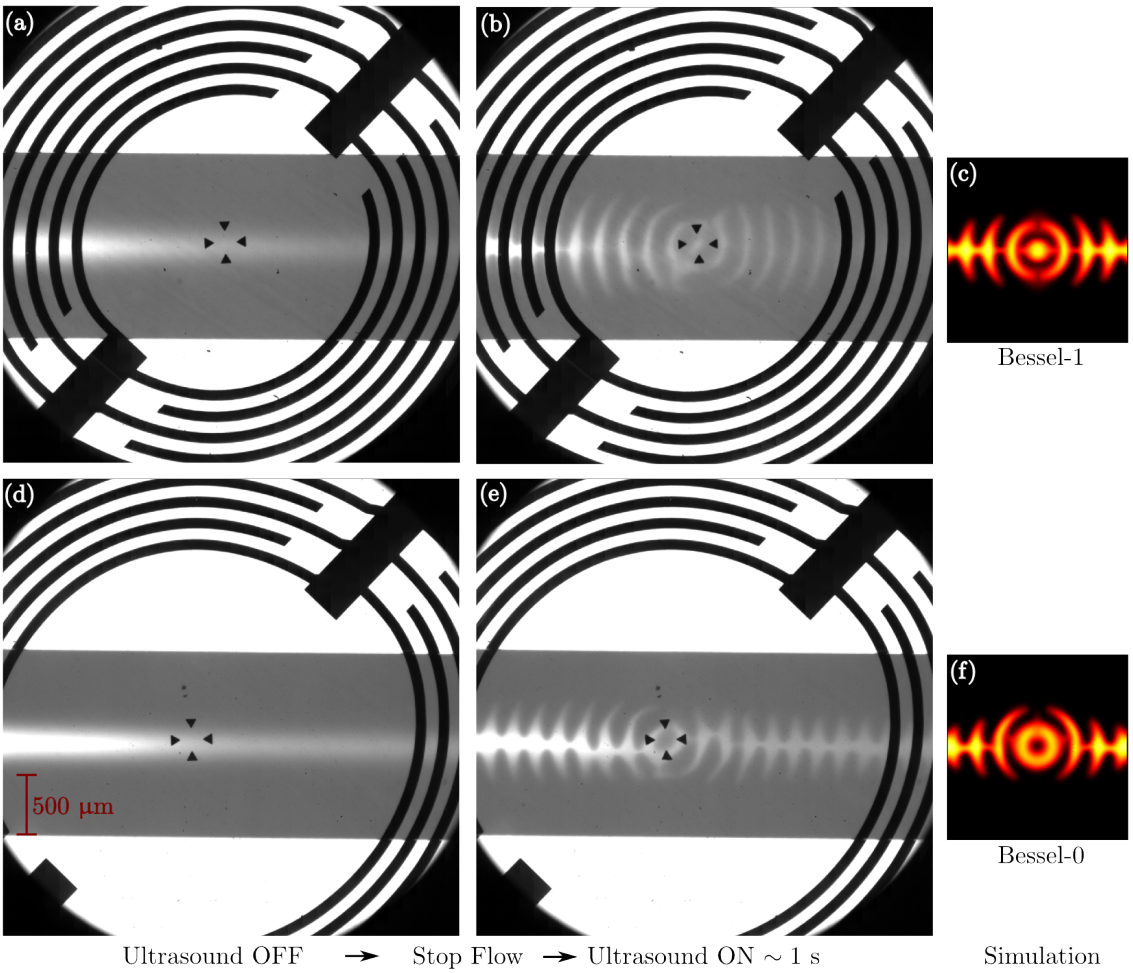

Figure 11.2: Acoustic patterning of inhomogeneous miscible fluids obtained by an initial lamination of 50 w/vol% aqueous Ficoll-PM400 solution (bright fluid) in dyed water (dark fluid) using the integrated acoustic tweezers (black spiraling IDTs). Top: patterning in a Bessel-1 vortex with **(a)** the initial condition, **(b)** the pattern obtained after ~ 1 s with the ultrasound on, and **(c)** the pattern obtained in a preliminary simulation. Bottom: **(d)-(f)** same as top, but in a Bessel-0 vortex. The denser high-concentration Ficoll-PM400 (bright fluid) is focused and evacuated, respectively, from the center of the Bessel-1 and Bessel-0 vortex. Work in progress.

The experimental data has not yet been fully processed, since experimental input required for running quantitatively comparable simulations, e.g, the acoustic energy density and the properties of the Ficoll-PM400 solution as a function of concentration, remain to be measured. New designs of the acoustical tweezers that reduce the anisotropy of the acoustic vortices are furthermore being tested. However, the raw data suggest that all of the operations (i) to (iii) are possible with the right chip design, and that the experiments and the simulations are at least in qualitative agreement. In Fig. 11.2 are shown exper-

imental data for the patterns obtained in Bessel-1 and Bessel-0 vortices, as compared to preliminary simulations.

11.2 Detailed experiments on acoustic streaming in inhomogeneous fluids

This section discusses a recent remarkable finding on acoustic streaming in inhomogeneous fluids related to the experimental study in Paper V [5]. The extended study is carried out by the team of Paper V led by Wei Qiu, Department of Physics, Technical University of Denmark, under supervision of Per Augustsson, Department of Biomedical Engineering, Lund University, and Henrik Bruus, Department of Physics, Technical University of Denmark, with theoretical input and ideas provided by the author of this thesis.

11.2.1 Introduction to the experiments

In Paper V [5], iodixanol solutions were used to create inhomogeneous fluids with relative variations in the density ρ_0 of up to 10% and a nearly constant speed of sound c_0. In the present study, Ficoll solutions are used due to the lower diffusivity of Ficoll as compared to iodixanol, which grants more time to study the transition between inhomogeneous- and homogeneous-fluid streaming in a stop-flow experiment. The relative density variations can be made comparable to those of iodixanol solutions by using different concentrations of Ficoll. However, characterizing the Ficoll properties as a function of concentration, Wei Qiu has pointed out that the variation in speed of sound is not negligible in Ficoll solutions, as it is in iodixanol solutions. The measured streaming flow patterns, as seen in the light of this fact, leads to an interesting hypothesis discussed in the following.

11.2.2 Asymmetric acoustic streaming

In Fig. 11.3 is shown a plot of the raw particle positions in the channel cross-section comparable to those presented in Fig. 2(a) of Paper V [5], but with the initial inhomogeneity at the center of the channel made up of a 10% Ficoll-PM70 solution laminated by pure water at the sides. In this case, the initial density ρ_0 and speed of sound c_0 is, respectively, 3.5% and 1.7% higher at the center as compared to the sides. 500-nm-diameter polystyrene particles are used to track the flow. The particle positions in Fig. 11.3 are plotted at $\tau = 55$ s using the raw data in the symmetric 10 s interval 50 s $\leq \tau \leq$ 60 s, after stopping the flow in $\tau = 0$. The acoustic energy density is $E_{\mathrm{ac}} = 50$ Pa.

Inspecting Fig. 11.3, the streaming patterns are still suppressed, as in Paper V [5], but remarkably, the four streaming rolls are asymmetric along the horizontal width of the channel, with the vortex size Δ being larger near the center as compared to the sides. This feature is consistently reproduced in the experiments with Ficoll solutions. The phenomenon is not yet mapped out in parameter space, and the reason for the asymmetric streaming is not yet clear. However, a hypothesis has been formulated.

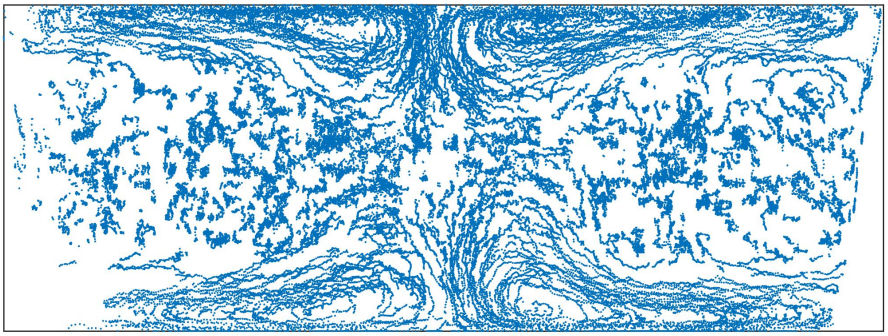

Figure 11.3: Experimental raw particle positions (blue points) in the channel cross-section of width $W = 375$ μm and height $H = 130$ μm (same chip as in Paper V [5]) mapping the acoustic streaming field in the inhomogeneous Ficoll-PM70 solution at time $\tau = 55$ s. Courtesy of Wei Qiu, Technical University of Denmark.

11.2.3 Hypothesis for explaining asymmetric acoustic streaming

The hypothesis seeks to explain the observed asymmetric streaming rolls as being caused by the gradient in the speed of sound c_0, which lead to the presence of a force term in the inhomogeneity-induced part of the acoustic force density $\boldsymbol{f}_{\rm ac}$ that is negligible in iodixanol solutions but not in Ficoll solutions. Indeed, the inhomogeneity-induced part of the acoustic force density, written in the weakly inhomogeneous limit of $\rho_0 = \rho_0^{(0)}[1+\hat{\rho}]$ and $c_0 = c_0^{(0)}[1+\hat{c}]$, with $|\hat{\rho}|, |\hat{c}| \ll 1$, is [4]

$$\boldsymbol{f}_{\rm ac}^{(1)\,\rm invisc} = E_{\rm ac}^{(0)}\Big[R(\boldsymbol{r})\,\boldsymbol{\nabla}\hat{\rho} + C(\boldsymbol{r})\,\boldsymbol{\nabla}\hat{c}\Big], \tag{11.1}$$

where $R(\boldsymbol{r})$ and $C(\boldsymbol{r})$ are the so-called field-shape functions, dependent on the shape of the homogeneous-fluid acoustic field, as introduced in Eq. (10b-c) of Paper IV [4].

Considering the coordinate system with the channel cross-section in $0 < y < W$ and $0 < z < H$, the acoustic field in the fundamental half-wave resonance excited at 2 MHz is in the horizontal y-direction, and the explicit expressions for $R(y)$ and $C(y)$ are [4],

$$R(y) = \cos(2ky), \quad C(y) = 1 + \cos(2ky), \quad \text{with} \quad k = \pi/W. \tag{11.2}$$

Although simple, the functions are plotted in Fig. 11.4. The function $R(y)$ is positive at the sides and negative at the center, explaining the focusing of a dense inhomogeneity from the bottom to the center of the channel [3]. Interestingly, however, $C(y)$ is positive throughout the channel. Since the gradients $\boldsymbol{\nabla}\hat{\rho}$ and $\boldsymbol{\nabla}\hat{c}$ point in the same direction as functions of Ficoll concentration, this means that the addition of the force term proportional to $\boldsymbol{\nabla}\hat{c}$ in Eq. (11.1) reduces the total inhomogeneity-induced acoustic force density $\boldsymbol{f}_{\rm ac}^{(1)\,\rm invisc}$ suppressing streaming near the center of the channel, while enhancing it at the sides. Following the reasoning of Paper V [5], this implies that the vortex size Δ is larger at the center as compared to the sides.

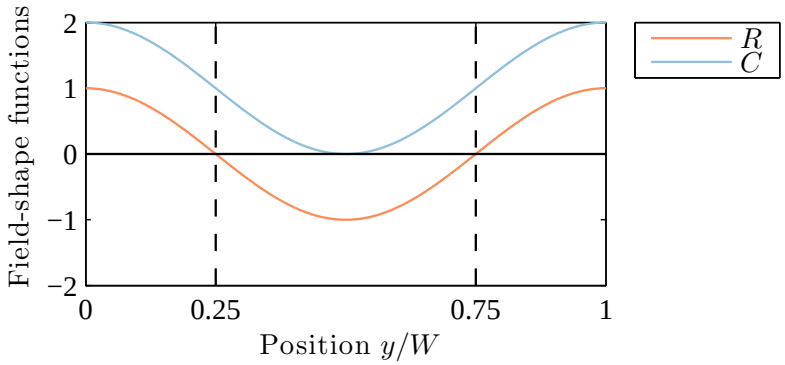

Figure 11.4: Field-shape functions $R(y)$ and $C(y)$, defined from Eq. (11.1), for the acoustic field in the fundamental half-wave resonance in the y-direction along the channel of width W, Eq. (11.2). $R(y)$ is negative at the center of the channel and positive at the sides, while $C(y)$ is positive everywhere.

Thus the hypothesis seems capable of explaining the experimental observation of asymmetric acoustic streaming in Ficoll solutions, Fig. 11.3, in relation to the observed symmetric acoustic streaming in iodixanol solutions [5]. As more experimental data becomes available, the hypothesis can be tested experimentally, as well as by simulations.

Remarkably, the theoretical framework developed in Papers III, IV and V [3, 4, 5] allows for immediate, simple, and transparent hypotheses to be formed about such complex phenomena as the asymmetric suppression of acoustic streaming in acoustically stabilized inhomogeneous fluids with variations in the density and the speed of sound.

Chapter 12

Conclusion and outlook

Conclusion

This thesis has laid the foundation for future studies of acoustofluidics in inhomogeneous fluids by presenting frameworks and methodology for designing and carrying out theoretical, numerical, and experimental studies of acoustofluidics in inhomogeneous fluids with variations in the fluid density and compressibility, e.g., due to a solute concentration field.

Novel analytical results for the acoustic force density acting on inhomogenous fluids have been derived and analyzed. Theoretically, numerically, and experimentally, it has been demonstrated that the non-dissipative inhomogeneity-induced acoustic force density leads to a dynamical relocation and stabilization of inhomogeneities in acoustic fields. It has further been demonstrated that the competition between the dissipative boundary-driven acoustic force density and the inhomogeneity-induced acoustic force density leads to a new class of altered and suppressed acoustic streaming flows, that evolve towards homogeneous-fluid streaming as the inhomogeneity is smeared by diffusion.

To model acoustofluidics in inhomogeneous fluids, the large separation in time scales between the fast-time-scale acoustics and the slow-time-scale hydrodynamics, which includes the acoustic streaming flows, has been used. This method yields a transparent modeling approach that allows the study of the complex slow-time-scale hydrodynamic flows resulting from the external acoustic and gravitational force densities, including effects of advection and diffusion of the solute that introduces the inhomogeneity. In the general case, where viscous inhomogeneous acoustics is considered, the model is a multiple-time-scale model that computes both the fast-time-scale acoustics and the slow-time-scale hydrodynamics resulting from the time-averaged force densities. However, in the weakly-inhomogeneous limit, the fast-time-scale inviscid acoustics is sufficiently described by the homogeneous-fluid acoustic fields, for which simple anaytical solutions exist. This allows the simulation of the slow-time-scale dynamics of weak inhomogeneities in acoustic fields without the need to resolve the acoustic time scale, unless streaming flows are to be included. The outlook points to theoretical work that could potentially allow the inclusion of the dissipative acoustic streaming force densities without the need to resolve the boundary layers on the fast acoustic time scale.

The ability of the acoustic force density to stabilize fluid inhomogeneities made possible the development of a microfluidic analog to density-gradient centrifugation, called iso-acoustic focusing, which was demonstrated for acousto-mechanical phenotyping of single white blood cells and cancer cells in continuous flow.

Experimental work in progress verifies the prediction that acoustic tweezers can be used to actively manipulate miscible-fluid interfaces and concentration fields at the microscale. The experimental work in progress furthermore highlights the utility of the theoretical framework developed in this thesis. Indeed, this framework, although derived from complex nonlinear acoustics equations, is simple enough in interpretation to build a strong physical intuition and form hypotheses about such complex nonlinear phenomena as the focusing of inhomogeneities in acoustic fields, and the asymmetric suppression of boundary-driven acoustic streaming in inhomogeneous fluids with variations in the density and the speed of sound.

In addition to the work on acoustofluidics in inhomogeneous fluids, the thesis also presents analytical results for the acoustic radiation force acting on a particle in an acoustical field in a thermoviscous fluid, thereby extending classical ideal-fluid results to include the effects of the thermal and viscous boundary layers developing around the particle. These boundary layers can lead to order-of-magnitude corrections to the radiation force, and in some cases even cause a sign-change in the radiation force.

Finally, an effort has been made to present a unifying approach to the *theory of nonlinear acoustic forces acting on fluids and particles in microsystems*. Thus, the theoretical results of this thesis on the non-dissipative acoustic force density acting on inhomogeneous fluids, as well as the classical results on the non-dissipative acoustic radiation force acting on a particle or an interface, and the dissipative acoustic force densities driving acoustic streaming, have been derived and discussed in terms of a single principal equation. The principal equation states that the acoustic force density is equal to the negative divergence in the time-averaged acoustic (pseudo-)momentum-flux-density tensor.

Outlook

Suggestions for future experimental work

A more complete experimental validation of the theory of the acoustic force density acting on inhomogeneous fluids is desirable. Using different solutes, the effect of gradients in both the density and the speed of sound on the resultant focusing of inhomogeneities should be studied in relation to the field-shape functions R and C, which would allow validation of the expression for the acoustic force density term by term. The effect on the acoustic streaming field is furthermore of interest.

Acoustofluidics in inhomogeneous fluids could also be studied in a different class of systems, e.g., using traveling surface acoustic waves instead of standing bulk waves, or using systems in which bulk acoustic streaming dominates over boundary-driven streaming. Inhomogeneities could also be introduced differently, e.g., by means of a temperature field instead of a solute concentration field.

Suggestions for future theoretical work

The theory of the generalized acoustic force density acting on inhomogeneous fluids including non-dissipative and dissipative force terms needs further investigation. Quite generally, it would be of interest to investigate the theory from a top-down phenomenological approach, as well as from a bottom-up molecular perspective.

Considering the phenomenological approach, it would be of value to explicitly split the generalized acoustic force density into its dissipative and non-dissipative terms, and to give analytical expressions for the different contributions in the boundary layer as well as in the bulk. Combined with the modeling approach of separation in time scales used in this thesis, such expressions would lead to a particularly transparent formalism for modeling a broad range of acoustofluidic phenomena. While the following equation does not represent a complete description of the generalized acoustic force density $\boldsymbol{f}_{\mathrm{ac}}$, it may describe a useful approach towards separating $\boldsymbol{f}_{\mathrm{ac}}$ into its components. Thus, one may consider equations of the form,

$$\begin{aligned}\boldsymbol{f}_{\mathrm{ac}}(p_1, \boldsymbol{\nabla} p_1, \eta_0, \boldsymbol{\nabla}\rho_0, \boldsymbol{\nabla}\kappa_0) = \; & R(p_1, \boldsymbol{\nabla} p_1)\boldsymbol{\nabla}\rho_0 + K(p_1, \boldsymbol{\nabla} p_1)\boldsymbol{\nabla}\kappa_0 + \boldsymbol{E}(p_1, \boldsymbol{\nabla} p_1)\eta_0 \\ & + \boldsymbol{D}(p_1, \boldsymbol{\nabla} p_1, \eta_0, \boldsymbol{\nabla}\rho_0, \boldsymbol{\nabla}\kappa_0). \end{aligned} \tag{12.1}$$

The sum of the first two terms proportional to $\boldsymbol{\nabla}\rho_0$ and $\boldsymbol{\nabla}\kappa_0$, respectively, is identified as the non-dissipative inhomogeneity-induced acoustic force density described in this thesis, with $R(p_1, \boldsymbol{\nabla} p_1)$ and $K(p_1, \boldsymbol{\nabla} p_1)$ being the generalized field-shape functions. The third term ($\propto \eta_0$) containing $\boldsymbol{E}(p_1, \boldsymbol{\nabla} p_1)$ describes the dissipative acoustic force density associated with acoustic streaming, and it may be split into its boundary-layer and bulk contributions responsible for Rayleigh and Eckart streaming, respectively. The deviation $\boldsymbol{D}(p_1, \boldsymbol{\nabla} p_1, \eta_0, \boldsymbol{\nabla}\rho_0, \boldsymbol{\nabla} c_0)$ describes interactions between the dissipative and non-dissipative force terms, and the difficulty lies in the analytical evaluation of this term. However, in the weakly inhomogeneous limit, where the acoustic fields may be evaluated in the homogeneous fluid, it should be possible. It furthermore seems likely that $\boldsymbol{D}$ is negligible in that limit.

Going further with the phenomenological description, one could consider the effect of gradients in the viscosity η_0, and further introduce the thermal parameters k_{th}, α_p, γ, and c_p into the expression for $\boldsymbol{f}_{\mathrm{ac}}$ in Eq. (12.1). This yields the addition of the thermal damping term in the bulk force density responsible for Eckart streaming. However, because a freely propagating wave propagates nearly adiabatically, the effect of gradients in the viscosity and in the thermal parameters is likely negligible, at least outside of boundary layers.

Considering the theory from a molecular perspective, it would be of considerable fundamental interest to determine if, and under which conditions, the expression for the inhomogeneity-induced acoustic force density can be justified from a molecular Boltzmann transport theory. Such a study may yield additional insights into the fundamental physics of the acoustic force density, and into the hypotheses used in its continuum derivation.

Bibliography

[1] J. T. Karlsen and H. Bruus, *Forces acting on a small particle in an acoustical field in a thermoviscous fluid*. Phys. Rev. E **92**, 043010 (2015).

[2] P. Augustsson, J. T. Karlsen, H.-W. Su, H. Bruus, and J. Voldman, *Iso-acoustic focusing of cells for size-insensitive acousto-mechanical phenotyping*. Nat. Commun. **7**, 11556 (2016).

[3] J. T. Karlsen, P. Augustsson, and H. Bruus, *Acoustic force density acting on inhomogeneous fluids in acoustic fields*. Phys. Rev. Lett. **117**, 114504 (2016).

[4] J. T. Karlsen and H. Bruus, *Acoustic tweezing and patterning of concentration fields in microfluidics*. Phys. Rev. Applied **7**, 034017 (2017).

[5] J. T. Karlsen, W. Qiu, P. Augustsson, and H. Bruus, *Acoustic streaming and its suppression in inhomogeneous fluids*. Phys. Rev. Lett **in press** (accepted 9 January 2018), https://arxiv.org/abs/1707.07369 (revised version included in this thesis).

[6] P. E. Watson, I. D. Watson, and R. D. Batt, *Total body water volumes for adult males and females estimated from simple anthropometric measurements.* The American Journal of Clinical Nutrition **33**(1), 27–39 (1980).

[7] M. Antfolk and T. Laurell, *Continuous flow microfluidic separation and processing of rare cells and bioparticles found in blood - a review*. Anal. Chim. Acta **965**, 9 – 35 (2017).

[8] E. K. Sackmann, A. L. Fulton, and D. J. Beebe, *The present and future role of microfluidics in biomedical research*. Nature **507**, 181 (2014).

[9] H. Bruus, J. Dual, J. Hawkes, M. Hill, T. Laurell, J. Nilsson, S. Radel, S. Sadhal, and M. Wiklund, *Forthcoming lab on a chip tutorial series on acoustofluidics: Acoustofluidics-exploiting ultrasonic standing wave forces and acoustic streaming in microfluidic systems for cell and particle manipulation*. Lab Chip **11**(21), 3579–3580 (2011).

[10] T. Laurell and A. Lenshof, *Microscale Acoustofluidics* (Royal Society of Chemistry) (2014).

[11] J. Friend and L. Y. Yeo, *Microscale acoustofluidics: Microfluidics driven via acoustics and ultrasonics*. Rev. Mod. Phys. **83**(2), 647–704 (2011).

[12] By Electron Microscopy Facility at The National Cancer Institute at Frederick (NCI-Frederick), Public Domain, https://commons.wikimedia.org/w/index.php?curid=407197.

[13] F. K. Balagaddé, L. You, C. L. Hansen, F. H. Arnold, and S. R. Quake, *Long-term monitoring of bacteria undergoing programmed population control in a microchemostat*. Science **309**(5731), 137 (2005).

[14] B. Mostert, S. Sleijfer, J. A. Foekens, and J. W. Gratama, *Circulating tumor cells (ctcs): Detection methods and their clinical relevance in breast cancer*. Cancer Treatment Reviews **35**(5), 463 – 474 (2009).

[15] M. Cristofanilli, G. T. Budd, M. J. Ellis, A. Stopeck, J. Matera, M. C. Miller, J. M. Reuben, G. V. Doyle, W. J. Allard, L. W. Terstappen, and D. F. Hayes, *Circulating tumor cells, disease progression, and survival in metastatic breast cancer*. New England Journal of Medicine **351**(8), 781–791 (2004).

[16] M. Antfolk, C. Magnusson, P. Augustsson, H. Lilja, and T. Laurell, *Acoustofluidic, label-free separation and simultaneous concentration of rare tumor cells from white blood cells*. Anal. Chem. **87**(18), 9322–9328 (2015).

[17] G. Kumar, N. Kumar, A. Taneja, T. Kaleekal, S. Tarima, E. McGinley, E. Jimenez, A. Mohan, R. A. Khan, J. Whittle, E. Jacobs, and R. Nanchal, *Nationwide trends of severe sepsis in the 21st century (2000-2007)*. CHEST **140**(5), 1223–1231 (2011).

[18] G. S. Martin, D. M. Mannino, S. Eaton, and M. Moss, *The epidemiology of sepsis in the united states from 1979 through 2000*. New England Journal of Medicine **348**(16), 1546–1554 (2003).

[19] P. Ohlsson, M. Evander, K. Petersson, L. Mellhammar, A. Lehmusvuori, U. Karhunen, M. Soikkeli, T. Seppä, E. Tuunainen, A. Spangar, P. von Lode, K. Rantakokko-Jalava, G. Otto, S. Scheding, T. Soukka, S. Wittfooth, and T. Laurell, *Integrated acoustic separation, enrichment, and microchip polymerase chain reaction detection of bacteria from blood for rapid sepsis diagnostics*. Anal. Chem. **88**(19), 9403–9411 (2016).

[20] J. Nilsson, M. Evander, B. Hammarström, and T. Laurell, *Review of cell and particle trapping in microfluidic systems*. Analytica Chimica Acta **649**(2), 141–157 (2009).

[21] A. Lenshof and T. Laurell, *Continuous separation of cells and particles in microfluidic systems*. Chem Soc Rev **39**(3), 1203–1217 (2010).

[22] D. Di Carlo, *Inertial microfluidics*. Lab Chip **9**, 3038–3046 (2009).

[23] M. D. Vahey and J. Voldman, *An equilibrium method for continuous-flow cell sorting using dielectrophoresis*. Anal. Chem. **80**(9), 3135–3143 (2008).

[24] N. Pamme and A. Manz, *On-chip free-flow magnetophoresis: Continuous flow separation of magnetic particles and agglomerates*. Anal. Chem. **76**(24), 7250–7256 (2004).

[25] D. G. Grier, *A revolution in optical manipulation*. Nature **424**, 810 (2003).

[26] P. Augustsson, C. Magnusson, M. Nordin, H. Lilja, and T. Laurell, *Microfluidic, label-free enrichment of prostate cancer cells in blood based on acoustophoresis*. Anal. Chem. **84**(18), 7954–7962 (2012).

[27] P. Li, Z. Mao, Z. Peng, L. Zhou, Y. Chen, P.-H. Huang, C. I. Truica, J. J. Drabick, W. S. El-Deiry, M. Dao, S. Suresh, and T. J. Huang, *Acoustic separation of circulating tumor cells*. PNAS **112**(16), 4970–4975 (2015).

[28] B. Hammarström, T. Laurell, and J. Nilsson, *Seed particle enabled acoustic trapping of bacteria and nanoparticles in continuous flow systems*. Lab Chip **12**, 4296–4304 (2012).

[29] D. Carugo, T. Octon, W. Messaoudi, A. L. Fisher, M. Carboni, N. R. Harris, M. Hill, and P. Glynne-Jones, *A thin-reflector microfluidic resonator for continuous-flow concentration of microorganisms: a new approach to water quality analysis using acoustofluidics*. Lab Chip **14**(19), 3830–3842 (2014).

[30] M. Antfolk, P. B. Muller, P. Augustsson, H. Bruus, and T. Laurell, *Focusing of sub-micrometer particles and bacteria enabled by two-dimensional acoustophoresis*. Lab Chip **14**, 2791–2799 (2014).

[31] B. Hammarström, B. Nilson, T. Laurell, J. Nilsson, and S. Ekström, *Acoustic trapping for bacteria identification in positive blood cultures with maldi-tof ms*. Anal. Chem. **86**(21), 10560–10567 (2014).

[32] A. Kumar, D. Roberts, K. E. Wood, B. Light, J. E. Parrillo, S. Sharma, R. Suppes, D. Feinstein, S. Zanotti, L. Taiberg, D. Gurka, A. Kumar, and M. Cheang, *Duration of hypotension before initiation of effective antimicrobial therapy is the critical determinant of survival in human septic shock**. Critical Care Medicine **34**(6) (2006).

[33] M. Nordin and T. Laurell, *Two-hundredfold volume concentration of dilute cell and particle suspensions using chip integrated multistage acoustophoresis*. Lab Chip **12**(22), 4610–4616 (2012).

[34] M. Wiklund, A. E. Christakou, M. Ohlin, I. Iranmanesh, T. Frisk, B. Vanherberghen, and B. Önfelt, *Ultrasound-induced cell-cell interaction studies in a multi-well microplate*. Micromachines **5**(1), 27 (2014).

[35] M. Evander and J. Nilsson, *Acoustofluidics 20: Applications in acoustic trapping*. Lab Chip **12**, 4667–4676 (2012).

[36] P. Augustsson and T. Laurell, *Acoustofluidics 11: Affinity specific extraction and sample decomplexing using continuous flow acoustophoresis.* Lab Chip **12**(10), 1742–1752 (2012).

[37] D. J. Collins, B. Morahan, J. Garcia-Bustos, C. Doerig, M. Plebanski, and A. Neild, *Two-dimensional single-cell patterning with one cell per well driven by surface acoustic waves.* Nat. Commun. **6**, 8686 (2015).

[38] C. Grenvall, C. Magnusson, H. Lilja, and T. Laurell, *Concurrent isolation of lymphocytes and granulocytes using prefocused free flow acoustophoresis.* Anal. Chem. **87**(11), 5596–5604 (2015).

[39] M. Evander, O. Gidlof, B. Olde, D. Erlinge, and T. Laurell, *Non-contact acoustic capture of microparticles from small plasma volumes.* Lab Chip **15**, 2588–2596 (2015).

[40] K. Lee, H. Shao, R. Weissleder, and H. Lee, *Acoustic purification of extracellular microvesicles.* ACS Nano **9**(3), 2321–2327 (2015).

[41] M. A. Burguillos, C. Magnusson, M. Nordin, A. Lenshof, P. Augustsson, M. J. Hansson, E. Elme, H. Lilja, P. Brundin, T. Laurell, and T. Deierborg, *Microchannel acoustophoresis does not impact survival or function of microglia, leukocytes or tumor cells.* PLOS ONE **8**(8), e64233 (2013).

[42] M. Wiklund, *Acoustofluidics 12: Acoustofluidics 12: Biocompatibility and cell viability in microfluidic acoustic resonators.* Lab Chip **12**, 2018–28 (2012).

[43] J.-L. Thomas, R. Marchiano, and D. Baresch, *Acoustical and optical radiation pressure and the development of single beam acoustical tweezers.* Journal of Quantitative Spectroscopy and Radiative Transfer **195**, 55 – 65 (2017).

[44] G. Sitters, D. Kamsma, G. Thalhammer, M. Ritsch-Marte, E. J. G. Peterman, and G. J. L. Wuite, *Acoustic force spectroscopy.* Nat. Meth. **12**(1), 47–50 (2015).

[45] B. W. Drinkwater, *Dynamic-field devices for the ultrasonic manipulation of microparticles.* Lab Chip **16**, 2360–2375 (2016).

[46] T. Laurell, F. Petersson, and A. Nilsson, *Chip integrated strategies for acoustic separation and manipulation of cells and particles.* Chem. Soc. Rev. **36**(3), 492–506 (2007).

[47] P. Augustsson, R. Barnkob, S. T. Wereley, H. Bruus, and T. Laurell, *Automated and temperature-controlled micro-piv measurements enabling long-term-stable microchannel acoustophoresis characterization.* Lab Chip **11**(24), 4152–4164 (2011).

[48] I. Leibacher, S. Schatzer, and J. Dual, *Impedance matched channel walls in acoustofluidic systems.* Lab Chip **14**, 463–470 (2014).

[49] X. Ding, S.-C. S. Lin, B. Kiraly, H. Yue, S. Li, I.-K. Chiang, J. Shi, S. J. Benkovic, and T. J. Huang, *On-chip manipulation of single microparticles, cells, and organisms using surface acoustic waves*. PNAS **109**(28), 11105–11109 (2012).

[50] S. B. Q. Tran, P. Marmottant, and P. Thibault, *Fast acoustic tweezers for the two-dimensional manipulation of individual particles in microfluidic channels*. Appl. Phys. Lett. **101**(11), 114103 (2012).

[51] A. Riaud, J.-L. Thomas, E. Charron, A. Bussonnière, O. Bou Matar, and M. Baudoin, *Anisotropic swirling surface acoustic waves from inverse filtering for on-chip generation of acoustic vortices*. Phys. Rev. Applied **4**, 034004 (2015).

[52] A. Riaud, J.-L. Thomas, M. Baudoin, and O. Bou Matar, *Taming the degeneration of bessel beams at an anisotropic-isotropic interface: Toward three-dimensional control of confined vortical waves*. Phys. Rev. E **92**, 063201 (2015).

[53] A. Riaud, M. Baudoin, O. Bou Matar, L. Becerra, and J.-L. Thomas, *Selective manipulation of microscopic particles with precursor swirling rayleigh waves*. Phys. Rev. Applied **7**, 024007 (2017).

[54] C. R. P. Courtney, C. E. M. Demore, H. Wu, A. Grinenko, P. D. Wilcox, S. Cochran, and B. W. Drinkwater, *Independent trapping and manipulation of microparticles using dexterous acoustic tweezers*. Appl. Phys. Lett. **104**(15), 154103 (2014).

[55] A. Marzo, S. A. Seah, B. W. Drinkwater, D. R. Sahoo, B. Long, and S. Subramanian, *Holographic acoustic elements for manipulation of levitated objects*. Nat. Commun. **6**, 8661 (2015).

[56] D. Baresch, J.-L. Thomas, and R. Marchiano, *Observation of a single-beam gradient force acoustical trap for elastic particles: Acoustical tweezers*. Phys. Rev. Lett. **116**, 024301 (2016).

[57] K. Melde, A. G. Mark, T. Qiu, and P. Fischer, *Holograms for acoustics*. Nature **537**(7621), 518–522 (2016).

[58] A. Franklin, A. Marzo, R. Malkin, and B. W. Drinkwater, *Three-dimensional ultrasonic trapping of micro-particles in water with a simple and compact two-element transducer*. Appl. Phys. Lett. **111**(9), 094101 (2017).

[59] P. Hahn, I. Leibacher, T. Baasch, and J. Dual, *Numerical simulation of acoustofluidic manipulation by radiation forces and acoustic streaming for complex particles*. Lab Chip **15**, 4302–4313 (2015).

[60] J. W. Strutt, Baron Rayleigh, *The theory of sound volume I* (Macmillan and co, London), 2nd edn. (1894).

[61] T. M. Squires and S. R. Quake, *Microfluidics: Fluid physics at the nanoliter scale*. Rev. Mod. Phys. **77**, 977–1026 (2005).

[62] H. Bruus, *Theoretical Microfluidics* (Oxford University Press, Oxford) (2008).

[63] P. S. Epstein and R. R. Carhart, *The absorption of sound in suspensions and emulsions. I. water fog in air*. J. Acoust. Soc. Am. **25**, 553–565 (1953).

[64] J. Allegra and S. Hawley, *Attenuation of sound in suspensions and emulsions - theory and experiments*. J. Acoust. Soc. Am. **51**(5), 1545–1564 (1972).

[65] L. D. Landau and E. M. Lifshitz, *Statistical Physics, Part 1*, vol. 5 (Butterworth-Heinemann, Oxford), 3rd edn. (1980).

[66] L. D. Landau and E. M. Lifshitz, *Theory of Elasticity. Course of Theoretical Physics*, vol. 7 (Pergamon Press, Oxford), 3rd edn. (1986).

[67] P. M. Morse and K. U. Ingard, *Theoretical Acoustics* (Princeton University Press, Princeton NJ) (1986).

[68] W. W. L. Au, A. A. Pack, M. O. Lammers, L. M. Herman, M. H. Deakos, and K. Andrews, *Acoustic properties of humpback whale songs*. J. Acoust. Soc. Am. **120**(2), 1103–1110 (2006).

[69] A. Širović, J. A. Hildebrand, and S. M. Wiggins, *Blue and fin whale call source levels and propagation range in the southern ocean*. J. Acoust. Soc. Am. **122**(2), 1208–1215 (2007).

[70] National Research Council, *Ocean Noise and Marine Mammals* (The National Academies Press, Washington, DC) (2003).

[71] R. Barnkob, P. Augustsson, T. Laurell, and H. Bruus, *Measuring the local pressure amplitude in microchannel acoustophoresis*. Lab Chip **10**(5), 563–570 (2010).

[72] J. van't Oever, R. Frentrop, D. Wijnperlé, H. Offerhaus, D. van den Ende, J. Herek, and F. Mugele, *Imaging local acoustic pressure in microchannels*. Appl. Opt. **54**(21), 6482–6490 (2015).

[73] S. Lakämper, A. Lamprecht, I. A. T. Schaap, and J. Dual, *Direct 2d measurement of time-averaged forces and pressure amplitudes in acoustophoretic devices using optical trapping*. Lab Chip **15**, 290–300 (2015).

[74] A. Lamprecht, S. Lakamper, T. Baasch, I. A. T. Schaap, and J. Dual, *Imaging the position-dependent 3d force on microbeads subjected to acoustic radiation forces and streaming*. Lab Chip **16**, 2682–2693 (2016).

[75] M. Wiklund, R. Green, and M. Ohlin, *Acoustofluidics 14: Applications of acoustic streaming in microfluidic devices*. Lab Chip **12**, 2438–2451 (2012).

[76] M. Faraday, *On a peculiar class of acoustical figures; and on certain forms assumed by groups of particles upon vibrating elastic surfaces*. Philos. Trans. R. Soc. London **121**, 299–340 (1831).

[77] Lord Rayleigh, *On the circulation of air observed in Kundt's tubes, and on some allied acoustical problems*. Philos. Trans. R. Soc. London **175**, 1–21 (1884).

[78] H. Schlichting, *Berechnung ebener periodischer grenzeschichtströmungen*. Phys. Z. **33**, 327–335 (1932).

[79] P. B. Muller, M. Rossi, A. G. Marín, R. Barnkob, P. Augustsson, T. Laurell, C. J. Kähler, and H. Bruus, *Ultrasound-induced acoustophoretic motion of microparticles in three dimensions*. Phys. Rev. E **88**, 023006 (2013).

[80] P. Tho, R. Manasseh, and A. Ooi, *Cavitation microstreaming patterns in single and multiple bubble systems*. J. Fluid Mech. **576**, 191–233 (2007).

[81] C. Eckart, *Vortices and streams caused by sound waves*. Phys. Rev. **73**, 68–76 (1948).

[82] A. Riaud, M. Baudoin, O. Bou Matar, J.-L. Thomas, and P. Brunet, *On the influence of viscosity and caustics on acoustic streaming in sessile droplets: an experimental and a numerical study with a cost-effective method*. J. Fluid Mech. **821**, 384–420 (2017).

[83] W. L. Nyborg, *Acoustic streaming due to attenuated plane waves*. J. Acoust. Soc. Am. **25**(1), 68–75 (1953).

[84] W. L. Nyborg, *Acoustic streaming near a boundary*. J. Acoust. Soc. Am. **30**(4), 329–339 (1958).

[85] J. Lighthill, *Acoustic streaming*. J Sound Vibr **61**(3), 391–418 (1978).

[86] N. Riley, *Steady streaming*. Annu. Rev. Fluid Mech. **33**, 43–65 (2001).

[87] G. Swift, *Thermoacoustic engines*. J. Acoust. Soc. Am. **84**(4), 1145–1180 (1988).

[88] M. Hamilton, Y. Ilinskii, and E. Zabolotskaya, *Acoustic streaming generated by standing waves in two-dimensional channels of arbitrary width*. J. Acoust. Soc. Am. **113**(1), 153–160 (2003).

[89] M. Hamilton, Y. Ilinskii, and E. Zabolotskaya, *Thermal effects on acoustic streaming in standing waves*. J. Acoust. Soc. Am. **114**(6, Part 1), 3092–3101 (2003).

[90] A. A. Doinikov and A. Bouakaz, *Theoretical investigation of shear stress generated by a contrast microbubble on the cell membrane as a mechanism for sonoporation*. J. Acoust. Soc. Am. **128**(1), 11–19 (2010).

[91] J. Wu and W. L. Nyborg, *Ultrasound, cavitation bubbles and their interaction with cells*. Adv. Drug Deliv. Rev. **60**(10), 1103 – 1116 (2008).

[92] P. Marmottant and S. Hilgenfeldt, *Controlled vesicle deformation and lysis by single oscillating bubbles*. Nature **423**(6936), 153–156 (2003).

[93] R. Barnkob, P. Augustsson, T. Laurell, and H. Bruus, *Acoustic radiation- and streaming-induced microparticle velocities determined by microparticle image velocimetry in an ultrasound symmetry plane*. Phys. Rev. E **86**, 056307 (2012).

[94] A. Marin, M. Rossi, B. Rallabandi, C. Wang, S. Hilgenfeldt, and C. J. Kähler, *Three-dimensional phenomena in microbubble acoustic streaming*. Phys. Rev. Applied **3**, 041001 (2015).

[95] F. Guo, Z. Mao, Y. Chen, Z. Xie, J. P. Lata, P. Li, L. Ren, J. Liu, J. Yang, M. Dao, S. Suresh, and T. J. Huang, *Three-dimensional manipulation of single cells using surface acoustic waves*. PNAS **113**(6), 1522–1527 (2016).

[96] L. D. Landau and E. M. Lifshitz, *Fluid Mechanics*, vol. 6 (Pergamon Press, Oxford), 2nd edn. (1993).

[97] C. Lee and T. Wang, *Near-boundary streaming around a small sphere due to 2 orthogonal standing waves*. J. Acoust. Soc. Am. **85**(3), 1081–1088 (1989).

[98] J. Lei, M. Hill, and P. Glynne-Jones, *Numerical simulation of 3d boundary-driven acoustic streaming in microfluidic devices*. Lab Chip **14**(3), 532–541 (2014).

[99] J. Lei, P. Glynne-Jones, and M. Hill, *Comparing methods for the modelling of boundary-driven streaming in acoustofluidic devices*. Microfluidics and Nanofluidics **21**(2), 23 (2017).

[100] M. W. H. Ley, *Effective modelling of acoustofluidic devices*. PhD thesis, Department of Physics, Technical University of Denmark (2017).

[101] L. V. King, *On the acoustic radiation pressure on spheres*. Proc. R. Soc. London, Ser. A **147**(861), 212–240 (1934).

[102] K. Yosioka and Y. Kawasima, *Acoustic radiation pressure on a compressible sphere*. Acustica **5**, 167–173 (1955).

[103] L. P. Gorkov, *On the forces acting on a small particle in an acoustical field in an ideal fluid*. Sov. Phys.–Dokl. **6**(9), 773–775 (1962), [Doklady Akademii Nauk SSSR **140**, 88 (1961)].

[104] F. Petersson, L. Åberg, A. M. Sward-Nilsson, and T. Laurell, *Free flow acoustophoresis: microfluidic-based mode of particle and cell separation*. Anal. Chem. **79**(14), 5117–23 (2007).

[105] C. Grenvall, P. Augustsson, J. R. Folkenberg, and T. Laurell, *Harmonic microchip acoustophoresis: A route to online raw milk sample precondition in protein and lipid content quality control*. Anal. Chem. **81**(15), 6195–6200 (2009).

[106] Y. Liu, D. Hartono, and K.-M. Lim, *Cell separation and transportation between two miscible fluid streams using ultrasound*. Biomicrofluidics **6**(1), 012802 (2012).

[107] I. Leibacher, P. Hahn, and J. Dual, *Acoustophoretic cell and particle trapping on microfluidic sharp edges.* Microfluid Nanofluid **19**(4), 923–933 (2015).

[108] C. R. P. Courtney, B. W. Drinkwater, C. E. M. Demore, S. Cochran, A. Grinenko, and P. D. Wilcox, *Dexterous manipulation of microparticles using bessel-function acoustic pressure fields.* Appl. Phys. Lett. **102**, 123508 (2013).

[109] C. E. M. Démoré, P. M. Dahl, Z. Yang, P. Glynne-Jones, A. Melzer, S. Cochran, M. P. MacDonald, and G. C. Spalding, *Acoustic tractor beam.* Phys. Rev. Lett. **112**, 174302 (2014).

[110] E. H. Brandt, *Acoustic physics. Suspended by sound.* Nature **413**(6855), 474–5 (2001).

[111] W. Xie and B. Wei, *Parametric study of single-axis acoustic levitation.* Appl. Phys. Lett. **79**(6), 881–883 (2001).

[112] D. Foresti, M. Nabavi, M. Klingauf, A. Ferrari, and D. Poulikakos, *Acoustophoretic contactless transport and handling of matter in air.* PNAS **110**(31), 12549–12554 (2013).

[113] D. Foresti and D. Poulikakos, *Acoustophoretic Contactless Elevation, Orbital Transport and Spinning of Matter in Air.* Phys. Rev. Lett. **112**(2), 024301 (2014).

[114] R. J. Imani and E. Robert, *Acoustic separation of submicron solid particles in air.* Ultrasonics **63**, 135 – 140 (2015).

[115] R. S. Budwig, M. J. Anderson, G. Putnam, and C. Manning, *Ultrasonic particle size fractionation in a moving air stream.* Ultrasonics **50**(1), 26 – 31 (2010).

[116] M. Anderson, R. S. Budwig, K. Line, and J. Frankel, *Use of acoustic radiation pressure to concentrate small particles in an air flow.* Proc. Ultrasonics Symp. IEEE **1**, 481–484 (2002).

[117] A. A. Doinikov, *Acoustic radiation force on a spherical particle in a viscous heat-conducting fluid .1. general formula.* J. Acoust. Soc. Am. **101**(2), 713–721 (1997).

[118] S. D. Danilov and M. A. Mironov, *Mean force on a small sphere in a sound field in a viscous fluid.* J. Acoust. Soc. Am. **107**(1), 143–153 (2000).

[119] M. Settnes and H. Bruus, *Forces acting on a small particle in an acoustical field in a viscous fluid.* Phys. Rev. E **85**, 016327 (2012).

[120] T. Hasegawa, *Acoustic radiation force on a sphere in a quasistationary wave field-theory.* J. Acoust. Soc. Am. **65**(1), 32–40 (1979).

[121] D. Baresch, J.-L. Thomas, and R. Marchiano, *Three-dimensional acoustic radiation force on an arbitrarily located elastic sphere.* J. Acoust. Soc. Am. **133**(1), 25–36 (2013).

[122] A. A. Doinikov, *Acoustic radiation pressure on a compressible sphere in a viscous fluid.* J. Fluid Mech. **267**(1), 1 (1994).

[123] A. A. Doinikov, *Acoustic radiation force on a spherical particle in a viscous heat-conducting fluid .2. force on a rigid sphere.* J. Acoust. Soc. Am. **101**(2), 722–730 (1997).

[124] A. A. Doinikov, *Acoustic radiation force on a spherical particle in a viscous heat-conducting fluid. 3. Force on a liquid drop.* J. Acoust. Soc. Am. **101**(2), 731–740 (1997).

[125] R. E. Challis, M. J. W. Povey, M. L. Mather, and A. K. Holmes, *Ultrasound techniques for characterizing colloidal dispersions.* Rep. Prog. Phys. **68**(7), 1541–1637 (2005).

[126] P. Glynne-Jones, P. P. Mishra, R. J. Boltryk, and M. Hill, *Efficient finite element modeling of radiation forces on elastic particles of arbitrary size and geometry.* J. Acoust. Soc. Am. **133**(4), 1885–1893 (2013).

[127] S. Annamalai, S. Balachandar, and M. K. Parmar, *Mean force on a finite-sized spherical particle due to an acoustic field in a viscous compressible medium.* Phys. Rev. E **89**, 053008 (2014).

[128] A. Lenshof, C. Magnusson, and T. Laurell, *Acoustofluidics 8: Applications in acoustophoresis in continuous flow microsystems.* Lab Chip **12**, 1210–1223 (2012).

[129] P. Thevoz, J. D. Adams, H. Shea, H. Bruus, and H. T. Soh, *Acoustophoretic synchronization of mammalian cells in microchannels.* Anal. Chem. **82**(7), 3094–3098 (2010).

[130] C. W. Shields, L. M. Johnson, L. Gao, and G. P. Lopez, *Elastomeric negative acoustic contrast particles for capture, acoustophoretic transport, and confinement of cells in microfluidic systems.* Langmuir **30**(14), 3923–3927 (2014).

[131] J. D. Adams and H. T. Soh, *Tunable acoustophoretic band-pass particle sorter.* Appl. Phys. Lett. **97**(6), 064103 (2010).

[132] R. Barnkob, C. J. Kahler, and M. Rossi, *General defocusing particle tracking.* Lab Chip **15**, 3556–3560 (2015).

[133] S. M. Hagsäter, T. G. Jensen, H. Bruus, and J. P. Kutter, *Acoustic resonances in microfluidic chips: full-image micro-PIV experiments and numerical simulations.* Lab Chip **7**(10), 1336–1344 (2007).

[134] P. B. Muller, R. Barnkob, M. J. H. Jensen, and H. Bruus, *A numerical study of microparticle acoustophoresis driven by acoustic radiation forces and streaming-induced drag forces.* Lab Chip **12**, 4617–4627 (2012).

[135] N. Nama, R. Barnkob, Z. Mao, C. J. Kähler, F. Costanzo, and T. J. Huang, *Numerical study of acoustophoretic motion of particles in a pdms microchannel driven by surface acoustic waves.* Lab Chip **15**, 2700 (2015).

[136] M. W. H. Ley and H. Bruus, *Continuum modeling of hydrodynamic particle-particle interactions in microfluidic high-concentration suspensions.* Lab Chip **16**, 1178–1188 (2016).

[137] H. Faxén, *The resistance against the movement of a rigour sphere in viscous fluids, which is embedded between two parallel layered barriers.* Ann Phys **68**(10), 89–119 (1922).

[138] H. Brenner, *The slow motion of a sphere through a viscous fluid towards a plane surface.* Chem Eng Sci **16**, 242–251 (1961).

[139] M. Hoyos and A. Castro, *Controlling the acoustic streaming by pulsed ultrasounds.* Ultrasonics **53**, 70 (2013).

[140] P. B. Muller and H. Bruus, *Theoretical study of time-dependent, ultrasound-induced acoustic streaming in microchannels.* Phys. Rev. E **92**, 063018 (2015).

[141] Z. Mao, P. Li, M. Wu, H. Bachman, N. Mesyngier, X. Guo, S. Liu, F. Costanzo, and T. J. Huang, *Enriching nanoparticles via acoustofluidics.* ACS Nano **11**(1), 603–612 (2017).

[142] D. J. Collins, Z. Ma, J. Han, and Y. Ai, *Continuous micro-vortex-based nanoparticle manipulation via focused surface acoustic waves.* Lab Chip **17**, 91–103 (2017).

[143] C. P. Nielsen, *Introduction to weak form modeling in COMSOL ver. 1.3.* Department of Physics, Technical University of Denmark (2013).

[144] H. Bruus, *Lecture notes for DTU course 10350: Numerical studies in physics ver. 6.* Department of Physics, Technical University of Denmark (2018).

[145] COMSOL Multiphysics 5.2, www.comsol.com (2015).

[146] P. B. Muller and H. Bruus, *Numerical study of thermoviscous effects in ultrasound-induced acoustic streaming in microchannels.* Phys. Rev. E **90**(4), 043016 (2014).

[147] R. T. Beyer, *Radiation pressure – the history of a mislabeled tensor.* J. Acoust. Soc. Am. **63**(4), 1025–1030 (1978).

[148] L. Brillouin, *Tensors in Mechanics and Elasticity* (Academic, New York) (1964).

[149] C. P. Lee and T. G. Wang, *Acoustic radiation pressure.* J. Acoust. Soc. Am. **94**(2), 1099–1109 (1993).

[150] B. L. Smith and G. W. Swift, *Measuring second-order time-average pressure.* J. Acoust. Soc. Am. **110**(2), 717–723 (2001).

[151] S. R. de Groot and P. Mazur, *Non-equilibrium thermodynamics* (Dover) (1984).

[152] N. Bertin, H. Chraïbi, R. Wunenburger, J.-P. Delville, and E. Brasselet, *Universal morphologies of fluid interfaces deformed by the radiation pressure of acoustic or electromagnetic waves.* Phys. Rev. Lett. **109**, 244304 (2012).

[153] Z. Fan, D. Mei, K. Yang, and Z. Chen, *Acoustic radiation torque on an irregularly shaped scatterer in an arbitrary sound field.* J. Acoust. Soc. Am. **124**(5), 2727–2732 (2008).

[154] E. M. Darling and D. D. Carlo, *High-throughput assessment of cellular mechanical properties.* Annu. Rev. Biomed. Eng. **17**(1), 35–62 (2015).

[155] W. H. Grover, A. K. Bryan, M. Diez-Silva, S. Suresh, J. M. Higgins, and S. R. Manalis, *Measuring single-cell density.* PNAS **108**(27), 10992–10996 (2011).

[156] A. K. Bryan, A. Goranov, A. Amon, and S. R. Manalis, *Measurement of mass, density, and volume during the cell cycle of yeast.* PNAS **107**(3), 999–1004 (2010).

[157] S. Deshmukh, Z. Brzozka, T. Laurell, and P. Augustsson, *Acoustic radiation forces at liquid interfaces impact the performance of acoustophoresis.* Lab Chip **14**, 3394–3400 (2014).

[158] J. T. Karlsen, *Theory of thermoviscous acoustofluidics in microsystems.* MSc thesis, Department of Physics, Technical University of Denmark (2014).

[159] H. Bruus, *Acoustofluidics 1: Governing equations in microfluidics.* Lab Chip **11**, 3742 – 3751 (2011).

[160] L. Schmid, D. A. Weitz, and T. Franke, *Sorting drops and cells with acoustics: acoustic microfluidic fluorescence-activated cell sorter.* Lab Chip **14**, 3710–3718 (2014).

[161] V. Vandaele, P. Lambert, and A. Delchambre, *Non-contact handling in microassembly: Acoustical levitation.* Precis. Eng. **29**(4), 491–505 (2005).

[162] L. L. Foldy, *The multiple scattering of waves. i. general theory of isotropic scattering by randomly distributed scatterers.* Phys. Rev. **67**(3-4), 107–119 (1945).

[163] P. Lloyd and M. V. Berry, *Wave propagation through an assembly of spheres: IV. Relations between different multiple scattering theories.* Proc. Phys. Soc. **91**(3), 678–688 (1967).

[164] D. J. McClements and M. J. W. Povey, *Scattering of ultrasound by emulsions.* J. Phys. D **22**(1), 38–47 (1989).

[165] V. J. Pinfield, *Acoustic scattering in dispersions: improvements in the calculation of single particle scattering coefficients.* J. Acoust. Soc. Am. **122**(1), 205–221 (2007).

[166] W. Wagner and A. Pruss, *The iapws formulation 1995 for the thermodynamic properties of ordinary water substance for general and scientific use.* J. Phys. Chem. Ref. Data **31**(2), 387–535 (2002).

[167] M. L. Huber, R. A. Perkins, A. Laesecke, D. G. Friend, J. V. Sengers, M. J. Assael, I. N. Metaxa, E. Vogel, R. Mares, and K. Miyagawa, *New international formulation for the viscosity of h2o.* J. Phys. Chem. Ref. Data **38**(2), 101–125 (2009).

[168] M. L. Huber, R. A. Perkins, D. G. Friend, J. V. Sengers, M. J. Assael, I. N. Metaxa, K. Miyagawa, R. Hellmann, and E. Vogel, *New international formulation for the thermal conductivity of h2o.* J. Phys. Chem. Ref. Data **41**(3), 033102 (2012).

[169] J. N. Coupland and D. J. McClements, *Physical properties of liquid edible oils.* J. Am. Oil Chem. Soc. **74**, 1559–1564 (1997).

[170] E. S. Domalski and E. D. Hearing, *Heat Capacities and Entropies of Organic Compounds in the Condensed Phase. Volume III.* J. Phys. Chem. Ref. Data **25**(1), 1 (1996).

[171] S. S. Chang and A. B. Bestul, *Heat capacities for atactic polystyrene of narrow molecular weight distribution to 360Â˚K.* J. Polym. Sci. A-2 Polym. Phys. **6**(5), 849–860 (1968).

[172] M. J. Holmes, N. G. Parker, and M. J. W. Povey, *Temperature dependence of bulk viscosity in water using acoustic spectroscopy.* J. Phys. Conf. Ser. **269**(1), 012011 (2011).

[173] R. Chanamai and D. J. Mcclements, *Ultrasonic attenuation of edible oils.* J. Am. Oil Chem. Soc. **75**(10), 1447–1448 (1998).

[174] G. Prangsma, A. Alberga, and J. Beenakker, *Ultrasonic determination of the volume viscosity of N2, CO, CH4 and CD4 between 77 and 300 K.* Physica **64**(2), 278–288 (1973).

[175] W. Ran and J. R. Saylor, *The directional sensitivity of the acoustic radiation force to particle diameter.* J. Acoust. Soc. Am. **137**(6), 3288 (2015).

[176] G. B. Arfken and H. J. Weber, *Mathematical Methods for Physicists* (Elsevier, New York), 6th edn. (2005).

[177] O. Otto, P. Rosendahl, A. Mietke, S. Golfier, C. Herold, D. Klaue, S. Girardo, S. Pagliara, A. Ekpenyong, A. Jacobi, M. Wobus, N. Topfner, U. F. Keyser, J. Mansfeld, E. Fischer-Friedrich, and J. Guck, *Real-time deformability cytometry: on-the-fly cell mechanical phenotyping.* Nat. Meth. **12**, 199–202 (2015).

[178] O. Manneberg, B. Vanherberghen, J. Svennebring, H. M. Hertz, B. Onfelt, and M. Wiklund, *A three-dimensional ultrasonic cage for characterization of individual cells.* Appl Phys Lett **93**(6), 063901–3 (2008).

[179] X. Ding, Z. Peng, S.-C. S. Lin, M. Geri, S. Li, P. Li, Y. Chen, M. Dao, S. Suresh, and T. J. Huang, *Cell separation using tilted-angle standing surface acoustic waves.* PNAS **111**(36), 12992–12997 (2014).

[180] M. A. H. Weiser and R. E. Apfel, *Extension of acoustic levitation to include the study of micron-size particles in a more compressible host liquid.* J. Acoust. Soc. Am. **71**(5), 1261–1268 (1982).

[181] D. Hartono, Y. Liu, P. L. Tan, X. Y. S. Then, L.-Y. L. Yung, and K.-M. Lim, *On-chip measurements of cell compressibility via acoustic radiation.* Lab Chip **11**, 4072–4080 (2011).

[182] F. Petersson, A. Nilsson, C. Holm, H. Jönsson, and T. Laurell, *Separation of lipids from blood utilizing ultrasonic standing waves in microfluidic channels.* Analyst **129**(10), 938–43 (2004).

[183] A. Nilsson, F. Petersson, H. Jönsson, and T. Laurell, *Acoustic control of suspended particles in micro fluidic chips.* Lab Chip **4**(2), 131–5 (2004).

[184] O. Manneberg, S. M. Hagsäter, J. Svennebring, H. M. Hertz, J. P. Kutter, H. Bruus, and M. Wiklund, *Spatial confinement of ultrasonic force fields in microfluidic channels.* Ultrasonics **49**(1), 112–119 (2009).

[185] G. Hertz and H. Mende, *Der schallstrahlungsdruck in flüssigkeiten.* Z. Phys. **114**(5), 354–367 (1939).

[186] K. Bücks and H. Müller, *über einige beobachtungen an schwingenden piezoquarzen und ihrem schallfeld.* Z. Phys. **84**(1-2), 75–86 (1933).

[187] A. Hanson, E. Domich, and H. Adams, *Acoustical liquid drop holder.* Rev. Sci. Instrum. **35**(8), 1031–1034 (1964).

[188] A. Y. Rednikov and S. S. Sadhal, *Acoustic/steady streaming from a motionless boundary and related phenomena: generalized treatment of the inner streaming and examples.* J. Fluid. Mech. **667**, 426–462 (2011).

[189] D. Ahmed, A. Ozcelik, N. Bojanala, N. Nama, A. Upadhyay, Y. Chen, W. Hanna-Rose, and T. J. Huang, *Rotational manipulation of single cells and organisms using acoustic waves.* Nat. Commun. **7**, 11085 (2016).

[190] M. F. Hamilton and D. T. Blackstock (eds.), *Nonlinear Acoustics* (Acoustical Society of America, Melville, NY) (2008).

[191] M. J. Marr-Lyon, D. B. Thiessen, and P. L. Marston, *Passive stabilization of capillary bridges in air with acoustic radiation pressure.* Phys. Rev. Lett. **86**, 2293–2296 (2001).

[192] H. Bruus, *Acoustofluidics 2: Perturbation theory and ultrasound resonance modes.* Lab Chip **12**, 20–28 (2012).

[193] P. G. Bergmann, *The wave equation in a medium with a variable index of refraction.* J. Acoust. Soc. Am. **17**(4), 329–333 (1946).

[194] L. Zhang and P. L. Marston, *Acoustic radiation torque and the conservation of angular momentum (l).* J. Acoust. Soc. Am. **129**(4), 1679–1680 (2011).

[195] T. M. Keenan and A. Folch, *Biomolecular gradients in cell culture systems.* Lab Chip **8**, 34–57 (2008).

[196] S. Takayama, J. C. McDonald, E. Ostuni, M. N. Liang, P. J. A. Kenis, R. F. Ismagilov, and G. M. Whitesides, *Patterning cells and their environments using multiple laminar fluid flows in capillary networks.* PNAS **96**(10), 5545–5548 (1999).

[197] S. K. W. Dertinger, D. T. Chiu, N. L. Jeon, and G. M. Whitesides, *Generation of gradients having complex shapes using microfluidic networks.* Anal. Chem. **73**(6), 1240–1246 (2001).

[198] A. L. Bernassau, C. R. P. Courtney, J. Beeley, B. W. Drinkwater, and D. R. S. Cumming, *Interactive manipulation of microparticles in an octagonal sonotweezer.* Appl. Phys. Lett. **102**(16), 164101 (2013).

[199] B. T. Hefner and P. L. Marston, *An acoustical helicoidal wave transducer with applications for the alignment of ultrasonic and underwater systems.* J. Acoust. Soc. Am. **106**(6), 3313–3316 (1999).

[200] G. P. Chini, Z. Malecha, and T. D. Dreeben, *Large-amplitude acoustic streaming.* J. Fluid Mech. **744**, 329–351 (2014).

[201] O. Manneberg, B. Vanherberghen, B. Onfelt, and M. Wiklund, *Flow-free transport of cells in microchannels by frequency-modulated ultrasound.* Lab Chip **9**(6), 833–837 (2009).

[202] J. Atencia and D. J. Beebe, *Controlled microfluidic interfaces.* Nature **437**, 648–655 (2005).

[203] J. Brody, P. Yager, R. Goldstein, and R. Austin, *Biotechnology at low reynolds numbers.* Biophysical Journal **71**(6), 3430 – 3441 (1996).

[204] J. P. Brody and P. Yager, *Diffusion-based extraction in a microfabricated device.* Sensors and Actuators A **58**(1), 13 – 18 (1997).

[205] B. H. Weigl and P. Yager, *Microfluidic diffusion-based separation and detection.* Science **283**(5400), 346–347 (1999).

[206] A. Hatch, A. E. Kamholz, K. R. Hawkins, M. S. Munson, E. A. Schilling, B. H. Weigl, and P. Yager, *A rapid diffusion immunoassay in a t-sensor.* Nature Biotechnology **19**, 461–465 (2001).

[207] A. E. Kamholz, B. H. Weigl, B. A. Finlayson, and P. Yager, *Quantitative analysis of molecular interaction in a microfluidic channel: The t-sensor*. Anal. Chem. **71**(23), 5340–5347 (1999).

[208] K. Choi, A. H. Ng, R. Fobel, and A. R. Wheeler, *Digital microfluidics*. Annu. Rev. Anal. Chem. **5**(1), 413–440 (2012).